Phase-Coded FMCW for Automotive Radars

Kumbul, U.

DOI
10.4233/uuid:1a678f17-c9c5-46c7-aca2-0dea1f00d1fa

Publication date
2023

Document Version
Final published version

Citation (APA)
Kumbul, U. (2023). *Phase-Coded FMCW for Automotive Radars*. [Dissertation (TU Delft), Delft University of Technology]. https://doi.org/10.4233/uuid:1a678f17-c9c5-46c7-aca2-0dea1f00d1fa

Phase-Coded FMCW for Automotive Radars

Utku Kumbul

PHASE-CODED FMCW FOR AUTOMOTIVE RADARS

PHASE-CODED FMCW FOR AUTOMOTIVE RADARS

Dissertation

for the purpose of obtaining the degree of doctor
at Delft University of Technology
by the authority of the Rector Magnificus, Prof. dr. ir. T.H.J.J. van der Hagen,
chair of the Board for Doctorates
to be defended publicly on
Wednesday 15 March 2023 at 17:30 o'clock

by

Utku KUMBUL

Master of Science in Electrical and Electronics Engineering,
TOBB University of Economics and Technology, Turkey
born in Antalya, Turkey

This dissertation has been approved by the promotors.

Composition of the doctoral committee:

Rector Magnificus,	chairperson
Prof. dr. A. Yarovoy	Delft University of Technology, promotor
Prof. dr. C. S. Vaucher	Delft University of Technology, promotor
Dr. N. Petrov	Delft University of Technology, copromotor

Independent members:

Prof. dr. ir. M. Vossiek	Friedrich Alexander Universität Erlangen, Germany
Prof. dr. ir. K. Doris	Eindhoven University of Technology
Prof. dr. ir. F.M.J. Willems	Eindhoven University of Technology
Prof. dr. L.C.N. de Vreede	Delft University of Technology
Prof. dr. ir. G.J.T. Leus	Delft University of Technology, reserve member

This work is part of the research programme “Coded Radar for Interference Suppression in Super-Dense Environments" (CRUISE) and is performed within the TU Delft Industry Partnership Program (TIPP), which is funded by NXP Semiconductors N.V. and Holland High Tech Systems and Materials (TKIHTSM/18.0136).

Keywords: Automotive Radar, Phase-Coded Chirps, Mutual Orthogonality, MIMO Radar, Interference Mitigation, Radar Signal Processing.

Printed by: Ipskamp Printing, Enschede, The Netherlands.

Front & Back: Design by Utku Kumbul.

ISBN 978-94-6384-420-8

An electronic version of this dissertation is available at
`http://repository.tudelft.nl/`.

Author e-mail: kumbul.utku@gmail.com

To my family and friends, for their love, support and encouragement

CONTENTS

LIST OF ACRONYMS

ADAS	Advanced Driver Assistance Systems
ADC	Analog-to-Digital Converter
AF	Ambiguity Function
AWG	Arbitrary Waveform Generator
BPSK	Binary Phase Shift Keying
CDMA	Code Division Multiple Access
COTS	Commercially Available Off-The-Shelf
CPI	Coherent Pulse Integration
CW	Continuous Wave
DDMA	Doppler Division Multiple Access
DFT	Discrete Fourier Transform
FFT	Fast Fourier Transform
FMCW	Frequency Modulated Continuous Wave
GMSK	Gaussian Minimum Shift Keying
IF	Intermediate Frequency
IIR	Infinite Impulse Response
ISL	Integrated Sidelobe Level
LFM	Linear Frequency Modulation
LO	Local Oscillator
LPF	Low Pass Filter
MIMO	Multiple-Input-Multiple-Output
NN	Neural Network
PC-FMCW	Phase-Coded Frequency Modulated Continuous Wave
PLC	Phase Lag Compensation
PMCW	Phase Modulated Continuous Wave
PRI	Pulse Repetition Interval
PSL	Peak Sidelobe Level
RCS	Radar Cross Section
RF	Radio Frequency
SISO	Single-Input-Single-Output
SNR	Signal-to-Noise Ratio
SPC-FMCW	Smoothed Phase-Coded Frequency Modulated Continuous Wave
TDMA	Time Division Multiple Access
V2V	Vehicle-to-Vehicle
ZCZ	Zero Correlation Zone

SUMMARY

Autonomous driving is a new emerging technology that will enhance traffic safety. Automotive radars are essential to attaining autonomous driving since they can function in adverse weather conditions and are used for detection, tracking, and classification in traffic settings. However, the dramatic growth in the number of radar sensors used for automotive radars has raised concerns about spectral congestion and the coexistence of radar sensors. The mutual interference between multiple radar sensors downgrades the sensing performance of automotive radar and needs to be mitigated. Moreover, automotive radars have limited processing power, preventing them from using computationally heavy techniques to countermeasure interference. This thesis aims at developing, evaluating and verifying a robust waveform with required processing steps suitable for automotive radars to boost the coexistence of multiple radar sensors. To achieve this task, phase-coded frequency modulated continuous wave (PC-FMCW) and necessary processing steps are studied.

The first step is taken by investigating the sensing properties of the PC-FMCW waveforms and possible receiver strategies in Chapter 2. It is demonstrated that the ambiguity function of the code is sheared after frequency modulation. Moreover, different binary phase codes are examined with the PC-FMCW waveforms, and their sensing performance is compared in terms of integrated sidelobe level. Subsequently, two receiver approaches based on the dechirping process to decrease the sampling demands of the PC-FMCW waveforms are examined. The sensing performance of the investigated receiver approaches is compared, and the trade-offs between the sensing performance and the code bandwidth are analyzed. Moreover, the PC-FMCW waveform is applied to a real scenario, and the sensing performance of the investigated receiver structures is validated experimentally.

Chapter 3 investigates the beat signal spectrum widening due to coding and explores the smoothed phase-coded frequency modulated continuous wave (SPC-FMCW) to improve the sensing performance in the limited receiver analogue bandwidth. The abrupt phase changes seen in binary phase-coded signal is analyzed, and a phase smoothing operation to reduce the spectral broadening of the coded beat signals is proposed. The introduced SPC-FMCW waveforms are analyzed in different domains and compared with the binary phase coding. It is shown that the proposed smoothing operation decreases the spectral broadening of the coded beat signal and improves the sensing performance of the waveform.

In Chapter 4, the limitation in the group delay filter receiver approach is investigated, and the appropriate receiver strategy with low computational complexity is designed to process the PC-FMCW waveforms. The impact of the group delay filter on the coded beat signal is examined in detail, and a phase lag compensation is proposed to enhance decoding performance. It is demonstrated that performing phase lag compensation on the transmitted code eliminates the undesired effects of the group delay filter, and the

beat signal is recovered properly after decoding. Then, the properties of the resulting waveforms are theoretically examined, and the sensing performance improvement over the existing approach is demonstrated. Moreover, both sensing and cross-isolation performance of the introduced waveforms with proposed processing steps are validated experimentally.

Chapter 5 studies the PC-FMCW waveforms for a coherent multiple-input-multiple-output (MIMO) radar. To this end, the MIMO ambiguity functions of the PC-FMCW waveform with different code families are investigated for their separation capability and compared with the PMCW waveform. It is illustrated that the PC-FMCW ambiguity function outperforms the PMCW one in terms of range resolution, Doppler tolerance, and sidelobe level for the identical types of codes. Afterwards, the developed phase lag compensated waveform with a single transmitter-receiver approach is performed to a coherent MIMO radar, and a novel PC-FMCW MIMO structure is proposed in Chapter 5. The introduced MIMO structure jointly utilizes phase coding in both fast-time and slow-time to achieve low sidelobe levels in the range-Doppler-azimuth domains while maintaining high range resolution, unambiguous velocity, good Doppler tolerance and low sampling requirements. The sensing performance of the introduced MIMO structure is evaluated and compared with the state-of-the-art techniques. Moreover, the proposed MIMO structure's practical limitations are investigated and demonstrated. In addition, the sensing performance of the developed approach with the simultaneous transmission is verified experimentally.

Finally, the interference resilience and communication capabilities of the developed PC-FMCW radar have been studied in Chapter 6. First, the automotive radar interference problem between various types of continuous waveforms is examined. The interference analysis formulation is extended to PC-FMCW waveforms, and a generalised radar-to-radar interference equation is proposed. The introduced equation can be utilised to quickly and accurately derive the numerous interference scenarios discussed in the literature. In addition, the proposed equation's validity to characterise the victim radar's time-frequency distribution is demonstrated experimentally using the commercially available off-the-shelf automotive radar transceivers. Afterwards, the robustness of the developed PC-FMCW radar against different types of FMCW interference cases is examined, and an improvement in the sensing performance over the conventional FMCW waveform is demonstrated. Moreover, the communication performance of the PC-FMCW with dechirping receivers is compared, and the trade-off between the bit error rate and the code bandwidth is investigated.

This thesis shows that the developed PC-FMCW radar structure can provide high mutual orthogonality to enhance the functioning of multiple radars within the same frequency bandwidth while sustaining the low sampling demand and good sensing performance. Consequently, the introduced approach can be effectively utilized by automotive radars to mitigate mutual interference between multiple radar sensors and improve the sensing performance of simultaneous MIMO transmission. Although the focus is on the application in an automotive radar context, the developed approach can also be used in other radar fields.

SAMENVATTING

Autonoom rijden is een opkomende technologie die de verkeersveiligheid zal verbeteren. Motorvoertuigradars zijn essentieel voor autonoom rijden, omdat ze kunnen functioneren in ongunstige weersomstandigheden en worden gebruikt voor detectie, doelvolging en classificatie in verkeerssituaties. De dramatische groei van het aantal sensoren dat wordt gebruikt voor motorvoertuigradars heeft echter geleid tot bezorgdheid over spectrale congestie en het simultaan functioneren van radarsensoren. De wederzijdse interferentie tussen meerdere radarsensoren verlaagt de detectieprestaties van motorvoertuigradars en moet worden beperkt. Bovendien hebben motorvoertuigradars een beperkte verwerkingskracht, waardoor ze geen rekenkundige zware technieken kunnen gebruiken om interferentie tegen te gaan. Dit proefschrift is gericht op het ontwikkelen, evalueren en verifiëren van een robuuste golfvorm, alsmede de vereiste verwerkingsstappen voor autoradars om het simultaan functioneren van meerdere radarsensoren te stimuleren. Om dit doel te bereiken worden phase-coded frequency modulated continuous wave (PC-FMCW) en noodzakelijke verwerkingsstappen bestudeerd.

De eerste stap wordt gezet door het onderzoeken van de detectie-eigenschappen van de PC-FMCW-golfvormen en mogelijke ontvangerstrategieën in Hoofdstuk 2. Er wordt aangetoond dat de ambiguïteitsfunctie van de code afschuift na frequentiemodulatie. Bovendien worden verschillende binaire fasecodes onderzocht met de PC-FMCW-golfvormen en hun detectieprestaties worden vergeleken in termen van geïntegreerd zijlobniveau. Vervolgens worden twee ontvangerbenaderingen onderzocht op basis van het dechirpingproces om de bemonsteringsvereisten van de PC-FMCW-golfvormen te verminderen. De detectieprestaties van de onderzochte ontvangerbenaderingen worden vergeleken en de afweging tussen de detectieprestaties en de codebandbreedte wordt geanalyseerd. Bovendien wordt de PC-FMCW-golfvorm toegepast op een reëel scenario en wordt de waarnemingsprestatie van de onderzochte ontvangerstructuren experimenteel gevalideerd.

Hoofdstuk 3 onderzoekt de verbreding van het spectrum van het signaal op de verschilfrequentie als gevolg van codering en onderzoekt een fasegecodeerde, frequentiegemoduleerde draaggolf met gladde fase-overgangen (SPC-FMCW) om de waarnemingsprestaties in de beperkte analoge bandbreedte van de ontvanger te verbeteren. De abrupte faseveranderingen die worden gezien in het binaire fasegecodeerde signaal worden geanalyseerd en er wordt een fasevergladding voorgesteld om de spectrale verbreding van de gecodeerde verschilfrequentiesignalen te verminderen. De geïntroduceerde SPC-FMCW-golfvormen worden in verschillende domeinen geanalyseerd en vergeleken met de binaire fasecodering. Er wordt aangetoond dat de voorgestelde vergladdingsoperatie de spectrale verbreding van het gecodeerde slagsignaal vermindert en de detectieprestaties van de golfvorm verbetert.

In hoofdstuk 4 wordt de beperking van de ontvangerbenadering met groepsvertragingsfilters onderzocht en wordt de juiste ontvangerstrategie met lage rekenkundige

complexiteit ontworpen om de PC-FMCW-golfvormen te verwerken. De invloed van het groepsvertragingsfilter op het gecodeerde verschilfrequentiesignaal wordt in detail onderzocht en er wordt een fasevertragingcompensatie voorgesteld om de decoderingsprestaties te verbeteren. Het is aangetoond dat het uitvoeren van fasevertragingscompensatie op de verzonden code de ongewenste effecten van het groepsvertragingsfilter elimineert, en dat het verschilfrequentiesignaal correct wordt hersteld na decodering. Vervolgens worden de eigenschappen van de resulterende golfvormen theoretisch onderzocht en wordt de verbetering van de detectieprestaties ten opzichte van de bestaande aanpak gedemonstreerd. Bovendien worden zowel de detectie- als de kruisisolatieprestaties van de geïntroduceerde golfvormen met voorgestelde verwerkingsstappen experimenteel gevalideerd.

Hoofdstuk 5 bestudeert de PC-FMCW-golfvormen voor een coherente MIMO-radar (multiple-input-multiple-output). Hiertoe worden de MIMO-ambiguïteitsfuncties van de PC-FMCW-golfvorm met verschillende codefamilies onderzocht op hun scheidingsvermogen en vergeleken met de PMCW-golfvorm. Geïllustreerd wordt dat de PC-FMCW-ambiguïteitsfunctie beter presteert dan de PMCW-functie in termen van afstandsresolutie, Doppler-tolerantie en zijlobniveau voor identieke soorten codes. Daarna wordt de ontwikkelde fasevertragingsgecompenseerde golfvorm met een enkele zender ontvangerbenadering aangepast voor een coherente MIMO-radar, en een nieuwe PC-FMCW MIMO-structuur wordt voorgesteld in Hoofdstuk 5. De geïntroduceerde MIMO-structuur maakt gebruik van fasecodering in zowel fast-time en slow-time om lage zijlobniveaus te bereiken in de afstand-Doppler-azimuth-domeinen met behoud van een hoge resolutie, ondubbelzinnige snelheid, goede Doppler-tolerantie en lage bemonsteringsvereisten. De detectieprestaties van de geïntroduceerde MIMO-structuur worden geëvalueerd en vergeleken met referenties uit recente literatuur. Bovendien worden de praktische beperkingen van de voorgestelde MIMO-structuur onderzocht en gedemonstreerd. Bovendien worden de detectieprestaties van de ontwikkelde benadering met de gelijktijdige verzending experimenteel geverifieerd.

Ten slotte zijn de interferentiebestendigheid en communicatiemogelijkheden van de ontwikkelde PC-FMCW-radar bestudeerd in hoofdstuk 6. Eerst wordt het interferentieprobleem van autoradar tussen verschillende soorten continue golfvormen onderzocht. De formulering van de interferentieanalyse wordt uitgebreid naar PC-FMCW-golfvormen en er wordt een algemene radar-naar-radar-interferentievergelijking voorgesteld. De geïntroduceerde vergelijking kan worden gebruikt om snel en nauwkeurig de talrijke in de literatuur besproken interferentiescenario's af te leiden. Bovendien wordt de validiteit van de voorgestelde vergelijking om de tijd-frequentieverdeling van de slachtofferradar te karakteriseren, experimenteel aangetoond met behulp van de commercieel verkrijgbare kant-en-klare radarzendontvangers voor auto's. Daarna wordt de robuustheid van de ontwikkelde PC-FMCW-radar tegen verschillende soorten FMCW-interferentiegevallen onderzocht en wordt een verbetering van de detectieprestaties ten opzichte van de conventionele FMCW-golfvorm aangetoond. Bovendien worden de communicatieprestaties van de PC-FMCW met dechirping-ontvangers vergeleken en wordt de wisselwerking tussen de bitfoutfrequentie en de codebandbreedte onderzocht.

Dit proefschrift laat zien dat de ontwikkelde PC-FMCW-radarstructuur een hoge onderlinge orthogonaliteit kan bieden om het functioneren van meerdere radars binnen

dezelfde frequentiebandbreedte te verbeteren, terwijl een lage bemonsteringsvereiste en goede detectieprestaties worden gehandhaafd. Bijgevolg kan de geïntroduceerde benadering effectief worden gebruikt door motorvoertuigradars om wederzijdse interferentie tussen meerdere radarsensoren te verminderen en de detectieprestaties van gelijktijdige MIMO-transmissie te verbeteren. Hoewel de focus ligt op de toepassing in een motorvoertuigradarcontext, kan de ontwikkelde aanpak ook worden gebruikt in andere radargerelateerde vakgebieden.

1

INTRODUCTION

1

1.1. AUTOMOTIVE RADAR: MOTIVATION, REQUIREMENTS AND CHALLENGES

Traffic accidents are seen by modern society as one of the major threats to the quality and duration of life. These safety concerns raise a growing interest towards self-driving cars, and autonomous driving has become a new emerging technology that will improve road safety. The latest developments in autonomous driving technology highlight the significance of sensors that are being used in vehicles. Autonomous driving depends on a variety of sensors such as radar, lidar, and camera to enable different levels of advanced driver assistance systems (ADAS) [1]. Among these sensors, radar plays a key role in achieving autonomous driving for detection, tracking and classification in traffic environments, as they can operate under diverse weather conditions. Recent improvements in semiconductors and integrated circuits enable the low-cost production of single-chip automotive radar [2, 3].

Currently, the automotive radar sensors operate within the spectrum from 76 to 81 GHz [4]. Most modern vehicles are already equipped with radar systems to enhance road safety [5]. These radars widely use linear frequency modulated continuous wave (FMCW) as the FMCW waveform requires a very simple hardware structure and small analogue bandwidth of the receiver. However, discrimination of the FMCW waveforms is limited and multiple radars operating simultaneously within the same frequency band are likely to cause mutual interference [6–8]. Therefore, the increase in the radar-equipped vehicles on the road raises concern regarding the spectrum crowding and the coexistence of multiple radar sensors [9–11]. Moreover, the mutual interference problem is expected to be very challenging in the future as the vehicles require more radar sensors to acquire comprehensive self-awareness about the environment [12]. The radar-to-radar interference scenario is illustrated in Figure 1.1. Note that the received interference signal power is usually stronger than the target return, as the interference signal has one-way propagation. Depending on the spectral characteristic of the interference, two types of interference cases might occur between the FMCW radars; namely, wide-band interference and narrow-band interference [13–16]. The wide-band interference occurs when the interference has a different chirp slope from the victim radar as illustrated in Figure 1.2 and raises the noise floor of the victim radar [13]. Such an increase in the noise floor results in

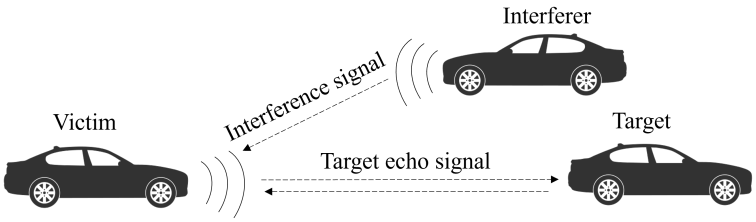

Figure 1.1: Illustration of the radar-to-radar interference scenario.

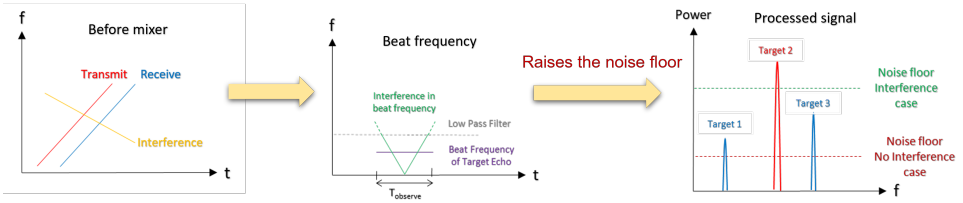

Figure 1.2: Illustration of the wide-band interference scenario in the FMCW radar. Wide-band interference creates a 'V-shape' in beat frequency and raises the noise floor interference.

a loss of dynamic range and might cause the masking of weak target echoes. To highlight this issue, we consider three targets and demonstrate the processed signal response in Figure 1.2. The narrow-band interference scenario happens when the interference has the same chirp slope with the victim radar as demonstrated in Figure 1.3 and leads to ghost targets within the victim radar in a fully synchronous case [16]. Consequently, both of these interference cases degrade the detection performance and functionality of the radar system that is being interfered with, known as the 'victim radar' [17–21]. As the fully autonomous system is the future demand from automotive radar sensors, the dependability of the sensors is very critical, and there is absolutely no room for sensing failures. Therefore, it is imperative to mitigate interference from radar signals effectively.

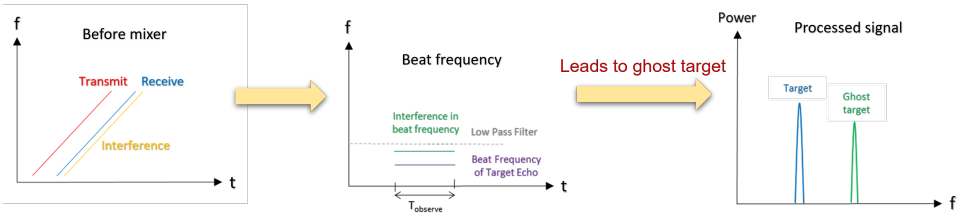

Figure 1.3: Illustration of the narrow-band interference scenario in the FMCW radar. Narrow-band interference creates a beat signal similar to target echo and leads to a ghost target.

The interference mitigation problem in automotive radar signals has been an active and challenging research topic to acquire reliable target detection [22]. At the moment, there are no regulations on waveform structure and modulation schemes for automotive radars. Consequently, many approaches have been studied to mitigate interference or compensate its effects [11]. However, since the various criteria should be taken into account for real-time automotive radar, such as the realization of the hardware and processing cost, it is still unclear which approach is the best for interference countermeasure technique [17].

In addition, the automotive radar needs to provide comprehensive and accurate information about the environment. Thus, one of the key requirements of automotive radar is to provide a high angular resolution, which depends on the number and size of the antenna elements. Multiple-input-multiple-output (MIMO) radar can synthesize a virtual array with a large aperture while using a relatively small number of antenna

elements, and thus they are commonly used in automotive radars to achieve high angular resolution [23]. However, the mutual orthogonality between transmitting channels needs to be ensured for the synthesis of such a virtual array. Moreover, the joint sensing and communication systems have received remarkable attention in autonomous driving technology to reduce spectral congestion [24–26]. Currently, autonomous driving systems use wireless sensors for vehicle-to-vehicle (V2V) communication and radar sensors for sensing. Combining the sensing and V2V communication functionalities is expected to reduce the radio frequency spectrum crowding [27–29]. To enable joint sensing and communication, many different approaches are studied [30–36]. However, automotive radars have limited processing power, preventing them from using computationally heavy techniques for these requirements. Therefore, applicable interference mitigation methods and waveforms with high mutual orthogonality to improve the independent operation of multiple radars within the same frequency bandwidth are still a focus of interest.

1.2. OVERVIEW OF EXISTING INTERFERENCE MITIGATION APPROACHES

The mitigation of the interference between automotive radars has gathered growing interest since the number of automotive radars sensors on the roads is increasing while the spectrum available for their use remains the same [5, 9]. Consequently, various methods are studied to countermeasure the automotive radar interference [9, 11, 12]. These methods have different advantages and limitations since they combat the interference using different transmission-reception principles, waveform types and signal processing techniques. For ease of following, the interference mitigation techniques can be categorized into two main groups: interference avoidance and interference suppression approaches.

INTERFERENCE AVOIDANCE

The interference avoidance approaches adjust the radar system parameters to avoid interference and minimize the probability of interference. These approaches can be listed below.

Frequency altering and hopping techniques: are used to change the frequency of the radar to avoid interference. In most of these techniques, the received interference and its center frequency are required to be detected and estimated. Subsequently, the center frequency of the victim radar is shifted to the available frequency band. For the automotive radar application, [37] adapts the behaviour of bats to switch the transmit frequency of the chirp while the carrier frequency of the chirp is changed randomly after every sweep in [38]. Alternatively, the waveform sequences that maintain minimum frequency separation between transmitting frequencies are used in [39]. The frequency altering and hopping methods can effectively avoid automotive radar interference when a frequency spectrum is accessible for usage. However, these methods will fall short when the number of automotive radars increases in the environment.

Cooperative time and frequency scheduling techniques: are used to avoid interference by coordinating automotive radars' transmitted system parameters. In these approaches, each radar is assigned to use different time, frequency and space resources to avoid mutual interference. To achieve this, [40, 41] utilizes separate time and fre-

quency slots based on long pulse sequences while [42] uses a dynamic radar parameter assignment algorithm. Alternatively, [43–45] use radar suitable for joint sensing and communication, where communication is built on a decentralized carrier sense multiple access protocols and is used to adjust the timing of radar transmission. Although the cooperative time and frequency scheduling techniques can potentially avoid interference, these approaches suffer when the frequency spectrum is highly occupied and the allocated resources are limited.

INTERFERENCE SUPPRESSION

The interference suppression approaches seek to lessen the interference's negative impacts by suppressing the interference. These approaches can be listed below.

Digital beamforming and nulling approaches: aim to cancel out the signal energy coming from the direction of interference. In these approaches, the beamforming is performed in a way that the steering vector at the direction of interference is nulled (null-steering) for interference mitigation. To achieve this, the direction of an interferer is estimated in the time domain and then cancelled using an adaptive beamformer in [46]. Moreover, analytical and experimental investigation of this approach is studied in [47]. A similar approach that uses digital beam steering with multiple receiving channels to eliminate interference direction is discussed in [48]. However, these approaches rely on the precise estimation of the interference direction before the beamforming, which raises the computational complexity. To reduce the dependency on precise estimation, an adaptive method that recursively calculates the beamforming weights and suppresses the interference at the output of the beamformer is proposed in [49]. Despite the fact that beamforming and nulling techniques can be used for interference mitigation, the possibility of ignoring (nulling) the target echo around the direction of the interference limits the utilization of these approaches.

Interference removing and signal recovering approaches: try to eliminate the interference from the distorted signal and then repair the useful signal back. To this end, many different approaches are studied for automotive radars. In particular, the interference is estimated from the time-domain samples and removed from the received signal in [50–53]. Moreover, [54] uses complex baseband oversampled receiver to detect interference in IF bands and suppress it before range processing while [55] tries to mitigate interference by using interpolation of beat frequency in short-time Fourier Transform, phase matching and reconfigured linear prediction coefficients estimation. Alternatively, [56] identifies the interference by using image processing methods such as maximally stable external regions algorithm on time-frequency image of the signal and uses zeroing on interfered part of the signal. However, these techniques heavily rely on interference detection and fall short of detecting interference in the presence of strong target reflections. Thus, more adaptive approaches, such as iterative filtering, weighted envelope normalization algorithm in the time domain, and adaptive noise canceller techniques, are respectively suggested in [57–59]. Similarly, the interference is mitigated by using matrix pencil and matrix completion algorithms in [21]. In addition, sparsity-based signal separation approaches have been studied to blindly separate the interference from the useful signal. In particular, [60] uses wavelet analysis to detect the wanted signal and separate it from the interference, while [61] utilizes a sparse sampling signal recovery algorithm

to mitigate distorted signal parts. In [62, 63], the authors propose a signal separation and reconstruction algorithm based on a dual-basis pursuit problem. Alternatively, [64] introduces a fast orthogonal matching pursuit algorithm to separate interference signals from the target signal with minimal loss of information. However, both these adaptive techniques and sparsity-based approaches are computationally heavy and difficult to realize by the limited processing power of the current automotive radars. Moreover, relying on interference detection, requiring proper restoration of the signal to avoid rising the sidelobe due to missing samples after interference removal, and the potential to remove or suppress the useful target information masked by interference limits the utilization of the interference removing and signal recovering techniques.

Orthogonal waveform techniques: rely on (nearly) orthogonal transmission and reception principle by securing orthogonality in different domains, e.g. time, frequency, chirp slope, antenna polarization, or their joint combination [11]. In particular, [65] uses chirp sequence sets whose frequency slopes are different from that of the neighbouring vehicles, while [66] addresses the ghost target problem in a multi-target situation by transmitting triangle chirp waveforms. Similarly, [67] utilizes an orthogonal pattern in the change of frequency ramp slope of the chirp to identify the beat frequency of a particular radar. An alternative method, which uses scalable fast chirp FMCW radar, where chirp direction alternates accordingly to reduce the time duration of the interference, is proposed in [68, 69]. However, these methods suffer due to sharing a limited frequency spectrum. Another solution for orthogonal waveform transmission is achieved via antenna polarization and modulation of the carrier frequency with different codes, such as maximum length sequence, Gold sequence, and pseudo-random noise sequence [70–73]. However, having limited polarization options, antenna elements to be coded, and the possible mismatch in decoding restrict the interference mitigation capability of these approaches. To address these issues, the code signal can be used to modulate the phase changes with respect to time. To this end, [74] introduces a cross-channel interference suppression method by using polarimetric FMCW radar with dual-orthogonal sounding signals while [75, 76] design orthogonal pseudo-noise waveforms to reduce mutual interference. Similarly, the phase-coded signals with good auto and cross correlations are used to modulate continuous wave (CW) signals or chirp signals to enhance the orthogonality of the waveforms [77–85]. However, these methods suffer from different limitations, such as spreading the radio frequency (RF) or beat spectrum, losing range or Doppler resolution, high sidelobe levels due to imperfection in decoding, and high sampling requirements. If these limitations are handled properly, the orthogonal waveform design and transmission have the potential to blindly suppress the interference signal and thus can be utilized for interference mitigation effectively.

To sum up, mitigating interference becomes an important issue for an automotive radar to perform safety-critical functions properly. Different interference scenarios and the limited processing power of automotive radars make the mitigation problem challenging. Although various mitigation techniques have been developed, they have different limitations to mitigating interference effectively. Therefore, existing methods may not ensure effective interference mitigation in a congested environment, and more sophisticated techniques, such as communication-like channel access control, are required. To this end, new waveforms based on the phase-coded chirp signals [86] are investigated

in this thesis. Moreover, this thesis presents the detailed analysis, implementation and experimental validation of such waveforms in a radar system for the first time.

1.3. RESEARCH OBJECTIVES AND APPROACH

The objectives of this research are to develop, evaluate and verify the robust waveform with necessary processing steps applicable to real-time automotive radars for enhancing the independent operation of multiple radars within the same frequency bandwidth, which is essential for the interference mitigation problem and realization of the simultaneous MIMO transmission.

The present approaches for interference mitigation have different kinds of limitations, as mentioned in Section 1.2. Recent improvements in automotive radar hardware technology allow the use of different waveforms and modulation schemes to enhance orthogonality, thus making possible implementation of advanced approaches for interference mitigation. The FMCW signal provides good sensing performance and is widely used in automotive radars. However, its sensing performance is downgraded in case of interference. The phase-coded continuous wave (PMCW) improves the mutual orthogonality of the transmitted waveform and offers more resilience to interference. However, the RF spreading and poor sensing performance of the PMCW signal hold its potential usage in automotive radars.

A promising approach to overcome the aforementioned limitations is modulating the chirp signal with a phase coding signal. To this end, the phase-coded frequency modulated continuous wave (PC-FMCW) is suggested [85–89]. The PC-FMCW waveforms is expected to maintain all the advantages of the FMCW signal while providing the high mutual orthogonality required for the interference mitigation problem, a realization of the simultaneous MIMO transmission and joint sensing communication. In the state-of-the-art, the dechirping-based receiver strategy is adjusted for the PC-FMCW waveforms to decrease the waveform sampling requirements. However, the existing receiver approaches and the coding schemes have different limitations. Particularly, the most promising processing approach performs dechirping followed by the alignment of the coded beat signals using the group delay filter. However, the group delay filter causes an unwanted quadratic phase shift on the phase-coded signal, which leads to an increase in the sidelobe levels. Moreover, binary phase shift keying (BPSK) phase coding, which is commonly used in the existing approaches, results in a sharp change in the signal time derivative and a very broad instantaneous spectrum. Limited bandwidth of the front-end and dynamic range of ADC will result in filtering the spectrum and changing the properties of the coded waveform. These sharp changes in the frequency spectrum downgrade the radar performance and need to be compensated before processing the signal.

In this research, the waveform properties, sensing performance and limitations of the existing receiver structures of the PC-FMCW waveform are investigated. Subsequently, the low-cost and computationally efficient transceiver architecture, including required processing steps, is developed to address the current limitations of the state-of-the-art techniques. Moreover, the sensing performance of the introduced transceiver architecture and its application to simultaneous MIMO transmission is evaluated numerically and verified experimentally.

1

1.4. NOVELTIES AND MAIN RESULTS

- The sensing properties of the phase-coded FMCW waveforms with binary phase codes are studied using the ambiguity function. It is seen that the PC-FMCW waveforms have good Doppler tolerance and high range resolution while providing high mutual orthogonality. Moreover, different code families in application to the PC-FMCW waveforms are investigated, and their sensing performance is compared for the first time. It is shown that the correlation property of the code is changed due to frequency modulation, and different code families can provide very similar sensing performance for the PC-FMCW waveform. Moreover, the filter bank receiver and the group delay filter receiver are analyzed theoretically to process the PC-FMCW waveforms with low ADC sampling requirements. The trade-off between sensing performance and the code bandwidth is demonstrated for both processing methods. The sensing performance of the filter bank and group delay filter receivers are compared numerically and illustrated experimentally for the first time. It is shown that the group delay dispersion effect degrades the sensing performance of the group delay filter receiver and becomes crucial as the code bandwidth increases.

- The BPSK coded beat signal is studied analytically in different domains, and the widening of the beat spectrum due to coding is investigated for the first time. The phase smoothing operation is proposed to enhance spectral efficiency in the beat frequency, and the SPC-FMCW waveforms are obtained. The introduced smoothed phase-coded beat signals are analyzed and derived in different domains for the first time. It is demonstrated that the proposed smoothing operation lowers the spectrum widening of the coded beat signal, and thus better sensing performance is achieved with the proposed SPC-FMCW waveforms in the limited ADC sampling scenario.

- The impact of the group delay filter receiver is analyzed in detail. The phase lag compensation is proposed to improve decoding performance, and novel waveforms are introduced to achieve better sensing and cross-isolation performance. The developed transceiver structure and properties of the new waveforms are evaluated and compared numerically for the first time. Furthermore, the sensing and cross-isolation performance of the introduced PC-FMCW waveforms are verified experimentally for the first time. Both numerical simulations and experimental measurements demonstrate that the developed waveform and processing steps can utilize large code bandwidth to provide high mutual orthogonality while keeping the good sensing performance and Doppler tolerance of the FMCW radar.

- The MIMO ambiguity function of the PC-FMCW waveform is investigated for the cross-isolation performance. The range-angle performance of the PC-FMCW waveform with different code families is examined and compared with the PMCW waveform for the first time. It is observed that the sidelobe levels in the PC-FMCW MIMO ambiguity function stay steady as the Doppler frequency raises. Furthermore, the developed new waveform is applied to simultaneous MIMO transmission, and a novel PC-FMCW MIMO structure is proposed. The performance of the introduced MIMO is assessed and compared with the state-of-the-art techniques. In addition,

the experimental verification and practical aspects of applying these waveforms to a coherent MIMO radar are demonstrated for the first time. It is shown that the proposed MIMO structure provides low sidelobe levels in the range-Doppler-azimuth domains while maintaining the high range resolution, unambiguous velocity and low sampling requirements.

- The existing automotive radar interference analysis is extended, and a novel generalised radar-to-radar interference equation is proposed. The interference characteristic of different waveforms in the automotive radars are analysed, and the introduced equation is verified experimentally for the first time. It is demonstrated that the proposed equation can adequately provide the various interference cases. Afterwards, the interference resilience of the developed PC-FMCW radar is investigated for the first time. It is shown that the developed PC-FMCW radar spreads the peak power of interference over the range-Doppler profile and therefore improves the robustness of the radar against both narrow-band and wide-band interference cases. In addition, the communication performance of the PC-FMCW with phase lag compensated group delay filter and filter bank receivers are compared for the first time. It is demonstrated that the former receiver provides worse communication performance as the code bandwidth increases and its application to communication is limited by the bit error rate degradation.

1.5. OUTLINE OF THE THESIS

The remainder of this thesis is structured as follows:

Chapter 2 investigates the sensing properties of the phase-coded FMCW waveforms and possible receiver strategies to process PC-FMCW waveforms. The ambiguity function is used to examine the sensing property of the waveform. It is illustrated that the ambiguity function of the code is sheared after modulating with the chirp signal. Two receiver structures with low ADC sampling are examined, and their sensing capabilities are analyzed. The sensing performance of the investigated receiver structures is demonstrated and compared experimentally.

Chapter 3 studies the beat signal spectrum broadening due to coding and investigates the smoothed PC-FMCW waveforms to enhance the sensing performance of the waveform in the limited ADC sampling scenario. It analyzes the abrupt phase changes seen in BPSK coding and proposes a phase smoothing operation to decrease the spectral widening of the coded beat signals. The resulting waveforms are derived and demonstrated in different domains. Then, the investigated waveforms are processed with the group delay filter receiver, and their sensing performance is compared.

Chapter 4 investigates a receiver structure to address the current limitations in the existing receiver approach. It analyzes the impact of the group delay filter and proposes compensation for the undesired effect of the group delay filter. The phase lag compensation is applied to the phase-coded signal before transmission, and decoding performance is improved. The properties of the introduced waveform are analyzed theoretically and demonstrated experimentally. The simulation and experimental results demonstrate that the investigated waveform with the introduced receiver approach provides good sensing performance while achieving high mutual orthogonality.

Chapter 5 extends the previously proposed single transmitter-receiver approach to coherent PC-FMCW MIMO radar. The range-angle profiles of the PC-FMCW MIMO ambiguity function with different code families are investigated and compared. Then, a novel PC-FMCW MIMO structure, which jointly utilizes both fast-time and slow-time coding, is proposed to reduce sidelobe levels while preserving high range resolution, unambiguous velocity, good Doppler tolerance and low sampling needs. The sensing performance and practical aspects of the introduced PC-FMCW MIMO structure are evaluated theoretically and verified experimentally. The numerical simulations and experiments demonstrate that the proposed MIMO can combine the benefits of FMCW waveforms with the capability of achieving low sidelobe levels in the range-Doppler-azimuth domains for simultaneous transmission.

Chapter 6 studies the mutual interference problem between automotive radars. The existing interference analysis is extended, and a generalised radar-to-radar interference equation is proposed. The introduced equation and characteristics of different interference scenarios are verified experimentally by using real-time automotive radars. Afterwards, the robustness of the PC-FMCW radar against different types of FMCW interference is examined, and the resulting improvement in the sensing performance is compared with the FMCW radar. Moreover, the communication capabilities of the PC-FMCW waveform are investigated. It is shown that the bit error rate degradation increases with code bandwidth.

Chapter 7 contains the conclusions and gives recommendations for possible future research.

2

PHASE-CODED FMCW: WAVEFORM PROPERTIES AND RECEIVERS

The sensing properties of the phase-coded FMCW waveform with different binary phase codes are investigated. It is shown that the ambiguity function of the FMCW signal modulated with a phase code corresponds to sheared ambiguity function of the code itself. The range profiles of PC-FMCW with different code families are analyzed and compared in terms of integrated sidelobe level. Furthermore, two receiver structures of the phase-coded FMCW signals with low ADC sampling requirements, namely the filter bank and group delay filter approaches, are investigated and compared. The sensing performance comparison of the investigated receivers is demonstrated via numerical simulations and experimental results.

Parts of this chapter have been published in:

U. Kumbul, N. Petrov, F. van der Zwan, C. S. Vaucher, and A. Yarovoy, "Experimental investigation of phase coded FMCW for sensing and communications", in *2021 15th European Conference on Antennas and Propagation (EuCAP)*, pp. 1-5, 2021.

U. Kumbul, N. Petrov, C. S. Vaucher, and A. Yarovoy, "Receiver structures for phase modulated FMCW radars", in *2022 16th European Conference on Antennas and Propagation (EuCAP)*, pp. 1-5, 2022.

U. Kumbul, N. Petrov, C. S. Vaucher, and A. Yarovoy, "Sensing performance of different codes for phase-coded FMCW radars", in *2022 19th European Radar Conference (EuRAD)*, pp. 1-4, 2022.

2.1. INTRODUCTION

As already mentioned in Chapter 1, radars are used for detection, tracking and classification under various weather conditions. They are key sensors for advanced driver-assistance systems to acquire self-awareness about the environment. Consequently, the number of radar-equipped vehicles on the road is predicted to grow in future and raise the spectral intensity [9]. Currently, there are no regulations on waveform structure, and there are two competing waveform classes for automotive radars: PMCW and FMCW [11]. The PMCW waveforms can carry information and provide high mutual orthogonality to improve the robustness of the radar against interference [83]. However, the PMCW waveforms require high sampling from ADC to achieve high range resolution [17]. Moreover, the PMCW waveform has poor Doppler tolerance, and the orthogonality between codes heavily suffers from the Doppler frequency shift due to the target's movement [84]. On the other hand, the FMCW waveforms can provide high range resolution, low sidelobes, and good Doppler tolerance. Moreover, the simple hardware implementation and low sampling requirements from ADC favour the utilization of the FMCW waveforms in the automotive radars [17]. However, these benefits of the FMCW waveforms come with the price of having limited distinctness.

Lately, the phase-coded FMCW waveform has attracted much attention due to taking advantage of both FMCW and PMCW [86–93]. Applying coding to FMCW improves the waveform diversity and ensures the discrimination of self-transmitted signals from the waveforms transmitted by other radars [85, 94]. Furthermore, phase-coded FMCW enables joint sensing and communication [32, 33, 95–100]. Initially, the full-band match filter receiver is used to process the PC-FMCW waveforms in [86]. For the matched filtering operation, the received signal is convoluted with the complex conjugate of the transmitted signal. The traditional matched filtering operation in the digital domain requires the acquisition of the signals with total bandwidth. As a result of high sampling demands, conventional full-band matched filtering is not suitable for automotive radars since the processing power is limited. To reduce the sampling requirement from the analogue receive bandwidth, the conventional matched filter for PC-FMCW can be realized via performing filter bank after dechirping [33], or it can be approximated by using the group delay filter receiver [85, 88]. Both of these receiver approaches apply dechirping based processing methods to decrease the sampling demands of ADC [101].

In this chapter, we investigate the sensing properties of the phase-coded FMCW waveforms and analyze the existing receiver approaches for the PC-FMCW waveforms. The chapter is structured as follows. We recall the signal models and radar system parameters definitions for common automotive radar waveforms in Section 2.2. Then, we examine the ambiguity function of PC-FMCW for a single transmitter case and compare the range profiles corresponding to PC-FMCW modulated with different code families in 2.3. Then in Section 2.4, two receiver approaches suitable for automotive radars with low ADC sampling requirements; the filter bank receiver applied to the dechirped signal and the group delay filter receiver, are investigated to reconstruct the range profile from the received signal. Subsequently, the sensing performance comparison of existing receivers and the impact of the waveform parameters on the radar performance are presented in Section 2.5. Furthermore, we demonstrate the measurement results for the investigated receivers in Section 2.6. Finally, the conclusions are drawn in Section 2.7.

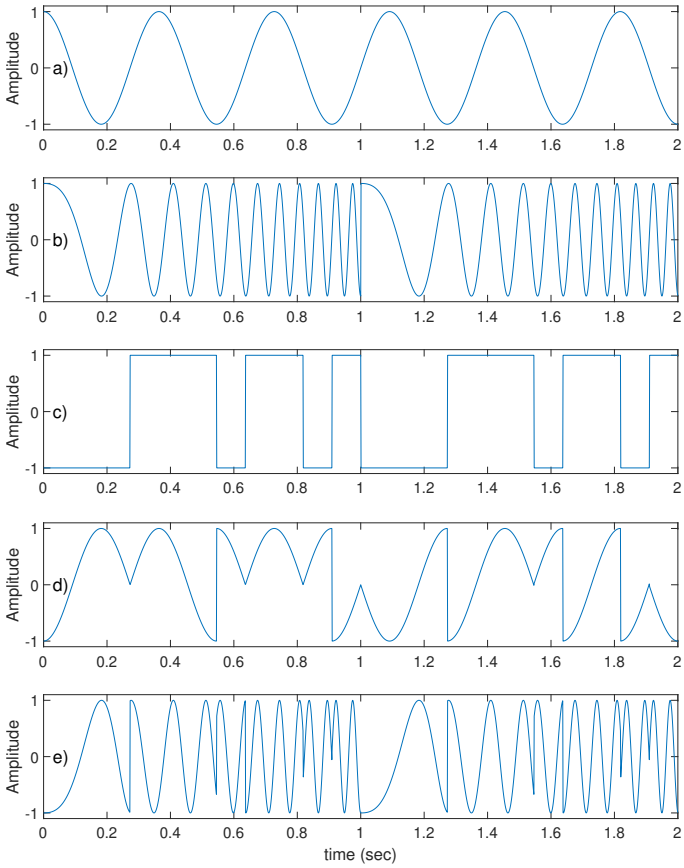

Figure 2.1: Illustration of the real part of typical radar waveforms: a) Continuous wave (CW) signal b) Frequency modulated continuous wave (FMCW) signal c) Binary phase code (Baseband BPSK signal) d) Phase modulated continuous wave (PMCW) signal e) Phase-coded frequency modulated continuous wave (PC-FMCW) signal.

2.2. WAVEFORMS

This section describes the signal models for common automotive radar waveforms. The transmitted signals for different types of automotive radar waveforms are illustrated in Figure 2.1. Subsequently, the automotive radar system parameters defined by different types of waveforms are summarized in Table 2.1.

2.2.1. CW

Continuous wave (CW) is utilized to achieve a high duty cycle and thus higher average power on transmit. The transmitted signal for the CW radar can be represented as:

$$x_{\mathrm{CW}}(t) = e^{-j(2\pi f_c t)}, \tag{2.1}$$

where f_c is the carrier frequency. The real part of the CW signal is shown in Figure 2.1 a. In the CW radar, an electromagnetic wave is transmitted continuously, and the reflected

echoes from the targets are received simultaneously [102]. On the receiver side, the received signal is mixed with the complex conjugate of a transmitted signal. The mixer output gives the signal at the Doppler frequency of the target. The velocity resolution of CW radar is inversely proportional to the duration of the observation (measurement) time T_{obs}. However, without any modulation, the continuous nature of the waveform can not obtain the round-trip delay, which is required for target range estimation.

2.2.2. FMCW

Linear frequency modulated continuous wave has been one of the most used waveforms in automotive radars [5]. This modulation scheme transmits continuous waveforms that have linearly changing frequencies. The transmitted signal for the FMCW radar can be represented as:

$$x_{\text{FMCW}}(t) = e^{-j(2\pi f_c t + \pi k t^2)}, \tag{2.2}$$

where k is the slope of the linear frequency modulated waveform and is equal to the ratio of bandwidth and sweep duration, described as $k = B/T$. The real part of the FMCW signal is shown in Figure 2.1 b. One of the main advantages of FMCW is stretch processing (dechirping) to reduce the sampling requirements of radar systems [103]. During dechirping process, the received signal and transmit signal are mixed and low pass filtered to obtain a baseband signal. The resulting baseband signal, which is also known as the beat signal, contains range and velocity information of the target in terms of sinusoidal components [104]. In the traditional FMCW radar, a single chirp at one measurement time is transmitted. This situation restricts the discrimination of multiple moving targets within one measurement. To cope with ambiguities, different ramp slopes must be used for conventional FMCW [105]. In the modern approach, this drawback is dealt with using chirp sequences within one measurement time. By using chirp sequence, i.e. fast chirps, the range and Doppler information are disassociated, and thus they can be analysed within a single measurement using two-dimensional Fourier transform [106]. In chirp sequence radar, the range resolution is inversely proportional to the chirp bandwidth. The velocity resolution is determined by the total duration of the chirp sequence, which equals the number of pulses N_p times the chirp duration. Moreover, the maximum range is determined by the maximum beat frequency, which equals half of the sampling frequency f_s. Hence, the FMCW radar can provide high range and velocity resolution with a relatively simple hardware design. Despite providing good sensing performance, the FMCW radars suffer from mutual interference, and without additional techniques to secure orthogonality, they are not applicable to simultaneous MIMO transmission.

2.2.3. PMCW

Phase modulated continuous wave (PMCW) is another well-known waveform that is used by automotive radars. In the PMCW radar, the transmitted signal is modulated by changing the phase of the waveform. This phase change is controlled by a code sequence, and for that reason, the phase modulation is also called phase coding (PC) or pseudo-noise (PN) sequencing [75]. The transmitted signal for the PMCW radar can be represented as:

$$x_{\text{PMCW}}(t) = s(t)e^{-j(2\pi f_c t)}, \tag{2.3}$$

where $s(t)$ is a single period of a transmitted phase code signal with chip bandwidth B_c and chip duration $T_c = 1/B_c$. In automotive radars, state-of-the-art techniques commonly use binary phase shift keying (BPSK) as a phase modulation scheme, where the phase changes between $\{0, \pi\}$ [82]. The real parts of BPSK and PMCW signals are illustrated in Figure 2.1 c and d, respectively. To process the PMCW waveform, the received signal is down-converted to the baseband, and the baseband signal is correlated with the complex conjugate of the transmitted code sequence [82]. In the PMCW radar, the range resolution is a function of chip (code) bandwidth, while the velocity resolution is defined by the number of chips L_c times the chip duration. Several code families have been studied in the literature, including binary code sequences such as Barker, M-sequence, Gold and Kasami in [107–109], and poly-phase codes in [27, 87, 102, 110]. Depending on the code selection and design, low cross-correlation and low-range sidelobes can be achieved [111]. The optimal code selection varies with the requirement of the application. However, PMCW is vulnerable to Doppler frequency shifts due to target motion, and its poor Doppler tolerance needs to be compensated. Moreover, PMCW has high sampling requirements to obtain high range resolution [17].

2.2.4. PC-FMCW

Phase-coded frequency modulated continuous wave (PC-FMCW) has been proposed to achieve good sensing performance while enhancing mutual orthogonality between waveforms [27]. In the PC-FMCW radar, both the frequency and phase of the transmitted signal change over time. The transmitted signal for a phase-coded FMCW radar can be written as:

$$x_{\text{PC-FMCW}}(t) = s(t)e^{-j(2\pi f_c t + \pi k t^2)}, \tag{2.4}$$

where $s(t) = \exp\left(j\phi(t)\right)$ is the phase-coded signal that controls the phase changes inside the chirp. The current technology in automotive radar uses the BPSK coding to modulate the phase of the FMCW waveform [112], and thus the phase changes between $\{0, \pi\}$ according to the phase sequence ϕ_n. Then the phase-coded signal can be represented as:

$$s(t) = \sum_{n=1}^{N_c} e^{j\phi_n} \text{rect}\left(\frac{t - (n - 1/2)T_c}{T_c}\right), \tag{2.5}$$

where $\text{rect}(t)$ is the rectangle function and n defines the chip index. The real part of the PC-FMCW signal is illustrated in Figure 2.1 e. The phase of the waveform is constant during the chip duration T_c. As the phase changes from 0 to π or vice versa, then a phase of the waveform is shifted 180 degrees (Figure 2.1). The duration of the chip (code) is defined by the number of chips per chirp as $T_c = T/N_c$, where N_c denotes the number of chips within one chirp. Consequently, increasing N_c raises the bandwidth of the code as $B_c = N_c/T$. In this thesis, we assume that the bandwidth of $s(t)$ is much smaller than the chirp bandwidth $B_c \ll B$. To process the received PC-FMCW signal, the dechirping and decoding strategy is adapted to reduce sampling requirements from analogue-to-digital converter. A detailed explanation of such receivers is given in Section 2.4. Thus, similar to the FMCW radars, the range resolution is a function of the chirp bandwidth, and the velocity resolution is determined by the chirp duration times the number of chirp pulses.

Table 2.1: Automotive radar system parameters defined by different types of waveforms

	Waveforms			
	CW	**FMCW**	**PMCW**	**PC-FMCW**
Processing technique	Conjugate Mixing	Dechirping	Correlator	Dechirping and decoding
Range resolution	No range information	$\Delta R = \frac{c}{2B}$	$\Delta R = \frac{c}{2B_c}$	$\Delta R = \frac{c}{2B}$
Velocity resolution	$\Delta v = \frac{c}{2f_c T_{obs}}$	$\Delta v = \frac{c}{2f_c N_p T}$	$\Delta v = \frac{c}{2f_c L_c T_c}$	$\Delta v = \frac{c}{2f_c N_p T}$
Maximum range	No range information	$R_{\max} = \frac{cT}{4B} f_s$	$R_{\max} = \frac{cT_c}{2}$	$R_{\max} = \frac{cT}{4B} f_s$
Maximum velocity	$v_{\max} = \frac{c}{4f_c T_{obs}}$	$v_{\max} = \frac{c}{4f_c T}$	$v_{\max} = \frac{c}{4f_c T_c}$	$v_{\max} = \frac{c}{4f_c T}$
ADC rate	≤ 1 MHz	≤ 80 MHz	≤ 1 GHz	≤ 80 MHz

2.3. AMBIGUITY FUNCTION OF PC-FMCW

In this section, we use the ambiguity function (AF), which is a principal tool for studying radar waveforms and corresponds to the outcome of the matched filter. When the transmitted signal (2.4) is reflected from a target at a range R_0 moving with a constant radial velocity v_0, the round trip delay between radar and target can be given as:

$$\tau(t) = \frac{2\,(R_0 + v_0\, t)}{c} = \tau_0 + \frac{2\, v_0}{c}\, t, \tag{2.6}$$

For the narrow band, the received signal is a linearly delayed copy of the transmitted signal with a corresponding Doppler shift. Accounting propagation and back-scattering effects by complex coefficient α_0, the received signal can be represented as:

$$x_{\mathrm{r}}(t) = \alpha_0\, x_{\mathrm{t}}(t - \tau(t)) + n(t) \tag{2.7}$$

where $n(t)$ represents the received noise signal. The received signal acquisition time T_{aq}= $[0, T+T_r]$, where T_r is the pulse repetition interval and for the continuous wave T_r=T. In the white noise scenario, the optimum receiver that jointly maximizes signal-to-noise ratio (SNR) for each range-Doppler hypothesis is the matched filter [113]. After down-conversion with the carrier tone to the base-band, the matched filter receiver convolves the received signal with the complex conjugate of the transmitted signal as:

$$x_{\mathrm{MF}}(t) = \int_{-\infty}^{\infty} x_{\mathrm{r}}(\zeta)\, x_{\mathrm{t}}{}^{*}(t - \zeta)\, d\zeta, \tag{2.8}$$

where $(\cdot)^*$ denotes the complex conjugate. The matched filter output contains the range information about the target. Note that conventional matched filtering requires the sampling of the signal with its full band. As a result of high sampling demands, conventional matched filtering is not suitable for radars where the processing power is limited. To

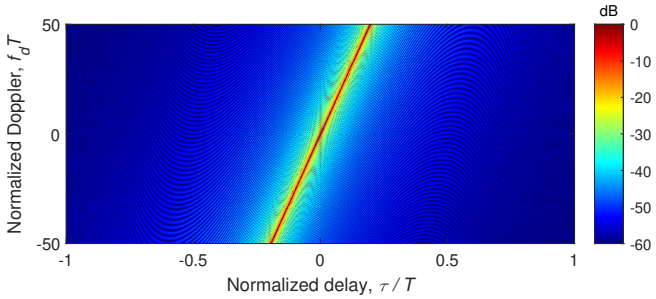

a)

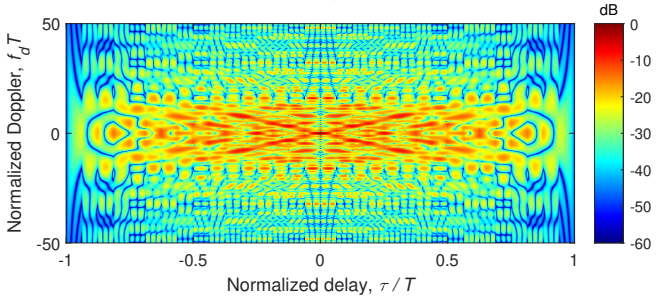

b)

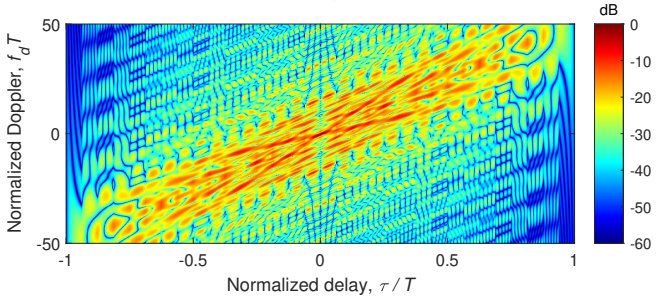

c)

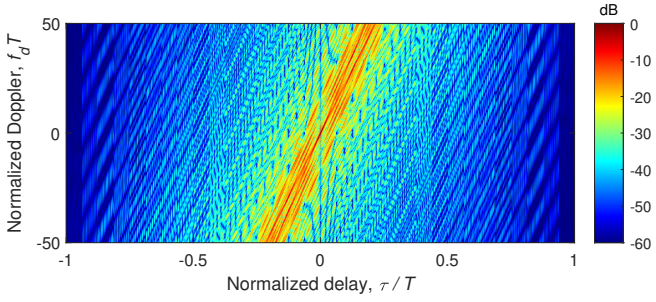

d)

Figure 2.2: Ambiguity functions of a) LFM B=10 MHz b) PMCW c) PC-FMCW B=2 MHz d) PC-FMCW B=10 MHz. The shearing effect of LFM on the ambiguity function of phase-coded signal with $B_c = 0.62$ MHz is observed.

overcome this problem, the matched filter can be realized via filter bank after dechirping, or it can be approximated by using the group delay filter receiver (see Section 2.4). Both of these receiver approaches significantly decrease the sampling requirements of analog-to-digital converter (ADC) [101]. In this section, we focus on the matched filter and the ambiguity function to set the boundaries for the sensing performance of the waveform with different code families.

The ambiguity function is widely used for studying radar waveforms and determines the range-Doppler resolution of the transmitted signal for a chosen system parameters [113]. The narrow-band ambiguity function of signal $x(t)$ can be written as a linear (aperiodic) convolution of a signal with its time-delayed and frequency-shifted replica:

$$\left|\chi(x(t);\tau,f_d)\right| = \left|\int_{-\infty}^{\infty} x(t)\, x^*(t-\tau) e^{j2\pi f_d t}\, dt\right|, \tag{2.9}$$

where τ is the delay and f_d is the Doppler frequency shift. In [113], it is proved that adding the linear frequency modulation, which is equivalent to a quadratic-phase modulation, shears the resulting ambiguity function. This main property of the ambiguity function can be represented as:

$$\left|\chi(s(t)\exp\left(j\pi k t^2\right);\tau,f_d)\right| \Longleftrightarrow \left|\chi(s(t);\tau,f_d - k\tau)\right|. \tag{2.10}$$

Consequently, the ambiguity function of PC-FMCW is a sheared version of the coding signal ambiguity function, and this shearing effect is proportional to the chirp slope. In the following numerical simulations, we select $T = 25.6\ \mu$s and $B = 10$ MHz for the chirp signal. Moreover, we use chip bandwidth $B_c = 0.62$ MHz for the random phase-coded signal, and no repetitions of the code over the duration of the signal are performed. Note that the chirp bandwidths selected herein are different from those found in automotive radars ($B = 300$ MHz) to illustrate the shearing effect clearly. As mentioned in the introduction, one of the advantages of FMCW signal is its high range resolution and good Doppler tolerance. This behaviour can be seen in Figure 2.2 a, where the ambiguity function of the linear frequency modulation (LFM) signal is demonstrated. However, the ambiguity function of PMCW has poor Doppler tolerance as shown in Figure 2.2 b, and thus the PMCW signal often requires a special process for moving targets to compensate for the poor Doppler tolerance. We observe the shearing effect phenomenon in Figure 2.2 c, where the ambiguity function of PC-FMCW with $B = 2$ MHz is demonstrated. Due to this shearing effect, the ambiguity function of PC-FMCW has a range-Doppler coupling similar to FMCW. As shown in Figure 2.2 d, the Doppler tolerance of PC-FMCW has substantially improved compared to PMCW by increasing the chirp bandwidth to $B = 10$ MHz.

In addition, we compare the ambiguity functions of PMCW and PC-FMCW in Figure 2.3 to observe the advantages of PC-FMCW over PMCW clearly. It can be seen that the PMCW signal with $B_c = 0.625$ MHz is very sensitive to Doppler frequency shifts caused by the target motion, which makes this waveform vulnerable to target motion. On the other hand, the ambiguity function of PC-FMCW has range-Doppler coupling similar to the chirp signal and thus has good Doppler tolerance [114]. In automotive radars, the Doppler shift can be estimated over multiple sequentially transmitted waveforms; hence the coupling between range and Doppler can be resolved. It is important to note that

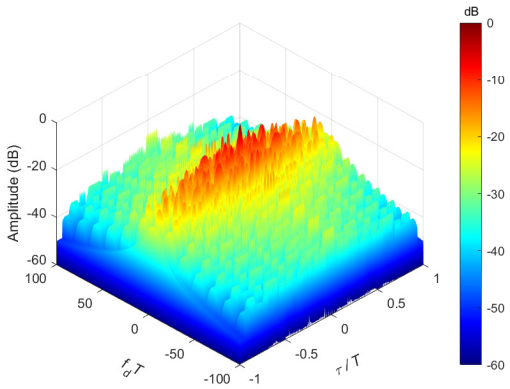

a)

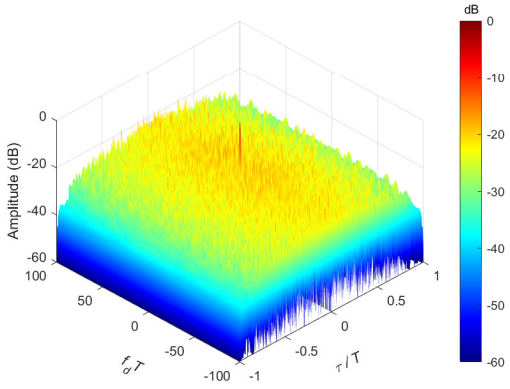

b)

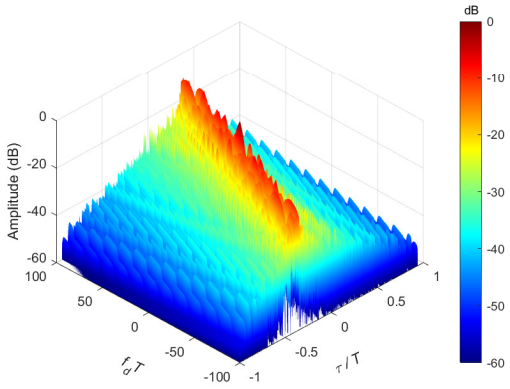

c)

Figure 2.3: Range-Doppler ambiguity function of normalized delay versus normalized Doppler a) PMCW with $B_c = 0.62$ MHz b) PMCW with $B_c = 10$ MHz c) PC-FMCW with $B_c = 0.62$ MHz and $B = 10$ MHz.

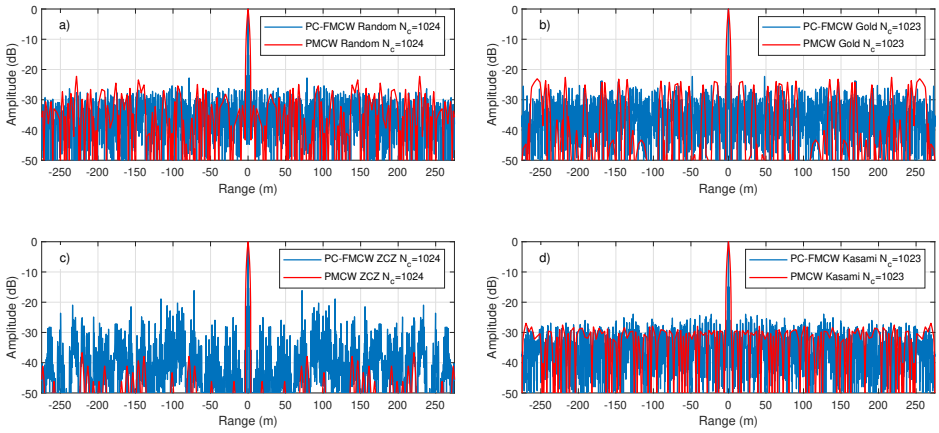

Figure 2.4: Range profile comparison of PMCW and PC-FMCW with different code families; a) Random b) Gold c) ZCZ d) Kasami.

dechirping based processing methods will be used to process the PC-FMCW waveforms. After dechirping, the range resolution will be determined by the chirp bandwidth while the ADC sampling requirements will remain low and the code bandwidth will be the limiting factor for the required ADC sampling. Thus, we compare the full bandwidth of PC-FMCW with the code bandwidth of PMCW. Note that in the case of PMCW, the code bandwidth needs to be increased up to $B_c = 10$ MHz, which further raises the sampling requirement of ADC in the receiver, to achieve the same range resolution. Therefore, PC-FMCW has the advantages of mutual orthogonality while keeping the advantages of the FMCW signal such as good Doppler tolerance and high range resolution by using the typical chirp bandwidth values. These facts favour the usage of PC-FMCW over PMCW.

2.3.1. DIFFERENT CODE FAMILIES TO USE WITH PC-FMCW

In this subsection, we compare the zero Doppler cut (range profile) of the ambiguity functions of PC-FMCW modulated with different code families, namely random, Gold, zero correlation zone (ZCZ) and Kasami codes [111], which have different sidelobe levels. Although these codes are optimized for periodic auto-correlation properties, they still exhibit reasonable aperiodic auto-correlation properties. We consider an automotive radar scenario where the transmitting PC-FMCW has a chirp duration $T = 25.6$ μs with a carrier frequency $f_c = 77$ GHz, and chirp bandwidth $B = 300$ MHz. The BPSK sequence is used as a phase-coded signal to modulate FMCW. Hence, the amplitude of the phase-coded signal is constant and changes between $\{-1, 1\}$. We use $N_c = 1024$ number of chips per chirp. Thus the bandwidth of the code signal becomes $B_c = N_c / T = 40$ MHz.

The ambiguity functions of PC-FMCW and PMCW are simulated by using the same code families. The comparison of the range profiles with the zero Doppler cut is demonstrated in Figure 2.4. It can be seen that the random code provides ~ 23 dB dynamic range with the chosen system parameters, while the Gold code provides the same dynamic range with lower sidelobes in the far range. Moreover, it is observed that the range profile

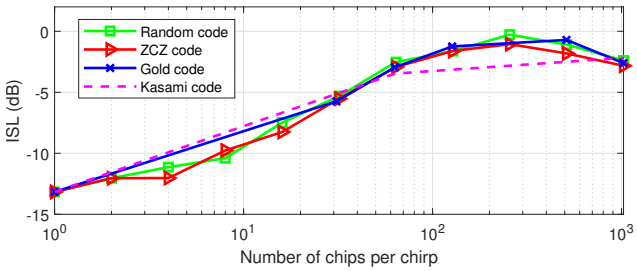

Figure 2.5: Integrated side lobe level comparison of PC-FMCW with different code families.

of the code itself (PMCW) is changed essentially after modulating with the chirp signal (PC-FMCW). This behaviour can be seen especially for the ZCZ code in Figure 2.4 c. The ZCZ code, as the name implies, is a code that tries to find a zone with zero correlation, and the range profile of the ZCZ code has sidelobes less than ~ -40 dB close to the main lobe. However, adding linear frequency modulation alters the code property, and its sidelobe is raised to ~ -15 dB. Thus, the design of optimal code for PC-FMCW is a problem to be considered in future. As for the Kasami code, we see that it has a dynamic range of ~ 30 dB without chirp and modulating with chirp increases its dynamic range to ~ 23 dB with a slightly different range profile than the Gold code.

Next, we assess the sidelobe levels of different code families by using integrated sidelobe level (ISL). Since we consider automotive radar applications, we only take into account ISL between range interval ± 250 meter noted as the interval $[r_1, r_4]$. Then ISL

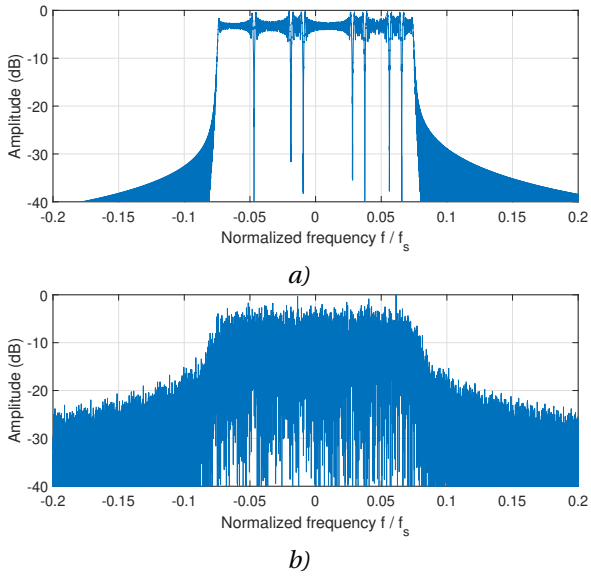

Figure 2.6: Spectrum of the transmitted PC-FMCW with random phase-coded signal a) $N_c = 16$, relative code bandwidth $B_c/B = 0.002$ b) $N_c = 1024$, relative code bandwidth $B_c/B = 0.133$.

can be defined as [115]:

$$\mathrm{ISL} = 10\log_{10}\left(\frac{\int_{r_1}^{r_2}\left|\chi(\tau,0)\right|^2 \mathrm{d}\tau + \int_{r_3}^{r_4}\left|\chi(\tau,0)\right|^2 \mathrm{d}\tau}{\int_{r_2}^{r_3}\left|\chi(\tau,0)\right|^2 \mathrm{d}\tau}\right), \tag{2.11}$$

where the interval $[r_2, r_3]$ defines the main lobe, and $\chi(\tau,0)$ is the zero Doppler cut of the ambiguity function of signal $x(t)$.

ISL of PC-FMCW with investigated code families are compared and illustrated as a function of the number of chips per chirp in Figure 2.5. It is seen that the ISL of investigated code families are comparable, and their ISL raise as the number of chips per chirp increases. This behaviour is expected because the bandwidth of the code becomes comparable to the chirp bandwidth and spectrum leakage outside of the chirp bandwidth leads to increased sidelobes. To illustrate this issue, we compare two values of the relative bandwidth of the code with chirp bandwidth as B_c/B in Figure 2.6. It can be observed that the power of spectrum leakage outside of the chirp bandwidth at normalized frequency $f/f_s = 0.15$ increased ~ 20 dB as the relative code bandwidth changed from 0.002 to 0.133. Thus, the relative code bandwidth limits the sensing performance and should be considered in the system design.

2.4. RECEIVER STRUCTURES FOR PC-FMCW

In this section, we investigate dechirping based processing approaches for the PC-FMCW waveforms. The received PC-FMCW signal reflected from the target is the round trip delayed version of the transmitted PC-FMCW and can be written as:

$$x_{\mathrm{R}}(t) = \alpha_0 s(t-\tau(t)) e^{-j\left(2\pi f_c(t-\tau(t))+\pi k(t-\tau(t))^2\right)}, \tag{2.12}$$

where α_0 is a complex amplitude proportional to the target back-scattering coefficient and propagation effects. As explained in Section 2.1, the dechirping and decoding strategy is adapted to decrease the sampling demands from ADC. The dechirping receiver structure exploits the instantaneous frequency differences between the transmitted and received chirps, as shown in Figure 2.7. In the dechirping process, the received PC-FMCW signal is mixed with the complex conjugate of the uncoded FMCW signal. Then, the mixer output can be written as:

$$\begin{aligned} x_{\mathrm{M}}(t) =& x_{\mathrm{R}}(t) x_{\mathrm{FMCW}}(t)^* \\ =& \alpha_0\, s(t-\tau(t)) e^{-j\left(2\pi f_c(t-\tau(t))+\pi k(t-\tau(t))^2\right)} e^{j(2\pi f_c t+\pi k t^2)} \\ =& \alpha_0\, s(t-\tau(t)) e^{-j\left(2\pi f_c t-2\pi f_c\tau(t)+\pi k t^2-2\pi k\tau(t)t+\pi k\tau^2(t)\right)} e^{j(2\pi f_c t+\pi k t^2)} \\ =& \alpha_0\, s(t-\tau(t)) e^{j\left(2\pi f_c\tau(t)+2\pi k\tau(t)t-\pi k\tau^2(t)\right)}, \end{aligned} \tag{2.13}$$

where $(\cdot)^*$ denotes the complex conjugate. The resulting beat signal contains the range and Doppler information of the target. However, the Doppler frequency shift in one beat signal is typically much smaller than the beat frequency resolution (one range cell) and can be neglected. As explained earlier, chirp sequence radars use multiple chirps to estimate the Doppler frequency shift from the phase shift within multiple beat signals.

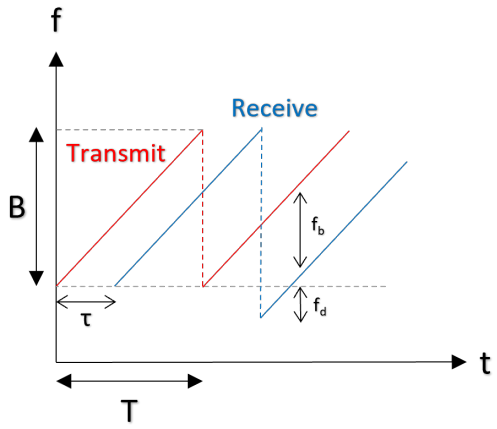

Figure 2.7: Illustration of the chirp sequence and dechirping process.

Assume a radar transmits N_p number of chirp pulses (sweeps) for Doppler processing and define the fast-time term as $t = t' - mT$, where $t \in [0,\ T]$, m is the index of the chirp pulse for slow-time and t' is the total duration of the one snapshot or frame. Then the round trip delay becomes:

$$\tau(t+mT) = \frac{2(R_0 + v_0(t+mT))}{c} = \tau_0 + \frac{2v_0}{c}(t+mT). \tag{2.14}$$

where R_0 is the range, v_0 is the velocity, and c is the speed of light. Subsequently, the mixer output in both fast-time and slow-time representation can be written as:

$$\begin{aligned} x_{\mathrm{M}}(t,m) =& \alpha_0 s(t-\tau(t+mT))\, e^{j(2\pi f_c \tau(t+mT))} e^{j(2\pi k\tau(t+mT)t)} e^{-j(\pi k\tau^2(t+mT))} \\ =& \alpha_0 s\left(t - \tau_0 - \frac{2v_0}{c}mT - \frac{2v_0}{c}t\right) e^{j(2\pi f_c\tau_0 + 2\pi f_c \frac{2v_0}{c}mT + 2\pi f_c \frac{2v_0}{c}t)} \\ & e^{j(2\pi k\tau_0 t + 2\pi k\frac{2v_0}{c}mTt + 2\pi k\frac{2v_0}{c}t^2)} e^{-j(\pi k\tau^2(t+mT))}. \end{aligned} \tag{2.15}$$

Since the velocity of the target is much smaller than the speed of light as $v_0 \ll c$, the terms with $\tau^2(t+mT)$ and t^2 in the nominator and c^2 in the denominator can be neglected due to their small values. Then, the mixer output becomes:

$$\begin{aligned} x_{\mathrm{M}}(t,m) \approx& \alpha_0 s\left(t - \tau_0 - \frac{2v_0}{c}mT - \frac{2v_0}{c}t\right) e^{j(2\pi f_c\tau_0 + 2\pi f_c\frac{2v_0}{c}mT + 2\pi(f_c\frac{2v_0}{c} + k\tau_0)t + 2\pi k\frac{2v_0}{c}mTt)} \\ =& \alpha_0 s\left(t - \tau_0 - \frac{2v_0}{c}mT - \frac{2v_0}{c}t\right) e^{j(2\pi f_c\tau_0 + 2\pi f_d mT + 2\pi(f_d+f_b)t + 2\pi k f_d mTt)}, \end{aligned} \tag{2.16}$$

where $f_d = \frac{2v_0 f_c}{c}$ is the Doppler frequency and $f_b = k\tau_0$ is the beat frequency. For typical automotive radars parameters, the target displacement within a single chirp duration is

much smaller than the range resolution cell as the term $\frac{2v_0}{c}t \ll \frac{c}{2B}$, and thus it can be omitted. In addition, we assume the code bandwidth is much smaller than the chirp bandwidth $B_c \ll B$. Thus, the term $\frac{2v_0}{c}mT$ over coherent pulse integration time $\frac{2v_0}{c}mT \ll \frac{c}{2B_c}$ and it can be neglected. Moreover, the term $2\pi k f_d mTt$ is related to the range migration, i.e. the target displacement due to target movement. In general, no range migration occurs within one chirp duration as it is small compared to Doppler resolution $\frac{1}{mT}$ in automotive radars, and thus it can be neglected. However, the range migration term can be crucial over coherent pulse integration (CPI) time for very fast-moving targets. In case range migration is crucial, it can be considered in the signal processing chain with conventional solutions [102, 116]. Furthermore, the Doppler frequency shift term related to the fast-time is typically smaller than beat frequency resolution in automotive radars, i.e. $f_d \ll f_s/N$, where f_s is the sampling frequency of the beat signal and N is the number of fast-time samples. Thus, we can approximate $2\pi(f_d + f_b)t \approx 2\pi f_b t$ during fast-time processing without loss of generality. Finally, the term $\exp(j2\pi f_c \tau_0)$ is a constant phase term and can be incorporated into α_0. Consequently, the mixer output in both fast-time and slow-time representation becomes:

$$x_{\mathrm{M}}(t,m) = \alpha_0 s(t-\tau_0) e^{j(2\pi f_d mT + 2\pi f_b t)}. \tag{2.17}$$

The Doppler term $\exp(j2\pi f_d mT)$ will be used for velocity estimation in the slow-time processing. The slow-time processing is straightforward and the same as in the conventional FMCW automotive radars. The signal related to the fast-time processing part contains two main components: the delayed phase-coded signal and a tone at the beat frequency. The beat signal term is standard for dechipring of LFM signals. However, the delayed code term $s(t-\tau_0)$ needs to be considered before extracting the range of the target. Since the range estimation is only related to the fast-time processing part, we focus on signal analysis in fast-time. The mixer output only related to the fast-time processing part can be recast as:

$$x_{\mathrm{M}}(t) = \alpha_0 s(t-\tau_0) e^{j(2\pi f_b t)},\ t \in [0, T] \tag{2.18}$$

In the following subsections, we investigate two receiver approaches to process coded beat signals.

2.4.1. FILTER BANK RECEIVER

The form of (2.18) can be alternatively interpreted if we denote $f_{VD} = f_b = k\tau_0$ as a virtual Doppler frequency shift. In this formulation, it resembles the response of a general waveform $s(t)$ with the time delay τ_0 and Doppler frequency shift f_{VD}. Note that by definition, f_{VD} is of the same order of magnitude as the bandwidth of the modulation signal $s(t)$. In this case, the optimal receiver in white noise is a matched filter for each range-Doppler hypothesis [104]. It can be realized either via a filter bank for all possible range-Doppler hypotheses or via performing Doppler processing prior to range compression (if f_{VD} and τ were unknown independent parameters). Here $f_{VD} = k\tau_0$. Thus the filter bank should be done only in the range dimension. A similar approach called compensated stretch processing was earlier discussed in [33]. The receiver then performs:

$$y(\tau) = \int_0^T x_{\mathrm{M}}(t) s^*(t-\tau) e^{-j(2\pi k\tau t)} dt \tag{2.19}$$

The received (complex) beat signal sampled by analog-to-digital converter (ADC) operating at the sampling frequency f_s is stored in vector $\mathbf{x}_M \in \mathbb{C}^{N\times 1}$, defined by:

$$\mathbf{x}_M = \alpha_0 s\left(n/f_s - \tau_0\right) e^{j(2\pi k \tau_0 n/f_s)}, \tag{2.20}$$

where $t = n/f_s, n = 0,\ldots,N-1$.

The second part of the integral in (2.19) for the fixed τ can be given via a Hadamard product of two vectors $\mathbf{a}(\tau)\odot\mathbf{s}(\tau)$:

$$\begin{aligned}\mathbf{a}(\tau) &= e^{j(2\pi k \tau n/f_s)},\\ \mathbf{s}(\tau) &= s\left(n/f_s - \tau\right),\end{aligned} \tag{2.21}$$

with $n = 0,\ldots,N-1$, $\mathbf{a}(\tau),\mathbf{s}(\tau) \in \mathbb{C}^{N\times 1}$. Stacking the steering vectors of beat signal and delayed modulation signal as columns in $N \times N_r$ matrices $\mathbf{A} = [\mathbf{a}(\tau_0),\ldots,\mathbf{a}(\tau_{N_r})]$ and $\mathbf{S} = [\mathbf{s}(\tau_0),\ldots,\mathbf{s}(\tau_{N_r})]$ with N_r being the predefined number of range cells in the range grid, it is possible to write the convolution (2.19) via a matrix-vector product:

$$\mathbf{y} = (\mathbf{A}\odot\mathbf{S})^H \mathbf{x}_M \tag{2.22}$$

Note that the conventional FMCW processing (with no extra modulation) can be equivalently shown considering $\mathbf{S} = \mathbf{1}^{N\times N_r}$.

In a real system operating with real (not complex) signals, down-conversion (2.18) should be followed by the low-pass filter to remove high-frequency components. In case of $s(t)$ being a signal with large power outside the main beam, as it is for binary phase shift keying (BPSK) sequence with the bandwidth comparable to f_s, then the binary signal before and after filtering will be significantly different. That will lead to the distortion of the range profile. This can be compensated by filtering the reference modulation signal $s(t)$ with the same low-pass filter prior to applying it in (2.22). That will significantly reduce range profile distortion due to signal mismatch. It should be noted that the filter bank receiver approach leads to the computational complexity of Discrete Fourier Transform (DFT) $\mathcal{O}(N^2)$. A more efficient implementation via Fractional Fourier transform has been recently proposed, hence being still more costly than the group delay filter receiver discussed below [117].

2.4.2. GROUP DELAY FILTER RECEIVER

The range information of the target is embedded in the beat signal, and it can be obtained by applying Fast Fourier Transform (FFT). However, the modulation signal $s(t-\tau_0)$ should be removed from the dechirped signal before extracting the range information via FFT. For a short-range radar application $s(t-\tau_0) \approx s(t)$, then the dechirped signal can be demodulated by multiplying (2.18) with $s^*(t)$ directly [97]. However, the applicability of this processing is limited to the short-range applications with $R_{\max} \le c/(2B_c)$, where B_c is the bandwidth of phase-coded signal $s(t)$. For applications where the aforementioned range requirement can not be satisfied, then the responses in all the range cells should be aligned in fast-time before demodulation to compensate the time delay τ_0. This alignment can be realized via the group delay filter as proposed in [85, 88].

Consider a group delay filter with unity magnitude response as:

$$H_g(f) = \exp\big(j\theta(f)\big), \tag{2.23}$$

where the filter has the group delay $\tau_g(f)$. The group delay is the time delay of the narrow-band signal at a chosen frequency and is equal to the first derivative of the filter phase response. For proper demodulation of $s(t-\tau_0)$, the filter should eliminate the delay τ_0. Thus the required linear group delay is:

$$\tau_g(f)\big|_{f=f_b} = -\frac{1}{2\pi}\frac{d\theta(f)}{df}\Big|_{f=f_b} = -\tau_0 = -f_b/k. \tag{2.24}$$

Taking the integral of (2.24) over the frequency variable f, the phase response of the group delay filter $H_g(f)$ becomes:

$$\theta(f) = \frac{\pi f^2}{k}. \tag{2.25}$$

The derived filter is applied to the dechirped signal (2.18) in the frequency domain, followed by demodulation in the fast-time, which yields the response [88]:

$$\begin{aligned} y_0(t) &= \mathscr{F}^{-1}\{\mathscr{F}\{x_M(t)\}H_g(f)\}s^*(t) \\ &= \alpha_0 \exp\big(j2\pi f_b t\big)\exp\big(j\epsilon(t)\big). \end{aligned} \tag{2.26}$$

Note that the group delay filter eliminated τ_0 for each beat signal and allows demodulation at ranges $R_{\max} \geq c/(2B_c)$. The derived filter has a quadratic frequency component within its phase response. Consequently, the filter leads to the so-called group delay dispersion effect expressed via the residual phase error $\exp\big(j\epsilon(t)\big)$. For a narrow-band modulation signal with the bandwidth $B_c \ll f_s$, the residual phase error can be neglected. However, the narrow-band assumption can not be applied if B_c is comparable to f_s, which will lead to the distortion of range response. To improve the sensing performance, compensation of the group delay dispersion effect will be discussed in Chapter 4. The group delay filter receiver approach leads to the computational complexity of FFT $\mathcal{O}(N\log_2(N))$.

2.5. SENSING PERFORMANCE OF EXISTING RECEIVERS

In this section, we compare the sensing performance of the signal processing described above. Assume an automotive radar transmitting phase modulated FMCW at carrier frequency $f_c = 77$ GHz with chirp duration $T = 12.8$ μs, and chirp bandwidth $B = 200$ MHz. The dechirped signal (2.18) is filtered by Hamming low-pass filter (LPF), if not mentioned otherwise, with the cut-off frequency $f_{\text{cut}} = \pm 20$ MHz. The sampling frequency for the beat signal is $f_s = 40$ MHz. For Doppler processing, $N_p = 32$ number of chirp pulses, where each sweep uses a different modulation signal, is considered.

The modulation signal $s(t)$ is selected as random BPSK sequence with $s(t) \in \{-1, 1\}$. The bandwidth of the modulation signal B_c is controlled with the number of chips per chirp N_c as $B_c = N_c/T$. E.g. a modulation signal with a $N_c = 256$ has a bandwidth $B_c = 20$ MHz. To prevent signal mismatch, we apply the same LPF to the modulation signal used for demodulation in both receivers. To focus on the waveform sensing properties, we

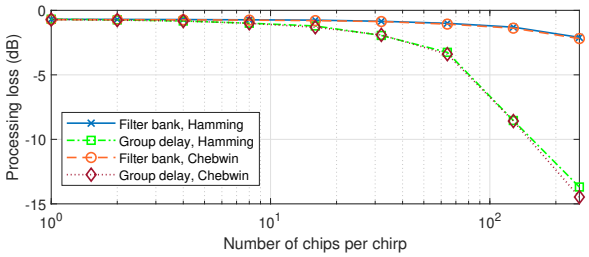

Figure 2.8: Processing loss vs number of chips per chirp.

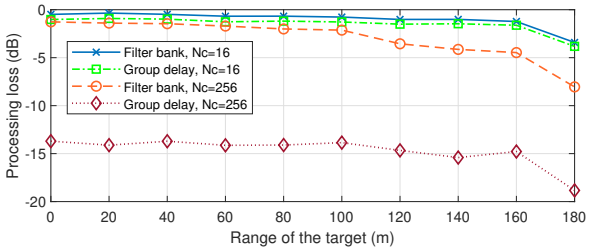

Figure 2.9: Processing loss vs range of the target.

consider a noise-free scenario with a single target at the range $R_0 = 100$ m and the radial velocity $v_0 = -20$ m/s.

First, we investigated the signal processing loss versus the number of chips per chirp for both processing approaches in Figure 2.8. It should be noted that the processing loss means the loss in processing gain and will cause SNR loss in the noisy scenario. For a long code, the bandwidth of the modulation signal becomes large, and LPF suppresses some parts of the signal, which leads to processing loss common for both receivers. For comparison, we also considered LPF with 60 dB Chebyshev window and noticed that the type of LPF has a minor effect on the processing loss (Figure 2.8).

Next, we illustrated the processing loss as the function of the target range in Figure 2.9. As the beat frequency (proportional to the target range) approaches the cut-off frequency of LPF, a part of the spectrum of the modulated signal is filtered out, which leads to processing loss. Moreover, the group delay filter receiver suffers from high residual phase error when the bandwidth of the modulation signal increases. This can be explained by the dispersion of the BPSK signal due to the group delay filter. As shown in Figure 2.10, the BPSK signal has a wide spectrum in the time instances of the phase shifts, and the group delay filter applies different time delays to each frequency component. This leads to interference between adjacent phase shifts and degrades the demodulation performance. As a consequence, the range profile becomes distorted and can be seen as processing loss in Figure 2.8 and Figure 2.9. The dispersion effect is more crucial for long code sequences (a short time interval between chips).

For the selected radar parameters, the processing loss is comparable up to $N_c = 16$ for both processing techniques while the processing loss of the group delay method rapidly increases up to ~ 15 dB as the numbers of chips per chirp become $N_c = 256$.

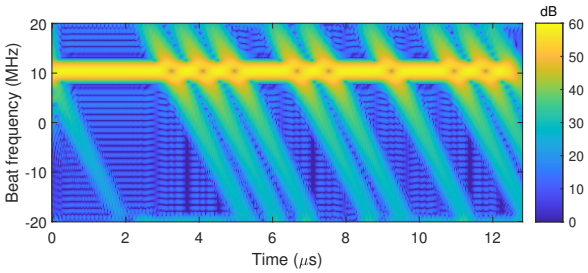

Figure 2.10: Spectrogram of group delay filter output for $N_c = 16$.

This processing loss behaviour can be seen in Figure 2.11, where the range profiles of both processing methods are compared for different numbers of chips per chirp. It can be observed that in the vicinity of the target, the response follows the Sinc-like shape, expected for LFM processing. This region is defined by the main-beam width of the modulation $s(t)$. Outside of this region, the response has a noise-like pattern, typical for a random BPSK sequence. The level of this noisy sidelobe is determined by the time-bandwidth product of the modulation sequence, i.e. $-10\log_{10}(TB_c)$ for each modulated chirp. It can be seen in Figure 2.11 that the group delay filter approach has lower sidelobes compared to the filter bank approach in case of a small number of chips per chirp. However, the matched filter provides better performance for the long code sequences as it still recovers the main lobe properly.

To assess the sidelobe level, we compared the integrated sidelobe level (ISL) for both processing methods defined as [115]:

$$\mathrm{ISL} = 10\log_{10}\left(\frac{\int_{-\infty}^{a}|y(f_d,\tau)|^2 d\tau + \int_{b}^{\infty}|y(f_d,\tau)|^2 d\tau}{\int_{a}^{b}|y(f_d,\tau)|^2 d\tau}\right), \tag{2.27}$$

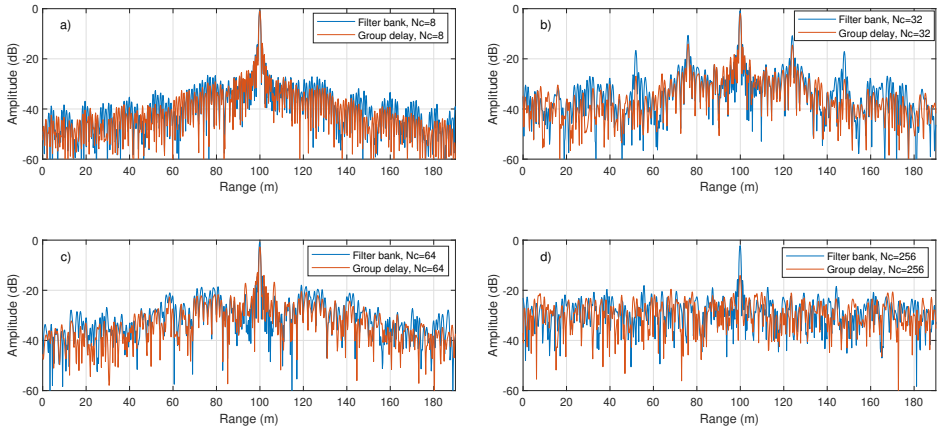

Figure 2.11: Comparison of the range profile for both processing approaches.

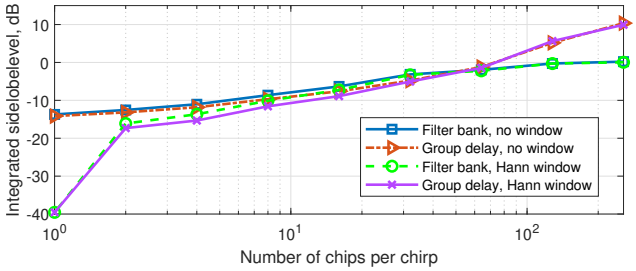

Figure 2.12: Comparison of the integrated sidelobe level vs number of chips per chirp for both processing techniques.

where the interval $[a,b]$ contains the energy of the main lobe, and y is the signal for a given Doppler value f_d.

The ISL of the investigated processing methods is compared and demonstrated versus the number of chips per chirp in Figure 2.12. It is observed that the ISL of the group delay filter method up to the number of chips per chirp $N_c = 64$ is slightly lower compared to the filter bank approach. This is expected as the group delay filter method has lower sidelobes and similar processing loss for a small number of chips per chirp, while the range profile of both processing methods looks very similar for a $N_c = 64$. However, the filter bank approach provides less processing loss with a comparable sidelobe level as the

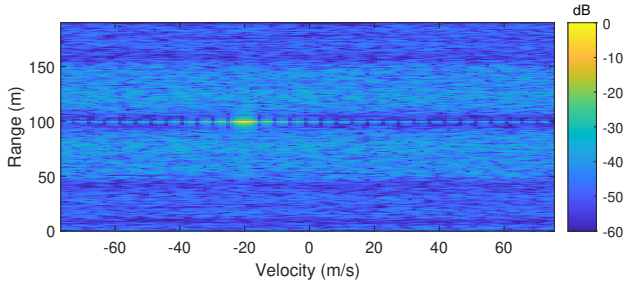

Figure 2.13: Filter bank approach, range-Doppler profile for $N_c = 64$.

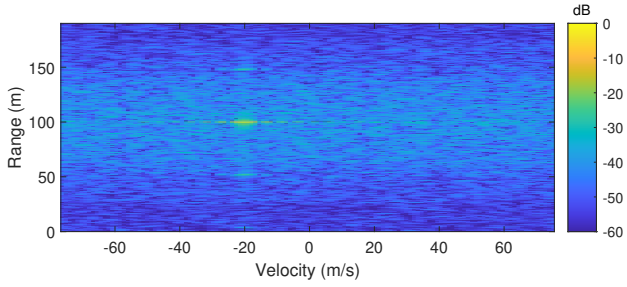

Figure 2.14: Group delay filter approach, range-Doppler profile for $N_c = 64$.

number of chips per chirp increases, and thus the ISL of the group delay method becomes higher for the number of chips per chirp $N_c > 64$ as shown in Figure 2.12.

Finally, we investigated the range-Doppler profiles of both processing methods. The number of chips per chirp is selected as $N_c = 64$ since both methods have similar ISL values. The range-Doppler profiles are demonstrated in Figure 2.13 and Figure 2.14 for filter bank and group delay methods, respectively. Both figures show that the investigated processing methods detect the moving target at -20 m/s. Note that the group delay filter approach uses FFT, and therefore it has the computational complexity of $\mathcal{O}(N\log_2(N))$ where the filter bank method uses DFT which has the $\mathcal{O}(N^2)$ as computational complexity.

2.6. EXPERIMENTS

In this section, we experimentally validate the sensing performance of the investigated processing methods. The experimental assessment of the investigated processing approaches has been done using PARSAX, which is an S-band polarimetric Doppler radar [118]. We have transmitted phase-coded FMCW at carrier frequency $f_c = 3.315$ GHz with chirp duration $T = 1$ ms, and chirp bandwidth $B = 40$ MHz. The modulation signal $s(t)$ is selected as zero correlation-zone (ZCZ) code family and we set the number of chips per chirp $N_c = 1024$. Thus, the modulation signal has a bandwidth $B_c = 1.024$ MHz. Moreover, we transmitted $N_p = 128$ chirps with identical codes for Doppler processing.

During measurements, we observe a moving car located at 1178 m away from the radar with a radial velocity ~ 15 m/s. We have applied two investigated processing approaches to the collected data. In addition, we have performed full-band matched filtering as discussed in [97] for comparison. The range profiles estimated with approaches are compared and demonstrated in Figure 2.15. Furthermore, range-Doppler profiles of full-band matched filter, filter bank and group delay filter approaches are shown in Figure 2.16, Figure 2.17, and Figure 2.18, respectively. The noise level is estimated from another target-free Doppler cell and used to normalize the signal power (represented as a black dashed line). The group delay filter approach suffers from residual phase error that leads to high processing loss for a long code sequence, as demonstrated in Figure 2.8. As a result, the group delay filter receiver as proposed in the state-of-the-art provides the worst sensing

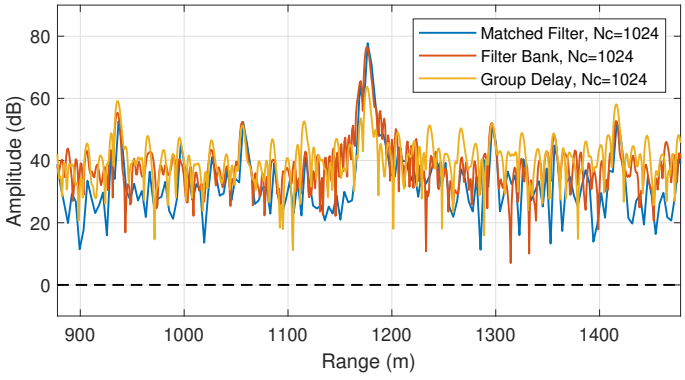

Figure 2.15: Moving target experiment: Comparison of the range profile for the three processing approaches.

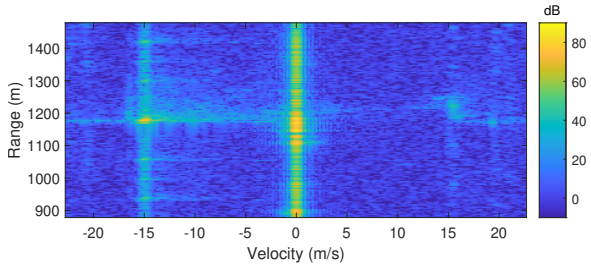

Figure 2.16: Moving target experiment: Range-Doppler profile for full-band matched filter approach.

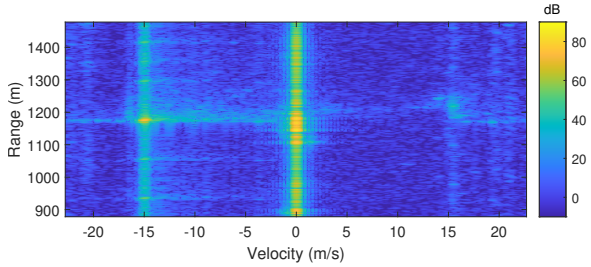

Figure 2.17: Moving target experiment: Range-Doppler profile for filter bank approach.

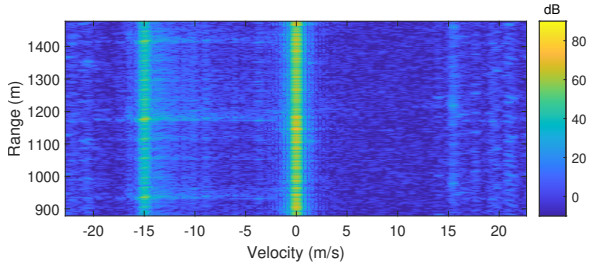

Figure 2.18: Moving target experiment: Range-Doppler profile for group delay filter approach.

performance. The full-band matched filter and filter bank approaches provide similar range profiles, and both of them outperform the group delay filter approach for this long code sequence scenario.

2.7. CONCLUSIONS

This chapter explores the sensing properties of the phase-coded FMCW waveform and possible receiver strategies suitable for automotive radars. To this end, common automotive radar waveforms and their signal models are revisited. Then, the ambiguity function of PC-FMCW is investigated, and the shearing effect of the chirp signal as a carrier is examined. It is illustrated that modulating with the chirp signal shears the ambiguity function of the phase-coded signal. Due to the shearing effect, the ambiguity function of PC-FMCW has a range-Doppler coupling similar to FMCW. This coupling

between range and Doppler can be resolved since the Doppler shift can be estimated over multiple sequentially transmitted waveforms in automotive radars. Consequently, the PC-FMCW waveform has good Doppler tolerance and high range resolution similar to FMCW. In addition, different code families, namely random, Gold, ZCZ and Kasami codes, are investigated to use with the PC-FMCW waveform. The zero Doppler cuts of the ambiguity function are shown for the investigated code families, and their sensing performance has been compared. It has been demonstrated that the sidelobe values in the range profile of PC-FMCW might be essentially different from the sidelobe levels of code auto-correlation function. In particular, the investigated code families provide comparable ISL. Thus, different codes with different auto-correlation functions provide very similar sensing performance for PC-FMCW. Moreover, it is shown that the relative code bandwidth with respect to chirp bandwidth limits the sensing performance, and the ISL raises as the number of chips per chirp increases. Hence, the relative code bandwidth needs to be considered in the system design.

Afterwards, the dechirping process is examined, and two receiver approaches based on the stretch processing are studied for the PC-FMCW waveforms. To this end, the filter bank (compensated stretch processing) and group delay filter receivers with low ADC sampling requirements have been studied analytically and verified experimentally. The filter bank has been applied to the sampled data after dechirping for all ranges of interest. Such a method, however, raises the computational complexity ($\mathcal{O}(N^2)$) compared to the standard stretch processing ($\mathcal{O}(N\log_2(N))$) as it obtains the range information via matrix multiplication instead of FFT. The group delay filter receiver, on the other hand, adjusts the dechirping and decoding strategy to lower the computational complexity. In the group delay filter receiver, the dechirping is followed by the alignment of the coded beat signals for targets at different ranges using an ideal group delay filter. After alignment, all coded beat signals are decoded with the reference code, and the target range information is extracted from the beat signals via FFT ($\mathcal{O}(N\log_2(N))$). Thus, the limited processing power of automotive radars favours the utilization of the group delay filter receiver. However, the group delay filter causes a quadratic phase shift (group delay dispersion effect) on the dechirped signal and distorts the received code. Consequently, this distortion significantly degrades decoding performance when codes with a high number of phase changes per chirp (meaning large code bandwidth) are used.

In addition, the sensing performance of the investigated receivers is compared with numerical simulations and measurements. The trade-off between sensing performance and the code bandwidth of the waveform is demonstrated in terms of the integrated sidelobe level for both processing methods. Increasing the number of chips per chirp raises the code bandwidth, and some part of the signal spectrum is filtered out by LPF, which leads to the processing loss. This processing loss increases as the target range (i.e. corresponding beat frequency) approaches the cut-off frequency of LPF. It is shown that both processing receiver structures give comparable range profiles for short to moderate bandwidth of the code signal, while the filter bank approach provides favourable performance as the number of chips increases. This is due to the fact that the group delay filter suffers from the dispersion effect and the processing loss increases substantially in case of large code bandwidth. Such performance degradation limits the code bandwidth and, associated with it, signal isolation or communication data rate.

3

SMOOTHED PC-FMCW WAVEFORM AND ITS PROPERTIES

Smoothed phase-coded frequency modulated continuous waveform (SPC-FMCW), which aims to enhance the waveforms' sensing performance in the limited receive's analogue bandwidth, is studied. The spectrum widening due to abrupt phase changes seen in the BPSK coding is investigated analytically, and a phase smoothing operation is proposed to decrease the spectral widening of the coded beat signals. The Gaussian filter is applied to obtain smooth waveform phase transitions, and two SPC-FMCW waveforms based on the Gaussian binary coding and Gaussian minimum phase shift keying (GMSK) coding are obtained. The resulting waveforms are examined and derived in different domains. The investigated waveforms' instantaneous frequencies and spectral widening behaviours are compared via numerical simulations. Subsequently, the investigated waveforms are processed with the group delay filter receiver, and their sensing performance is assessed. It is demonstrated that the GMSK PC-FMCW waveform provides better sensing performance as the code bandwidth increases and becomes comparable to ADC sampling frequency.

Parts of this chapter have been published in:

U. Kumbul, N. Petrov, C. S. Vaucher, and A. Yarovoy, "Smoothed phase-coded FMCW: Waveform properties and transceiver architecture", in *IEEE Transactions on Aerospace and Electronic Systems*, pp. 1-18, 2022.

3.1. INTRODUCTION

As explained in Chapter 1, waveform coding has been widely used in radars for the purpose of unique waveform recognition [11]. In particular, the PMCW waveform has been used to improve the radar's robustness against interference [83]. However, such coding spreads the RF spectrum of the waveform over a wide bandwidth and requires a dramatic increase in the receiver's analogue bandwidth to achieve high range resolution. On the other hand, the PC-FMCW waveforms can offer high range resolution via stretch processing as the parameter that determines the range resolution becomes the chirp bandwidth. In the PC-FMCW radar, the resulting dechirped signal has two signal components: the delayed phase-coded signal and a tone at the beat frequency as explained in Chapter 2. The code present in the resulting dechirped signal spreads the IF spectrum (spectrum broadening) of the beat signal.

Increasing the code bandwidth (using a longer code sequence) improves the mutual orthogonality between transmitted waveforms [94]. However, the widening of the beat signal raises the required LPF cut-off frequency and, associated with it, the ADC sampling from the receiver side. The minimum ADC sampling needs to be at least two times the LPF cut-off frequency. In case of insufficient selection of the LPF cut-off frequency, some parts of the coded beat signal are lost, i.e. rejected by the LPF of the receiver before decoding. Filtering of the coded beat signal spectrum changes the waveform properties, and the decoding becomes imperfect. This imperfection decreases the dynamic range of the radar and leads to the masking of weak targets [94]. Since automotive radars have a limited ADC sampling power on the receiver side, the spectrum broadening of the coded beat signal needs to be decreased.

The most popular phase coding scheme used for PC-FMCW in the preliminary studies [8, 85] was binary phase shift keying (BPSK). The BPSK coding causes abrupt phase changes that lead to a large spectrum widening of the beat signal. As a consequence, the BPSK signal only with a small bandwidth compared to the sampling frequency (a few chips per chirps) can be used for sensing [97]. In the case of BPSK code bandwidth being comparable to the sampling frequency of ADC, the sidelobe level significantly increases [94]. To decrease the spectrum broadening, we can apply smoother to the code signal. Therefore, other phase modulation types with lower spectral broadening and, thus, better sensing performance are still of much interest.

In this chapter, the smoothed phase-coded frequency modulated continuous waveform (SPC-FMCW) is studied to decrease the spectral widening of the coded beat signal and enhance the sensing performance of the waveforms in the limited receiver analogue bandwidth. The phase smoothing operation is proposed to obtain a smooth phase transition that addresses the bandwidth limitations of BPSK. For analysis, we have used the Gaussian filter as a smoother and derived the SPC-FMCW waveforms in time, frequency and instantaneous frequency domains. Subsequently, we have investigated the SPC-FMCW waveform properties analytically and compared their sensing performance. The remainder of this chapter is structured as follows. We analyze the beat signal spreading due to the BPSK coding in Section 3.2. Then in Section 3.3, we investigate the phase smoothing operation and compare the spectral characteristics of the derived waveforms. Then, we evaluate and assess the sensing performance of the investigated waveforms in Section 3.4. Finally, we draw the conclusion remarks in Section 3.5.

3.2. BEAT SIGNAL SPREADING ANALYSIS

As explained in Chapter 2, the dechirping operation (stretch processing) gives the beat signal. This beat signal exists within the time of the chirp duration and analytically can be written with the rectangle function rect$(t) = 1$, where $t \in [-T/2,\ T/2]$ and zero otherwise. In the FMCW radar, the mixer output contains the beat signal and can be represented as:

$$x_{\mathrm{M_{fmcw}}}(t) = \alpha_0 \frac{1}{T} \mathrm{rect}\left(\frac{t-\tau_0-\frac{T}{2}}{T}\right) e^{j(2\pi f_b t)}, \tag{3.1}$$

where $f_b = k\tau_0$ and $k = B/T$. In the frequency-domain, taking Fourier Transform of (3.1) leads to a single tone signal shifted to beat frequency as:

$$\begin{aligned} X_{\mathrm{M_{fmcw}}}(f) &= \mathscr{F}\left\{\alpha_0 \frac{1}{T} \mathrm{rect}\left(\frac{t-\tau_0-\frac{T}{2}}{T}\right) e^{j(2\pi f_b t)}\right\} \\ &= \alpha_0 \,\mathrm{sinc}\big((f-f_b)\,T\big)\, e^{-j(2\pi(f-f_b)\tau_0)}, \end{aligned} \tag{3.2}$$

where the first null of the sinc function is decided by $1/T$. As mentioned in the introduction, the BPSK coding is commonly used for PC-FMCW radar in the preliminary studies [8, 85, 95, 112] due to its simplicity. Hereafter, we denote the BPSK code as $s_{\mathrm{bpsk}}(t) = c(t)$ to discriminate different coding schemes. The transmitted code term for the BPSK coding can be represented as:

$$s_{\mathrm{bpsk}}(t) = c(t) = e^{j\phi_{\mathrm{bpsk}}(t)} = \sum_{n=1}^{N_c} e^{j\phi_n} \mathrm{rect}\left(\frac{t-(n-1/2)T_c}{T_c}\right), \tag{3.3}$$

where N_c is the number of chips within one chirp, $T_c = T/N_c$ is the chip duration, rectangle function equals to 1 where $t \in [-T_c/2,\ T_c/2]$ and zero otherwise. Herein, ϕ_n denotes the phase corresponding to the n^{th} bit of the N_c bits sequence. For the BPSK PC-FMCW radar, we can replace $s(t-\tau_0)$ term with $c(t-\tau_0)$ in the mixer output (2.18) given in Chapter 2. Then, the mixer output becomes:

$$\begin{aligned} x_{\mathrm{M_{bpsk}}}(t) &= \alpha_0 \frac{1}{T} c(t-\tau_0) e^{j(2\pi f_b t)} \\ &= \alpha_0 \frac{1}{T} \sum_{n=1}^{N_c} e^{j\phi_n} \mathrm{rect}\left(\frac{t-\tau_0-(n-1/2)T_c}{T_c}\right) e^{j(2\pi f_b t)}. \end{aligned} \tag{3.4}$$

Subsequently, the frequency-domain representation of the mixer output can be written as:

$$\begin{aligned} X_{\mathrm{M_{bpsk}}}(f) &= \mathscr{F}\left\{\alpha_0 \frac{1}{T} \sum_{n=1}^{N_c} e^{j\phi_n} \mathrm{rect}\left(\frac{t-\tau_0-(n-1/2)T_c}{T_c}\right) e^{j(2\pi f_b t)}\right\} \\ &= \alpha_0 \frac{1}{T} C(f-f_b) e^{-j(2\pi(f-f_b)\tau_0)} \\ &= \alpha_0 \frac{T_c}{T} \mathrm{sinc}\big((f-f_b)\,T_c\big) \sum_{n=1}^{N_c} e^{j\phi_n} e^{-j\left(2\pi(f-f_b)(\tau_0+(n-\frac{1}{2})T_c)\right)}. \end{aligned} \tag{3.5}$$

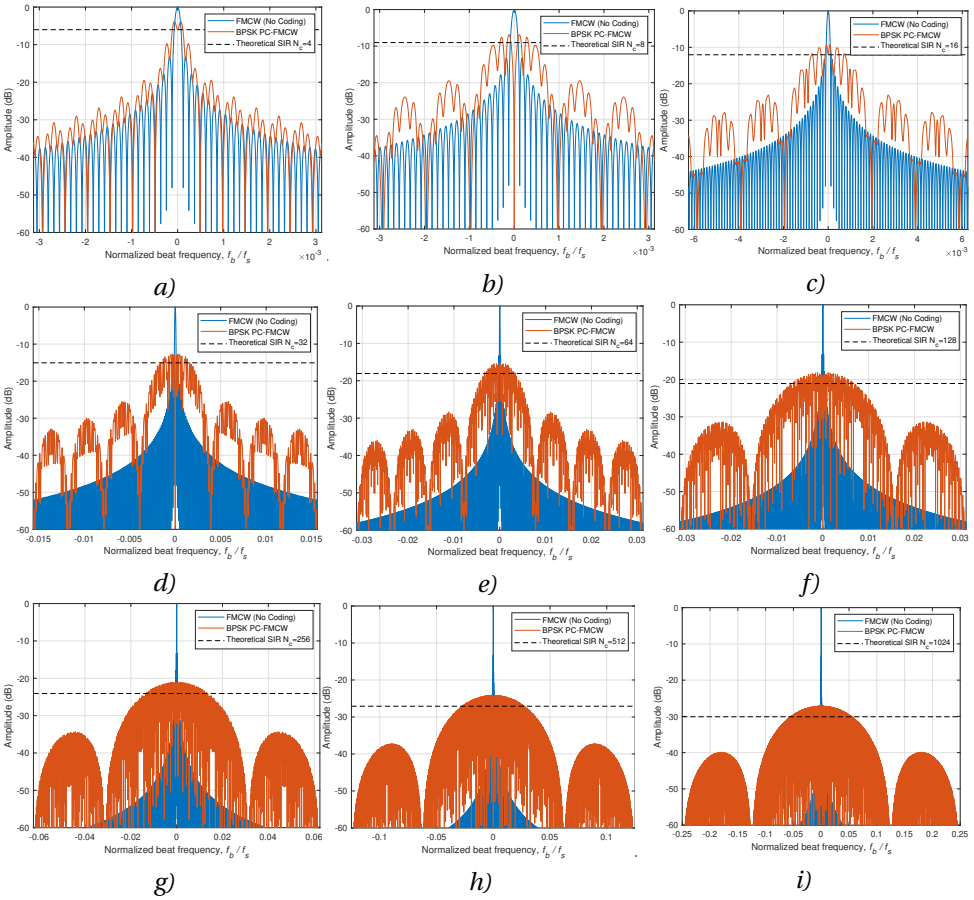

Figure 3.1: Comparison of the beat signal and BPSK coded beat signal for different number of chips per chirp: a) $N_c = 4$ b) $N_c = 8$ c) $N_c = 16$ d) $N_c = 32$ e) $N_c = 64$ f) $N_c = 128$ g) $N_c = 256$ h) $N_c = 512$ i) $N_c = 1024$.

Note that the coding spreads the spectrum of the beat signal, and the first null of the sinc function is determined by the $B_c = 1/T_c$. Moreover, the peak power of the mixer output becomes T_c/T. Therefore, the coded beat signal peak power is decreased (suppressed) by a factor of $N_c = T/T_c$ compared to the FMCW radar (no coding case). The theoretical limit of this suppression in dB can be calculated as:

$$10\log_{10}\left(\frac{T}{T_c}\right) = 10\log_{10}(N_c). \tag{3.6}$$

To examine the suppression of beat signal peak power due to coding, we investigate the spectrum of the coded beat signals with $\tau_0 = 0$ for different numbers of chips per chirp in Figure 3.1. For numerical simulations, we use chirp (sweep) duration $T = 51.2\ \mu$s, chirp bandwidth $B = 2$ GHz, and the ADC sampling frequency $f_s = 160$ MHz. Moreover, we normalize the beat frequency with the maximum beat frequency, which is determined

Table 3.1: Trade-off between theoretical SIR improvement and chip bandwidth

Number of chips per chirp	Normalized Chip Bandwidth (B_c/f_s)	Theoretical SIR Improvement (dB)	Simulated Peak Power Suppression (dB)
No coding case	0.12×10^{-3}	0	0
4	0.48×10^{-3}	6	3.85
8	0.97×10^{-3}	9	6.88
16	0.002	12	9.27
32	0.004	15	12.64
64	0.008	18	15.45
128	0.016	21	18.14
256	0.032	24	21.09
512	0.064	27	24.08
1024	0.125	30	27.09

by the ADC sampling frequency as $f_{b_{\max}} = f_s/2$. We use the same system parameters for the follow-up figures in Section 3.3, if not mentioned otherwise.

It can be observed in Figure 3.1 that multiplying with code sequence spreads the coded-beat signal energy, and the peak power of the coded beat signal is decreased as a function of N_c. Notice that this suppression can be utilized for improving cross-isolation between transmitting channels in coherent MIMO radar as explained in Chapter 5. Furthermore, it can be used for radar-to-radar interference mitigation as explained in Chapter 6 and will provide signal-to-interference (SIR) improvement. In such a scenario, the source signal transmitted by the victim radar gets rid of the code term after ideal decoding and obtains a beat signal similar to the FMCW radar (no coding case). However, interfering signals from other sources that are not matched to this code will remain coded, i.e. their peak power will be suppressed according to the number of chips per chirp. For instance, the theoretical limit of the suppression with $N_c = 128$ equals to $10\log_{10}(N_c) = 21$ dB compared to the no coding case and hence the victim radar can achieve 21 dB SIR improvements on interference suppression. However, random phase coding causes a (pseudo) noise-like behaviour and the simulated maximum peak power suppression is lower than the theoretical limit as shown in Figure 3.1. Particularly, we observe that the simulated maximum peak power of the coded beat signal is suppressed 18.14 dB for $N_c = 128$ case. It is important to note that the bandwidth of the code needs to be increased for greater SIR improvement. However, this raises the sampling demands from ADC. Thus, there is a trade-off between SIR improvement and the ADC sampling requirements. In Table 3.1, we demonstrated the chip bandwidth normalized with sampling frequency becomes $B_c/f_s = 0.125$ for the selected parameters with $N_c = 1024$ to achieve 30 dB theoretical SIR improvement. The BPSK coding results in a sharp change of the phase and thus leads to a very broad instantaneous spectrum. The limited bandwidth of ADC causes filtering of the coded beat signal spectrum, which changes waveform properties. Consequently, the decoding becomes imperfect and thus increases the sidelobe level. To decrease the spectrum broadening, we can apply smoother to the code signal.

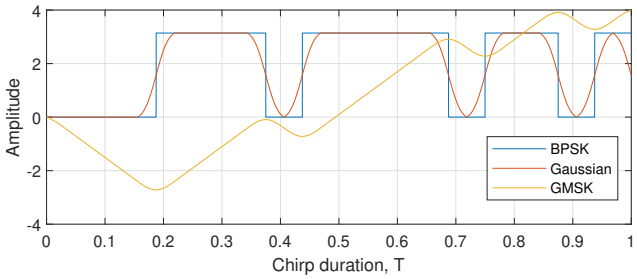

Figure 3.2: Illustration of the phase types ($N_c = 16$): BPSK, Gaussian, and GMSK.

3.3. SMOOTHED PC-FMCW

This section presents the smoothing operation to improve the phase transition of the state-of-the-art waveform and reduces its spectral widening of the coded beat signal to obtain SPC-FMCW.

3.3.1. BPSK PC-FMCW

In the BPSK coding, the phase changes $\phi_{\text{bpsk}}(t) \in \{0, \pi\}$ as shown in Figure 3.2. To investigate the impact of the sharp phase changes, analyzing the instantaneous frequency of the phase-coded signal is complementary as it provides an additional perspective that may not easily be seen on the signal's time or frequency domain representation. The instantaneous frequency is equal to the first derivative of the phase with respect to time. The phase of the BPSK code sequence $\phi_{\text{bpsk}}(t)$ can be written with the summation of unit step functions as:

$$\phi_{\text{bpsk}}(t) = \sum_{n=1}^{N_c} (\phi_{n+1} - \phi_n)\, u(t - nT_c). \tag{3.7}$$

Then, the instantaneous frequency for the BPSK code sequence can be written by taking the derivative of the $\phi_{\text{bpsk}}(t)$ as [8]:

$$\frac{1}{2\pi}\frac{d}{dt}\phi_{\text{bpsk}}(t) = \frac{1}{2\pi}\sum_{n=1}^{N_c} (\phi_{n+1} - \phi_n)\, \delta(t - nT_c), \tag{3.8}$$

where δ denotes the Dirac delta function. The proof is given in Appendix A. The spectrogram of BPSK is demonstrated in Figure 3.3 a. It can be seen that the abrupt phase changes cause a short burst in the spectrogram at the time instances of phase shifts, which mathematically comes from the derivatives of unit step functions and is represented as Dirac delta in (3.8).

In addition, the frequency spectrum of the BPSK coded beat signal (3.5) with $\tau_0 = 0$ is shown in Figure 3.4 in blue color. As explained earlier, the first null for the mixer output of BPSK PC-FMCW is defined by the $\text{sinc}\left((f - f_b)\, T_c\right)$ function. Therefore, the first null location of the coded beat signal for BPSK PC-FMCW can be calculated as:

$$f_b + B_c. \tag{3.9}$$

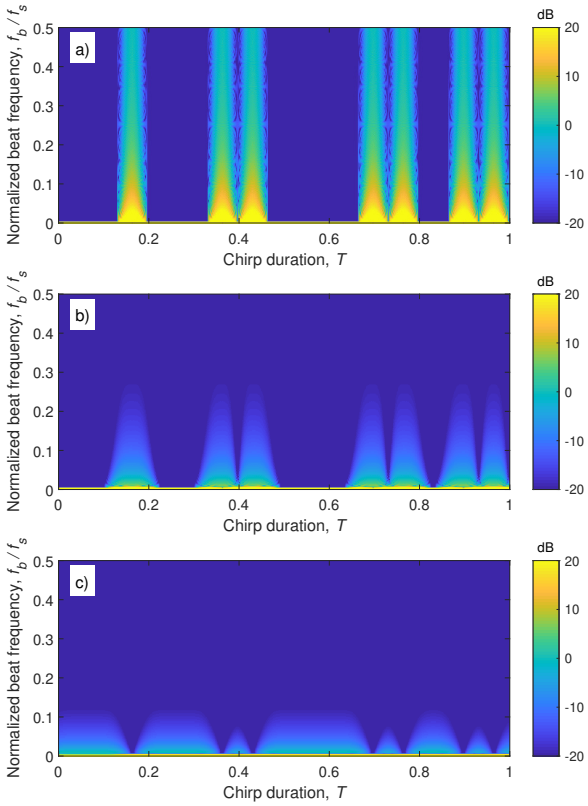

Figure 3.3: Spectrogram of the coded beat frequency signal associated with three PC-FMCW waveforms (N_c = 16): a) BPSK PC-FMCW b) Gaussian PC-FMCW c) GMSK PC-FMCW.

Assume we have an ideal Brick-wall low pass filter as:

$$L(f) = \text{rect}\left(\frac{f}{f_{\text{cut}}}\right). \tag{3.10}$$

The output of low pass filter can be represented as:

$$O(f) = X_{\text{M}}(f)L(f). \tag{3.11}$$

To include the k^{th} null, the cut-off frequency of LPF can be written as:

$$\begin{aligned} f_{\text{cut}} &\geq f_{b_{\max}} + \frac{1}{T_c}k_{\text{null}}^{\text{th}} \\ &\geq f_{b_{\max}} + \frac{N_c}{T}k_{\text{null}}^{\text{th}} \\ &\geq k\tau_{\max} + \frac{N_c}{T}k_{\text{null}}^{\text{th}} \\ &\geq \frac{1}{T}\left(\frac{2BR_{max}}{c} + N_c k_{\text{null}}^{\text{th}}\right). \end{aligned} \tag{3.12}$$

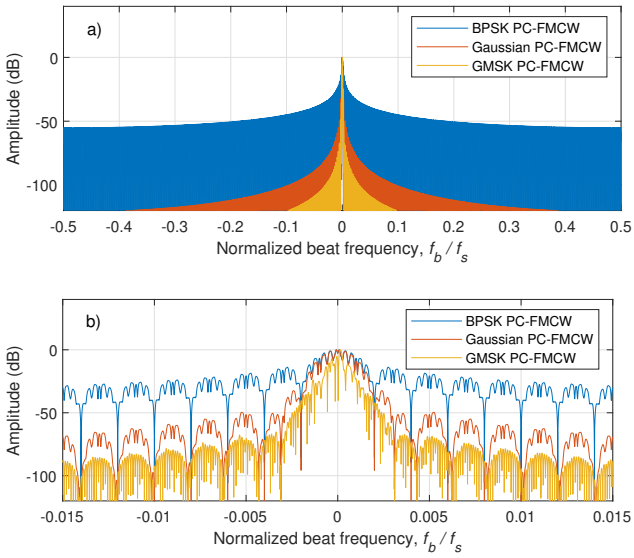

Figure 3.4: Frequency spectrum comparison for the coded beat signals associated with three PC-FMCW waveforms with $N_c = 16$: a) Full-band b) Zoomed.

where $f_{b_{\max}} = k\tau_{\max}$ is the maximum beat frequency and $\tau_{\max} = 2R_{\max}/c$ is the maximum round trip delay for the stationary target at the maximum range $R_{\max}$. The minimum ADC sampling requirement should be at least two times the cut-off frequency of LPF f_{cut}.

The BPSK coding results in substantial spectrum widening of the beat signal due to rapid phase shifts. Thus, the BPSK coding requires the sampling of a few multiples of code bandwidth. The spectrum width of a signal $x(t)$ can be calculated as [119, 120]:

$$\sigma_{\text{f}} = \sqrt{\frac{1}{\text{P}} \int_{-\infty}^{\infty} (f - \mu_f)^2 \left|X(f)\right|^2 df}, \tag{3.13}$$

where the total power of the spectrum can be defined as:

$$\text{P} = \int_{-\infty}^{\infty} \left|X(f)\right|^2 df, \tag{3.14}$$

and the mean frequency of the spectrum can be written as:

$$\mu_f = \frac{1}{\text{P}} \int_{-\infty}^{\infty} f \left|X(f)\right|^2 df. \tag{3.15}$$

The spectrum width of the coded beat signals associated with three PC-FMCW waveforms versus number of chips per chirp is shown in Figure 3.5. It can be seen that the spectrum widening of the coded beat signal increases as the number of chips per chirp raises (code bandwidth becomes larger, e.g. the normalized code bandwidth becomes $B_c/f_s = 0.12$ for $N_c = 1024$, $T = 51.2$ μs and $f_s = 160$ MHz). Using the BPSK code with large bandwidth comparable to the sampling frequency and filtering of the spectrum leads to an increased sidelobe level. To cope with this problem, we propose to apply a smoother.

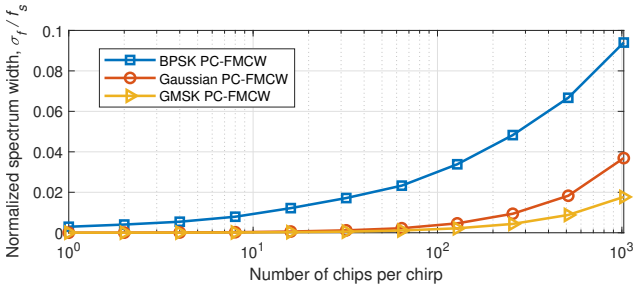

Figure 3.5: Spectrum width of the coded beat signals associated with three PC-FMCW waveforms versus number of chips per chirp.

3.3.2. GAUSSIAN PC-FMCW

A smoother can be applied to the phase of the code signal to reduce the spectrum widening of the coded beat signal. In this chapter, we have used the Gaussian filter as a smoother for analysis. However, a different smoothing filter can be selected depending on the required spectral behavior of the application. The Gaussian filter can be represented as:

$$\begin{aligned} h(t) &= \sqrt{\frac{2\pi}{\ln 2}} B_s e^{-\frac{2\pi^2 {B_s}^2}{\ln 2} t^2} \\ &= \frac{\eta}{\sqrt{\pi}} e^{-\eta^2 t^2}, \end{aligned} \tag{3.16}$$

where $\eta = \sqrt{\frac{2\pi^2 B_s^2}{\ln 2}}$ and B_s is the 3-dB bandwidth of the Gaussian filter. Then, the frequency response of the Gaussian filter can be written as [121]:

$$\begin{aligned} H(f) &= \mathscr{F}\left\{ \frac{\eta}{\sqrt{\pi}} e^{-\eta^2 t^2} \right\} \\ &= \frac{\eta}{\sqrt{\pi}} \int_{-\infty}^{\infty} e^{-\eta^2 t^2} e^{-j2\pi f t}\, dt \\ &= \frac{\eta}{\sqrt{\pi}} \int_{-\infty}^{\infty} e^{-\left(\eta^2 t^2 + j\frac{2\pi\eta f t}{\eta} + \left(j\frac{\pi f}{\eta}\right)^2 - \left(j\frac{\pi f}{\eta}\right)^2\right)} dt \\ &= \frac{\eta}{\sqrt{\pi}} e^{-\frac{\pi^2 f^2}{\eta^2}} \int_{-\infty}^{\infty} e^{-\left(\eta t + j\frac{\pi f}{\eta}\right)^2} dt \\ &= \frac{1}{\sqrt{\pi}} e^{-\frac{\pi^2 f^2}{\eta^2}} \int_{-\infty}^{\infty} e^{-(y)^2} dy \\ &= e^{-\frac{\pi^2 f^2}{\eta^2}} \\ &= e^{-\frac{\ln(2)}{2}\left(\frac{f}{B_s}\right)^2}. \end{aligned} \tag{3.17}$$

Applying Gaussian filter to the binary code, we obtained the Gaussian binary code with a phase $\phi_{\text{gauss}}(t) = \phi_{\text{bpsk}}(t) \otimes h(t)$ as demonstrated in Figure 3.2. The phase of the

Gaussian binary code can be written with the summation of error functions as:

$$\begin{aligned}\phi_{\text{gauss}}(t) &= \phi_{\text{bpsk}}(t) \otimes h(t) \\ &= \frac{1}{2}\sum_{n=1}^{N_c}(\phi_{n+1}-\phi_n)\,\text{erf}\big(\eta(t-nT_c)\big),\end{aligned} \tag{3.18}$$

where erf(t) represents the error function. Then, the instantaneous frequency for the Gaussian binary code sequence can be written by taking the derivative of the $\phi_{\text{gauss}}(t)$ as:

$$\frac{1}{2\pi}\frac{d}{dt}\phi_{\text{gauss}}(t) = \frac{\eta}{2\pi\sqrt{\pi}}\sum_{n=1}^{N_c}(\phi_{n+1}-\phi_n)e^{-\eta^2(t-nT_c)^2}. \tag{3.19}$$

The proof is given in Appendix A.

The equation (3.19) shows that the abrupt phase changes are smoothed by the Gaussian filter, and the term $e^{-\eta^2(t-nT_c)^2}$ is expected when the phase changes with respect to time. This can be seen in Figure 3.3 b that the phase changes cause Gaussian shape in the spectrogram of the Gaussian binary code.

In addition, the mixer output of Gaussian PC-FMCW in the time-domain can be represented as:

$$x_{\text{Mgauss}}(t) = \alpha_0\frac{1}{T}\left(c(t-\tau_0)\otimes h(t-\tau_0)\right)e^{j(2\pi f_b t)}, \tag{3.20}$$

and its frequency spectrum can be written as:

$$\begin{aligned}X_{\text{Mgauss}}(f) &= \mathscr{F}\left\{\alpha_0\frac{1}{T}\left(c(t-\tau_0)\otimes h(t-\tau_0)\right)e^{j(2\pi f_b t)}\right\} \\ &= \alpha_0\frac{1}{T}C(f-f_b)\,H(f-f_b)\,e^{-j(2\pi(f-f_b)\tau_0)} \\ &= \alpha_0\frac{T_c}{T}\,\text{sinc}\big(\big(f-f_b\big)T_c\big)\,e^{-\frac{\ln(2)}{2}\left(\frac{f-f_b}{B_s}\right)^2}\sum_{n=1}^{N_c}e^{j\phi_n}\,e^{-j\left(2\pi(f-f_b)(\tau_0+(n-\frac{1}{2})T_c)\right)}.\end{aligned} \tag{3.21}$$

Herein, it is important to note that the spectrum of the BPSK PC-FMCW (3.5) is multiplied by the filter response $H(f)$ due to phase smoothing. In this study, we consider Gaussian filter for SPC-FMCW waveform, but this equation can be written with any other filter without loss of generality. As seen in (3.21), the first null of the mixer output for the Gaussian PC-FMCW waveform is decided by the sinc function bounded with the Gaussian filter $H(f)$. Consequently, the first null location becomes $f_b + B_s$, and the required cut-off frequency to include the main lobe becomes:

$$f_{\text{cut}} \geq f_{b_{\max}} + B_s. \tag{3.22}$$

The frequency spectrum of the mixer output for Gaussian PC-FMCW (3.21) is demonstrated in Figure 3.4 in red color. Here, the 3-dB bandwidth of the Gaussian filter is set to two times the chip bandwidth $B_s = 2B_c$. We observe that using a Gaussian filter reduces the spectrum widening of the coded beat signal. This can be seen in Figure 3.5 where the spectrum width of the coded beat signal is lowered for Gaussian PC-FMCW compared to the BPSK coded signal.

3.3.3. GMSK PC-FMCW

Gaussian minimum shift keying (GMSK) is a popular modulation scheme in communication due to its low spectral spread [122]. In GMSK coding, the binary code signal is filtered by a Gaussian filter, and the filtered code is integrated over time [122, 123]. The resulting phase of the GMSK code becomes:

$$\phi_{\text{gmsk}}(t) = \int_{-\infty}^{\infty} \phi_{\text{gauss}}(t)\,dt = \int_{-\infty}^{\infty} \big(\phi_{\text{bpsk}}(t) \otimes h(t)\big)\,dt. \tag{3.23}$$

The phase changes of the GMSK code are demonstrated in Figure 3.2 in yellow color. It can be seen that the phase changes become smoother. Then, the instantaneous frequency for the GMSK phase code can be obtained by taking the derivative of $\phi_{\text{gmsk}}(t)$ as:

$$\frac{1}{2\pi}\frac{d}{dt}\phi_{\text{gmsk}}(t) = \frac{1}{4\pi}\sum_{n=1}^{N_c}(\phi_{n+1}-\phi_n)\,\text{erf}\big(\eta(t-nT_c)\big). \tag{3.24}$$

The proof is given in Appendix A. The (3.24) demonstrates that the Dirac delta term seen in BPSK coding due to abrupt phase change is replaced by the term $\text{erf}\big(\eta(t-nT_c)\big)$ for the GMSK phase code. This behaviour can be observed in Figure 3.3 c, where the phase changes lead to error functions (combination of left and right parts gives a smoothed rectangle shape) in the spectrogram of the GMSK phase code.

Subsequently, the mixer output of GMSK PC-FMCW in the time-domain can be represented as:

$$x_{\text{M}_{\text{gmsk}}}(t) = \alpha_0 \frac{1}{T} e^{j\phi_{\text{gmsk}}(t-\tau_0)} e^{j(2\pi f_b t)}, \tag{3.25}$$

and its spectrum for the coded beat signal can be written as [121]:

$$X_{\text{M}_{\text{gmsk}}}(f) \approx \alpha_0 \frac{T_c}{T}\,\text{sinc}^2\big((f-f_b)\,T_c\big)\,e^{-\frac{\ln(2)}{2}\left(\frac{f-f_b}{B_s}\right)^2}\sum_{n=1}^{N_c} e^{j\phi_n} e^{-j2\pi(f-f_b)(\tau(t)+(n-1/2)T_c)}. \tag{3.26}$$

Similar to the Gaussian case, the Gaussian filter $H(f)$ bounds the frequency components of the mixer output for GMSK PC-FMCW as shown in (3.26). Thus, the first null location becomes $f_b + B_s$, and the required cut-off frequency to include the main lobe is the same as (3.22). In addition, GMSK PC-FMCW has a sinc^2 term instead of a sinc function, which is seen in the BPSK code. This is because the GMSK phase code has a smoothed triangular shape while BPSK has a rectangular one, as illustrated in Figure 3.2.

The spectrum of the mixer output for the GMSK PC-FMCW waveform (3.26) is shown in Figure 3.4 in yellow color. It can be seen that taking the square of the sinc function and bounding it by the Gaussian filter further reduces the spectrum widening of the coded beat signal. We observe this in Figure 3.5 as the spectrum width of the coded beat signal is minimal for GMSK PC-FMCW in comparison to both BPSK PC-FMCW and Gaussian PC-FMCW. Consequently, better sensing performance, i.e. lower sidelobe level, is expected for the GMSK PC-FMCW waveform when the bandwidth of the code increases and becomes comparable to the ADC sampling.

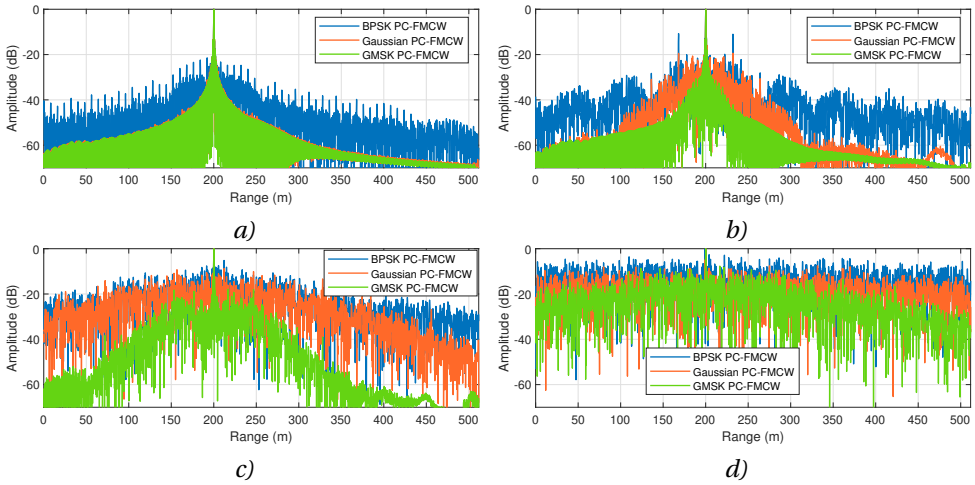

Figure 3.6: Range profile comparison for three PC-FMCW waveforms with $N_p = 1$ chirp pulse: a) $N_c = 16$ b) $N_c = 64$ c) $N_c = 256$ d) $N_c = 1024$.

3.4. SENSING PERFORMANCE COMPARISON

This section provides the sensing performance comparison for three investigated PC-FMCW waveforms; BPSK PC-FMCW, Gaussian PC-FMCW and GMSK PC-FMCW. For processing the waveforms, we use the group delay filter receiver as explained in Chapter 2. Assume an automotive radar operates at a carrier frequency $f_c = 77$ GHz and transmits the investigated waveforms with the chirp duration $T = 25.6$ μs and the chirp bandwidth $B = 300$ MHz. The phase-coded signal $s(t)$ is selected as a random code sequence for all three PC-FMCW waveforms. To obtain a smoothed phase transition, the 3-dB bandwidth of the Gaussian filter is set to two times the chip bandwidth. We use N_c number of chips per chirp, i.e. the chip duration $T_c = T/N_c$ and the bandwidth of the code $B_c = N_c/T$. For the selected system parameters, the code bandwidth becomes $B_c = 10$ MHz for $N_c = 256$ while it raises to $B_c = 40$ MHz for $N_c = 1024$.

On the receiver side, the dechirped signal (mixer output of each investigated waveform) is low-pass filtered with the cut-off frequency $f_{\text{cut}} = \pm 40$ MHz and sampled with $f_s = 80$ MHz. As a consequence, we have $N = 2048$ range cells (fast-time samples) for the selected system parameters. We perform the same LPF to the reference phase-coded signal before decoding to prevent a signal mismatch. The group delay filter is applied to the sampled signal, and the resulting signal is decoded with the reference phase-coded signal. After decoding, we take FFT to obtain the range profile. To focus on the sensing performance, we consider a noise-free scenario with a single target at the range $R_0 = 200$ m and the radial velocity $v_0 = -10$ m/s. In addition, we normalize all the figures by the maximum value.

First, we investigate the sensing performance of three investigated PC-FMCW waveforms with a single chirp pulse $N_p = 1$. We demonstrate the range profile comparison for investigated waveforms in Figure 3.6. It can be seen that the Gaussian PC-FMCW and GMSK PC-FMCW provide a Sinc-like shape similar to conventional LFM processing in

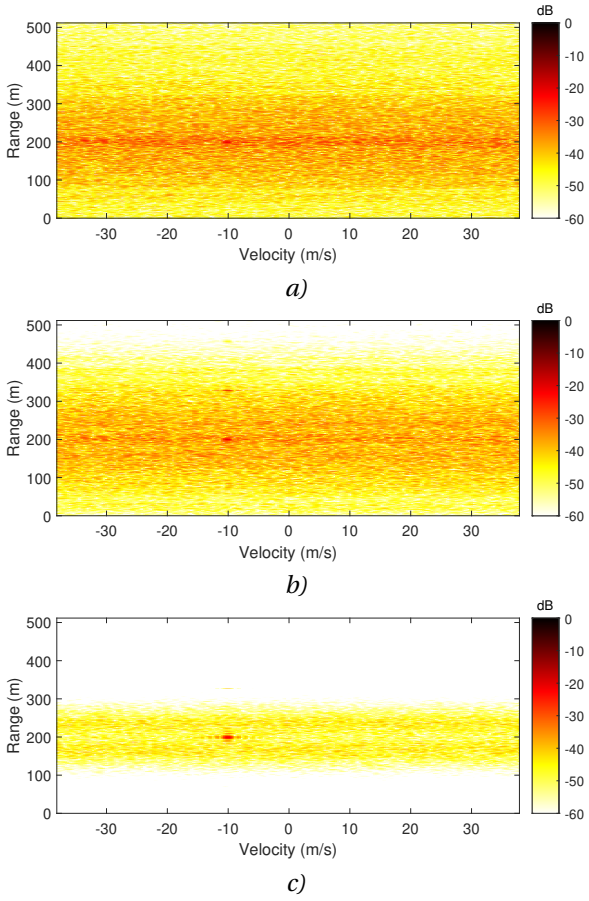

Figure 3.7: Range-Doppler profile comparison for three PC-FMCW ($N_c = 256$ and $N_p = 64$): a) BPSK PC-FMCW b) Gaussian PC-FMCW c) GMSK PC-FMCW.

the $N_c = 16$ case, while the BPSK PC-FMCW has wide spectrum broadening and filtering of the spectrum raises its sidelobe level. In addition, the abrupt phase changes inside the BPSK coding are significantly affected by the group delay dispersion effect, and hence the BPSK PC-FMCW has the highest sidelobe level due to imperfect decoding. We observe that increasing the number of chips per chirp up to $N_c = 1024$ raises the sidelobe level for all three investigated waveforms. Among them, the increase in the sidelobe level is minimal for GMSK PC-FMCW. This is because the phase smoothing operation reduces the spectral broadening and the impact of the group delay dispersion effect. Particularly, the GMSK PC-FMCW provides the lowest sidelobe level as the number of chips increases from $N_c = 16$ to $N_c = 1024$.

Next, we examine the range-Doppler profile of the investigated waveform with $N_c = 256$. To this end, we consider $N_p = 64$ number of chirp pulses transmitted for Doppler processing, where each chirp uses a different phase code signal $s(t)$. We show the range-

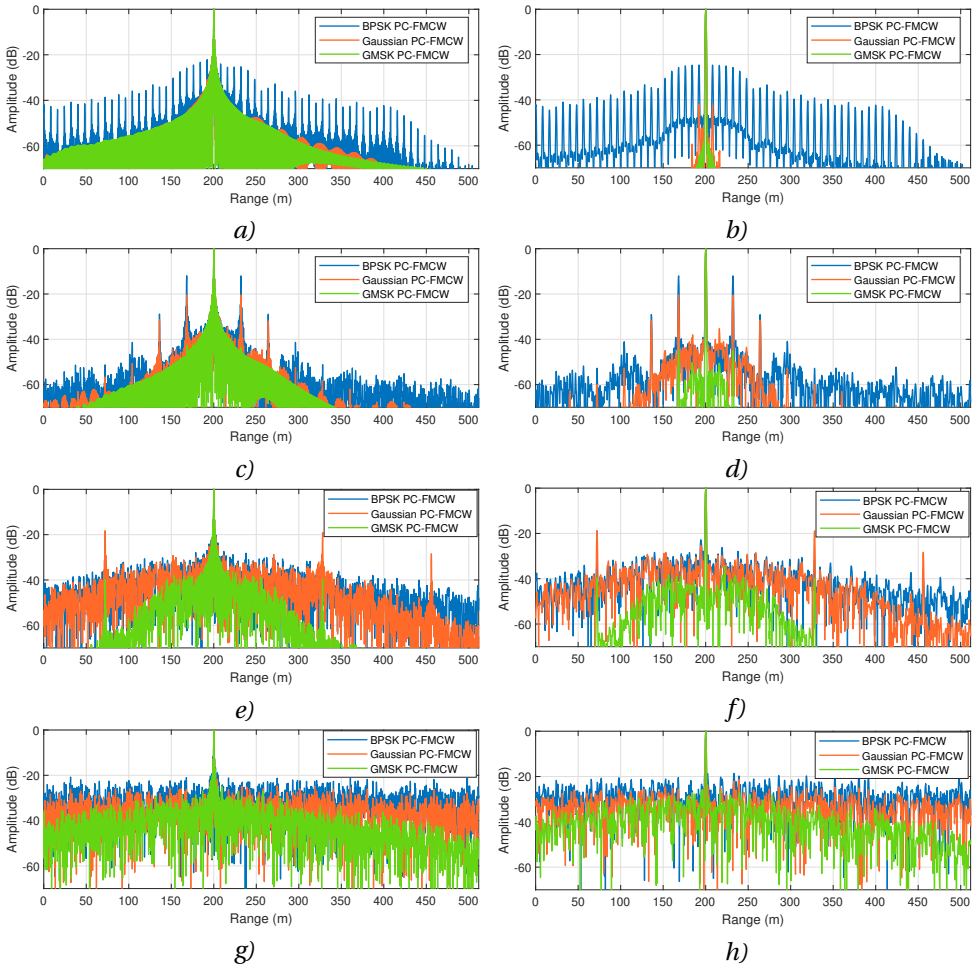

Figure 3.8: Range profile comparison for three PC-FMCW waveforms with $N_p = 64$ chirp pulses. Rectangle windowing on the left column and Chebyshev windowing (80 dB) on the right column: a-b) $N_c = 16$ c-d) $N_c = 64$ e-f) $N_c = 256$ g-h) $N_c = 1024$.

Doppler profile of three investigated waveforms in Figure 3.7. We observe that the GMSK PC-FMCW has the lowest sidelobe level and spectral widening compared to BPSK PC-FMCW and Gaussian PC-FMCW. This can help to avoid masking weak target returns outside the mainlobe. Herein, it should be noted that there is a processing gain from the slow-time $10\log_{10}(N_p) = 18$ dB for perfectly orthogonal codes. However, the codes are not perfectly orthogonal after the dispersion effect and filtering, which raises the sidelobe level compared to the ideal case. To illustrate this, we compare the range profile of the investigated waveforms with $N_p = 64$ chirp pulses in Figure 3.8. In addition, we apply 80 dB Chebyshev window in the fast-time before taking FFT and compare the results with the rectangle windowing case. It can be seen that Gaussian PC-FMCW has the local

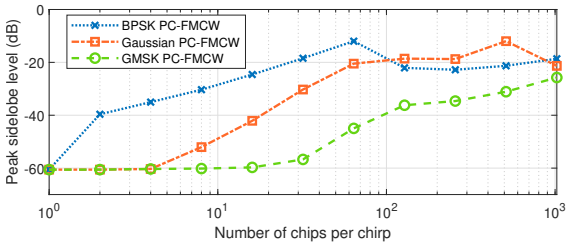

Figure 3.9: PSL of the three PC-FMCW waveforms versus the number of chips per chirp. $R = 200$ m and $N_p = 64$.

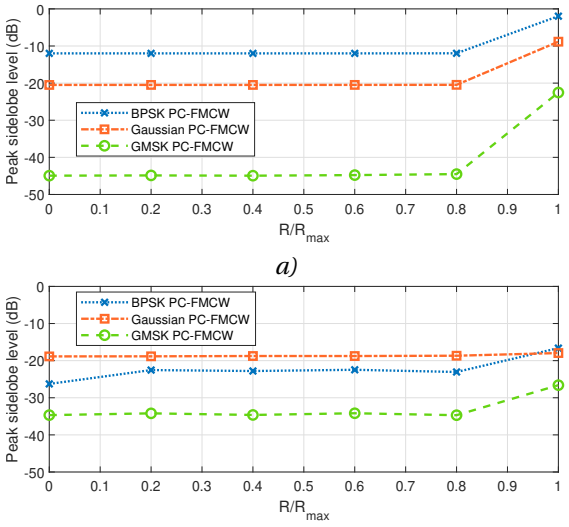

Figure 3.10: PSL of the three PC-FMCW waveforms with $N_p = 64$ chirp pulses versus the normalized range of the target with respect to the maximum range: a) $N_c = 64$ b) $N_c = 256$.

peaks between phase-coded signals, and the powers of these peaks are summed up over coherent pulse processing. As a result, Gaussian PC-FMCW provides the worst dynamic range for the $N_c = 256$ case.

Finally, we demonstrate the peak sidelobe level (PSL) of the three investigated waveforms versus the number of chips per chirp in Figure 3.9. Herein, 80 dB Chebyshev window is applied to the decoded signal before taking FFT. The PSL of a signal is determined by the maximum amplitude outside of the main lobe in the range domain. We observe that the PSL of BPSK PC-FMCW rapidly raises as N_c increases. On the other hand, GMSK PC-FMCW keeps a low sidelobe level and achieves ~ -60 dB PSL up to $N_c = 32$. Thereafter, the PSL of GMSK PC-FMCW increases. In addition, we demonstrate the PSL of investigated waveforms as a function of the normalized target range in Figure 3.10. As explained earlier, the filtering of the spectrum becomes crucial for PC-FMCW as the target approaches the maximum range. We observe that GMSK PC-FMCW has the lowest PSL among investigated waveforms and provides the best sensing performance.

3.5. CONCLUSIONS

This chapter studies the smoothed phase-coded FMCW waveforms to lower the spectrum widening due to the phase-coded signal. For this purpose, we mathematically analyzed the beat signal spreading and derived the spectrum of the BPSK coded beat signal. We observe that the peak power of the coded beat signal is decreased as the number of chips per chirp increases (resulting in larger code bandwidth). Then, the impact of the spectrum widening due to the abrupt phase changes of BPSK is investigated. It is shown that the abrupt phase changes cause a short burst in the spectrogram at the time instances of phase shifts (mathematically represented as Dirac delta) in the BPSK coding. These short bursts widen the spectrum of the coded beat signals. Hence, filtering of the spectrum will increase the sidelobe levels in the limited receiver analogue bandwidth.

The phase smoothing operation is performed to address the bandwidth limitations of BPSK. The Gaussian filter is proposed to smooth the phase transition of PC-FMCW, and two waveforms are derived, namely Gaussian PC-FMCW and GMSK PC-FMCW. The introduced waveforms are examined in time, frequency and instantaneous frequency domains. We observe that the Dirac delta term due to abrupt phase changes seen in BPSK coding is smoothed with the Gaussian filter. Subsequently, the spectrum broadening of the three investigated waveforms is demonstrated and compared. It is shown that the spectrum widening of the coded beat signal associated with GMSK PC-FMCW is the lowest (especially for large code bandwidth) compared to both BPSK PC-FMCW and Gaussian PC-FMCW. Afterwards, we process the investigated waveforms with the group delay filter receiver and compare their sensing performance as a function of code bandwidth. The spectrum broadening and the group delay dispersion effect become crucial as the code bandwidth grows, and hence PSL of the investigated waveforms increases. It is demonstrated that the degradation in PSL is minimal for GMSK PC-FMCW as the phase smoothing operation helps to lower the spectral broadening and the impact of the group delay dispersion. Consequently, the GMSK PC-FMCW waveform provides the lowest PSL and has favourable sensing performance among the investigated waveforms.

4

RECEIVER DESIGN FOR PC-FMCW RADAR

The impact of the group delay filter is investigated, and compensation for the undesired effect of the group delay filter is proposed. The quadratic phase lag compensation is performed before waveform transmission to enhance decoding. The phase lag compensated SPC-FMCW is introduced to improve the coexistence of multiple radars operating within the same frequency bandwidth. The properties of the introduced waveform are analysed theoretically and demonstrated experimentally. Both simulation and experimental results show that the introduced waveform with the investigated processing steps helps combine all advantages of the FMCW waveform, including hardware simplicity and small operational bandwidth of the receiver, with the advantages of phase coding.

Parts of this chapter have been published in:

U. Kumbul, N. Petrov, C. S. Vaucher, and A. Yarovoy, "Smoothed phase-coded FMCW: Waveform properties and transceiver architecture", in *IEEE Transactions on Aerospace and Electronic Systems*, pp. 1-18, 2022.

4.1. INTRODUCTION

In Chapter 2, we have investigated the existing receiver approaches for the PC-FMCW waveforms. As already mentioned, the conventional matched filtering operation in the digital domain demands the acquisition of the received signal with total bandwidth. Hence, this processing approach could not reduce the analogue receive bandwidth, and the key disadvantage of PMCW has been transferred to PC-FMCW. To decrease the sampling requirement of the receiver, the dechirping and decoding receiver strategy is adjusted for PC-FMCW. However, the coded beat signals are needed to be aligned to perform appropriate decoding. In [85, 88], the alignment of the beat signals is realized by using an ideal group delay filter, and the range information of the target is extracted from the beat signals after decoding. However, the group delay filter causes a quadratic phase shift (group delay dispersion effect) on the phase-coded signal. This additional quadratic phase shift distorts the received code. Thus the decoding becomes imperfect, which raises the sidelobes of the range profile.

In this chapter, we investigate the impact of the group delay filter in detail. Then, we introduce the phase lag compensation to enhance decoding. The introduced phase lag compensation is applied to the transmitted phase code before transmission to eliminate the undesired effect of the group delay filter. Subsequently, the properties of the introduced waveform are investigated analytically. In addition, we have applied the proposed waveforms to a real scenario and examined their sensing performance experimentally. The rest of the chapter is organised as follows. Section 4.2 gives the state-of-the-art transceiver structure and examines the impact of the group delay filter. Section 4.3 provides the phase lag compensation, and Section 4.4 investigates waveform properties of the resulting waveforms. Section 4.5 demonstrates the application of the waveforms to a real scenario. Finally, Section 4.6 highlights the concluding remarks.

4.2. IMPACT OF GROUP DELAY FILTER

This section examines the effect of the group delay filter in detail. The state-of-the-art transceiver structure of PC-FMCW [85] is illustrated in Figure 4.1. As already explained in Chapter 2, the mixer output in fast-time can be written as:

$$x_{\mathrm{M}}(t) = \alpha_0\, s(t-\tau_0) e^{j(2\pi f_b t)}, \tag{4.1}$$

where $f_b = k\tau_0$ is the beat frequency. It should be noted that there will be an additional term $\exp(2\pi f_d\, mT)$ for velocity estimation in slow-time processing, where m is the index of the chirp pulse. Since the group delay filter and decoding are only related to the fast-time processing part, we focus on signal analysis in fast-time. The slow-time processing is straightforward and the same as in the conventional FMCW automotive radars. By taking the Fourier transform, the frequency-domain representation of the mixer output can be

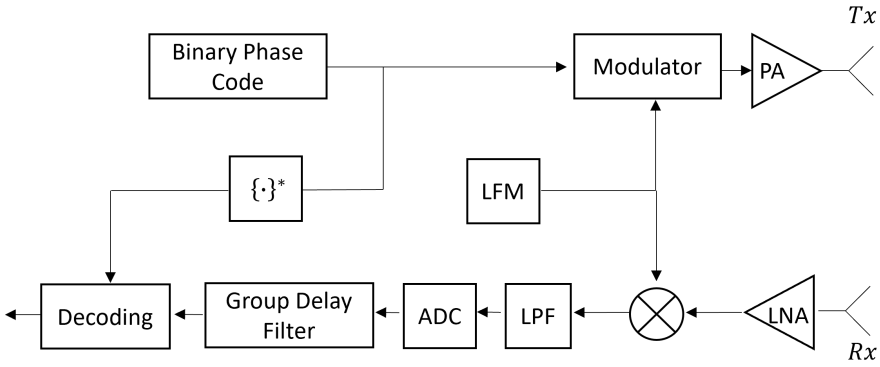

Figure 4.1: Block diagram of the state-of-the-art PC-FMCW transceiver structure.

obtained as:

$$
\begin{aligned}
X_{\mathrm{M}}(f) &= \alpha_0 \int_{-\infty}^{\infty} s(t-\tau_0) e^{j(2\pi f_b t)} e^{-j2\pi f t}\, dt \\
&= \alpha_0 \int_{-\infty}^{\infty} s(t-\tau_0) e^{-j(2\pi(f-f_b)t)}\, dt \qquad \text{Let} \quad t_1 = t-\tau_0, \quad dt_1 = dt \\
&= \alpha_0 \int_{-\infty}^{\infty} s(t_1) e^{-j(2\pi(f-f_b)t_1)} e^{-j(2\pi(f-f_b)\tau_0)}\, dt_1 \\
&= \alpha_0 e^{-j(2\pi(f-f_b)\tau_0)} \int_{-\infty}^{\infty} s(t_1) e^{-j(2\pi(f-f_b)t_1)}\, dt_1 \\
&= \alpha_0 S(f-f_b) e^{-j(2\pi(f-f_b)\tau_0)} \\
&= \alpha_0 S(f-f_b) e^{-j\left(\frac{2\pi f_b}{k}(f-f_b)\right)},
\end{aligned}
\tag{4.2}
$$

where for the final equality we used $\tau_0 = f_b/k$.

In the decoding process, the mixer output (4.1) is multiplied with the complex conjugate of the reference phase code for compensating phase changes initiated by the transmitted phase code. For a short-range radar application e.g. indoor monitoring, the delay can be neglected $s(t-\tau_0) \approx s(t)$, and the mixer output can be decoded by multiplying (4.1) with $s^*(t)$ directly [97]. However, this assumption does not hold for the applications with $R \geq c/(2B_c)$, where B_c is the bandwidth of phase-coded signal $s(t)$. For these applications, each coded beat signal (the response in all the range cells) is required to be aligned in fast-time to compensate the time delay before decoding. This alignment can be realized via the group delay filter either in time-domain [85], or frequency-domain [88]. Assume we have a group delay filter with frequency response:

$$
H_{\mathrm{g}}(f) = |H_{\mathrm{g}}(f)| \angle H_{\mathrm{g}}(f) = e^{j\theta(f)}, \tag{4.3}
$$

and unity magnitude, $|H_{\mathrm{g}}(f)| = 1, \forall f$. The Taylor series expansion of the phase response $\theta(f)$ around f_b can be found as:

$$
\theta(f)\big|_{f=f_b} = \theta(f_b) + \frac{d\theta(f)}{df}\Big|_{f=f_b} (f-f_b) + \sum_{m=2}^{\infty} \frac{1}{m!} \frac{d^m\theta(f)}{df^m}\Big|_{f=f_b} (f-f_b)^m. \tag{4.4}
$$

Expanding the second term yields:

$$\theta(f)\big|_{f=f_b} = \theta(f_b) + f\,\frac{d\theta(f)}{df}\big|_{f=f_b} - f_b\,\frac{d\theta(f)}{df}\big|_{f=f_b} + \sum_{m=2}^{\infty}\frac{1}{m!}\frac{d^m\theta(f)}{df^m}\big|_{f=f_b}(f-f_b)^m. \quad (4.5)$$

To ease of mathematical manipulations, let:

$$\begin{aligned} d &= \theta(f_b) - f_b\,\frac{d\theta(f)}{df}\big|_{f=f_b} \\ p &= \frac{d\theta(f)}{df}\big|_{f=f_b} \\ \varphi(f) &= \sum_{m=2}^{\infty}\frac{1}{m!}\frac{d^m\theta(f)}{df^m}\big|_{f=f_b}(f-f_b)^m. \end{aligned} \quad (4.6)$$

Note that $\varphi(f)$ term is small compared to the first two terms due to the Taylor series expansion. We apply the group delay filter by multiplying the mixer output spectrum as:

$$\begin{aligned} Z_o(f) &= X_M(f)H_g(f) \\ &= \alpha_0 S(f-f_b)e^{-j\left(\frac{2\pi f_b}{k}(f-f_b)\right)}e^{j(d+pf)}e^{j\varphi(f)}. \end{aligned} \quad (4.7)$$

Taking the inverse Fourier transform of the group delay filter output gives:

$$\begin{aligned} z_o(t) =& \mathscr{F}^{-1}\left\{\alpha_0 S(f-f_b)e^{-j\left(\frac{2\pi f_b}{k}(f-f_b)\right)}e^{j(d+pf)}\right\} \otimes \mathscr{F}^{-1}\left\{e^{j\varphi(f)}\right\} \\ =& z_1(t)\otimes z_2(t). \end{aligned} \quad (4.8)$$

The resulting signal can be considered as the convolution of two signals as $z_o(t) = z_1(t) \otimes z_2(t)$. The right part of the convolution $z_2(t) = \mathscr{F}^{-1}\left\{e^{j\varphi(f)}\right\}$ comes from the higher order terms in Taylor series expansion and leads to so-called dispersion effect. The left part of the convolution $z_1(t)$ causes the group delay that we are interested in and it can be obtained as:

$$\begin{aligned} z_1(t) &= \mathscr{F}^{-1}\left\{\alpha_0 S(f-f_b)e^{-j\left(\frac{2\pi f_b}{k}(f-f_b)\right)}e^{j(d+pf)}\right\} \\ &= \int_{-\infty}^{\infty}\alpha_0 S(f-f_b)e^{-j\left(\frac{2\pi f_b}{k}(f-f_b)\right)}e^{j(d+pf+2\pi ft)}\,df \quad \text{Let} \quad f_1 = f-f_b,\ df_1 = df \\ &= \int_{-\infty}^{\infty}\alpha_0 S(f_1)e^{-j\left(\frac{2\pi f_b}{k}(f_1)\right)}e^{j(d+p(f_1+f_b)+2\pi(f_1+f_b)t)}\,df_1 \\ &= \int_{-\infty}^{\infty}\alpha_0 S(f_1)e^{j\left(2\pi f_1(t-\frac{f_b}{k}+\frac{p}{2\pi})\right)}\,df_1\ e^{j(d+f_b(2\pi t+p))} \\ &= \alpha_0 s\left(t-\frac{f_b}{k}+\frac{p}{2\pi}\right)e^{j(d+f_b(2\pi t+p))} \\ &= \alpha_0 s\left(t-\tau_0+\frac{1}{2\pi}\frac{d\theta(f)}{df}\big|_{f=f_b}\right)e^{j\left(\theta(f_b)-f_b\frac{d\theta(f)}{df}\big|_{f=f_b}+f_b\left(2\pi t+\frac{d\theta(f)}{df}\big|_{f=f_b}\right)\right)} \\ &= \alpha_0 s\left(t-\tau_0+\frac{1}{2\pi}\frac{d\theta(f)}{df}\big|_{f=f_b}\right)e^{j\left(\theta(f_b)-f_b\frac{d\theta(f)}{df}\big|_{f=f_b}+2\pi f_b t+f_b\frac{d\theta(f)}{df}\big|_{f=f_b}\right)} \\ &= \alpha_0 s\left(t-\tau_0-\tau_g(f)\right)e^{j(2\pi f_b t)}e^{j(\theta(f_b))}. \end{aligned} \quad (4.9)$$

As a result, the filter leads to the group delay $\tau_g(f)$, which is the first derivative of the phase response and shifts the envelope of the signal. To align coded beat signals, the group delay needs to eliminate τ_0. Thus, the required group delay can be found as:

$$\tau_{\mathrm{g}}(f)\big|_{f=f_b} = -\frac{1}{2\pi}\frac{d\theta(f)}{df}\Big|_{f=f_b} = -\tau_0 = -f_b/k, \tag{4.10}$$

and consequently, the first derivative of the phase response can be written as:

$$\frac{d\theta(f)}{df}\Big|_{f=f_b} = \frac{2\pi f_b}{k}. \tag{4.11}$$

The group delay filter which gives the required group delay in (4.11) can be written as:

$$H_{\mathrm{g}}(f) = e^{j\theta(f)} = e^{j\frac{\pi f^2}{k}}, \tag{4.12}$$

The other terms of the resulting Taylor expansion can be found as:

$$\begin{aligned} \theta(f_b) &= \frac{\pi {f_b}^2}{k} \\ \frac{d^2\theta(f)}{df^2} &= \frac{2\pi}{k} \\ \frac{d^m\theta(f)}{df^m} &= 0 \qquad m \geq 3. \end{aligned} \tag{4.13}$$

and the frequency characteristic of the required group delay filter can be expressed by the resulting Taylor expansion of its phase response around f_b as:

$$\theta(f)\big|_{f=f_b} = \frac{\pi {f_b}^2}{k} + \frac{2\pi f_b}{k}(f-f_b) + \frac{\pi}{k}(f-f_b)^2. \tag{4.14}$$

Finally, multiplying the mixer output spectrum with the frequency characteristic of the filter gives:

$$\begin{aligned} Z_{\mathrm{o}}(f) &= X_{\mathrm{M}}(f)e^{j\left(\frac{\pi {f_b}^2}{k} + \frac{2\pi f_b}{k}(f-f_b) + \frac{\pi}{k}(f-f_b)^2\right)} \\ &= \alpha_0 S(f-f_b)e^{-j\left(\frac{2\pi f_b}{k}(f-f_b)\right)}e^{j\left(\frac{\pi {f_b}^2}{k} + \frac{2\pi f_b}{k}(f-f_b) + \frac{\pi}{k}(f-f_b)^2\right)} \\ &= \alpha_0 S(f-f_b)e^{j\left(\frac{\pi {f_b}^2}{k} + \frac{\pi}{k}(f-f_b)^2\right)} \\ &= \alpha_0 S(f-f_b)e^{j\left(\frac{\pi}{k}(f-f_b)^2\right)}, \end{aligned} \tag{4.15}$$

where for the last equality we incorporated $\exp\left(\frac{\pi {f_b}^2}{k}\right)$ into α_0 as it is a constant phase term (does not depend on frequency f). Then, taking the inverse Fourier transform of the group delay filter output (4.15) gives:

$$\begin{aligned} z_{\mathrm{o}}(t) &= \mathscr{F}^{-1}\left\{\alpha_0 S(f-f_b)e^{j\left(\frac{\pi}{k}(f-f_b)^2\right)}\right\} \\ &= \mathscr{F}^{-1}\left\{\alpha_0 S(f-f_b)\right\} \otimes \mathscr{F}^{-1}\left\{e^{j\left(\frac{\pi}{k}(f-f_b)^2\right)}\right\} \\ &= \left(\alpha_0 s(t)\, e^{j(2\pi f_b t)}\right) \otimes \mathscr{F}^{-1}\left\{e^{j\left(\frac{\pi}{k}(f-f_b)^2\right)}\right\}. \end{aligned} \tag{4.16}$$

Note that the delay τ_0 is eliminated after the group delay filter for each coded beat signal. Moreover, the derived group delay filter has a quadratic frequency component within its phase response and applies different time delays to each frequency component. Consequently, the filter causes the so-called group delay dispersion effect shown as term $e^{j(\frac{\pi}{k}(f-f_b)^2)}$, which leads to a non-linear shift on the spectrum of the code signal. By substituting $\zeta = -j\frac{\pi}{k}$ and $f_1 = f - f_b$, the dispersion effect can be written as:

$$
\begin{aligned}
h_{\text{dis}}(t) =& \mathscr{F}^{-1}\left\{e^{j\left(\frac{\pi}{k}(f-f_b)^2\right)}\right\} \\
&= \int_{-\infty}^{\infty} e^{-\zeta {f_1}^2} e^{j2\pi f_1 t}\, df_1\, e^{j2\pi f_b t} \\
&= e^{j2\pi f_b t} \int_{-\infty}^{\infty} e^{-\left(\zeta {f_1}^2 - j\frac{2\pi\sqrt{\zeta} f_1 t}{\sqrt{\zeta}} + \left(j\frac{\pi t}{\sqrt{\zeta}}\right)^2 - \left(j\frac{\pi t}{\sqrt{\zeta}}\right)^2\right)} df_1 \\
&= e^{j2\pi f_b t} \int_{-\infty}^{\infty} e^{-\left(\sqrt{\zeta} f_1 - j\frac{\pi t}{\sqrt{\zeta}}\right)^2} e^{\left(j\frac{\pi t}{\sqrt{\zeta}}\right)^2} df_1 \\
&= e^{j2\pi f_b t}\, e^{-\frac{\pi^2 t^2}{\zeta}} \int_{-\infty}^{\infty} e^{-\left(\sqrt{\zeta} f_1 - j\frac{\pi t}{\sqrt{\zeta}}\right)^2} df_1 \quad \text{Let} \gamma = (\sqrt{\zeta} f_1 - j\frac{\pi t}{\sqrt{\zeta}}),\ d\gamma = \sqrt{\zeta} df_1 \\
&= \frac{1}{\sqrt{\zeta}}\, e^{j2\pi f_b t}\, e^{-\frac{\pi^2 t^2}{\zeta}} \int_{-\infty}^{\infty} e^{-\gamma^2} d\gamma \\
&= \frac{1}{\sqrt{\zeta}}\, e^{j2\pi f_b t}\, e^{\frac{-\pi^2 t^2}{\zeta}} \sqrt{\pi} \\
&= \frac{1}{\sqrt{-j\frac{\pi}{k}}}\, e^{j2\pi f_b t}\, e^{-\frac{\pi^2 t^2}{-j\frac{\pi}{k}}} \sqrt{\pi} \\
&= \sqrt{-\frac{k}{j}}\, e^{\pi \frac{k t^2}{j}}\, e^{j2\pi f_b t}.
\end{aligned}
\tag{4.17}
$$

Subsequently, the mixer output in time domain (4.16) can be written as:

$$
z_0(t) = \alpha_0\, e^{j2\pi f_b t}\, (s(t) \otimes h_{\text{dis}}(t)). \tag{4.18}
$$

The spectrogram of the BPSK phase-coded beat signals is shown in Figure 4.2, where the system parameters are selected as $B = 2$ GHz, $T = 51.2$ μs and $N_c = 16$. Subsequently. the code bandwidth $B_c = \frac{N_c}{T} = 0.31$ MHz with these parameters ($N_c = 16$). We use the same system parameters for the follow-up figures, if not mentioned otherwise. Moreover, we normalize the beat frequency with the maximum beat frequency, which is determined by the ADC sampling frequency as $f_{b_{\max}} = f_s/2$. In Figure 4.2, we compare three cases: before the group delay filter, after the group delay filter and after decoding the group delay filter output. Herein, we consider three targets at different ranges. It can be seen that each coded beat signal has different time delays (associated with their corresponding range) before the group delay filter (Figure 4.2 a). After using the group delay filter, we observe that each coded beat signal is aligned at the beginning (Figure 4.2 b). Note that the signals

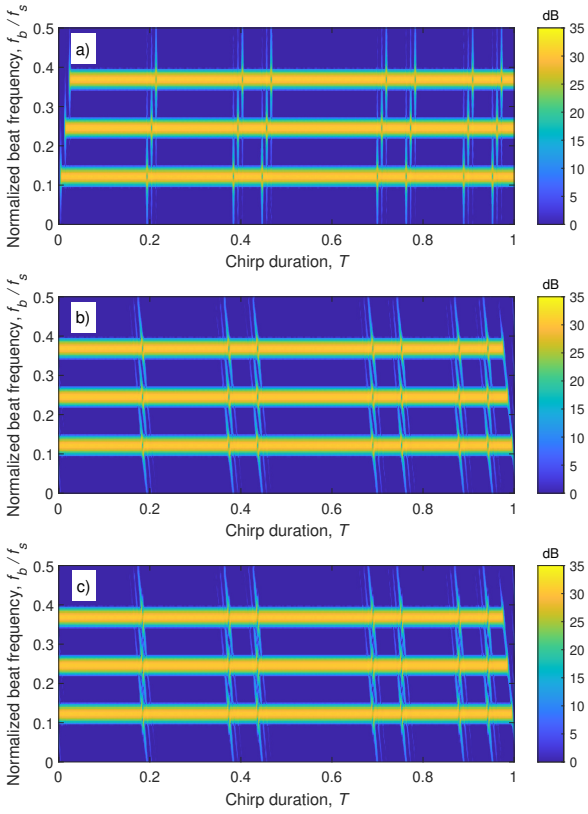

Figure 4.2: Spectrogram of the BPSK phase-coded beat signals ($N_c = 16$): a) Before the group delay filter b) After the group delay filter c) After decoding the group delay filter output.

with lower frequency are shifted less compared to signals with higher frequency. As a result of coded beat signal alignment, the decoding can be performed by multiplying the group delay filter output with the complex conjugate of the reference phase code. In an ideal decoding, the multiplication of codes gives $s(t)s^*(t) = e^{j\phi(t)}e^{-j\phi(t)} = 1$. However, the spectrum of the code signal is shifted non-linearly ((Figure 4.2 b) as it is convolved with $h_{\text{dis}}(t)$. Thus decoding becomes imperfect, and the code term is not removed properly (Figure 4.2 c). The decoded beat signal can be written as [88]:

$$\begin{aligned} z_{\text{d}}(t) &= z_{\text{o}}(t)s^*(t) \\ &= \alpha_0 e^{j2\pi f_b t}\left(s(t) \otimes h_{\text{dis}}(t)\right) s^*(t) \\ &= \alpha_0 e^{j2\pi f_b t}\left(e^{j\phi(t)} \otimes h_{\text{dis}}(t)\right) e^{-j\phi(t)} \\ &= \alpha_0 e^{j2\pi f_b t}\, e^{j\epsilon(t)}, \end{aligned} \tag{4.19}$$

where $\epsilon(t)$ is the residual phase error due to the group delay filter dispersion that causes imperfection in decoding. The dispersion effect can be neglected for a narrow-band signal

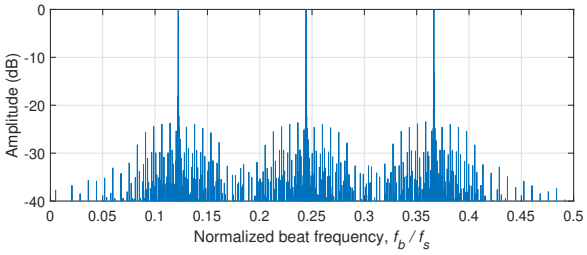

Figure 4.3: The distorted range profile of decoded signal after the group delay filter ($N_c = 64$).

where the bandwidth of the phase-coded signal is very small compared to the sampling frequency $B_c \ll f_s$. However, the dispersion effect becomes crucial for a signal with a wide spectrum where B_c is comparable to f_s. One example of such a signal is the BPSK phase-coded beat signal. In the time instance of phase shifts, the BPSK signal has a wide-spread spectrum due to abrupt phase changes. Applying non-linear phase shifts to its spectrum leads to huge imperfections in decoding. Consequently, the BPSK signal suffers from the distorted range profile after decoding, as demonstrated in Figure 4.3, where we use $N_c = 64$. The distortion of the range profile raises for the long code sequences (the bandwidth of the chips increase). We will address the compensation of the group delay dispersion effect by applying quadratic phase lag to the waveform before transmission in Section 4.3.

4.3. PHASE LAG COMPENSATED WAVEFORMS

This section introduces the phase lag compensated waveforms. The proposed block diagram of a radar with phase lag compensated waveform is shown in Figure 4.4. The signals that are modified due to the implementation of the phase lag compensation are denoted with a symbol $\hat{(\cdot)}$.

The group delay filter applies different time delays to each frequency component and causes a dispersion effect on the phase-coded signal, which leads to a distorted range profile, as explained in Section 4.2. To eliminate the undesired effect of the group delay filter, we perform quadratic phase lag compensation on the transmitted code by multiplying its spectrum with the quadratic phase term as [124]:

$$\hat{S}(f) = S(f)e^{-j\frac{\pi f^2}{k}}. \tag{4.20}$$

Then the mixer output (4.1) becomes:

$$\hat{x}_{\mathrm{M}}(t) = \alpha_0 \hat{s}(t-\tau_0)e^{j(2\pi f_b t)}, \tag{4.21}$$

and

$$\hat{X}_{\mathrm{M}}(f) = \alpha_0 S(f-f_b)e^{-j\left(\frac{2\pi f_b}{k}(f-f_b)+\frac{\pi}{k}(f-f_b)^2\right)}, \tag{4.22}$$

for time and frequency domain representation, respectively. Subsequently, the output of

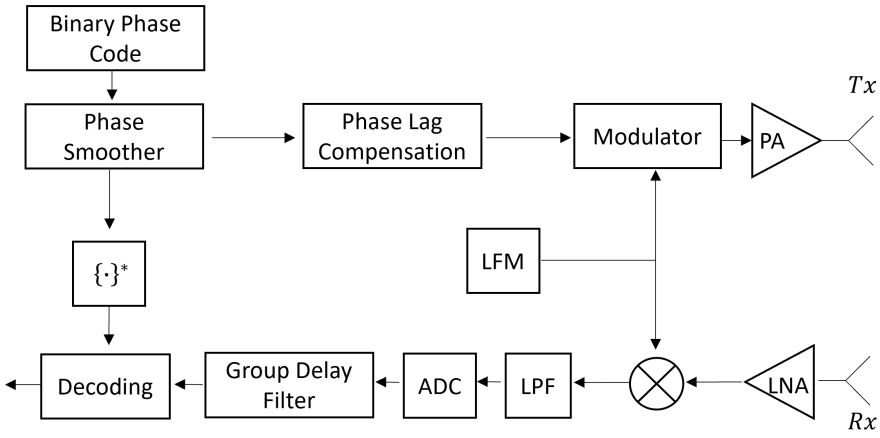

Figure 4.4: Block diagram of the proposed PC-FMCW transceiver structure.

the group delay filter in the frequency domain becomes:

$$\begin{aligned}\hat{Z}_{\mathrm{o}}(f) &= \hat{X}_{\mathrm{M}}(f)e^{j\left(\frac{\pi {f_b}^2}{k}+\frac{2\pi f_b}{k}(f-f_b)+\frac{\pi}{k}(f-f_b)^2\right)} \\ &= \alpha_0 S(f-f_b)e^{j\left(\frac{\pi {f_b}^2}{k}\right)} \\ &= \alpha_0 S(f-f_b),\end{aligned} \tag{4.23}$$

where $\exp\left(\frac{\pi {f_b}^2}{k}\right)$ is a constant phase term (does not depend on frequency f), and thus it can be incorporated into α_0. Note that the undesired term $\frac{\pi}{k}(f-f_b)^2$ caused by the phase response of the filter (4.14) is eliminated with the phase lag compensation. In parallel to this research, another study was conducted, and similar results were obtained in [125]. After taking the inverse Fourier transform, the time-domain representation of the new group delay filter output (4.23) becomes:

$$\hat{z}_{\mathrm{o}}(t) = \alpha_0 s(t)\, e^{j(2\pi f_b t)}. \tag{4.24}$$

In addition, we can shift the group delay filter output to the maximum delay (defined by maximum beat frequency, $\tau_{\max} = \frac{f_{b\max}}{k}$) by multiplying its spectrum with linear phase delay $\exp\left(-j2\pi f \tau_{\max}\right)$ for physical correctness and guarding the beginning of the next chirp. Consequently, the (4.24) is shifted to the maximum time delay as:

$$z_{\mathrm{a}}(t) = \alpha_0 s(t-\tau_{\max})\, e^{j(2\pi f_b t)}. \tag{4.25}$$

The spectrogram of the BPSK phase-coded beat signals with phase lag compensation applied is shown in Figure 4.5 ($B = 2$ GHz, $T = 51.2$ μs and $N_c = 16$) for three cases: before the group delay filter, after the group delay filter and after decoding the group delay filter output. Note that by using phase lag compensation, the spectrum of the code signals is non-linearly shifted in the opposite direction before emitting the signal (Figure 4.5 a).

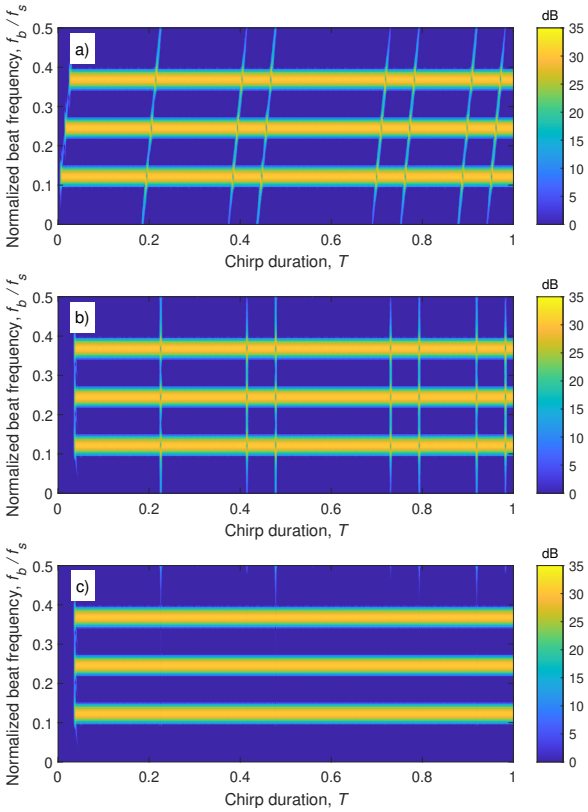

Figure 4.5: Spectrogram of the BPSK phase-coded beat signals ($N_c = 16$) with phase lag compensation applied: a) Before the group delay filter b) After the group delay filter c) After decoding the group delay filter output.

Then, we apply the group delay filter and an example of the resulting signal (4.25) can be seen in Figure 4.5 b. It is observed that the group delay dispersion effect on the code signal is eliminated, and each coded beat signal is perfectly aligned after the group delay filter. Subsequently, we can apply the decoding signal, which is the complex conjugate of the reference phase code shifted to maximum beat frequency, and the decoded beat signal becomes:

$$\begin{aligned} \hat{z}_{\mathrm{d}}(t) &= z_{\mathrm{a}}(t)s^{*}(t-\tau_{\max}) \\ &= \alpha_0 e^{j(2\pi f_b t)}. \end{aligned} \tag{4.26}$$

It can be seen in (4.26) that the code term is removed properly, and the residual phase error caused by the imperfection in decoding is eliminated by using the phase lag compensation (Figure 4.5 c). As a consequence, the distorted range profile shown in Figure 4.3 is recovered for a wide-band signal where B_c is comparable to f_s as illustrated in Figure 4.6. Moreover, the beat signals are obtained similar to the dechirped signal of conventional FMCW radar. This helps re-utilising all software algorithms previously developed for FMCW radar with the proposed waveform and transceiver structure.

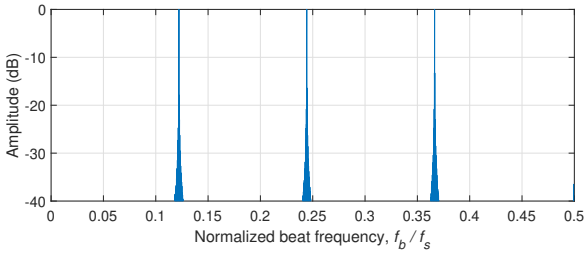

Figure 4.6: The recovered range profile of decoded signal after using phase lag compensation and group delay filter ($N_c = 64$).

4.4. WAVEFORM PROPERTIES OF PLC PC-FMCW

This section provides the properties of the phase lag compensated (PLC) PC-FMCW. We compare three PLC PC-FMCW with different coding schemes for the phase-coded signal; BPSK, Gaussian and GMSK as explained in Chapter 3. For the numerical simulations, we consider a radar operating with a carrier frequency $f_c = 3.315$ GHz and transmitting the investigated waveforms with the chirp duration $T = 1$ ms and the chirp bandwidth $B = 200$ MHz. The phase lag compensated signal $\hat{s}(t)$ is used for phase coding, and we have used the random code sequence for all three PC-FMCW. The duration of the chip T_c is controlled with the number of chips per chirp N_c as $T_c = T/N_c$. To achieve a smoothed phase transition, the 3-dB bandwidth of the Gaussian filter is set to two times the chip bandwidth $B_s = 2B_c$. On the receiver side, (4.21) is low-pass filtered with the cut-off frequency $f_{\text{cut}} = \pm 20$ MHz and sampled with $f_s = 40$ MHz. As a consequence, we have $N = 40000$ range cells (fast-time samples) for this setting. The group delay filter is applied to the sampled signal to align the beat signals of different targets. Before decoding, the same LPF is applied to the reference phase-coded signal to prevent a signal mismatch. To focus on the waveform properties, we assume a noise-free scenario in the numerical simulations.

4.4.1. SENSING

The sensing performance of the phase lag compensated waveforms is assessed by using the investigated processing method and compared with FMCW. After proper decoding, the code term is removed, and the beat signal is recovered similar to the dechirped signal of traditional FMCW as explained in Section 4.3.

To investigate the Doppler tolerance of the waveforms and proposed receiver strategy, we simulate the received signal after dechirping (4.1) as a function of Doppler frequency shift and plot the outcome of the introduced processing approach in a form similar to the ambiguity function in Figure 4.7. The presented plots show the behaviour of FMCW and three phase lag compensated PC-FMCW with $N_c = 1024$ after processing. It can be seen that the inclined ridge associated with the chirped waveform ambiguity function is present and the same in a, b, c, and d. Thus, all considered waveforms have the Doppler tolerance of FMCW and exhibit the range-Doppler coupling, determined by the slope of the carrier chirp. Note that the x-axis is zoomed out to highlight the sidelobe differences between waveforms, and hence the inclined ridge seems like a narrow line. In

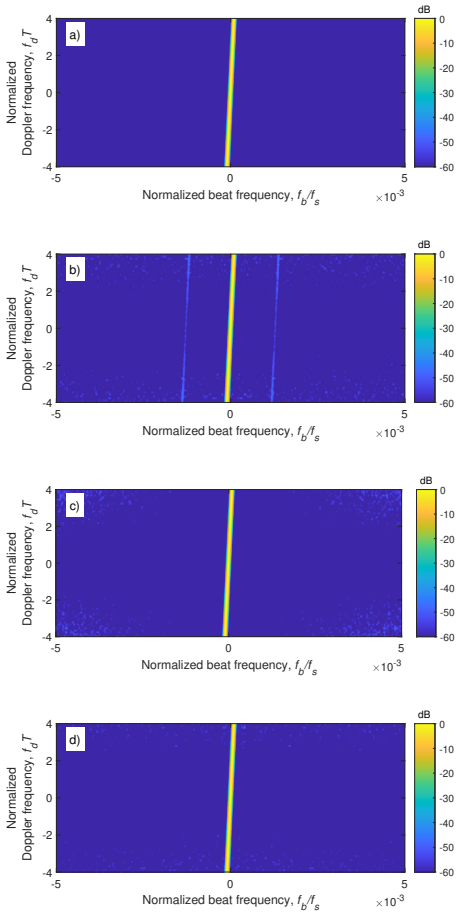

Figure 4.7: Range profile with different Doppler frequency for FMCW and the phase lag compensated PC-FMCW waveforms with $N_c = 1024$: a) FMCW b) BPSK c) Gaussian d) GMSK. The ridge is inclined in all cases but seems narrow due to zooming out the x-axis.

the vicinity of the main lobe, they all have an identical response, determined by 100 dB Chebyshev window, applied to the signals before range FFT. The sidelobes of three phase lag compensated PC-FMCW raises with the Doppler frequency shift; among them, the range profile degradation is minimal for GMSK.

The bandwidth of the chip B_c raises as the number of chips per chirp N_c increases. Consequently, the bandwidth of the chip becomes comparable to ADC sampling frequency, and the sidelobe level increases with the filtering of the spectrum. However, the spectrum widening of the coded beat signal is different for the three phase lag compensated PC-FMCW as explained in Chapter 3. Therefore, they provide different peak sidelobe level (PSL). The beat signal PSL is defined by the maximum amplitude of the

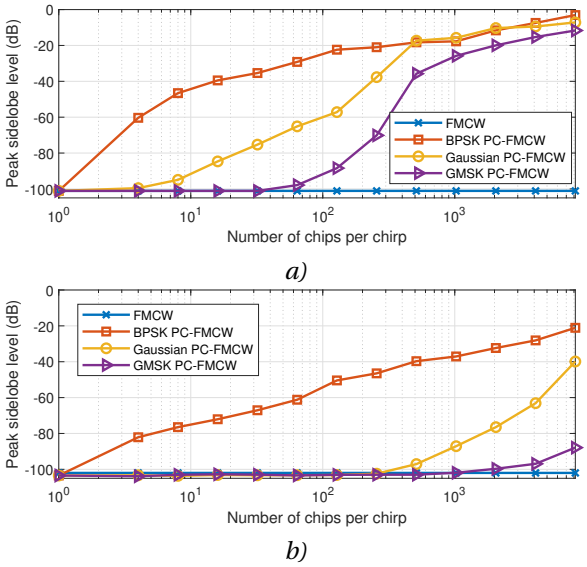

Figure 4.8: PSL of the investigated waveforms at normalized target range $R/R_{\max} = 0.4$ versus the number of chips per chirp: a) No phase lag compensation b) With phase lag compensation.

signal spectrum outside of the main lobe (first nulls) and can be written as:

$$\mathrm{PSL} = \max_{f \in \mathscr{L}} \left| \hat{Z}_{\mathrm{d}}(f) \right| \qquad \mathscr{L} = (-\infty, -f_l) \cup (f_r, \infty), \tag{4.27}$$

where f_l and f_r denote the frequency corresponding to the left and right parts of the first null, respectively, and $\mathscr{L}$ denotes the frequency interval.

Next, we investigate the zero Doppler cuts of waveforms and compare their respective peak sidelobe levels. PSL of the investigated waveform at normalized target range $R/R_{\max} = 0.4$ as a function of the number of chips per chirp is demonstrated in Figure 4.8 where the maximum range $R_{\max} = \frac{c f_{b_{\max}}}{2k}$ and the maximum beat signal is determined as $f_{b_{\max}} = f_s/2$. To highlight the benefits of performing phase lag compensation, we also demonstrate the sensing performance of investigated waveforms without performing phase lag compensation in Figure 4.8 a. It can be seen that applying phase lag compensation improves the PSL of three PC-FMCW waveforms (Figure 4.8 b). Still, PSL of BPSK PC-FMCW rapidly increases as the number of chips per chirp raises. On the other hand, we observe that the PSL of phase lag compensated GMSK PC-FMCW enhanced substantially, especially for long codes. Particularly, the PSL of GMSK PC-FMCW with $N_c = 1024$ improved from -25 dB to -100 dB by using phase lag compensation. Consequently, GMSK PC-FMCW can provide PSL similar to FMCW up to $N_c = 1024$ ($B_c = 1.024$ MHz for the selected parameters). In addition, we illustrated the PSL of phase lag compensated waveforms with $N_c = 1024$ as a function of the normalized target range in Figure 4.9. Note that the spectral widening and filtering of the spectrum become crucial for PC-FMCW as the target approaches the maximum range. GMSK PC-FMCW has favourable sensing performance among phase lag compensated waveforms and provides lower PSL.

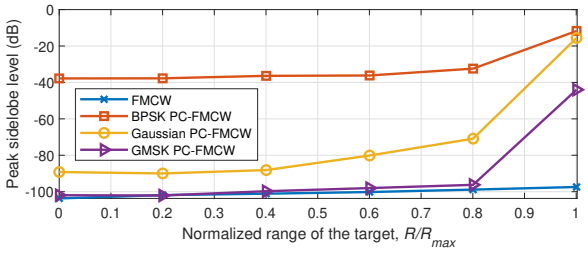

Figure 4.9: PSL of the investigated waveforms (with phase lag compensation) with $N_c = 1024$ versus the normalized range of the target with respect to the maximum range.

4

4.4.2. PEAK TO AVERAGE POWER RATIO

The quadratic phase lag compensation is applied to the spectrum of the transmitted code to eliminate the dispersion effect of the group delay filter. This quadratic phase lag compensation filter can be represented as:

$$H_{\text{lag}}(f) = e^{-j\frac{\pi f^2}{k}}, \tag{4.28}$$

and the phase lag compensated code term in the time-domain can be written as:

$$\hat{s}(t) = s(t) \otimes h_{\text{lag}}(t). \tag{4.29}$$

To analyse the effect of quadratic phase lag compensation on phase-coded signal, let $\xi = j\frac{\pi}{k}$, then the quadratic phase lag compensation filter in the time-domain can be written as:

$$\begin{aligned} h_{\text{lag}}(t) &= \mathscr{F}^{-1}\left\{e^{-j\frac{\pi f^2}{k}}\right\} \\ &= \int_{-\infty}^{\infty} e^{-\xi f^2} e^{j2\pi f t}\, df \\ &= e^{-\frac{\pi^2 t^2}{\xi}} \int_{-\infty}^{\infty} e^{-\left(\sqrt{\xi} f - j\frac{\pi t}{\sqrt{\xi}}\right)^2} df \\ &= \frac{1}{\sqrt{\xi}} e^{-\frac{\pi^2 t^2}{\xi}} \sqrt{\pi} \\ &= \sqrt{\frac{k}{j}} e^{-\pi\frac{kt^2}{j}}. \end{aligned} \tag{4.30}$$

Note that the resulting signal has the opposite sign of the time-domain representation of the group delay filter dispersion given in (4.17). This is expected because we are applying phase lag compensation to eliminate the dispersion effect. To analyze the effect of phase lag compensation filter on the amplitude of the code signal, let $\beta = \sqrt{\frac{\pi k}{j}}$, then the (4.30) becomes:

$$h_{\text{lag}}(t) = \frac{\beta}{\sqrt{\pi}} e^{-\beta^2 t^2} \tag{4.31}$$

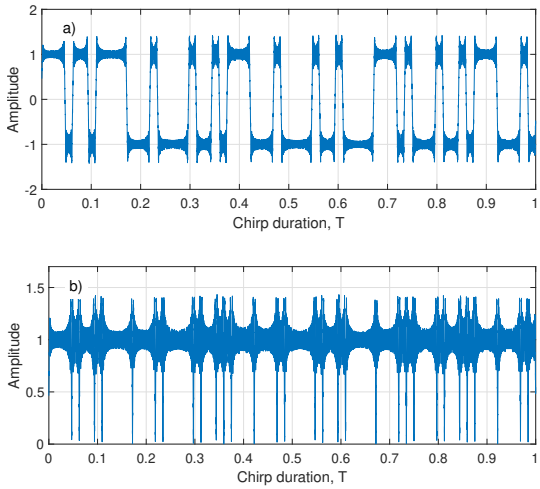

Figure 4.10: Time-varying amplitude due to phase lag compensation: a) BPSK code $N_c = 64$ b) Absolute value of the transmitted BPSK PC-FMCW.

Following the steps between (A.6) and (A.9) given in Appendix A, and replacing $\eta = \beta$, the convolution of the unit step function and phase lag compensation filter can be found as:

$$u(t) \otimes h_{\text{lag}}(t) = \frac{1}{2}\text{erf}\left(\sqrt{\frac{\pi k}{j}}\, t\right). \tag{4.32}$$

Subsequently, the result of the convolution for the BPSK code sequence becomes:

$$\begin{aligned} \hat{s}(t) &= c(t) \otimes h_{\text{lag}}(t) \\ &= \frac{1}{2}\sum_{n=1}^{N_c} e^{j(\phi_{n+1}-\phi_n)}\text{erf}\left(\sqrt{\frac{\pi k}{j}}\,(t - nT_c)\right). \end{aligned} \tag{4.33}$$

The amplitude of the phase lag compensated BPSK code is shown in Figure 4.10 a. The quadratic phase lag compensation applies different time delays to each frequency component of the transmitted phase code. During phase changes, the phase-coded signal has a wide spectrum and shifting the frequency components non-linearly creates ripples in the time-domain signal with $N_c = 64$ (Figure 4.10 a). Moreover, the time interval between phase changes becomes shorter for a long code sequence, and ripples in the time-domain are collectively summed up as the adjacent phase shifts interfering with each other. Therefore, the amplitude of the transmitted waveform is not constant anymore (Figure 4.10 b).

The time-varying amplitude initiated by the phase lag compensation leads to a high peak-to-average power ratio (PAPR). The PAPR of the signal can be represented as:

$$\text{PAPR} = \frac{\max|x_{\text{T}}(t)|^2}{\lim_{T\to\infty}\frac{1}{2T}\int_{-T}^{T}|x_{\text{T}}(t)|^2\, dt}. \tag{4.34}$$

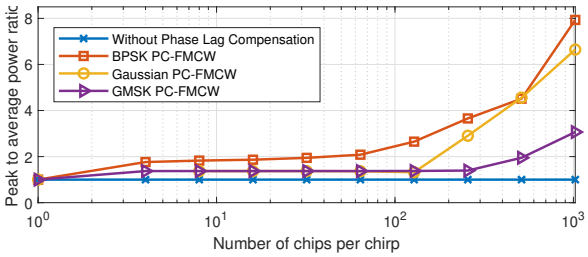

Figure 4.11: Comparison of PAPR versus number of chips per chirp for phase lag compensated PC-FMCW waveforms.

The PAPR of the investigated waveforms is compared as a function of N_c in Figure 4.11, where we used $T = 1$ ms, $B = 200$ MHz. It can be seen that the PAPR of the three PC-FMCW without phase lag compensation are constant and equal to 1. The PAPR increases for all three phase lag compensated PC-FMCW as N_c raises. However, the effect of the phase lag compensation and the resulting amplitude variation decrease as the phase transition becomes smoother. Note that the differences in PAPR between BPSK, Gaussian, and GMSK are comparable up to $N_c = 64$; thereafter, PAPR varies notably. For long code sequences, GMSK PC-FMCW provides the lowest PAPR, while BPSK PC-FMCW has the highest PAPR since the abrupt phase changes on the BPSK coding are affected more by the frequency-dependent shifts.

4.4.3. MUTUAL ORTHOGONALITY

The coding spreads the power of the signals in the beat frequency domain. As each transmitted PC-FMCW uses its phase-coded signal, only the correct signal passes through the received signal, which is matched to this code. The signals with other code sequences are not matched to this code, leading to the spread of the power over range. As explained in Chapter 3, the theoretical limits of the suppression are equal to the spreading factor and can be written as:

$$SP \equiv 10\log_{10}\left(\frac{T}{T_c}\right) = 10\log_{10}(N_c). \tag{4.35}$$

Assume the first radar (victim) transmits PC-FMCW with the phase lag compensated code $\hat{s}_1(t)$ to detect a target. The received signal reflected from the target with complex coefficient α_1 can be written as:

$$x_{\mathrm{R}_1}(t) = \alpha_1 \hat{s}_1(t-\tau_1) e^{-j\left(2\pi f_c(t-\tau_1)+\pi k(t-\tau_1)^2\right)} \tag{4.36}$$

To illustrate the mutual orthogonality assessment, consider the worst-case scenario when a second radar is perfectly synchronized with the first radar and transmits PC-FMCW with the phase lag compensated code $\hat{s}_2(t)$. The signal transmitted from the second radar is delayed in time and captured by the first radar with complex coefficient α_2 as:

$$x_{\mathrm{R}_2}(t) = \alpha_2 \hat{s}_2(t-\tau_2) e^{-j\left(2\pi f_c(t-\tau_2)+\pi k(t-\tau_2)^2\right)}, \tag{4.37}$$

where τ_2 is the round trip delay between the first and second radars. Subsequently, the total received signal on the first radar is the combination of received signals and can be

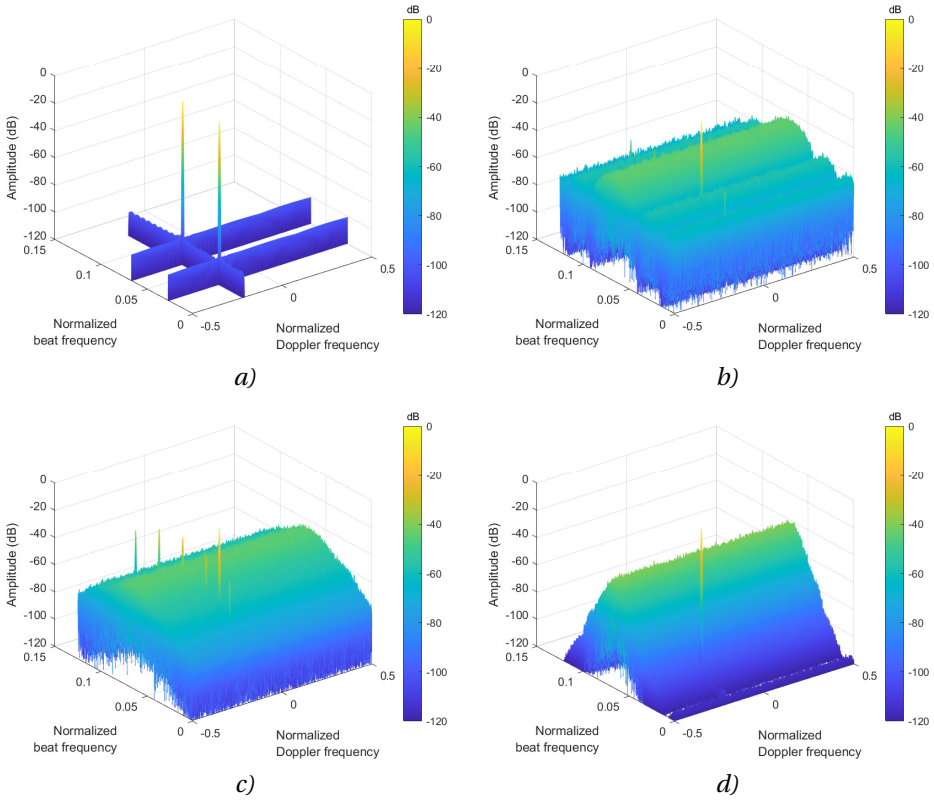

Figure 4.12: Comparison of cross-isolation between two beat signals associated with three phase lag compensated PC-FMCW waveforms with different random codes: a) FMCW (no code) b) BPSK c) Gaussian d) GMSK.

written as:

$$x_{\mathrm{R}}(t) = x_{\mathrm{R}_1}(t) + x_{\mathrm{R}_2}(t). \tag{4.38}$$

The total received signal is mixed and dechirped with the uncoded transmit signal of the first radar. The mixer output gives the summation of two coded beat signals. Subsequently, the group delay filter is applied to the mixer output and aligns coded beat signals at the maximum delay as discussed in Section 4.3. The output of the group delay filter can be represented as:

$$g_{\mathrm{o}}(t) = \alpha_1 s_1(t-\tau_{\max}) e^{j(2\pi k \tau_1 t)} + \alpha_2 s_2(t-\tau_{\max}) e^{j(2\pi k \tau_2 t)}. \tag{4.39}$$

During decoding, the group delay filter output is decoded with the complex conjugate of the first code shifted to the maximum delay $s_1(t-\tau_{\max})$. After decoding, the beat signal reflected from the target is obtained similar to the dechirped signal of conventional FMCW, while the beat signal initiated by the second radar remains coded as:

$$\begin{aligned} d_{\mathrm{o}}(t) =& d_1(t) + d_2(t) \\ =& \alpha_1 e^{j(2\pi k \tau_1 t)} + \alpha_2 s_1^*(t-\tau_{\max}) s_2(t-\tau_{\max}) e^{j(2\pi k \tau_2 t)}, \end{aligned} \tag{4.40}$$

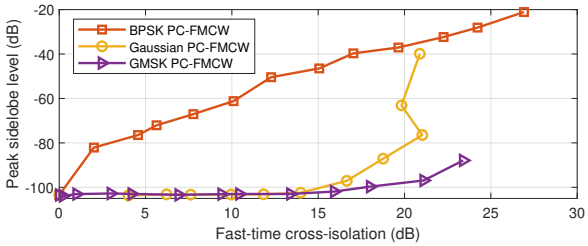

Figure 4.13: Comparison of PSL versus cross-isolation in fast-time for phase lag compensated PC-FMCW waveforms.

where $d_1(t)$ and $d_2(t)$ are the decoded signals. Subsequently, we investigate the cross-isolation between two beat signals in the spectrum of the decoded signal output. The cross-isolation can be defined as:

$$\text{Cross-isolation} = \frac{\max_{f\in\forall}\left|D_1(f)\right|}{\max_{f\in\forall}\left|D_2(f)\right|}, \tag{4.41}$$

where $D_1(f)$ and $D_2(f)$ are the spectrum of decoded signals associated with $d_1(t)$ and $d_2(t)$, respectively.

In Figure 4.12, we compare the cross-isolation between the two beat signals associated with PC-FMCW waveforms with different random code sequences. We consider the number of chips per chirp $N_c = 1024$ and the number of chirp pulses $N_p = 512$. It is shown in Figure 4.12 that the second radar causes a beat signal according to $f_{b_2} = k\tau_2$ which can be seen as a ghost target for a perfectly synchronized case (which is very difficult to generate in a real-life scenario and is just used for the proof of the mutual orthogonality concept), and it can not be distinguished from the target in the traditional FMCW (Figure 4.12 a). However, in the phase-coded FMCW cases, the beat signal initiated by the second radar f_{b_2} remains coded, and thus its power is spread over both fast-time and slow-time. This cross-isolation between two beat signals associated with BPSK PC-FMCW, Gaussian PC-FMCW, and GMSK PC-FMCW are given in Figure 4.12 b, c, and d, respectively. The theoretical upper-boundary limit regarding the suppression of the beat signal f_{b_2} is $10\log_{10}(N_p) + 10\log_{10}(N_c) = 57$ dB for a perfectly orthogonal code (combined with the suppression in both slow-time and fast-time). However, the three phase lag compensated PC-FMCW are not perfectly orthogonal after applying the phase lag compensation and filtering. Their resulting suppression behaviours in the fast-time are different according to their phase modulation type, as demonstrated in Figure 4.12. In particular, Gaussian PC-FMCW has the local peaks between phase-coded signals, and it gives the worst suppression performance. BPSK PC-FMCW spreads the power of f_{b_2} to all range cells as the spectrum of BPSK has a significant spectrum broadening of the beat signal. GMSK PC-FMCW spreads the power of the f_{b_2} as a Gaussian shape (Triangular in dB scale) over the range cells defined by the 3-dB bandwidth of the Gaussian filter (smoother bandwidth) B_s. Consequently, GMSK PC-FMCW has a narrower spreading characteristic than BPSK, which might help to avoid masking of targets with weak radar cross section (RCS) outside of the main lobe. Moreover, it can be seen in Figure 4.13 that

Figure 4.14: Illustration of the stationary target.

GMSK PC-FMCW can provide high cross-isolation while achieving low PSL. These facts favour the usage of GMSK PC-FMCW over BPSK PC-FMCW.

4.5. EXPERIMENTS

This section demonstrates the experimental results related to the sensing and cross-isolation performance of the phase lag compensated PC-FMCW waveforms. The experimental investigation of the waveforms has been done using PARSAX radar [118]. We use the proposed transceiver structure for each PC-FMCW, and we apply the traditional dechipring transceiver structure for the FMCW waveform, which is used as a benchmark. We use random code sequences with $N_c = 1024$ ($B_c = 1.024$ MHz) for the three phase lag compensated PC-FMCW and choose the system parameters as given in Table 4.1. To emphasize the advantage of GMSK, we choose ADC sampling frequency as $f_{\text{ADC}} = 2$ MHz so that the code bandwidth becomes comparable to ADC sampling. Moreover, we applied Chebyshev windowing with 80 dB suppression and compared it with a rectangle windowing case to highlight the sensing performance of the waveforms. In addition, we normalized all the range profiles by the maximum of the range profile.

Table 4.1: System Parameters

Chirp bandwidth	B	40 MHz
Chirp duration	T	1 ms
Intermediate frequency	f_{IF}	125 MHz
IF sampling frequency	f_s	400 MHz
Carrier frequency	f_c	3.315 GHz
ADC sampling frequency	f_{ADC}	2 MHz
Number of chips	N_c	1024
Chip duration	T_c	0.97μ s
Chip bandwidth	B_c	1.024 MHz
Smoother bandwidth	B_s	2.048 MHz

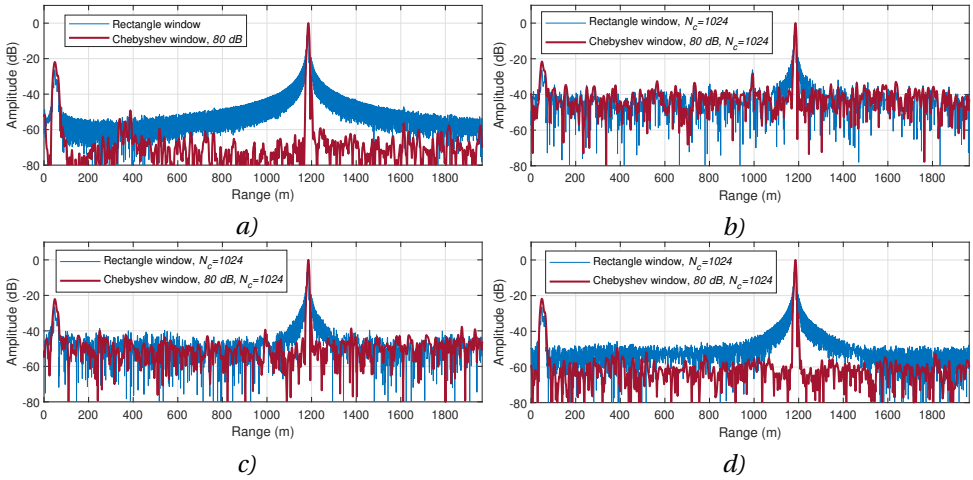

Figure 4.15: Stationary target range profiles for phase lag compensated PC-FMCW waveforms: a) FMCW b) BPSK c) Gaussian d) GMSK.

4.5.1. SENSING PERFORMANCE OF ONE WAVEFORM

In this subsection, we transmit only one waveform at a time to validate the sensing performance of the waveforms. The resulting waveforms are performed in the real scenario to detect both stationary and moving targets. Note that the experimental environment is dynamic for the moving target experiment. To detect the same car and compare the sensing performance of the waveforms, we transmit four waveforms sequentially with 128 chirp pulses in each waveform.

STATIONARY TARGET EXPERIMENT

For the stationary target experiment, we look at the chimney located at 1185 m away from the radar, as shown in Figure 4.14. The range profiles of the four different waveforms are demonstrated in Figure 4.15. At the chimney location, the noise-clutter level of the range profile is around ~ −60 dB for FMCW, and it provides ~ 60 dB dynamic range after applying Chebyshev windowing. It can be seen that BPSK and Gaussian have increased sidelobes and provide ~ 30 dB and ~ 40 dB dynamic ranges, respectively. This is due to

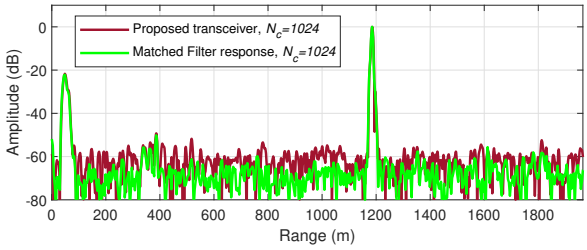

Figure 4.16: Range profile for phase lag compensated GMSK PC-FMCW in case of the proposed transceiver and Matched filter.

Figure 4.17: Illustration of the moving target.

the fact that BPSK and Gaussian have substantial broadening in the beat frequency and the coded beat signals have a wide spectrum. As a result, the sensing performance of BPSK and Gaussian suffers from limited ADC sampling. On the other hand, the widening of the coded beat signal spectrum is reduced by using GMSK as explained in Chapter 3. Thus, GMSK is expected to provide better sensing performance while the code bandwidth becomes comparable to ADC sampling. We observe this behaviour as GMSK provides the best and closest performance to FMCW by providing ~ 60 dB dynamic range in the vicinity of the chimney. In addition, we demonstrate the range profile of GMSK PC-FMCW by using Matched Filter receiving strategy and compared it with the response of the proposed transceiver structure in Figure 4.16. It can be seen that the proposed transceiver structure gives a very similar result to the matched filter response for GMSK PC-FMCW.

MOVING TARGET EXPERIMENT

The applicability of the investigated waveforms to a moving scene is validated by the moving target experiment where we observe the road and detect a moving car located at 1150 m with a radial velocity ~ 13 m/s as illustrated in Figure 4.17. We use $N_c = 1024$ for the three phase lag compensated PC-FMCW. The range-Doppler profiles of the waveforms are demonstrated in Figure 4.18 where the peak location of the target is obtained at 1150 m for each waveform. The noise level of the range profile is around ~ −55 dB for FMCW, and it has ~ 55 dB dynamic range after windowing (Figure 4.18 a). Similar to the stationary target scenario, GMSK provides the best sensing performance between three phase lag compensated PC-FMCW. In particular, the range profile of BPSK PC-FMCW has increased sidelobe level due to limited ADC sampling, and it provides a dynamic range around ~ 30 dB (Figure 4.18 b), while the sidelobe level of Gaussian PC-FMCW provides ~ 40 dB dynamic range (Figure 4.18 c). However, GMSK PC-FMCW provides ~ 55 dB dynamic range, and it has a range profile very similar to FMCW as shown in Figure 4.18 d. Consequently, GMSK PC-FMCW can provide similar sensing performance that is offered by FMCW, and it can also ensure the ability to distinguish different signals due to coding as discussed in Section 4.4.3.

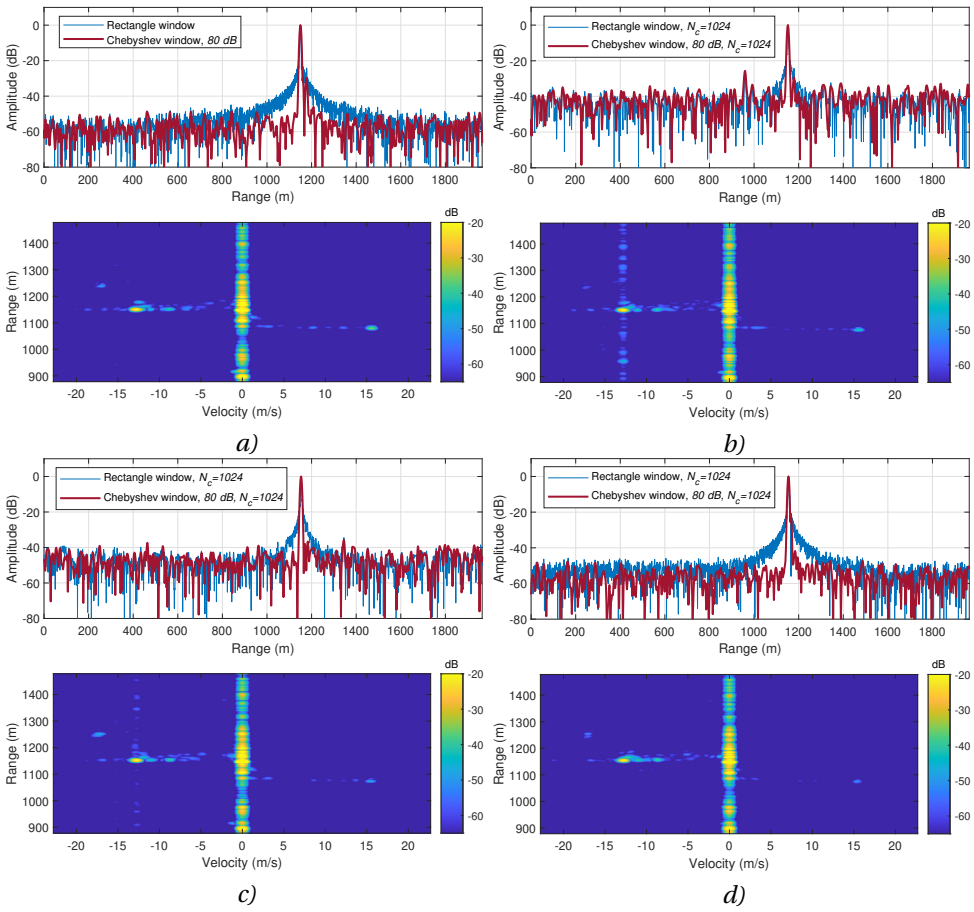

Figure 4.18: Moving target range and range-Doppler profiles for phase lag compensated PC-FMCW waveforms: a) FMCW b) BPSK c) Gaussian d) GMSK.

4.5.2. CROSS-ISOLATION PERFORMANCE BETWEEN TWO WAVEFORMS

In this subsection, we transmit two same types of waveforms simultaneously to validate the cross-isolation performance of the waveforms. For the proof of the mutual orthogonality concept and to mimic the worst-case scenario as explained in Section 4.4.3, we apply linear time delay to the second waveform before transmission so that it has a range offset compared to the first waveform that corresponds to 480 m. For each PC-FMCW, the first waveform uses phase lag compensated random code $\hat{s}_1(t)$ with $N_c = 1024$, and the second waveform uses phase lag compensated random code $\hat{s}_2(t)$ with $N_c = 1024$. Moreover, we use 32 chirp pulses, and each PC-FMCW chirp pulses use different random code sequences. Consequently, combined with the suppression in both slow-time and fast-time, the theoretical upper-boundary limit of cross-isolation is $10\log_{10}(32)+10\log_{10}(1024) = 45$ dB for a perfectly orthogonal code. However, the cross-isolation performance is expected to be degraded due to the loss of orthogonality between codes after applying the phase

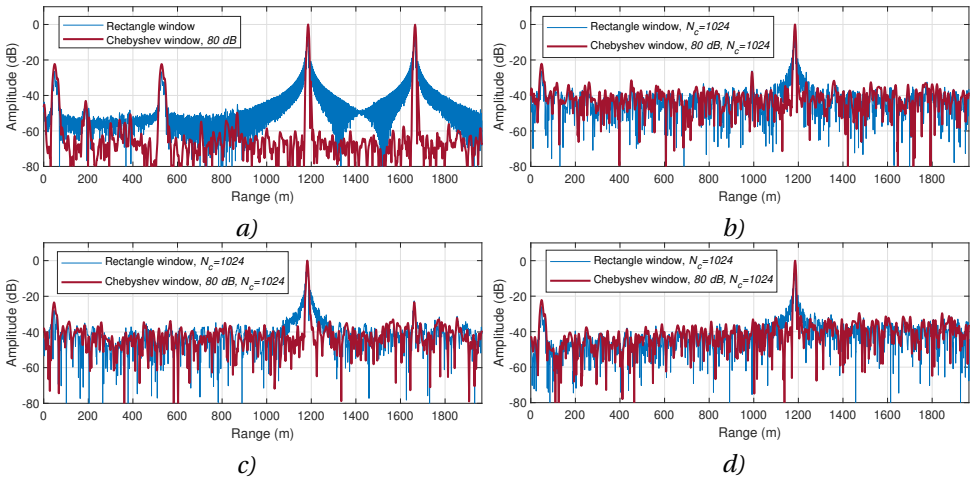

Figure 4.19: Cross-isolation experiment for a stationary target. Range profiles for phase lag compensated PC-FMCW waveforms: a) FMCW b) BPSK c) Gaussian d) GMSK.

lag compensation and filtering. The resulting two waveforms are transmitted together and performed in the real scenario to detect the chimney located at 1185 m away from the radar. Subsequently, the received signal for each PC-FMCW is processed with the proposed transceiver structure and decoded with the reference code $s_1(t)$.

The range profiles of the four different waveforms are demonstrated in Figure 4.19. It can be seen that the second FMCW waveform leads to a beat signal that causes ghost targets at 530 m and 1665 m in addition to real targets at 50 m and 1185 m. Since there is no mutual orthogonality between two FMCW waveforms, the second waveform can not be distinguished from the first waveform in the traditional FMCW radar. By using PC-FMCW waveforms, only the beat signal associated with the first waveform is decoded with $s_1(t)$ and the beat signal initiated by the second waveform is spread over both fast-time and slow-time as it remains coded. Consequently, the ghost targets created by the second waveform are suppressed using PC-FMCW. Among three phase lag compensated PC-FMCW, GMSK provides the best dynamic range. Particularly, Gaussian PC-FMCW provides weak suppression performance, and the ghost target still appears with ~ -22 dB power. BPSK PC-FMCW suppresses the ghost target power around ~ 34 dB but only provides ~ 26 dB dynamic range as it suffers from limited ADC sampling. On the other hand, GMSK suppresses the ghost target's power and provides ~ 40 dB dynamic range in the vicinity of the chimney. Thus, experimental results verify the advantages of GMSK PC-FMCW over BPSK PC-FMCW and Gaussian PC-FMCW.

4.6. CONCLUSIONS

This chapter explores the appropriate receiving strategy with a low sampling requirement and computational complexity suitable for automotive radars. We have analysed the group delay filter effect on the coded beat signals and performed the phase lag compensation on the transmitted phase-coded signal to eliminate the undesired effect of the group

delay filter. Consequently, the beat signals are recovered properly after the decoding.

The phase lag compensated SPC-FMCW waveform has been introduced as an efficient tool to enhance the coexistence of multiple radars within the same spectrum. To this end, the sensing performance of the three phase lag compensated waveforms, namely BPSK PC-FMCW, Gaussian PC-FMCW and GMSK PC-FMCW, have been investigated and compared. The properties of the investigated waveforms for the first time are analysed theoretically and verified experimentally. We observe that the inclined ridge associated with the chirped waveform ambiguity function is present, and thus all considered waveforms with investigated receiving strategy have the Doppler tolerance of FMCW. Then, the sensing performance of the investigated waveforms is compared as a function of code bandwidth. It is shown that the PSL, PAPR and the cross-isolation between signals increase as the bandwidth of the code raises for the three phase lag compensated PC-FMCW. Among them, the degradation in the PSL and PAPR is minimal for GMSK. Moreover, it is demonstrated that applying phase lag compensation improves the PSL of three PC-FMCW waveforms. In particular, PSL of phase lag compensated GMSK PC-FMCW improved substantially, especially for long codes.

In addition, we have demonstrated the experimental verification regarding the sensing and cross-isolation performance of the phase lag compensated PC-FMCW waveforms. First, only one waveform at a time is transmitted to validate the sensing performance of the waveforms. Then, we validate the cross-isolation performance of the waveforms by transmitting two same types of waveforms simultaneously. The simulations and the experimental results demonstrate that the phase lag compensated GMSK PC-FMCW can provide sensing performance similar to that of uncoded FMCW. At the same time, it can provide high mutual orthogonality that can be used to improve cross-isolation between multiple radars.

5

PC-FMCW MIMO RADAR

The MIMO ambiguity function of the PC-FMCW waveform is examined. The range-angle performance of the PC-FMCW with different code families is investigated and compared with the PMCW waveform. The advantages of the PC-FMCW ambiguity function over the PMCW one are demonstrated in terms of the Doppler tolerance and sidelobe level for the same types of codes. Moreover, the PC-FMCW waveform with a low sampling processing strategy is studied for coherent MIMO radar. The PC-FMCW MIMO structure, which jointly utilizes both fast-time and slow-time coding, is proposed to reduce sidelobe levels while preserving high range resolution, unambiguous velocity, good Doppler tolerance and low sampling needs. The sensing performance and practical aspects of the introduced PC-FMCW MIMO structure are evaluated theoretically and verified experimentally. The numerical simulations and experiments demonstrate that the proposed MIMO keeps the advantages of the FMCW waveform, including computational efficiency and low sampling demands, while having the ability to provide low sidelobe levels with simultaneous transmission.

Parts of this chapter have been published in:

U. Kumbul, N. Petrov, S. Yuan, C. S. Vaucher, and A. Yarovoy, "MIMO ambiguity functions of different codes with application to phase-coded FMCW radars", in *IET International Radar Conference (IET IRC 2022)*, pp. 1-6, 2022.

U. Kumbul, N. Petrov, C. S. Vaucher, and A. Yarovoy, "Phase-Coded FMCW for coherent MIMO radar", in *IEEE Transactions on Microwave Theory and Techniques*, pp. 1–13, 2022.

5.1. INTRODUCTION

The automobile radar must deliver thorough and precise information about its surroundings in order to accomplish completely autonomous driving. As a result, providing a high angular resolution, which depends on the quantity and size of the antenna components, is one of the primary needs of car radar. To achieve this task, the automotive radars utilize the MIMO radars to enhance angular resolution [23]. The MIMO radars exploit the spatial diversity between transmitting antenna elements to create virtual arrays with a large aperture while using a relatively small number of antenna elements. However, the utilization of such spatial diversity requires high mutual orthogonality between transmitting channels. In case of lack of mutual orthogonality, received waveform coming from other transmitted channels leads to self-interference and degrades the sensing performance of MIMO systems. Consequently, various transmitting schemes and radar waveforms with different pros and cons have been proposed to realize MIMO systems in automotive radars [23, 126]. Since there is no room for sensing failures in fully autonomous driving, the radar waveform that gives high mutual orthogonality with good sensing performance is still a focus of research [84].

The FMCW waveforms have been used in many radar applications as it provides high range resolution, low sidelobes, good Doppler tolerance and constant peak-to-average power ratio (PAPR) with a relatively low hardware complexity [27]. However, these benefits come with the price of having poor distinctness, and creating mutual orthogonality between FMCW signals often requires transmission schemes that lose unambiguous Doppler velocity and range resolution to achieve orthogonality [23]. Waveform coding is commonly used in radars to achieve unique waveform recognition [11]. Particularly, the PMCW waveforms have been used to achieve mutual orthogonality between transmitted waveforms in the MIMO systems [82, 83]. However, any PMCW waveform suffers from poor Doppler tolerance, and its usage requires a high sampling frequency in the receiver [17, 84]. To overcome the limitations of both FMCW and PMCW, applying phase-coding to FMCW has become a notable alternative. To this end, the PC-FMCW waveforms have been investigated to enhance the mutual orthogonality of the waveform and achieve simultaneous transmission for the MIMO systems while keeping the advantages of FMCW [127, 128].

In this chapter, we examine the MIMO ambiguity function of PC-FMCW waveform and investigate the utilization of the phase lag compensated PC-FMCW waveform with a low sampling receiving strategy for simultaneous MIMO transmission. We propose a novel PC-FMCW MIMO radar structure, which combines both fast-time and slow-time coding to lower sidelobes while maintaining simultaneous transmission of the waveforms, high range resolution, unambiguous velocity, good Doppler tolerance and low signal sampling requirements. Furthermore, for the first time in literature, we assess the performance of such waveforms in application to coherent MIMO radar. The rest of the chapter is structured as follows. Section 5.2 gives the overview of the MIMO transmitting schemes and compares their pros and cons. Then in Section 5.3, we study the MIMO ambiguity function for the separation capability of the PC-FMCW waveforms and compare range-angle performance of different code families in application to the PC-FMCW waveforms. Section 5.4 provides the signal model and requiring processing steps for the proposed PC-FMCW MIMO radar with a simultaneous transmission scheme. Subsequently, the

performance of the proposed MIMO radar is assessed in different domains and compared to the other state-of-the-art techniques in Section 5.5. Then, the experimental verification of the proposed MIMO radar is demonstrated in Section 5.6. Finally, Section 5.7 presents the conclusions remarks for this chapter.

5.2. OVERVIEW OF MIMO TRANSMISSION SCHEMES

This section overviews the automotive radar MIMO multiplexing schemes. As already mentioned in the introduction, the FMCW waveform is widely used by automotive radars, and antenna aperture size can be increased by using the MIMO system. For P transmit antennas and L receive antennas, a virtual array with $Q = P \times L$ elements can be synthesized. In order to synthesize such a virtual array, orthogonality between transmitted waveforms should be secured. To ensure orthogonality between transmitters, various transmitting schemes have been proposed for the FMCW waveforms [126]. These methods aim to achieve orthogonality between transmitters in either time, frequency, or code domains, which result in different advantages and disadvantages.

5.2.1. TDMA

The simplest approach to distinguish the received signals associated with different transmitters is time division multiple access (TDMA). In the TDMA transmission scheme, chirp sequences are consecutively transmitted one by one by each transmit antenna. However, the time duration between chirps transmitted by the same antenna becomes $T_{\text{PRI}} = PT$ as shown in Figure. 5.1, where T_{PRI} is the pulse repetition interval (PRI) and T is chirp duration. Consequently, the maximum unambiguous velocity of the target degraded by a factor of the number of transmitters P such as:

$$v_{\text{un}} = \frac{\lambda}{4T_{\text{PRI}}} = \frac{\lambda}{4PT}, \tag{5.1}$$

where $\lambda = c/f_c$ is the wavelength, c is the speed of light, and f_c is the carrier frequency of the waveform. Moreover, different transmitters illuminate a target at different time instances, which introduces a phase error for moving targets and increases the angle estimation errors [129]. To deal with this, various techniques are proposed to eliminate the phase migration introduced by every moving target in the virtual array response [129–131]. Another disadvantage of TDMA is that it provides lower power for the finite power per transmission channel. Although motion-induced phase error can be addressed, reducing the maximum unambiguous velocity by a factor of transmit channels prevents increasing the number of transmitters, and thus improving the angular resolutions is limited in the TDMA transmission scheme.

5.2.2. SLOW-TIME CDMA

Another method to achieve orthogonality between transmitting channels is slow-time code division multiple access (ST-CDMA). In the ST-CDMA transmission scheme, the phase codes are used to modulate the initial phases of each chirp pulse and let all transmit channels simultaneously transmit signals with different codes. One particular implementation of such coding is achieved using Doppler division multiple access (DDMA). In the

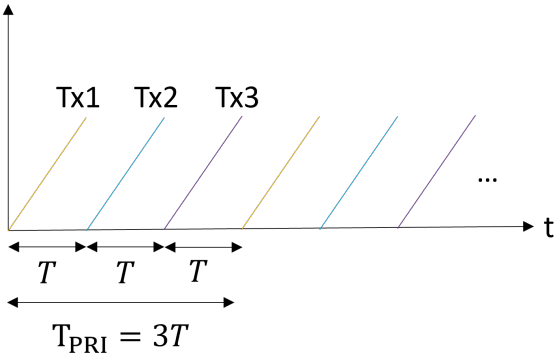

Figure 5.1: TDMA with 3 transmit channels for the FMCW waveforms.

DDMA transmission scheme, the phase shifts are set such that different transmit channels appear in different parts of the Doppler spectrum, and thus they emulate Doppler frequency shift [132]. However, sharing the Doppler spectrum downgrades the maximum unambiguous velocity by a factor of the number of transmit channels. Consequently, a target with a velocity higher than the reduced maximum unambiguous velocity will appear in the Doppler spectrum assigned to another transmit channel [132]. This disadvantage restrains increasing the number of transmitters and thus limits improving angular resolution using DDMA. In general ST-CDMA implementations, the phase codes are designed to spread signals of different transmitters throughout the full Doppler spectrum as pseudo noise after decoding in the slow-time with the reference phase code signal. As a result, maximum of $10\log_{10}(N_p)$ dB isolation between transmitter channels in slow-time can be achieved by using N_p chirp pulses [133]. However, decoding in the slow-time leads to increased sidelobes in the Doppler domain. Moreover, the code length and the number of chirp pulses are limited for the slow-time phase coding [126]. Hence, the slow-time phase coding alone is not enough to provide high mutual orthogonality and suffers from high Doppler sidelobes.

5.2.3. FAST-TIME CDMA

The fast-time code division multiple access (FT-CDMA) transmission scheme can provide high mutual orthogonality between transmitting channels to realize simultaneous transmission for the MIMO system. Consequently, the FT-CDMA transmission scheme can address the degradation problem in the maximum unambiguous velocity seen in the TDMA and DDMA transmission schemes; and the maximum unambiguous velocity of the target can be obtained as:

$$v_{\text{un}} = \frac{\lambda}{4T_{\text{PRI}}} = \frac{\lambda}{4T}. \tag{5.2}$$

For the purpose of fast-time coding, the circulating codes which use a small frequency shift are proposed to modulate FMCW waveforms in adjacent frequency bands [79]. On the other hand, such coding results in degradation in the range resolution. Alternatively, the circulating codes are used with slow-time coding for the pulses in [134]. However, this

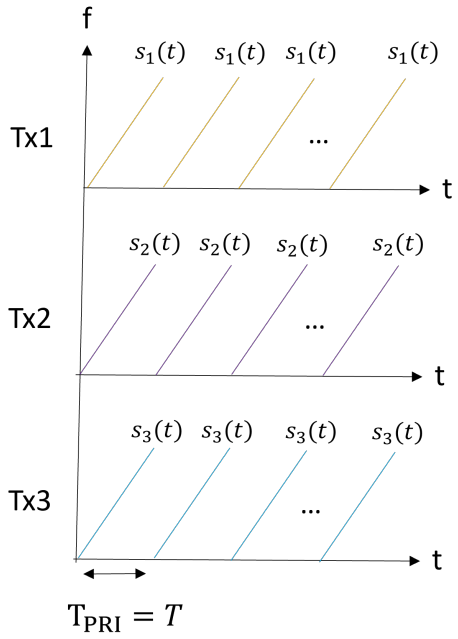

Figure 5.2: Fast-time CDMA with 3 transmit channels for the PC-FMCW waveforms.

method requires a special technique for Doppler processing, and the windowing function can not be applied to reduce sidelobes further. In [135], the chirp signal modulated with orthogonal frequency division multiplexing (OFDM) waveform is proposed to improve the range resolution. However, such a waveform imposes different limitations on the waveform parameter selection and is difficult to utilize.

The aforementioned limitations can be circumvented by using the PC-FMCW waveforms. The PC-FMCW waveform with fast-time coding is shown in Figure 5.2. In the PC-FMCW radar, the phase-coded signals are used to modulate the phase changes within the chirp, and a maximum of $10\log_{10}(N_c)$ dB isolation between transmitted signals can be achieved in fast-time by using N_c number of chips per chirp. Such PC-FMCW waveform keeps all the benefits of FMCW waveform, such as good Doppler tolerance and high range resolution as examined in Chapter 2. In addition, the PC-FMCW can provide high mutual orthogonality, which is necessary for the simultaneous MIMO transmission [127]. Moreover, the PC-FMCW waveforms can be jointly utilized with the slow-time coding to decrease the sidelobe levels further.

As already explained in Chapter 2, two approaches based on dechirping receiver structure have been proposed to lower the waveform sampling requirements in the receiver: the compensated stretch processing and the group delay filter [33, 85, 88]. The compensated stretch processing corresponds to performing filter bank for all ranges of interest, which requires high computational complexity compared to the standard stretch processing. The group delay filter, on the other hand, can be efficiently realized via infinite

impulse response (IIR) filter [85]. Thus, the limited processing power of automotive radars favours the utilization of the group delay filter receiver. However, the group delay filter causes a quadratic phase shift on the dechirped signal and distorts the received code signal. Consequently, this distortion significantly degrades decoding performance when codes with a high number of phase changes per chirp (meaning substantial code bandwidth) are used as shown in Chapter 2. Such performance degradation limits the code length and, associated with it, signal isolation. To deal with this issue, the phase smoothing operation is proposed to obtain smoothed phase code (e.g. Gaussian Minimum Shift Keying), and then the phase lag compensation (PLC) is applied to the transmitted phase code to eliminate the undesired effect of the group delay filter as explained in Chapter 4. In this chapter, we utilize both slow-time and fast-time coding for the introduced phase lag compensated PC-FMCW waveforms to realize coherent MIMO radar.

5.3. MIMO AMBIGUITY FUNCTION OF PC-FMCW

In this section, we investigate the MIMO ambiguity function of the PC-FMCW waveform to evaluate its separation capability. For this purpose, we use the full-band matched filtering to process the PC-FMCW waveform with a single chirp pulse. Assume the MIMO system simultaneously transmits PC-FMCW with different codes as:

$$x_{\mathrm{T}_p}(t) = s_p(t)\exp\left(-j\left(2\pi f_c t + \pi k t^2\right)\right) \tag{5.3}$$

where $1 \leq p \leq P$ is the index of the transmitter, P is the number of transmitters, and $s_p(t)$ is the phase-coded signal for identification of different transmitters, which needs to be orthogonal with each other. Consider the MIMO system has L number of receiving antenna elements, and the index of the receiver is represented with $1 \leq l \leq L$. The received signal at l^{th} receiver will be the round trip delayed version of the transmitted signal at p^{th} transmitter. Accounting propagation and back-scattering effects by complex coefficient α_0, the received signals can be represented as:

$$x_{\mathrm{R}_l}(t,\theta) = \alpha_0\, a_{\mathrm{R}_l}(\theta) \sum_{p=1}^{P} a_{\mathrm{T}_p}(\theta)\, x_{\mathrm{T}_p}(t-\tau(t)) + n_l(t), \tag{5.4}$$

where $n_l(t)$ represents the noise signal at l^{th} receiver. The terms $a_{\mathrm{T}_p}(\theta)$ and $a_{\mathrm{R}_l}(\theta)$ are obtained from the steering vectors of the transmitter and receiver antennas (assuming uniform linear arrays), respectively and can be written as:

$$a_{\mathrm{T}_p}(\theta) = e^{j2\pi d_t (p-1)\frac{sin(\theta)}{\lambda}}, \tag{5.5}$$

and

$$a_{\mathrm{R}_l}(\theta) = e^{j2\pi d_r (l-1)\frac{sin(\theta)}{\lambda}}, \tag{5.6}$$

where d_t and d_r are the spacing between transmitters and receivers, respectively, and λ is the wavelength. After down-conversion to base-band, the matched filter convolves the received signal with the complex conjugate of the transmitted signal as:

$$x_{\mathrm{MF}_{l,p}}(t,\theta) = \int_{-\infty}^{\infty} x_{\mathrm{R}_l}(\zeta,\theta)\, x^*_{\mathrm{T}_p}(t-\zeta)\, d\zeta. \tag{5.7}$$

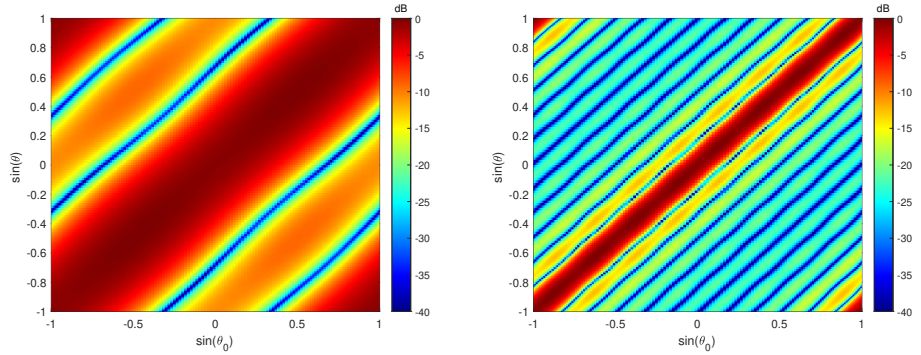

Figure 5.3: Hypothesis angle about the target position θ_0 versus the angle of the target θ for the PC-FMCW with the random code a) Transmit ambiguity function b) MIMO ambiguity function.

The information about the target can be extracted from the output of the matched filter.

The transmit ambiguity function in the absence of Doppler effect can be calculated from the matched filter output, i.e., a convolution of the transmitted signal with its delayed replica [79, 136]. Similarly, the MIMO ambiguity function is equal to the matched filter output and can be written as:

$$\left|\chi(\tau,\theta,\theta_0)\right| = \left|\sum_{l=1}^{L}\sum_{p=1}^{P}\int_{-\infty}^{\infty} x_{\mathrm{R}_l}(t,\theta)\, x^{*}_{\mathrm{T}_{p,l}}(t-\tau,\theta_0)\, dt\right|, \tag{5.8}$$

where θ is the actual angle of the target and θ_0 is the hypothesis angle about the target direction, respectively. Note the hypothesis signal also contains the angle information of the virtual array and can be represented as:

$$x_{\mathrm{T}_{p,l}}(t,\theta_0) = a_{\mathrm{R}_l}(\theta_0)\, a_{\mathrm{T}_p}(\theta_0)\, x_{\mathrm{T}_p}(t). \tag{5.9}$$

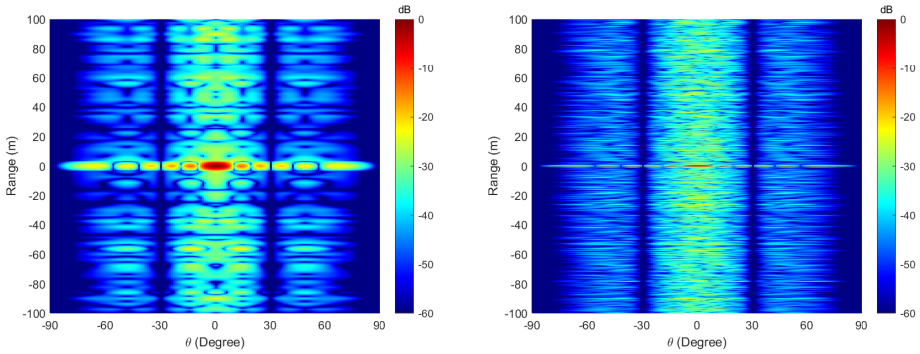

Figure 5.4: Range-angle profile of the MIMO ambiguity function ($\theta_0 = 0, f_d = 0$) with the random code a) PMCW b) PC-FMCW.

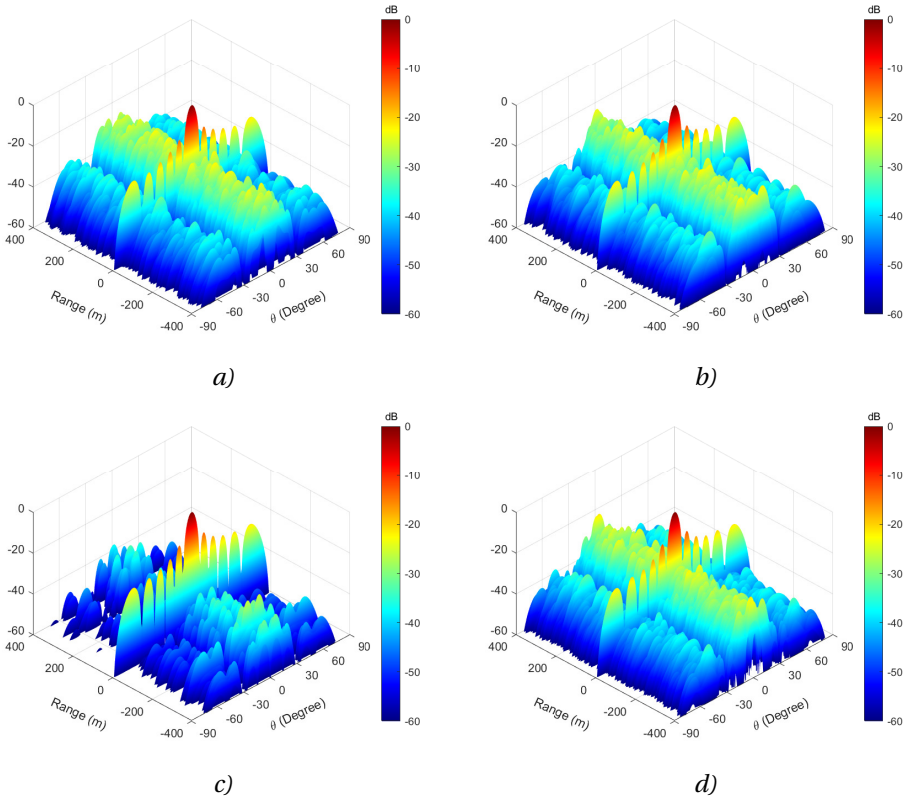

Figure 5.5: Range-angle profile of the MIMO ambiguity function ($\theta_0 = 0, f_d = 0$) for the PMCW with different codes a) Random (1024) b) Gold (1023) c) ZCZ (1024) d) Kasami (1023).

For the numerical simulations, we examine the MIMO ambiguity functions of the PC-FMCW radar obtained with different code families. Assume an automotive radar transmits PC-FMCW with a carrier frequency $f_c = 77$ GHz, chirp duration $T = 25.6$ μs and chirp bandwidth $B = 300$ MHz. We use the BPSK sequence as a phase-coded signal and choose $N_c = 1024$ number of chips per chirp. Thus, the bandwidth of the code signal is $B_c = N_c/T = 40$ MHz. We consider $P = 3$ transmitters and $L = 4$ receivers for the MIMO configuration, with $d_t = 2\lambda$ and $d_r = \lambda/2$, respectively. Consequently, the virtual array of the MIMO system has 12 elements with $\lambda/2$ spacing.

First, we simulate the transmit ambiguity and the MIMO ambiguity functions for PC-FMCW by using (5.8). Each phase-coded signal is selected as random codes, which are orthogonal to each other. The angular coverages of both ambiguity functions are shown in Figure 5.3 where the hypothesis angle about the target position θ_0 versus the actual target angle θ is computed for $\tau = 0$. Herein, the strong line along the diagonal axis indicates that beam-forming can be achieved without ambiguity. Then, we compare the MIMO ambiguity functions of PMCW and PC-FMCW for a zero Doppler frequency shift $f_d = 0$ and $\theta_0 = 0$ in Figure 5.4. For both waveforms, it is observed that the receiver

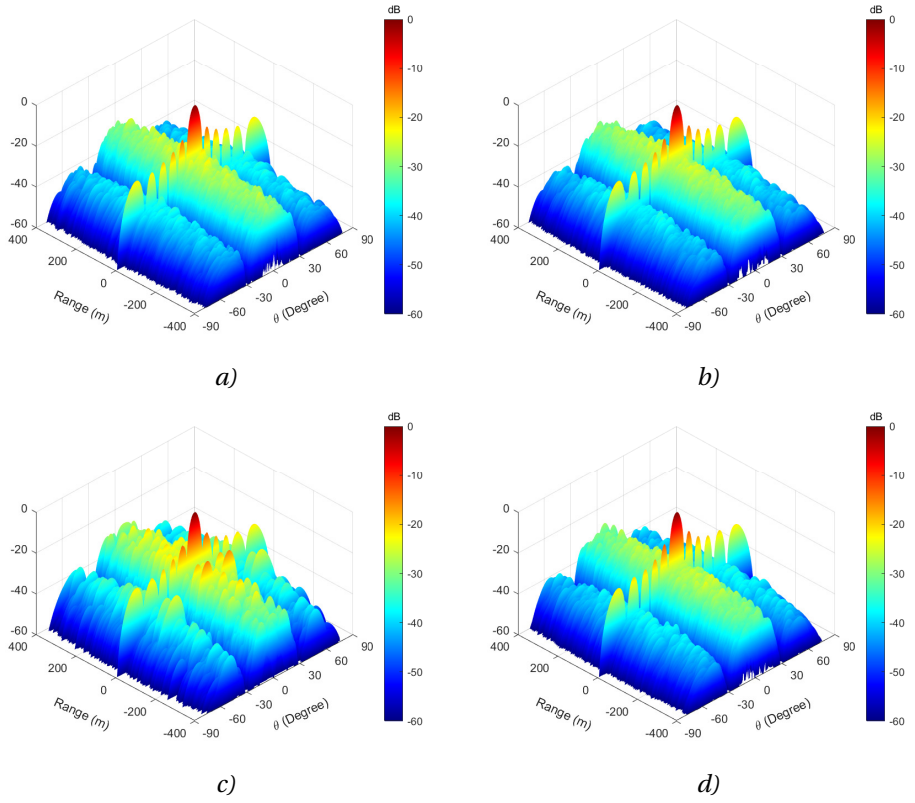

Figure 5.6: Range-angle profile of the MIMO ambiguity function ($\theta_0 = 0, f_d = 0$) for the PC-FMCW with different codes a) Random (1024) b) Gold (1023) c) ZCZ (1024) d) Kasami (1023).

can separate the simultaneously transmitted signals with the price of increased range sidelobes. However, PMCW has poor range resolution and needs to raise the bandwidth of the code, which increases the sampling demands on ADC, to achieve the same range resolution. Thus, the range resolution is improved substantially without increasing the receiver's analogue bandwidth by using PC-FMCW.

Next, the MIMO ambiguity functions of PMCW and PC-FMCW are simulated by using different code families for ($\theta_0 = 0, f_d = 0$). We choose four code families to compare with; Gold, Kasami, zero correlation zone (ZCZ), and random codes. The comparison of the range-angle profiles for both PMCW and PC-FMCW are illustrated in Figure 5.5 and Figure 5.6, respectively. For PMCW, the ZCZ code outperforms other codes and provides the best sensing performance. In the case of PC-FMCW, it is observed that the Gold, Kasami, and random codes provide similar range-angle performance, while the ZCZ code has much higher sidelobes. Herein, it should be noted that the sensing performance in the simultaneous MIMO transmission is mainly determined by the cross-correlation between waveforms, in comparison to the single transmitting case discussed in Chapter 2. Afterwards, we compare the range profiles of the MIMO ambiguity functions

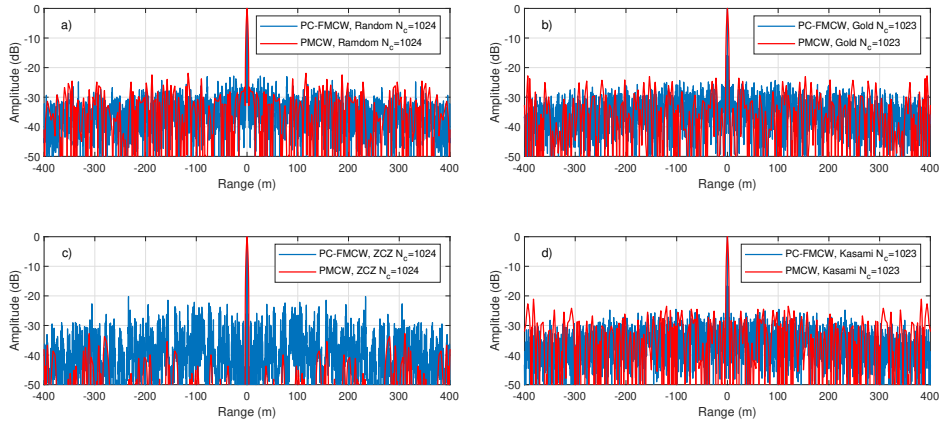

Figure 5.7: Range profile comparison of the MIMO ambiguity function ($\theta = 0, \theta_0 = 0, f_d = 0$) for the PMCW and PC-FMCW with different codes a) Random b) Gold c) ZCZ d) Kasami.

5

($\theta = 0, \theta_0 = 0, f_d = 0$) of both waveforms with different codes in Figure 5.7. We observe that the range profiles of PMCW and PC-FMCW are quite different as the code property is changed after modulating with the chirp signal. It can be seen that PC-FMCW provides a lower sidelobe level, especially in the far range as shown in the random, Gold and Kasami codes. However, PC-FMCW with the ZCZ code has notably higher sidelobe levels compared to PMCW. This is because the ZCZ code property that searches a zero correlation zone is destroyed by modulating with the chirp signal, and hence sidelobes are increased. Therefore, the code families optimized for PMCW might not be suitable for PC-FMCW, and proper code design for PC-FMCW is subject to be considered in future.

Finally, we investigate the influence of Doppler shift on the range-angle performance of both waveforms in Figure 5.8. For this purpose, the received signal is considered with

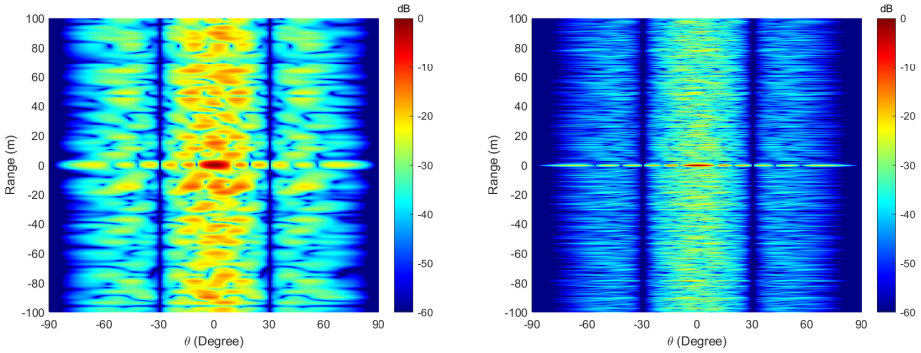

Figure 5.8: Range-angle profile of the MIMO ambiguity function ($\theta_0 = 0, f_d = 30$ kHz) with the random code a) PMCW b) PC-FMCW.

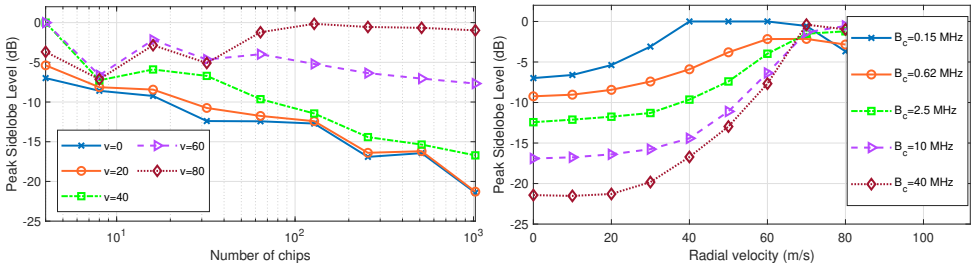

a) *b)*

Figure 5.9: MIMO ambiguity function of PMCW: a) PSL versus number of chips b) PSL versus radial velocity.

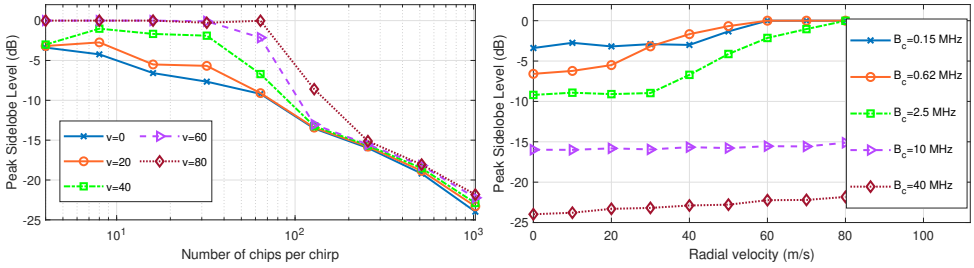

a) *b)*

Figure 5.10: MIMO ambiguity function of PC-FMCW: a) PSL versus number of chips per chirp b) PSL versus radial velocity.

a Doppler frequency shift $f_d = 30$ kHz (corresponds to the relative velocity $v \approx 60$ m/s). It is observed that the Doppler frequency shift raises the sidelobe levels and degrades the range-angle performance of PMCW. On the other hand, the range-angle profile of PC-FMCW is not affected significantly due to its good Doppler tolerance and provides sidelobe levels similar to zero Doppler shift. We can also observe this in the following simulations, where the peak sidelobe level (PSL) loss due to the Doppler frequency shift is investigated for PMCW and PC-FMCW in Figure 5.9 and Figure 5.10, respectively. It can be seen that the Doppler frequency shift is cruel for long code sequences and PSL of PMCW significantly decreases when the Doppler effect raises. However, the PC-FMCW waveform still provides similar PSL despite having a high Doppler frequency shift. These facts highlight the advantages of PC-FMCW over PMCW.

5.4. PROPOSED PC-FMCW MIMO RADAR

This section applies the introduced waveform and processing steps given in Chapter 4 to the MIMO system and provides the signal model for both fast-time and slow-time coded PC-FMCW. The block diagram of the proposed MIMO radar structure is illustrated in Figure 5.11.

Assume a MIMO radar simultaneously transmits the PC-FMCW waveforms, in which each chirp pulses use different phase lag compensated codes for both fast-time and

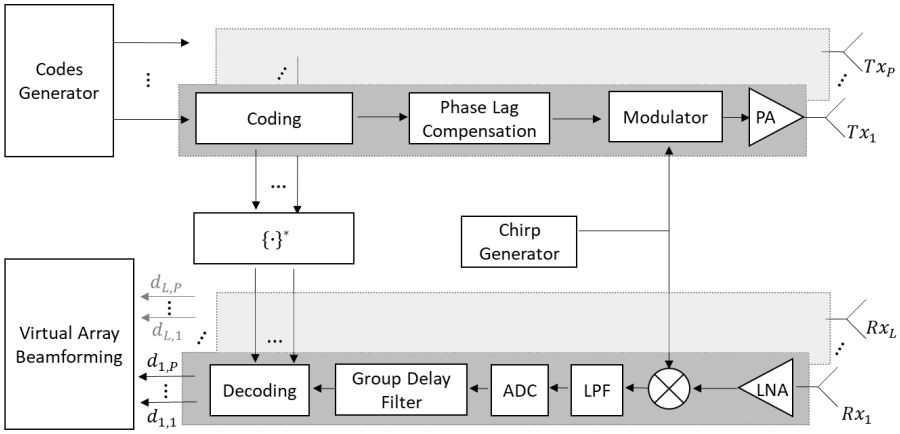

Figure 5.11: Block diagram of the PC-FMCW MIMO transceiver structure.

5

slow-time coding. The transmitted waveform for the p^{th} transmitter can be written as:

$$x_{\mathrm{T}_p}(t,m) = \hat{s}_{p,m}(t)e^{-j(2\pi f_c t+\pi k t^2)}, \tag{5.10}$$

where $1 \le p \le P$ is the index of the transmitter, $1 \le m \le N_p$ is the index of the chirp sequence, $t \in [0, T]$ is the fast-time term, T is the chirp duration, $k = B/T$ is the chirp slope, B is the chirp bandwidth, f_c is the carrier frequency, P is the number of transmitters, N_p is the number of chirp pulses, and $\hat{s}_{p,m}(t)$ is the phase-coded signal modified by a PLC filter. Here, transmitted codes need to be orthogonal with each other for the m^{th} chirp pulse and p^{th} transmitter. Consider the MIMO system has L number of receiving antenna elements, and the index of the receiver is represented with $1 \le l \le L$. The received signal at l^{th} receiver will be the round trip delayed version of the transmitted signal at p^{th} transmitter. The round trip delay $\tau(t,m)$ for a target with constant velocity can be written as:

$$\tau(t,m) = \frac{2\left(R_0 + v_0\left(t+mT\right)\right)}{c} = \tau_0 + \frac{2v_0}{c}\left(t+mT\right), \tag{5.11}$$

where R_0 is the range, v_0 is the velocity of the target. Then, the received signal reflected from a moving point-like target can be represented as:

$$x_{\mathrm{R}_l}(t,m) = \alpha_0\, a_{\mathrm{R}_l}(\theta) \sum_{p=1}^{P} a_{\mathrm{T}_p}(\theta)\, x_{\mathrm{T}_p}(t-\tau(t,m),m), \tag{5.12}$$

where α_0 is a complex amplitude proportional to the target back-scattering coefficient and propagation effects. Hereinafter, we substitute all the constant terms into α_0 without loss of generality. Moreover, we assume uniform linear arrays on transmitters and receivers are spaced with d_t and d_r. Subsequently, $a_{\mathrm{T}_p}(\theta)$ and $a_{\mathrm{R}_l}(\theta)$ are obtained from the steering vectors of the transmitter and receiver antennas, given in (5.5) and (5.6), respectively.

To get the beat signals, each received signal is mixed with the complex conjugate of the uncoded chirp signal as shown in (2.17). Then, the dechirped signals can be represented

as:

$$\begin{aligned} x_{\mathrm{M}_l}(t,m) &= x_{\mathrm{R}_l}(t,m)e^{j(2\pi f_c t+\pi k t^2)} \\ &= \alpha_0 a_{\mathrm{R}_l}(\theta)\sum_{p=1}^{P} a_{\mathrm{T}_p}(\theta)\hat{s}_{p,m}(t-\tau_0)e^{j(2\pi f_b t+2\pi f_d mT)}, \end{aligned} \tag{5.13}$$

Applying group delay filter eliminates the τ_0 term in code signals as explained in Chapter 4 and the resulting signal at l^{th} receiver becomes [94]:

$$x_{\mathrm{G}_l}(t,m) = \alpha_0 a_{\mathrm{R}_l}(\theta)\sum_{p=1}^{P} a_{\mathrm{T}_p}(\theta)s_{p,m}(t)e^{j(2\pi f_b t+2\pi f_d mT)}. \tag{5.14}$$

Subsequently, we can apply the decoding signal for each chirp pulse, which is the complex conjugate of the transmitted code. After applying decoding in each receiver channel, the decoding output signal at l^{th} receiver decoded with code signal at p^{th} transmit channel can be obtained as:

$$d_{l,p}(t,m) = x_{\mathrm{G}_l}(t,m)s^*_{p,m}(t). \tag{5.15}$$

After decoding, the code term is removed properly for the beat signals matched to the transmitted code. As a consequence, the beat signal matched to the transmitted signal is obtained similar to the dechirped signal of conventional FMCW radar while beat signals coming from other transmitted remain coded and suppressed. Moreover, this can be used to mitigate mutual interference between multiple radars. For orthogonal transmit channels, the virtual array with $Q = P \times L$ number of elements can be formed by stacking the decoding output signals and stored in vector as:

$$\boldsymbol{y}(t,m,q) = \begin{bmatrix} d_{1,1}(t,m) \\ \vdots \\ d_{L,1}(t,m) \\ \vdots \\ d_{1,P}(t,m) \\ \vdots \\ d_{L,P}(t,m) \end{bmatrix}. \tag{5.16}$$

where $1 \leq q \leq Q$ is the index of the virtual array. From (5.16), we can retrieve the range, Doppler and angle information of the target by performing a spectral analysis such as three-dimensional FFT.

5.5. PERFORMANCE ASSESSMENT

This section provides the performance assessment and limitations of the proposed PC-FMCW MIMO radar. For the numerical simulations, we consider an automotive radar operating with a carrier frequency $f_c = 77$ GHz has 3 transmit and 4 receive channels with antenna spacing $d_t = 2\lambda$ and $d_r = \lambda/2$ in the transmit and receiver subarrays, respectively. Subsequently, the virtual array of the MIMO system has 12 elements with $\lambda/2$ spacing. For

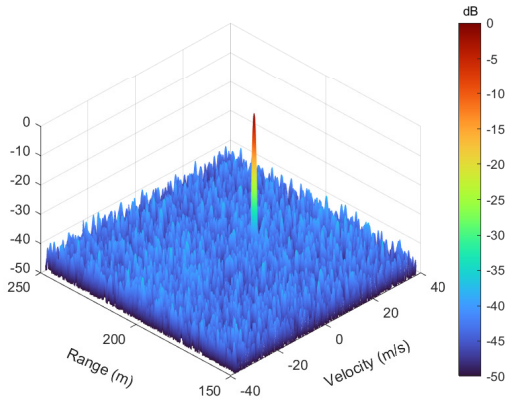

Figure 5.12: Range-Doppler profile for the proposed MIMO with $N_c = 1024$ and $N_p = 255$: $R = 200$ m, $v = 10$ m/s and $\theta = 20$ degree.

each transmit channel, we use a chirp signal with the chirp duration $T = 25.6$ μs and the chirp bandwidth $B = 300$ MHz is coded in both slow-time and fast-time with the phase-coded signal. The Gaussian Minimum Shift Keying (GMSK) is used to modulate phase-coded signal $s(t)$, and the 3-dB bandwidth of the Gaussian filter (smoother bandwidth) is set to two times the chip bandwidth [94]. Moreover, we utilize the random code sequences and perform phase lag compensation before transmission for each GMSK phase-coded signal. For the fast-time coding, we use $N_c = 1024$ number of chips per chirp. The duration of the chip T_c is controlled with the number of chips per chirp as $T_c = T/N_c$, and thus the code bandwidth becomes $B_c = 40$ MHz for $N_c = 1024$. Moreover, $N_p = 255$ number of chirp pulses are transmitted for Doppler processing and slow-time coding, where each chirp uses different phase lag compensated code signal $\hat{s}(t)$.

On the receiver side, dechirped signals (5.13) are low-pass filtered with the cut-off frequency $f_{\text{cut}} = \pm 40$ MHz and sampled with $f_s = 80$ MHz. As a consequence, we have $N = 2048$ range cells (fast-time samples) for this setting. The group delay filter is applied to the sampled signal to align the beat signals of different targets. Before decoding, the same LPF is applied to the reference phase-coded signal that is used for decoding to prevent a signal mismatch. To focus on the sensing performance, we assume a noise-free scenario with a single target at the range $R_0 = 200$ m, with a radial velocity $v_0 = 10$ m/s and a target angle $\theta = 20$ degree in the numerical simulations. As explained in Chapter 2 and Chapter 4, the investigated receivers perform different techniques for range processing, namely the filter bank, the group delay filter without PLC and the group delay filter with PLC. For each receiver technique, we apply 80 dB Chebyshev window in the range domain before processing. The Doppler and angle processing parts are the same for all processing approaches, and we apply 60 dB Chebyshev window in both Doppler and angle domains before taking their FFT, respectively. In addition, we normalize all the figures by the maximum value.

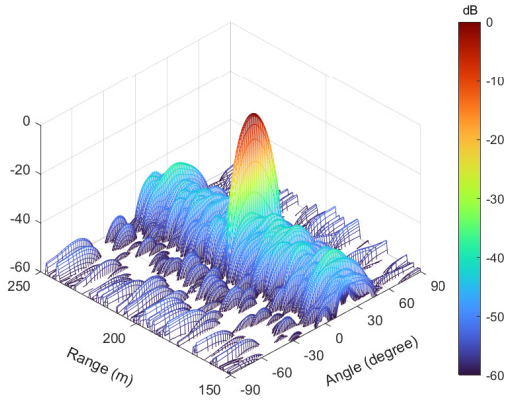

Figure 5.13: Range-Angle profile for the proposed MIMO with $N_c = 1024$ and $N_p = 255$: $R = 200$ m, $v = 10$ m/s and $\theta = 20$ degree.

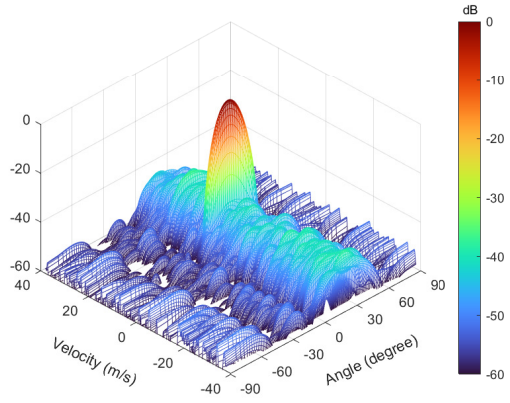

Figure 5.14: Velocity-Angle profile for the proposed MIMO with $N_c = 1024$ and $N_p = 255$: $R = 200$ m, $v = 10$ m/s and $\theta = 20$ degree.

5.5.1. SENSING PERFORMANCE

The sensing performance of the proposed MIMO radar is assessed by using the investigated processing method given in Section 5.4 and compared with the state-of-the-art processing techniques: filter bank and group delay filter without PLC.

Firstly, we investigate the sensing performance of the proposed MIMO in range, Doppler and angle domains. In Figure 5.12, we simulate the range-Doppler profile of the proposed MIMO radar. It can be seen that the target response follows the main lobe in the vicinity of the target. Outside of this region, the signal returns from the simultaneously transmitted channels spread over range and Doppler cells as a noise-like pattern due to both fast-time and slow-time coding. The mutual orthogonality between

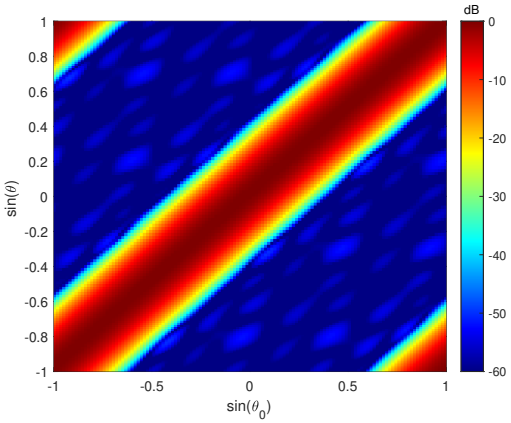

Figure 5.15: Target angle vs beamforming angle for the proposed MIMO with $N_c = 1024$ and $N_p = 255$: $R = 200$ m, $v = 10$ m/s.

simultaneously transmitted channels is determined by the $10\log_{10}(N_c)$ in fast-time and $10\log_{10}(N_p)$ in slow-time coding. Therefore, the theoretical limit of this suppression combined with the suppression in both slow-time and fast-time is 54 dB on average for perfectly orthogonal code. However, random phase coding causes a (pseudo) noise-like behaviour, and the sidelobe level is altering over the range-Doppler with a peak sidelobe level (PSL) is around ~ -40 dB. The PSL of a signal is determined by the maximum amplitude outside of the main lobe in a given domain. We demonstrate the range-angle profile in Figure 5.13 and the velocity-angle profile in Figure 5.14. Both figures show that the target at 20 degree has around ~ -56 dB PSL in the angle domain while having noise-like sidelobes in the range and Doppler domains. To highlight the angular coverage performance of the proposed MIMO radar, we simulate the received target angle versus the beamforming angle (Figure 5.15). Herein, the strong line along the diagonal axis indicates that beamforming can be achieved without ambiguity between simultaneously transmitted channels.

Afterwards, we evaluated the sidelobe level of the proposed MIMO radar as a function of chip numbers for fast-time coding and compared it with other approaches. Since

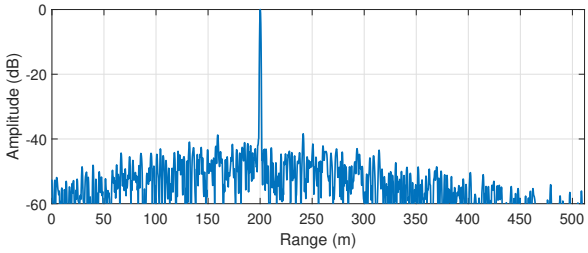

Figure 5.16: Range profile of the proposed MIMO for $N_c = 1024$, $N_p = 255$, $R = 200$ m, $v = 10$ m/s and $\theta = 20$ degree.

the sidelobes in the range and Doppler have a (pseudo) noise-like pattern, we consider integrated sidelobe level (ISL) as a performance metric. Moreover, the sidelobes in the range spread as a Gaussian shape due to GMSK coding (Fig 5.16). Therefore, we only take into account ISL in the interval noted as $[z_1, z_4]$. Then ISL in a particular domain can be defined as [115]:

$$\mathrm{ISL} = 10\log_{10}\left(\frac{\int_{z_1}^{z_2}|X(z)|^2\,dz + \int_{z_3}^{z_4}|X(z)|^2\,dz}{\int_{z_2}^{z_3}|X(z)|^2\,dz}\right), \tag{5.17}$$

where the interval $[z_2, z_3]$ defines the main lobe of a signal denoted as $X(z)$. In the numerical simulations, we consider the range ISL in the interval [150, 250] m and the Doppler ISL in the interval [5, 15] m/s, correspond to the code bandwidth $\pm 0.1 B_c$ and the unambiguous velocity $\pm 0.125 v_{un}$, respectively, for the selected system parameters.

The range ISL and Doppler ISL of the proposed MIMO radar are compared and illustrated as a function of fast-time code length in Figure 5.17 and Figure 5.18, respectively. Similarly, we demonstrate the angle PSL as a function of fast-time code length in Figure 5.19. It can be seen in Figure 5.17 that all investigated approaches have around ~ -80 dB range ISL for $N_c = 1$ case. When increasing the number of chips for fast-time coding, we observe that the proposed MIMO and the group delay filter without PLC provide similar performance up to $N_c = 128$, which is equivalent to $B_c = 5$ MHz for the chosen system parameters. Thereafter, the group delay filter without PLC suffers from the dispersion effect, and its sensing performance is downgraded substantially. On the other hand, the range ISL of the filter bank and proposed MIMO start to decrease and improve for the long code scenarios. Moreover, the proposed MIMO is computationally more efficient ($\mathcal{O}(N\log_2(N))$) than the filter bank approach ($\mathcal{O}(N^2)$) and provides the best sensing performance. Note that $N_p = 255$ chirps are still used for the slow-time coding in all three cases. Consequently, the Doppler ISL of three investigated approaches are around ~ -23 dB for $N_c = 1$. To investigate the trade-offs of slow-time coding, we use fixed chips for fast-time coding $N_c = 1024$ and illustrate the sidelobe levels of the proposed MIMO as a function of the number of coded chirp pulses in Figure 5.20. Here, the joint utilization of slow-time coding helps to reduce sidelobe levels in range and angle with the price of increased sidelobe levels in Doppler. In particular, the proposed MIMO can achieve -49 dB range ISL, -45 dB Doppler ISL and -54 dB angle PSL by using $N_c = 1024$ chips for fast-time coding and $N_p = 255$ chirp pulses for slow-time coding. It is important to note that all three investigated approach uses dechirping based receivers and lowers ADC sampling requirements compared to full-band matched filtering. As mentioned earlier, the suppression level improves as the number of chips for the fast-time coding raises. However, this also increases the sampling requirements for ADC as the code bandwidth B_c raises. Since we use ADC with sampling frequency 80 MHz, we increase the number of chips for fast-time up to $N_c = 1024$, which results in $B_c = 40$ MHz. To the best of our knowledge, this ADC sampling is the limit of the current generation of automotive radars. By increasing the ADC sampling rate, higher code bandwidth, i.e. more chips for fast-time coding, can be used to improve suppression.

5.5.2. DOPPLER TOLERANCE

Next, we investigate the Doppler tolerance of the proposed MIMO radar. As explained in the introduction, the PMCW waveform suffers from Doppler frequency shift and often re-

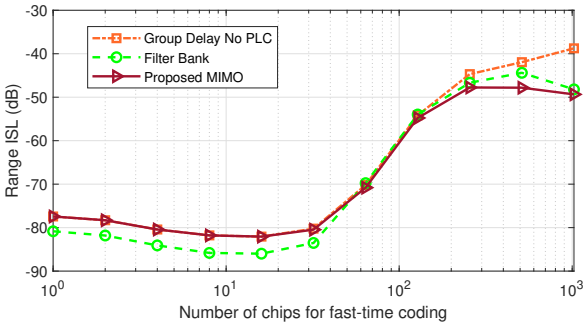

Figure 5.17: Range ISL versus number of chips for fast-time coding: $N_p = 255$, $R = 200$ m, $v = 10$ m/s and $\theta = 20$ degree.

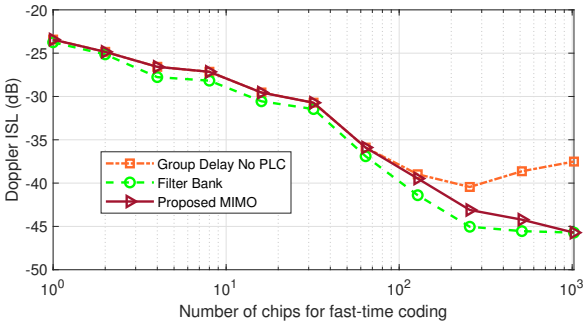

Figure 5.18: Doppler ISL versus number of chips for fast-time coding: $N_p = 255$, $R = 200$ m, $v = 10$ m/s and $\theta = 20$ degree.

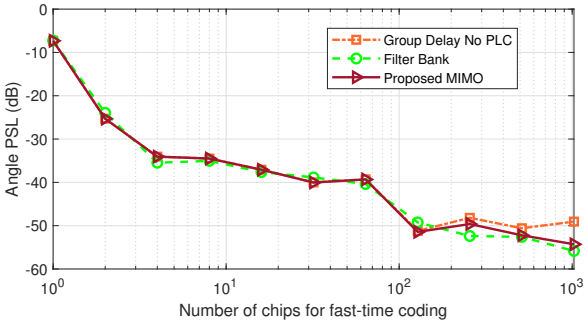

Figure 5.19: Angle PSL versus number of chips for fast-time coding: $N_p = 255$, $R = 200$ m, $v = 10$ m/s and $\theta = 20$ degree.

quires special techniques to compensate its poor Doppler tolerance [84]. However, using the chirp signal as a carrier shears the resulting ambiguity function of the phase-coded signal, i.e. the resulting ambiguity function's Doppler axis is changed to a linear combination of the Doppler frequency shift and delay [113]. Thus, the PC-FMCW waveforms have

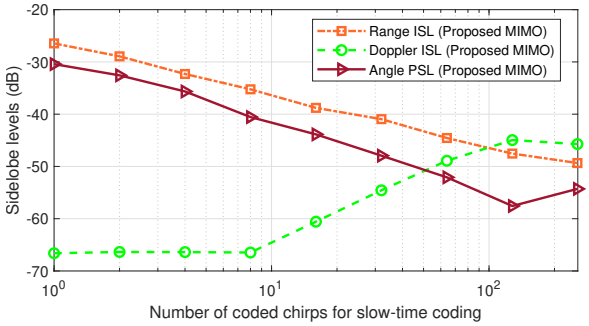

Figure 5.20: Sidelobe levels of the proposed MIMO versus number of coded chirps for slow-time coding: $N_c = 1024$, $R = 200$ m, $v = 10$ m/s and $\theta = 20$ degree.

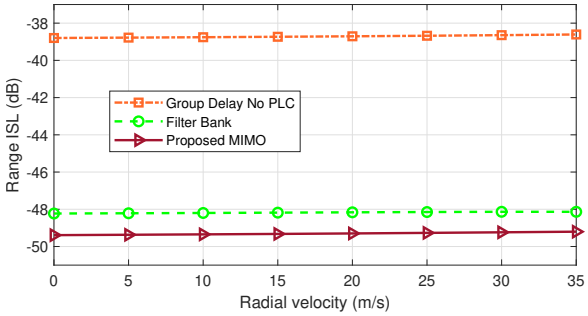

Figure 5.21: Range ISL versus radial velocity: $N_c = 1024$, $N_p = 255$, $R = 200$ m and $\theta = 20$ degree.

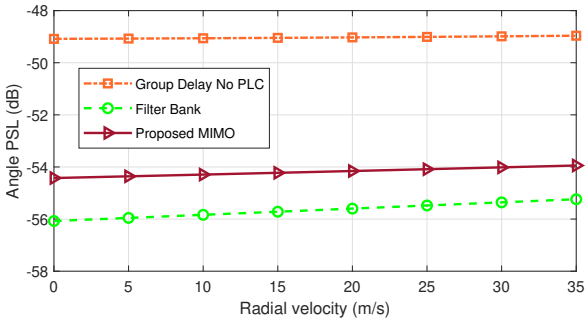

Figure 5.22: Angle PSL versus velocity: $N_c = 1024$, $N_p = 255$, $R = 200$ m and $\theta = 20$ degree.

good Doppler tolerance similar to the FMCW waveforms [127]. In order to demonstrate the Doppler tolerance of the proposed MIMO radar, we simulate the range ISL and angle PSL as a function of radial velocity in Figure 5.21 and Figure 5.22, respectively. In these simulations, we consider the scenario with $N_c = 1024$ number of chips for the fast-time coding and $N_p = 255$ pulses for the slow-time coding. It can be seen that the range ISL of the proposed MIMO radar is not affected by the Doppler shift, while the angle PSL

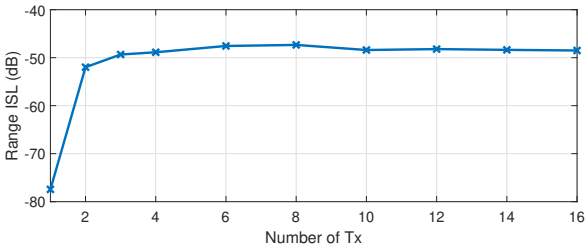

Figure 5.23: Range ISL for the proposed MIMO versus the number of transmitters: $N_c = 1024$, $N_p = 255$, $R = 200$ m, $v = 10$ m/s and $\theta = 20$ degree.

degraded only half dB from $v = 0$ to $v = 35$ m/s. Consequently, the PC-FMCW waveforms processed with all three investigated approaches provide good Doppler tolerance.

5.5.3. LIMITATIONS

In this subsection, we analyze the various limitation criteria for the proposed MIMO radar.

NUMBER OF TRANSMITTERS

Firstly, we investigate the range ISL as a function of the number of transmitters as shown in Figure 5.23, where we consider $N_c = 1024$ chips for the fast-time coding and $N_p = 255$ pulses for the slow-time coding. It can be observed that only one transmitter has around ~ -80 dB range ISL. This is expected because there is no other waveform to interfere with the transmitted signal, and the receiver can provide a high dynamic range after decoding with the reference code. However, the reflected signals coming from the other transmitters act as the interferer in the simultaneously transmitted MIMO system and are spread over the range-Doppler profile due to coding. As a result, the range ISL rapidly goes to -50 dB in the MIMO case. Thereafter, we observe that adding transmitters does not significantly increase the range ISL for the chosen system parameters. Thus, a higher number of transmitters can be used in other applications based on the system requirements, such as the unambiguous velocity.

MAXIMAL RANGE

The maximal range is determined as $R_{\max} = \frac{c f_{b_{\max}}}{2k}$ and the maximum beat signal is defined by the ADC sampling as $f_{b_{\max}} = f_s/2$. We investigate the range profile as a function of the maximal range in Figure 5.24, where we increase the target range for each of the six profiles plotted in the figure. Herein, we use $f_s = 80$ MHz and $B_c = 40$ MHz (for $N_c = 1024$) so that $B_c/f_s = 1/2$. Similarly, we demonstrate the velocity and angle profiles as a function of the maximal range in Figure 5.25 and Figure 5.26, respectively. It can be observed that the sidelobe levels are raised in the range, velocity, and angle profiles as the range of the target approaches the maximal range. This is due to the fact that the corresponding coded beat signal approaches the cut-off frequency of LPF (determined by the ADC sampling frequency) as the target range goes close to the maximal range, and hence some part of the coded beat signal spectrum is rejected by the low pass filter of the receiver before decoding. Such filtering of the spectrum leads to imperfect decoding and downgrades

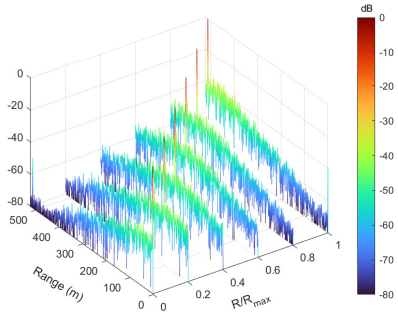

Figure 5.24: Range profile for the proposed MIMO as a function of the maximal range: $N_c = 1024$, $N_p = 255$, $v = 10$ m/s and $\theta = 20$ degree.

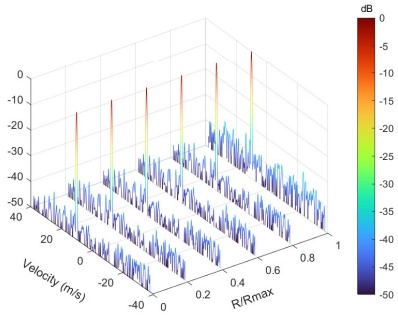

Figure 5.25: Doppler profile for the proposed MIMO as a function of the maximal range: $N_c = 1024$, $N_p = 255$, $v = 10$ m/s and $\theta = 20$ degree.

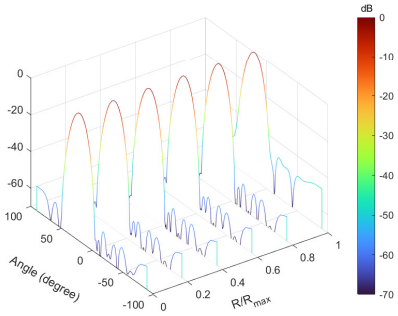

Figure 5.26: Angle profile for the proposed MIMO as a function of the maximal range: $N_c = 1024$, $N_p = 255$, $v = 10$ m/s and $\theta = 20$ degree.

the sensing performance. Therefore, the ADC sampling rate and its comparison to code bandwidth B_c / f_s have an impact on the sensing performance and should be considered

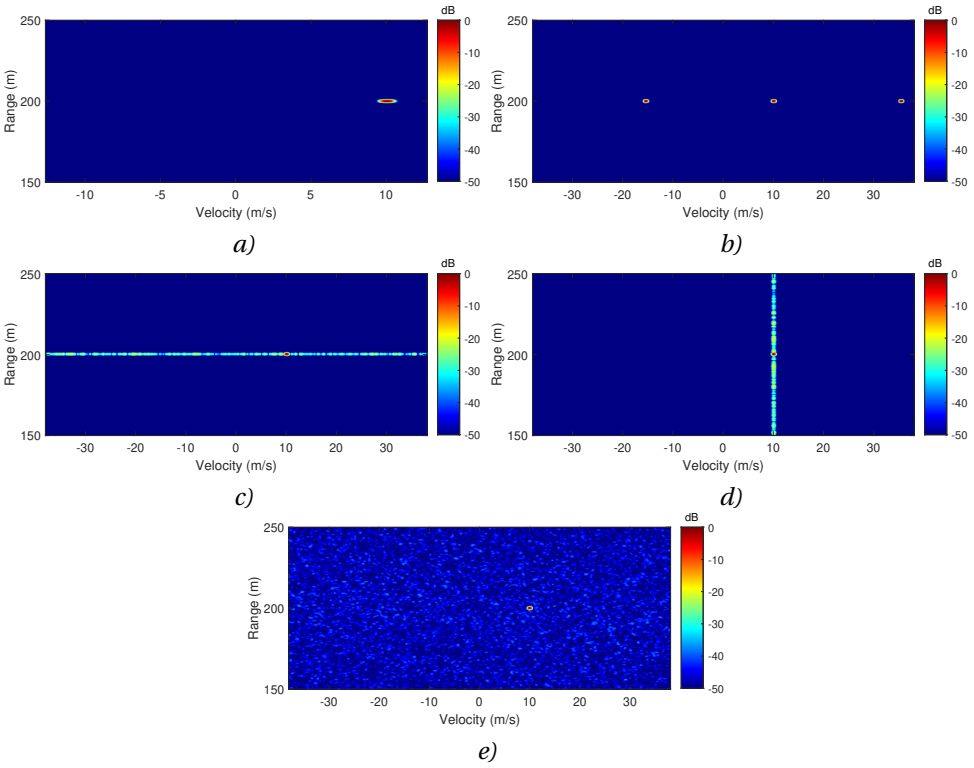

Figure 5.27: Comparison of the range-Doppler profiles for different MIMO schemes: a) TDMA FMCW b) DDMA FMCW c) ST-CDMA FMCW d) FT-CDMA PC-FMCW e) Proposed MIMO ($N_c = 1024$, $N_p = 255$, $R = 200$ m, $v = 10$ m/s and $\theta = 20$ degree).

in the system design. However, the range sidelobe level in the case of MIMO is mainly determined by cross-correlation between the transmitted signals, and thus has a minor dependency on the range, as compared to operation with a single transmitter case shown in Chapter 4.

5.5.4. COMPARISON WITH OTHER MIMO SCHEMES

In this subsection, we compare the sensing performance of the proposed MIMO radar with commonly used state-of-the-art MIMO techniques. For this purpose, we demonstrate and compare the range-Doppler profiles of different MIMO schemes with the proposed MIMO radar in Figure 5.27, where we used $N_p = 1024$ number of chips for fast-time coding and $N_p = 255$ number of chirps for slow-time coding. Note that the maximum unambiguous velocity $v_{\text{un}} = \lambda/4T_{\text{PRI}} = 38$ m/s for a chosen system parameters. It can be seen that the maximum unambiguous velocity is degraded by a factor of $P = 3$ and becomes $v_{\text{un}} = 12.6$ m/s with the TDMA transmission scheme due to an increase in the time duration between chirps transmitted by the same antenna (Figure 5.27 a). Similarly, the same target appears at other Doppler spectrum associated with different transmitters, and the maximum

unambiguous velocity is degraded by a factor of $P = 3$ with the DDMA transmission scheme as shown in Figure 5.27 b. Hence, this disadvantage restrains increasing the number of transmitters and improving the angular resolution with the TDMA and DDMA transmission schemes. The slow-time coding with FMCW and the fast-time coding with PC-FMCW overcome this degradation problem in the maximum unambiguous velocity and provide $v_{\text{un}} = 38$ m/s. However, the slow-time coding with FMCW suffers from high sidelobe levels in the Doppler domain, while the fast-time coding with PC-FMCW suffers from high sidelobe levels in the range domain (Figure 5.27 c-d). On the other hand, we observe that the proposed MIMO radar structure addresses the aforementioned limitations and achieves sidelobe levels below 40 dB in the range-Doppler profile without degrading the maximum unambiguous velocity or range resolution (Figure 5.27 e). Thus, the proposed MIMO radar structure can be utilized to achieve high angular resolution and good sensing performance.

5.6. EXPERIMENTS

This section demonstrates the experimental verification of the proposed MIMO structure. Since the experimental validation of the PC-FMCW waveforms is not possible with currently available automotive radars, we use the ASTAP radar system to demonstrate the proof of concept regarding the cross-isolation between simultaneously transmitted PC-FMCW waveforms and the beamforming on transmit. The ASTAP radar system consists of arbitrary waveform generator (AWG) Keysight M82190A, oscilloscope (Agilent Tech. DSO-X 91604A), up-down converters (RF amplifiers and mixers) and series-fed antenna patch array. This radar system architecture can support multiple input single output (MISO) configuration with multiple transmit channels and a single receiver channel. It

Table 5.1: Experiment System Parameters

Chirp bandwidth	B	200 MHz
Chirp duration	T	102.4 μs
Intermediate frequency	f_{IF}	300 MHz
Local oscillator	f_{LO}	9.7 GHz
Reference clock	f_{clk}	10 MHz
Carrier frequency	f_c	9.4 GHz
Wavelength	λ	0.032 m
ADC sampling frequency	f_{ADC}	40 MHz
Number of chips	N_c	1024
Chip duration	T_c	0.1μs
Chip bandwidth	B_c	10 MHz
Number of pulse	N_p	512
Number of receivers	N_{Rx}	1
Number of transmitters	N_{Tx}	4
Spacing between transmit elements	d_t	1.25λ

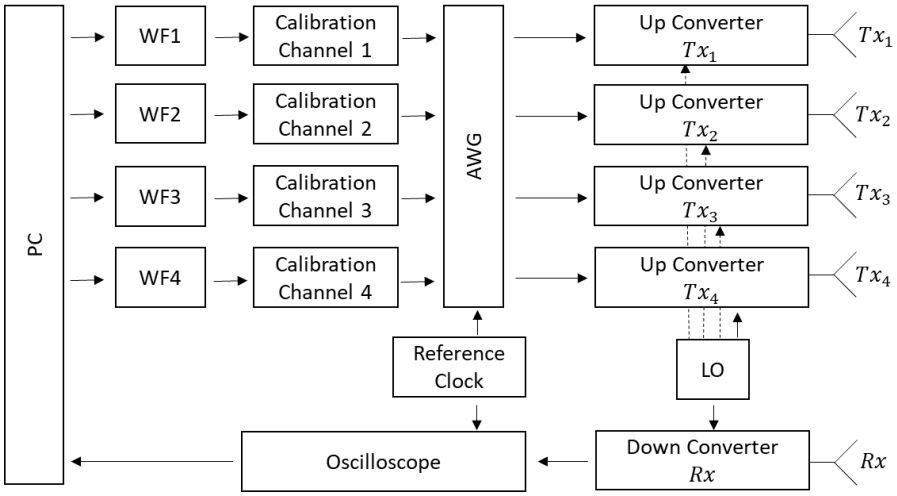

Figure 5.28: Block diagram of the radar system used in the measurements.

5

should be noted that there is no principal difference in operation between MIMO and MISO regarding the beamforming on transmit [137]. In this experiment, we choose the system parameters as given in Table 5.1 and use 4 transmit channels to demonstrate the proof of concept. We utilize the GMSK phase coding with $N_c = 1024$ random code sequences for fast-time coding, and each chirp pulse uses a different random phase-code signal for slow-time coding. Then, we perform phase lag compensation for each phase-coded signal and use 512 chirp pulses. The block diagram of the radar system used in the measurements is shown in Figure 5.28. Herein, the radio frequency and microwave subsystems inside the up and down converters produce different distortions for each

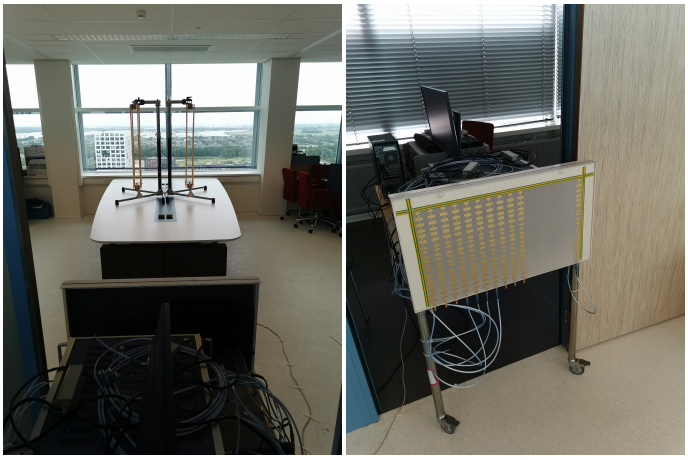

Figure 5.29: Illustration of the experimental setup and antennas.

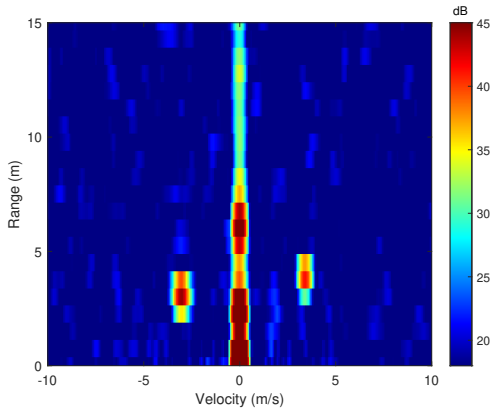

Figure 5.30: Experiment result: Range-Doppler profile for two moving pendulums.

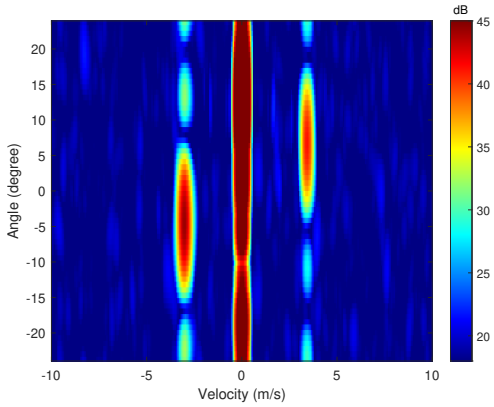

Figure 5.31: Experiment result: Angle-Velocity profile for two moving pendulums.

transmit channel. Without any calibration, such distortion downgrades the sensing performance. Thus, the frequency response of the system transfer function is measured for each channel with test measurement. Then, the inverse of corresponding transfer functions is applied to the spectrum of the waveform in each channel to compensate the system effect and do the calibration method as discussed in [138]. After calibration, the AWG produce the resulting PC-FMCW waveforms at an intermediate frequency (IF). Then, the analogue IF signals in each channel are up-converted to the radio frequency (RF) using a common local oscillator (LO). Subsequently, the resulting waveforms in each channel are simultaneously transmitted via multiple series-fed patch antenna array for coherent MISO transmission. On the receiver side, the reflected signals are captured by the single receive antenna and down-converted to IF. The received IF signal is recorded by the oscilloscope, which is synchronized with AWG using a reference clock. The recorded digital data is then processed by the introduced steps given in Section 5.4.

For the measurements, the resulting waveforms in each channel are simultaneously

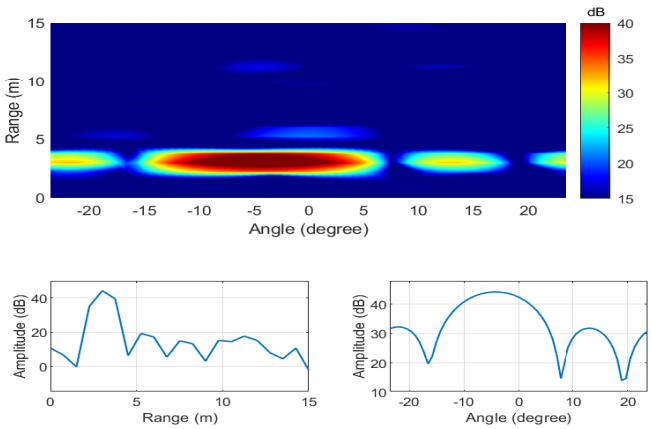

Figure 5.32: Experiment result: Range-Angle profile for the first pendulum.

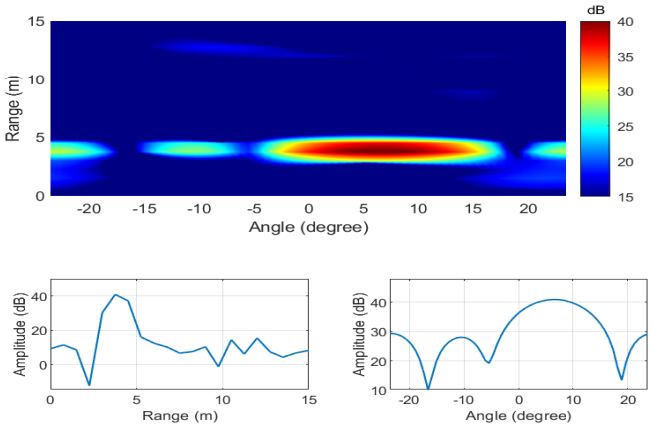

Figure 5.33: Experiment result: Range-Angle profile for the second pendulum.

transmitted to detect two moving targets (triangular reflectors are attached to pendulums) as illustrated in Figure 5.29. Herein, both pendulums are located 3.15 m away from the antenna, but one is on the left, and the other is on the right compared to the antenna array boresight. During experiments, we collect the data when one pendulum moves towards the radar and the other moves away from the radar. To process the collected data, we apply the group delay filter and decoding with the reference transmitted codes for each channel as explained in Section 5.4. Moreover, we apply Hamming windowing in range and Doppler to highlight sensing performance. Since the angular resolution is limited due to the available MISO configuration, we perform rectangular windowing in the angle domain. In addition, we estimate the noise level from the target-free Doppler cells and use it to normalize the processed signal power.

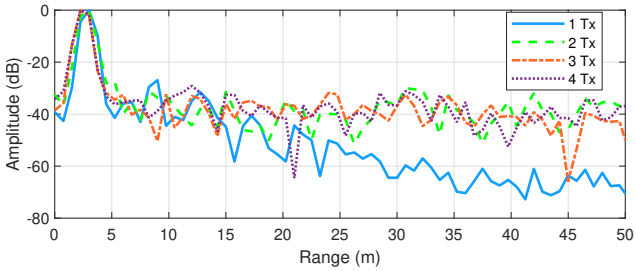

Figure 5.34: Experiment result: Range profiles by different numbers of transmitters.

After processing the received data and taking three-dimensional FFT over range, Doppler and angle domains, the incoherent summation over the angle domain is performed on the processed data to obtain range-Doppler profile as shown in Figure 5.30. We observe that the two moving targets appear along with clutter in the experimental environment. The peak location of the first moving target is obtained at $R_1 = 3$ m with radial velocity $v_1 = -3.04$ m/s, and the peak location of the second moving target is obtained at $R_2 = 3.34$ m with radial velocity $v_2 = 3.75$ m/s. Likewise, the velocities of two moving targets can be seen in Figure 5.31, where the corresponding angle-velocity map of the range cell having the maximum power is illustrated. Note that the fast-time and slow-time coding spread the power of simultaneously transmitted waveforms over the range-Doppler profile, and thus the sidelobes act like pseudo-random noise as explained in Section 5.5. Then, we take the $v_1 = -3.04$ m/s cut from the three-dimensional processed data and demonstrate the range-angle profile of the first moving target in Figure 5.32. It can be seen that the target is obtained at $\theta_1 = -4$ degree with the ~ 44 dB power. Similarly, we take the $v_2 = 3.75$ m/s cut from the three-dimensional processed data and show the range-angle profile of the second moving target in Figure 5.33. We observe that the second target is slightly far away from the radar and obtained at $\theta_2 = 6.19$ degree with the ~ 41 dB power. Consequently, the experimental results verify that the proposed approach has the ability to distinguish the simultaneously transmitted signals reflected from the moving targets at different angles.

Lastly, we investigate the sensing performance by different numbers of transmit channels. We consider only one moving target for all cases. Each scenario corresponds to different measurements, and thus range varies slightly. The normalized responses of the target corresponding to different numbers of transmitters are shown in Figure 5.34. One can observe that the sidelobe levels in the range profiles are similar for all multiple transmitter scenarios and remain stable with increasing transmit channels.

5.7. CONCLUSIONS

This chapter investigates the PC-FMCW waveforms in application to coherent MIMO radar. We overview the existing MIMO transmitting schemes and compare their advantages and disadvantages. It is demonstrated that the TDMA and DDMA transmission schemes have the disadvantage of losing maximum unambiguous velocity proportional to the number of transmitters, and hence improving the angular resolution is limited. The

ST-CDMA and FT-CDMA transmitting schemes can be utilized to deal with the maximum unambiguous velocity degradation problem; however, they suffer from high sidelobe levels in the Doppler or range domain, respectively.

Afterwards, the separation capabilities of the PC-FMCW waveform are studied, and the MIMO ambiguity functions of different code families with application to PC-FMCW are investigated. The range-angle profiles of the MIMO ambiguity functions are demonstrated for the random, Gold, ZCZ, and Kasami codes. As already mentioned in the single transmitter case, the correlation property of the code alters with the frequency modulation, and the range profile of PC-FMCW can be substantially different from the code property. Particularly, it is demonstrated that the ZCZ code, which is optimized to find the zero correlation zone, is not suitable to use with PC-FMCW. Moreover, the loss of mutual orthogonality due to the Doppler frequency shift is investigated for PMCW and PC-FMCW. It is observed that the orthogonality between codes heavily suffers from the Doppler frequency shift in the PMCW MIMO radar, and the sidelobe level raises substantially due to an increase in the target velocity. On the other hand, the PC-FMCW waveforms demonstrate good Doppler tolerance and provide sidelobe levels similar to zero Doppler shift. These results highlight the advantages of PC-FMCW over PMCW.

Finally, a novel PC-FMCW MIMO radar structure, based on dechirping and decoding receiving strategy to keep the low intermediate signal bandwidth, has been proposed to address current limitations in the state-of-the-art solutions. Phase lag compensation of the transmitted waveforms is used to improve decoding performance (avoid the quadratic phase shift after group delay filter), and phase codings in both fast-time and slow-time are jointly utilized to reduce the sidelobe levels. The performance assessment of phase lag compensated PC-FMCW waveforms for MIMO applications and the practical limitations on the system design of the introduced MIMO structure are analyzed numerically and verified experimentally for the first time. Both the numerical simulations and experimental results verify that the proposed MIMO structure can combine the benefits of FMCW waveforms, such as high range resolution, unambiguous velocity, good Doppler tolerance, low ADC sampling requirement and computational efficiency, with the capability of achieving low sidelobe levels in the range-Doppler-azimuth domains for simultaneous transmission. Consequently, the introduced system can be effectively utilized by automotive radar sensors to enhance the sensing performance of coherent MIMO transmission.

6

PC-FMCW: Interference Resilience and Communication Capabilities

Mutual interference between different radar waveforms used in automotive radar applications is investigated. The existing interference analysis is extended to a generalised radar-to-radar interference equation that covers most of the common interference scenarios for automotive radar systems. The outcome of the generalised equation is demonstrated for different types of waveforms, and the proposed equation is verified experimentally by using real-time automotive radars. Afterwards, the interference resilience and communication capabilities of the developed PC-FMCW radar are studied. The robustness of the PC-FMCW radar against different types of FMCW interference is investigated, and the improvement in the sensing performance is compared with the FMCW radar. Moreover, the communication performance of the PC-FMCW radars with the phase lag compensated group delay filter and filter bank receivers are compared. It is shown that the former receiver suffers from bit error rate degradation as the communication signal bandwidth increases.

Parts of this chapter have been published in:

U. Kumbul, F. Uysal, C. S. Vaucher, and A. Yarovoy, "Automotive radar interference study for different radar waveform types", in *IET Radar, Sonar & Navigation*, vol. 16, no. 3, pp. 564-577, 2022.

U. Kumbul, Y. Chen, N. Petrov, C. S. Vaucher, and A. Yarovoy, "Impacts of Mutual Interference Analysis in FMCW Automotive Radar," in *2023 17th European Conference on Antennas and Propagation (EuCAP)*, accepted.

U. Kumbul, N. Petrov, C. S. Vaucher, and A. Yarovoy, "Performance Analysis of Phase-Coded FMCW for Joint Sensing and Communication," in *2023 24th International Radar Symposium (IRS)*, submitted.

6.1. INTRODUCTION

Multiple radars operating simultaneously within the same frequency bandwidth cause mutual interference [6–8]. Thus, the increasing number of radars on the roads raises safety concerns regarding mutual interference in automotive systems [9]. In general, there are three types of interference. The first one is the interference caused by a strong return signal reflected by the platform (the radome or the bumper), or the coupling (spill-over) effect between transmitter and receiver. The second one is the interference caused by the other radars on the same vehicle, and within the same transceiver such as the MIMO system. Finally, the interference caused by other radars in the vicinity [5]. Interference of any kind downgrades the detection capability and functionality of a system that is being interfered with, known as the “victim radar" [17–19]. Consequently, various studies have been conducted on mitigating interference, using approaches with different processing costs and hardware complexity, as mentioned in Chapter 1. However, the structure of the interference varies according to the radar waveform type and its spectral characteristics [13–16]. To develop proper interference estimation or machine learning method, the relationship between the mutual interference signal parameters and their effect on the radar system performance needs to be understood. Therefore, it is important to analyse different interference scenarios for various automotive radar waveform types.

As explained earlier, the PC-FMCW waveforms have been investigated to enhance the mutual orthogonality of the waveforms. This mutual orthogonality is expected to improve radar’s robustness against mutual interference. In addition, the phase-coded signal can carry information, and the PC-FMCW waveforms can be used for communication purposes. In Chapter 4, we propose the phase lag compensated group delay filter receiver to improve the sensing performance while keeping the low sampling requirements. However, the impact of phase lag compensated group delay filter on the recovery of communication data and the communication performance of such a receiver have not been investigated yet. Thus, the interference resilience and communication capabilities of the developed PC-FMCW radar need to be studied.

In this chapter, the mutual interference problem between the victim radar and the interfering sensor with various types of continuous waveforms is examined, and the existing interference analysis is extended. Subsequently, the interference resilience and the communication capabilities of the developed PC-FMCW radar are studied. The chapter is structured as follows. The automotive radar interference of different radar waveforms is investigated analytically, and a generalised radar-to-radar interference equation to describe the characteristics (appearance) of the interference at the beat (intermediate) frequency is derived in Section 6.2. Then in Section 6.3, the utilisation of the proposed equation is discussed, and it is demonstrated that the different interference types can be directly obtained and adequately simulated by using the proposed equation. Moreover, the experimental verification of the proposed generalised interference equation is demonstrated for different scenarios using the commercially available off-the-shelf automotive radar transceivers. Then in Section 6.4, the interference resilience of the PC-FMCW radar against different types of FMCW interference is examined, and the resulting improvement in the sensing performance is compared with the FMCW radar. Then, the communication capabilities of the PC-FMCW radars with dechirping receivers are investigated in Section 6.5. Finally, Section 6.6 highlights the concluding remarks.

6.2. GENERALISED INTERFERENCE EQUATION

A variety of waveform types are used by automotive radars depending on the application, as explained in Chapter 2, and the structure of the mutual interference varies with the different radar waveform types. Hence, it is important to have a generalised interference equation which quantitatively describes as many scenarios as possible. This section introduces the generalised radar-to-radar interference equation for common automotive radar waveforms. To this end, we consider the PC-FMCW radar as a general case and investigate the instantaneous beat frequency of the victim radar to understand the features of the interference.

Assume a radar operating at carrier frequency f_c transmits the PC-FMCW waveform with a transmit power P_t as:

$$x_t(t) = \sqrt{P_t}s(t)\exp\left(-j2\pi(f_c t + \frac{1}{2}kt^2)\right), \tag{6.1}$$

where $t \in [0,\ T]$. For the following analytical derivations, we consider the BPSK coding is used for the phase-coded signal $s(t)$. Then, the phase term spans $\phi_n \in \{0, \pi\}$, and the BPSK coding signal can be mathematically written by using a phase term as follows:

$$s_{\text{bpsk}}(t) = \sum_{n=1}^{N_a} e^{j\phi_n}\text{rect}\left(\frac{t-(n-1/2)T_a}{T_a}\right), \tag{6.2}$$

where N_a is the number of chips within one sweep, T_a is the single-chip duration, calculated as $T_a = T/N_a$ and ϕ_n denotes the phase corresponding to the n^{th} bit of the N_a bit sequence. The received signal reflected from the target can be written as:

$$\begin{aligned} x_{r_{\text{target}}}(t) = &\alpha_0 \sum_{n=1}^{N_a} e^{j\phi_n}\text{rect}\left(\frac{t-\tau-(n-1/2)T_a}{T_a}\right) \\ &\times \exp\left(-j2\pi\left(f_c(t-\tau)+\frac{1}{2}k(t-\tau)^2\right)\right), \end{aligned} \tag{6.3}$$

where τ is the time delay between the victim radar and the target, $\alpha_0 = e^{j\varphi_0}\sqrt{P_{\text{target}}}$ is the amplitude of received target echo, P_{target} is the received power of the target echo, and $e^{j\varphi_0}$ is a constant phase term due to two-way propagation of the wave and the scattering coefficient from the target. Assume the interferer radar also transmits the PC-FMCW waveform and uses a different phase-coded signal with BPSK coding. Then the received interference can be written as:

$$\begin{aligned} x_{r_{\text{int}}}(t) = &\alpha_{\text{int}} \sum_{n=1}^{N_b} e^{j\phi_n}\text{rect}\left(\frac{t-\tau_{\text{int}}-(n-1/2)T_b}{T_b}\right) \\ &\times \exp\left(-j2\pi\left(f_{c\text{int}}(t-\tau_{\text{int}})+\frac{1}{2}k_{\text{int}}(t-\tau_{\text{int}})^2\right)\right), \end{aligned} \tag{6.4}$$

where τ_{int} is the time delay between the victim and interfering radars, $\alpha_{\text{int}} = e^{j\varphi_{\text{int}}}\sqrt{P_{\text{int}}}$ is the amplitude of received interference, P_{int} is the received power of the interference signal, $e^{j\varphi_{\text{int}}}$ is a constant phase term due to one-way propagation and the initial phase of

the interference, $f_{c\text{int}}$ is the carrier frequency, k_{int} is the slope, N_b is the number of chips within one sweep, $T_b = T_{\text{int}}/N_b$ is the chip duration and T_{int} is the sweep duration of the interfering radar, respectively. For the derivations, we assume the interference signal overlaps in time with the victim signal. Moreover, P_{target} and P_{int} can be obtained as:

$$P_{\text{target}} = \frac{P_t G_t G_r \lambda^2 \sigma}{(4\pi)^3 R^4{}_{\text{target}}}, \tag{6.5}$$

and

$$P_{\text{int}} = \frac{P_{t_{\text{int}}} G_{t_{\text{int}}} G_r \lambda^2{}_{\text{int}}}{(4\pi)^2 R^2{}_{\text{int}}}. \tag{6.6}$$

Here λ is the wavelength, G_t is the gain of the transmitting antenna, and G_r is the gain of the receiving antenna for the victim radar. Similarly, λ_{int} is the wavelength, $P_{t_{\text{int}}}$ is the transmitting power, and $G_{t_{\text{int}}}$ is the gain of the transmitting antenna for the interferer radar. The σ is the radar cross-section of the target, and R_{target} and R_{int} are the range of target and interferer radar, respectively. It should be noted that the power of interference is inversely proportional to the interference range, shown as $P_{\text{int}} \propto R_{\text{int}}^{-2}$, while the target echo is inversely proportional to the target range, described as $P_{\text{target}} \propto R_{\text{target}}^{-4}$. This may lead to the reception of a strong interferer signal that can mask the weak target echoes.

The total received signal in the victim radar is the combination of the target echo and the interfering signal and can be represented as:

$$x_r(t) = x_{r_{\text{target}}}(t) + x_{r_{\text{int}}}(t). \tag{6.7}$$

In this chapter, we use complex signals representation for ease of mathematical manipulations and assume a complex mixer is used. Note that the real signal representation should be used for a real heterodyne receiver. The received signal is mixed with the complex conjugate of the uncoded reference chirp signal (associated with the victim radar) for the dechirping process. The (complex) mixer output can be written as:

$$\begin{aligned} x_m(t) &= x_{r_{\text{target}}}(t) x_{\text{ref}}(t)^* + x_{r_{\text{int}}}(t) x_{\text{ref}}(t)^* \\ &= x_{m_{\text{target}}}(t) + x_{m_{\text{int}}}(t), \end{aligned} \tag{6.8}$$

where $(\cdot)^*$ denotes the complex conjugate and the uncoded reference chirp signal can be represented as $x_{\text{ref}}(t)^* = \exp\left(j2\pi(f_c t + \frac{1}{2} k t^2)\right)$. The mixer output consists of two components regarding the target and interference. Explicitly, the target component can be obtained as:

$$\begin{aligned} x_{m_{\text{target}}}(t) &= x_{r_{\text{target}}}(t) \exp\left(j2\pi(f_c t + \frac{1}{2} k t^2)\right) \\ &= \alpha_0 \sum_{n=1}^{N_a} e^{j\phi_n} \text{rect}\left(\frac{t - \tau - (n - 1/2) T_a}{T_a}\right) \\ &\quad \times \exp\left(j2\pi\left(f_c \tau + k\tau t - \frac{1}{2} k\tau^2\right)\right). \end{aligned} \tag{6.9}$$

Instantaneous spectrum can be used to determine the range of the target or the frequency of the interfering signal. If the instantaneous spectrum has a continuous part, it indicates

either phase jumps caused by phase coding of the signal as the instantaneous frequency is a derivative of the signal phase [106] or reception of the spread-spectrum interfering signal. Thus, the instantaneous frequency spectrum provides additional information about the signal features which can not be observed in the time-domain representation and can be used to characterize the signal waveform. The phase of the mixer output related to the target echo is obtained as:

$$\phi_{m_{\text{target}}}(t) = 2\pi\left(f_c\tau + k\tau t - \frac{1}{2}k\tau^2\right) + \phi_{\text{tar}_{\text{code}}}(t), \tag{6.10}$$

where

$$\phi_{\text{tar}_{\text{code}}}(t) = \sum_{n=1}^{N_a}\phi_n \text{rect}\left(\frac{t-\tau-(n-1/2)T_a}{T_a}\right). \tag{6.11}$$

Then, the instantaneous frequency of the mixer output of the target echo can be written as (see Appendix A for derivative of phase):

$$\begin{aligned} f_{i_{\text{target}}}(t) &= \frac{1}{2\pi}\frac{d}{dt}\phi_{m_{\text{target}}}(t) \\ &= \frac{1}{2\pi}(2\pi k\tau) + \frac{1}{2\pi}\frac{d}{dt}\phi_{\text{tar}_{\text{code}}}(t) \\ &= k\tau + \frac{1}{2\pi}\sum_{n=1}^{N_a}(\phi_{n+1}-\phi_n)\delta(t-\tau-nT_a). \end{aligned} \tag{6.12}$$

Similarly, the interference part is equal to:

$$\begin{aligned} x_{m_{\text{int}}}(t) &= x_{r_{\text{int}}}(t)\exp\left(j2\pi(f_c t + \frac{1}{2}kt^2)\right) \\ &= \alpha_{\text{int}}\sum_{n=1}^{N_b} e^{j\phi_n}\text{rect}\left(\frac{t-\tau_{\text{int}}-(n-1/2)T_b}{T_b}\right) \\ &\times \exp\left(j2\pi\left(t\left(f_c - f_{c\text{int}} + k_{\text{int}}\tau_{\text{int}}\right) + f_{c\text{int}}\tau_{\text{int}} + t^2\left(\frac{1}{2}k - \frac{1}{2}k_{\text{int}}\right) - \frac{1}{2}k_{\text{int}}\tau_{\text{int}}^2\right)\right). \end{aligned} \tag{6.13}$$

The phase of the mixer output related to the received interference is obtained as:

$$\begin{aligned} \phi_{m_{\text{int}}}(t) = 2\pi&\left(t\left(f_c - f_{c\text{int}} + k_{\text{int}}\tau_{\text{int}}\right) + f_{c\text{int}}\tau_{\text{int}} + t^2\left(\frac{1}{2}k - \frac{1}{2}k_{\text{int}}\right) - \frac{1}{2}k_{\text{int}}\tau_{\text{int}}^2\right) \\ &+ \phi_{\text{int}_{\text{code}}}(t), \end{aligned} \tag{6.14}$$

where

$$\phi_{\text{int}_{\text{code}}}(t) = \sum_{n=1}^{N_b}\phi_n \text{rect}\left(\frac{t-\tau_{\text{int}}-(n-1/2)T_b}{T_b}\right). \tag{6.15}$$

Subsequently, the instantaneous frequency of the mixer output of received interference

Table 6.1: Different Waveform Scenarios

Victim	Interference	N_a	k	N_b	k_{int}
CW	CW	$=0$	$=0$	$=0$	$=0$
CW	FMCW	$=0$	$=0$	$=0$	$\neq 0$
CW	PMCW	$=0$	$=0$	$\neq 0$	$=0$
CW	PC-FMCW	$=0$	$=0$	$\neq 0$	$\neq 0$
FMCW	CW	$=0$	$\neq 0$	$=0$	$=0$
FMCW	FMCW	$=0$	$\neq 0$	$=0$	$\neq 0$
FMCW	PMCW	$=0$	$\neq 0$	$\neq 0$	$=0$
FMCW	PC-FMCW	$=0$	$\neq 0$	$\neq 0$	$\neq 0$
PMCW	CW	$\neq 0$	$=0$	$=0$	$=0$
PMCW	FMCW	$\neq 0$	$=0$	$=0$	$\neq 0$
PMCW	PMCW	$\neq 0$	$=0$	$\neq 0$	$=0$
PMCW	PC-FMCW	$\neq 0$	$=0$	$\neq 0$	$\neq 0$
PC-FMCW	CW	$\neq 0$	$\neq 0$	$=0$	$=0$
PC-FMCW	FMCW	$\neq 0$	$\neq 0$	$=0$	$\neq 0$
PC-FMCW	PMCW	$\neq 0$	$\neq 0$	$\neq 0$	$=0$
PC-FMCW	PC-FMCW	$\neq 0$	$\neq 0$	$\neq 0$	$\neq 0$

can be obtained as (see Appendix A for derivative of phase):

$$\begin{aligned} f_{i_{\text{int}}}(t) &= \frac{1}{2\pi}\frac{d}{dt}\phi_{m_{\text{int}}}(t) \\ &= t(k-k_{\text{int}}) + (f_c - f_{c\text{int}} + k_{\text{int}}\tau_{\text{int}}) + \frac{1}{2\pi}\frac{d}{dt}\phi_{\text{int}_{\text{code}}}(t) \\ &= t(k-k_{\text{int}}) + (f_c - f_{c\text{int}} + k_{\text{int}}\tau_{\text{int}}) + \frac{1}{2\pi}\sum_{n=1}^{N_b}(\phi_{n+1}-\phi_n)\delta(t-\tau_{\text{int}}-nT_b). \end{aligned} \tag{6.16}$$

Finally, the mixer output in the victim radar can be recast as:

$$x_m(t) = \alpha_0 \exp\left(j\phi_{m_{\text{target}}}(t)\right) + \alpha_{\text{int}} \exp\left(j\phi_{m_{\text{int}}}(t)\right), \tag{6.17}$$

and the time-frequency distribution of the mixer output can be described as a combination of frequency components $f_{i_{\text{target}}}(t)$ and $f_{i_{\text{int}}}(t)$, shown as:

$$f_{i_m}(t) \supseteq \{f_{i_{\text{target}}}(t), f_{i_{\text{int}}}(t)\}. \tag{6.18}$$

where $B \supseteq A$ denotes "B is a superset of A".

It is important to note that the time-domain representation of the mixer output alone does not demonstrate all features of the interference. The interference appearance at the beat frequency is related to the waveform parameters and can be observed in time-frequency analysis (instantaneous frequency signature in spectrogram). Thus, we analysed the instantaneous spectrum of the mixer output and mathematically modelled

the signals at the victim radar. The instantaneous spectrum of the mixer output on the victim radar depends on the difference between chirp slopes for a given time, described as $t(k-k_{\text{int}})$, plus the difference between carrier frequencies $(f_c - f_{c\text{int}})$ plus the corresponding beat frequencies for both the target echo and the interference, illustrated as $(k_{\text{int}}\tau_{\text{int}} + k\tau)$, plus a summation of Dirac deltas due to the immediate phase changes.

Here, (6.17) and (6.18) represent the generalised radar-to-radar interference equation and its time-frequency distribution (instantaneous spectrum), respectively. The target and the interference response on the victim radar for different waveforms can be obtained using the proposed generalised radar-to-radar interference equation by setting the variables (N_a, k, N_b and k_{int}) as defined in Table 6.1.

6.3. UTILISATION AND EXPERIMENTS

This section discusses the utilisation of the generalised radar-to-radar interference equation and provides the experimental verification of it.

6.3.1. CHARACTERISTICS OF VARIOUS AUTOMOTIVE RADAR INTERFERENCE TYPES

This section investigates the characteristics of various automotive radar interference types. In automotive radar applications, different kinds of interference types can be observed under various radar setups. The generalised radar-to-radar interference equation covers all the scenarios given in Table 6.1 and can be applied to particular cases. Consequently, the proposed equation can be used to model and simulate interference on the victim radar. To illustrate the effectiveness of the generalised radar-to-radar interference equation, we consider the following scenarios for automotive radars. Characteristics of other common automotive radar interference cases can be seen in Appendix B.

FMCW RADAR VS FMCW INTERFERER

Assume both the victim and interferer radars use FMCW. As most automotive radars use FMCW, this scenario is very common on the road. Thus, various interference mitigation methods have been studied for this scenario, such as [52, 58, 69]. Following Table 6.1, set $N_a = 0$, $k \neq 0$, $N_b = 0$ and $k_{\text{int}} \neq 0$ in (6.17) and (6.18) to achieve the FMCW radar vs FMCW interferer case. The mixer output on the victim radar becomes:

$$x_m(t) = \alpha_0 \exp\left(j2\pi\left(f_c\tau + k\tau t - \frac{1}{2}k\tau^2\right)\right) + \alpha_{\text{int}} \exp\left(j2\pi\left(t\left(f_c - f_{c\text{int}} + k_{\text{int}}\tau_{\text{int}}\right) + f_{c\text{int}}\tau_{\text{int}} + t^2\left(\frac{1}{2}k - \frac{1}{2}k_{\text{int}}\right) - \frac{1}{2}k_{\text{int}}\tau_{\text{int}}^2\right)\right), \tag{6.19}$$

and its time-frequency distribution consists of:

$$f_{i_m}(t) \supseteq \{f_{i_{\text{target}}}(t), f_{i_{\text{int}}}(t)\}, \tag{6.20a}$$

$$f_{i_{\text{target}}}(t) = k\tau, \tag{6.20b}$$

$$f_{i_{\text{int}}}(t) = t(k-k_{\text{int}}) + (f_c - f_{c\text{int}}) + k_{\text{int}}\tau_{\text{int}}. \tag{6.20c}$$

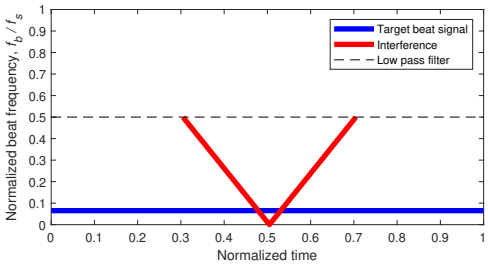

Figure 6.1: FMCW victim vs FMCW interference case. Time-frequency distribution of the mixer output for the FMCW victim radar is simulated by using the derived equation.

Note that the results are the same as those given in [11, 62, 139, 140]. Furthermore, we quantitatively analyze the influence of this interference on the victim radar's range-Doppler profile in Appendix C.

In Figure 6.1, the time-frequency distribution of the mixer output for the FMCW victim radar is simulated by using the derived equation for FMCW victim vs FMCW interference case. For illustration, we assume a real mixer is used to mimic a common scenario seen in automotive radars. We chose interference parameters with different chirp slopes, carrier frequencies and delays such that the captured interference leads to the "V-shape". It should be noted that half of the "V-shape" will be on the other side of the beat frequency, and the interference will lead to a diagonal line in case of the complex mixer. Here the $(f_c - f_{c\text{int}})$ and the $k_{\text{int}}\tau_{\text{int}}$ terms determine the starting point of the captured interference, while the $t(k-k_{\text{int}})$ term controls the slope of the "V-shape" and the wider or narrower interference shape can be observed depending on this term. In addition, the $k\tau$ term is the beat signal induced by the target; it is illustrated with the blue colour in Figure 6.1.

6

FMCW RADAR VS PC-FMCW INTERFERER

We can observe this scenario by using the generalised radar-to-radar interference equation, letting $N_a = 0$, $k \neq 0$, $N_b \neq 0$ and $k_{\text{int}} \neq 0$ in (6.17) and (6.18). The mixer output on the victim radar becomes:

$$\begin{aligned} x_m(t) = \alpha_0 \exp\left(j2\pi\left(f_c\tau + k\tau\, t - \frac{1}{2}k\tau^2\right)\right) \\ + \alpha_{\text{int}} \exp\left(j2\pi\left(t(f_c - f_{c\text{int}} + k_{\text{int}}\tau_{\text{int}}) + f_{c\text{int}}\tau_{\text{int}} + t^2(\frac{1}{2}k - \frac{1}{2}k_{\text{int}}) - \frac{1}{2}k_{\text{int}}\tau_{\text{int}}^2\right)\right) \\ \times \exp\left(\phi_{\text{int}_{\text{code}}}(t)\right), \end{aligned} \tag{6.21}$$

and its time-frequency distribution consists of:

$$f_{i_m}(t) \supseteq \{f_{i_{\text{target}}}(t), f_{i_{\text{int}}}(t)\}, \tag{6.22a}$$

$$f_{i_{\text{target}}}(t) = k\tau, \tag{6.22b}$$

$$f_{i_{\text{int}}}(t) = t(k-k_{\text{int}}) + (f_c - f_{c\text{int}}) + k_{\text{int}}\tau_{\text{int}} + \frac{1}{2\pi}\sum_{n=1}^{N_b}(\phi_{n+1} - \phi_n)\delta(t - \tau_{\text{int}} - nT_b). \tag{6.22c}$$

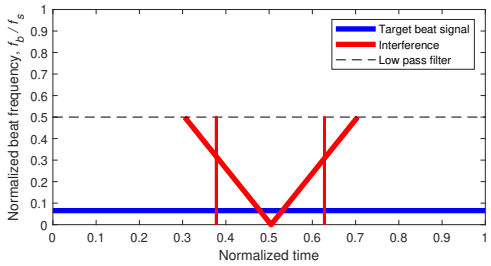

Figure 6.2: FMCW victim vs PC-FMCW interference case. Time-frequency distribution of the mixer output for the FMCW victim radar is simulated by using the derived equation. The abrupt phase changes due to coding are observable as a vertical line in the time-frequency distribution.

In Figure 6.2 the time-frequency distribution of the mixer output for the FMCW victim radar is simulated by using the derived equation for FMCW victim vs PC-FMCW interference case. For ease of comparison, we used the same interference parameters that we selected in the FMCW vs FMCW case. As a result, the $t(k-k_{\text{int}})$ term causes the "V-shape" for the captured interference, with the starting point being controlled by the $(f_c - f_{c_{\text{int}}})$ and $k_{\text{int}}\tau_{\text{int}}$ terms. In addition to the "V-shape", we observe the Dirac deltas on the time-frequency distribution of the victim radar due to the phase coding of the interference. The phase sequence changes from 0 to π and from π to 0 for the PC-FMCW interference radar, as shown in Figure 6.2.

PC-FMCW RADAR VS FMCW INTERFERER

This scenario in which PC-FMCW radar is interfered with by the FMCW waveform can be explored by choosing $N_a \neq 0$, $k \neq 0$, $N_b = 0$ and $k_{\text{int}} \neq 0$ in (6.17) and (6.18). The mixer output on the victim radar becomes:

$$x_m(t) = \alpha_0 \exp\left(j2\pi\left(f_c\tau + k\tau t - \frac{1}{2}k\tau^2\right) + \phi_{\text{tar}_{\text{code}}}(t)\right) + \alpha_{\text{int}} \exp\left(j2\pi\left(t\left(f_c - f_{c_{\text{int}}} + k_{\text{int}}\tau_{\text{int}}\right) + f_{c_{\text{int}}}\tau_{\text{int}} + t^2\left(\frac{1}{2}k - \frac{1}{2}k_{\text{int}}\right) - \frac{1}{2}k_{\text{int}}\tau_{\text{int}}^2\right)\right), \tag{6.23}$$

and its time-frequency distribution consists of:

$$f_{i_m}(t) \supseteq \{f_{i_{\text{target}}}(t), f_{i_{\text{int}}}(t)\}, \tag{6.24a}$$

$$f_{i_{\text{target}}}(t) = k\tau + \frac{1}{2\pi}\sum_{n=1}^{N_a}(\phi_{n+1} - \phi_n)\delta(t - \tau - nT_a), \tag{6.24b}$$

$$f_{i_{\text{int}}}(t) = t(k - k_{\text{int}}) + (f_c - f_{c_{\text{int}}}) + k_{\text{int}}\tau_{\text{int}}. \tag{6.24c}$$

In this case, the time-frequency distribution of the mixer output for the PC-FMCW victim radar consists of the beat signal $k\tau$, Dirac deltas $(\phi_{n+1} - \phi_n)\delta(t - \tau - nT_a)$ due to transmitted phase-coded signal, $t(k-k_{\text{int}})$, $(f_c - f_{c_{\text{int}}})$ and $k_{\text{int}}\tau_{\text{int}}$ terms due to the FMCW interference. Herein, $t(k-k_{\text{int}})$ term that will cause a diagonal line or "V-shape" and will control the slope of the resulting interference, while $(f_c - f_{c_{\text{int}}})$ and $k_{\text{int}}\tau_{\text{int}}$ terms

determine the starting point of the resulting interference. It is important to note that the PC-FMCW victim radar will multiply the mixer output with the complex conjugate of the transmitted code for decoding. After ideal decoding, the transmitted code term inside the target echo signal will get rid of the code term, and the interference signal will be coded with a complex conjugate of the transmitted phase-coded signal. As a consequence, the peak power of the interference signal will be spread and suppressed due to coding as explained in Chapter 3. In this section, we focus on the characteristic of interference in the victim radar's beat frequency before decoding. We will investigate this scenario and demonstrate the interference resilience of the PC-FMCW waveform in Section 6.4.

6.3.2. UTILISATION

The proposed equation can model most of the common types of automotive radar interference at the beat (intermediate) frequency. Moreover, the equation can help to analytically determine the slope of the "V-shape" as a function of system parameters of interfering radar. Thus, the equation can be used to simulate different interference scenarios accurately and support analysis of the impact of various interference types on target detection. In addition, the time-frequency distribution of the victim radar for the selected waveforms can be modelled by using the proposed equation. These interference models can be utilised to create data set for the interference classification, and they might be used to train a neural network (NN) [141]. The applications of the proposed interference equation to those fields are left as future research topics.

In addition, the introduced equation focuses on BPSK coding and single interferer case. However, it can be extended to other cases with multiple interference. In the following subsection, additional remarks regarding the different phase modulation schemes and multiple interference scenarios are discussed.

DIFFERENT PHASE MODULATION SCHEME

This chapter has focused on BPSK, as it is commonly used for commercially available off-the-shelf (COTS) radar systems such as PMCW [82] and PC-FMCW [85]. Therefore, the phase of the code term has discrete values (0 or π) during chip duration, as shown in (6.2). However, different phase modulation schemes can have phase values that vary over time. To include such a case, we can generally rewrite the phase term of the code as:

$$s(t) = e^{j\phi(t)}. \tag{6.25}$$

If the transmitted phase code of the victim radar has a value that is a function of time, the (6.11) and (6.12) need to be updated as:

$$\phi_{\mathrm{tar}_{code}}(t) = \phi(t), \tag{6.26}$$

and

$$f_{i_{\mathrm{target}}}(t) = k\tau + \frac{1}{2\pi}\frac{d}{dt}\phi(t), \tag{6.27}$$

respectively. Similarly, (6.15) and (6.16) should be updated accordingly for the interferer signal in cases where the phase value varies over time. The derivatives of different types of phase codes can be found in Appendix A.

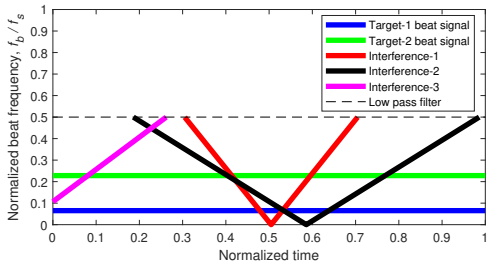

Figure 6.3: FMCW victim vs multiple FMCW interference case. Time-frequency distribution of the mixer output on the FMCW victim radar for the multiple interference scenario is simulated by using the derived equation.

MULTIPLE INTERFERENCE

In this chapter, we have investigated the fundamental problem of interference for different waveforms in the context of a single-input-single-output (SISO) system. Multiple transmitters within the same transceiver (such as a MIMO system) and other radars present on the same car and in the environment can cause multiple interference. When multiple interferers overlap in frequency and/or time, their combined impact can be computed as the superposition of all interferers, while the impact of a single interferer can be obtained using the proposed equation. Similarly, multiple targets scenario can be considered as the combination of all target echo signals, such that the mixer output on the victim radar becomes:

$$\begin{aligned} x_m(t) &= \sum_{r=1}^{R} x_{m_{\text{target,r}}}(t) + \sum_{p=1}^{P} x_{m_{\text{int,p}}}(t) \\ &= \sum_{r=1}^{R} \left\{ \alpha_{0,\text{r}} \exp\left(j2\pi \left(f_c \tau_r + k\tau_r t - \frac{1}{2} k {\tau_r}^2 \right) + \phi_{\text{tar}_{\text{code}}}(t) \right) \right\} \\ &+ \sum_{p=1}^{P} \left\{ \alpha_{\text{int,p}} \exp\Big(j2\pi (t(f_c - f_{c\text{int,p}} + k_{\text{int,p}}\tau_{\text{int,p}}) + f_{c\text{int,p}}\tau_{\text{int,p}} \right. \\ &\qquad \left. + t^2(\frac{1}{2}k - \frac{1}{2}k_{\text{int,p}}) - \frac{1}{2}k_{\text{int,p}}\tau_{\text{int,p}}^2) + \phi_{\text{int}_{\text{code,p}}}(t) \Big) \right\}, \end{aligned} \tag{6.28}$$

and the time-frequency distribution of the victim radar mixer output consists of:

$$f_{i_m}(t) \supseteq \{ f_{i_{\text{target,1}}}(t), \ldots, f_{i_{\text{target,R}}}(t), f_{i_{\text{int,1}}}(t), \ldots, f_{i_{\text{int,P}}}(t) \}, \tag{6.29}$$

where $x_{m_{\text{target,r}}}(t)$ is the mixer output and $f_{i_{\text{target,r}}}$ is the instantaneous frequency induced by the r^{th} target ($0 < r < R$). Similarly, the $x_{m_{\text{int,p}}}(t)$ is the mixer output and $f_{i_{\text{int,p}}}$ is the instantaneous frequency induced by the p^{th} interferer ($0 < p < P$). In Figure 6.3, the multiple interference scenario for FMCW victim vs FMCW interference is simulated. There we assume that each captured interference has a different chirp slope and carrier frequency. We also consider a second target with a different range and demonstrate its resulting beat frequency on the victim radar. Similarly, the impact of the distributed targets can be calculated as the linear superposition of the waveforms transmitted by the same radar.

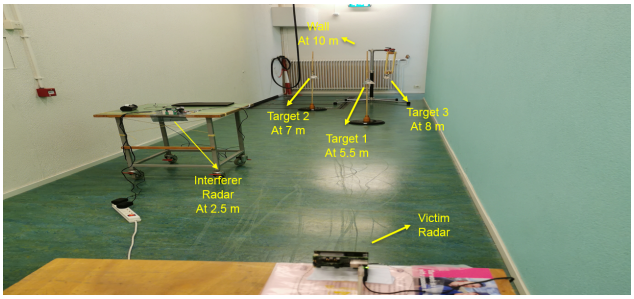

Figure 6.4: Experimental setup.

For the MIMO system, there are three different kinds of MIMO transmission realisations: time division, frequency division and code division. Without losing generality, it is possible to extend our derivation and experimental evaluation to different MIMO systems. Since the analysis and experimental verification still need to be done for all 3^2 combinations of MIMO transmission schemes with 4^2 combinations of victim and interference waveforms, these have not been included in this chapter.

6

6.3.3. EXPERIMENTAL VERIFICATION

In this section, we demonstrate the experimental results. Using COTS automotive radar sensors, multiple NXP automotive radar chipsets and their microcontrollers (TEF810X and S32R274) were programmed for phase coding as described in [112] and were synchronised to simulate the coherent scenario as described in [95]. The experimental setup included victim radar, interfering radar, and controlled stationary and moving targets as shown in Figure 6.4. In the experiments, we focused on investigating the following four scenarios: FMCW vs FMCW, PC-FMCW vs FMCW, FMCW vs PC-FMCW and PC-FMCW vs PC-FMCW. We used a BPSK code sequence with 4 chips to be able to observe the phase changes in our outputs clearly. The transmitted code for the PC-FMCW radars is set to $[1, -1, -1, 1]$, which corresponds to a phase change between 0 and π according to the code sequence. We used a time-frequency analysis, namely a spectrogram, to investigate the mixer output signals of the victim radar. We selected the system parameters such that interfering radar signals passed through the LPF of the victim radar and were captured by the victim radar's

Table 6.2: System Parameters

		Victim	**Interference**
Sweep duration	T	$102.4\mu s$	$102.4\mu s$
Bandwidth	B	$1.155GHz$	$1.2GHz$
Carrier frequency	f_c	$78.915GHz$	$78.98GHz$
Sampling frequency	f_s	$10MHz$	$10MHz$
Number of coding chips	N_c	4	4

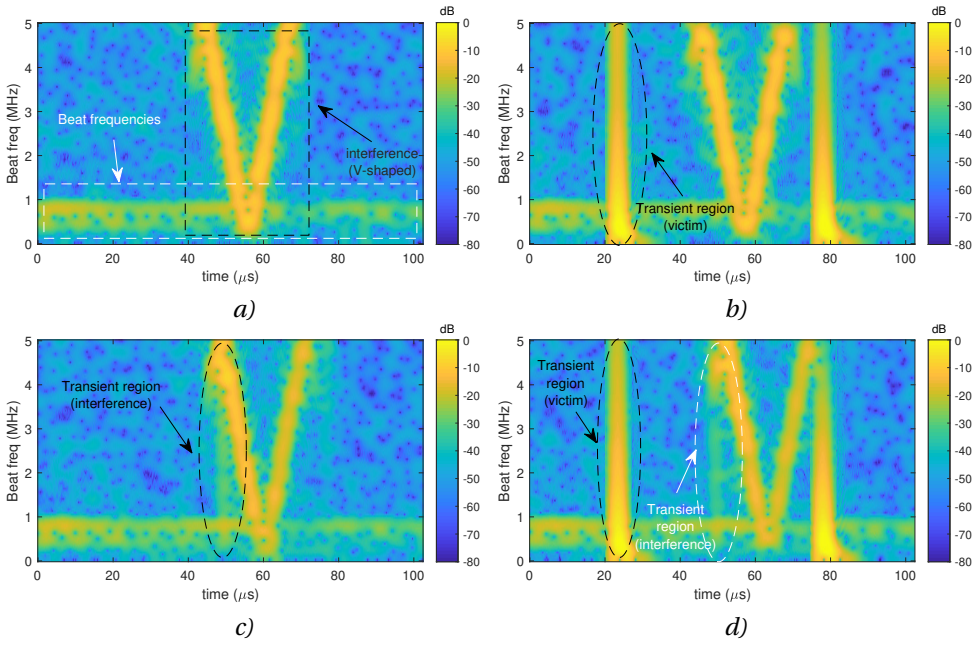

Figure 6.5: Spectrogram of the mixer output for the victim radar: a) FMCW vs FMCW b) PC-FMCW vs FMCW c) FMCW vs PC-FMCW d) PC-FMCW vs PC-FMCW.

ADC within the observation time. These system parameters for the experiments are given in Table 6.2. Note that the effects of the filters are not shown in (6.18), as each system has its own filter response. In this experiment, the convolution of Dirac deltas (due to the BPSK code) and the cascaded filter response created a transient region (short burst of oscillation) in one system when there was a sudden phase change.

In the first experiment, we used FMCW for both victim and interfering radars to verify equation (6.20). In the second experiment, we changed the signal transmitted by the victim radar to PC-FMCW and investigated the FMCW interference on the PC-FMCW radar. In the third experiment, we used FMCW as a victim radar and examined the effects of PC-FMCW as an interference on the FMCW radar. In the fourth and final experiment, we used PC-FMCW for both victim radar and interfering radars to verify (B.8). Note that the spectrogram parameters have been adjusted to emphasise the interference. The results are discussed in the following subsections.

SCENARIO 1 (FMCW RADAR VS FMCW INTERFERER)

The mixer output is shown in Figure 6.5 a, where the beat frequencies and the captured interfering signal are observed. According to (6.20) we expected the time-dependent term $t(k-k_{\text{int}})$ plus the difference between carrier frequencies $(f_c - f_{c_{\text{int}}})$ plus the corresponding beat frequencies for both target echo and interference, as $k\tau + k_{\text{int}}\tau_{\text{int}}$. As demonstrated in Figure 6.5 a, the target and interference returns induced the beat frequencies (shown in the white rectangle), while the interfering signal created a “V-shaped" signature (shown in the black rectangle) in the spectrogram of the FMCW victim radar.

The time-dependent term $t(k - k_{\text{int}})$ resulted in a “V-shape" for the chosen system parameters.

SCENARIO 2 (PC-FMCW RADAR VS FMCW INTERFERER)
As explained earlier, the immediate phase changes seen in the BPSK coding will cause a transient region during phase changes. Therefore, we also expected to see a transient region due to abrupt phase changes used on the victim radar's PC-FMCW waveform. These transient regions are observable in Figure 6.5 b when the phase changes from 0 to π and from π to 0. In addition, the target and FMCW interference induced beat frequencies and “V-shaped" interference, respectively.

SCENARIO 3 (FMCW RADAR VS PC-FMCW INTERFERER)
In this case, we expected to obtain a transient region due to immediate phase changes in the phase-coded signal associated with the interferer PC-FMCW radar. Moreover, the chirp signal in the PC-FMCW interferer is expected to create a “V-shape" similar to FMCW interference. When the phase changed, we observed that the interferer PC-FMCW radar did cause a weak transient region along with “V-shaped" interference on the FMCW victim radar, as illustrated in Figure 6.5 c.

SCENARIO 4 (PC-FMCW RADAR VS PC-FMCW INTERFERER)
In this final scenario, we expected to obtain the beat signals $k\tau + k_{\text{int}}\tau_{\text{int}}$ and the time-dependent term $t(k - k_{\text{int}})$ due to FMCW part of the interference. In addition to these terms, both the victim and interferer PC-FMCW radars are expected to create their own transient regions when the phase changes inside their phase-coded signals. As demonstrated in Figure 6.5 d, the corresponding beat frequencies and the “V-shaped" interference were obtained on the spectrogram. Furthermore, the victim PC-FMCW radar created the transient regions (shown in the black circle), and the interfering PC-FMCW radar produced the weak transient region (shown in the white circle) during the phase changes.

6.4. INTERFERENCE INFLUENCE ON PC-FMCW

This section investigates the radar-to-radar interference resilience of the developed PC-FMCW radar. To this end, we consider different FMCW interference scenarios and compare their impact on the FMCW and PC-FMCW victim radars' sensing performance. For the numerical simulations, we assume the FMCW and PC-FMCW victim radars operate at carrier frequency $f_c = 77$ GHz and transmit $N_p = 256$ chirp pulses with a chirp duration $T = 25.6$ μs and chirp bandwidth $B = 300$ MHz. In the case of PC-FMCW victim radar, each chirp signal is modulated with a phase-coded signal $s(t)$ in both slow-time and fast-time. We consider the GMSK coding scheme and use random code sequences. Moreover, we set the 3-dB bandwidth of the Gaussian filter to two times the chip bandwidth, and phase lag compensation is applied before transmission. Each chirp pulse uses different phase lag compensated code signal $\hat{s}(t)$ for slow-time coding, and we utilize $N_c = 1024$ number of chips per chirp for fast-time coding, i.e. the code bandwidth becomes $B_c = 40$ MHz with $N_c = 1024$ for this setting. In addition, we assume a complex Gaussian noise signal with power spectral density N_0 is captured along with the received signal. The

signal-to-noise ratio (SNR) can be defined as SNR = ${\alpha_0}^2/N_0$. We give the noise power N_0 relative to the absolute of α_0 and set SNR = −10 dB. Moreover, we consider all chirp pulses of victim radar are interfered with the FMCW interference radar operating at carrier frequency $f_{c_{\text{int}}} = 77$ GHz. We set the received interference signal amplitude $\alpha_{\text{int}} = 2\alpha_0$, i.e. the interference signal power is 6 dB higher than the victim radar signal power. As explained in Chapter 1, the captured interference might occur as the narrow-band (NB) interference or the wide-band (NB) interference based on the spectral characteristics of the interference. To investigate the impact of different scenarios, we simulate three interference cases. The first one is the fully coherent NB interference by letting $T_{\text{int}} = 25.6$ μs and $B_{\text{int}} = 300$ MHz. The second one is the coherent WB interference by letting $T_{\text{int}} = 25.6$ μs and $B_{\text{int}} = 200$ MHz. Finally, the third one is the non-coherent WB interference by letting $T_{\text{int}} = 9$ μs and $B_{\text{int}} = 200$ MHz. For all cases, we assume the interference radar is located at a range $R_{\text{int}} = 300$ m with a radial velocity $v_{\text{int}} = -20$ m/s, and the target is located at the range $R = 100$ m with a radial velocity $v = -10$ m/s. On the receiver side, the total received signal is dechirped with the reference chirp signal of victim radar. Then, the dechirped signal is sampled with $f_s = 80$ MHz and low-pass filtered with the cut-off frequency $f_{\text{cut}} = \pm 40$ MHz. As a result, we have $N = 2048$ range cells (fast-time samples) for the selected parameters. In the case of PC-FMCW victim radar, the group delay filter is applied to the sampled signal. The same LPF is applied to the reference phase-coded signal to prevent a signal mismatch, and then the decoding is performed. We apply 80 dB Chebyshev window in the range domain, and 60 dB Chebyshev window in the Doppler domain, before taking the two-dimensional FFT. In addition, we normalize the range-Doppler profiles with respect to the noise level to focus on the impact of interference.

First, we demonstrate the spectrogram of the FMCW victim radar with different FMCW interference cases in Figure 6.6. It can be seen that the received target echo creates a single tone beat signal in the dechirped signal in no interference case. Notice that the noise peak power is decreased after stretch processing (dechirping) and low-pass filtering. The suppression of the peak noise power after taking FFT is $10\log_{10}(BT) = 38$ dB for a single chirp and an additional $10\log_{10}(N_p) = 24$ dB after coherent pulse integration for Doppler processing. In case of the interference has the same chirp slope and chirp duration, i.e. $k_{\text{int}} = k$ and $T_{\text{int}} = T$, the coherent NB interference scenario occurs, and the received interference causes another single tone beat signal in the dechirped signal (Figure 6.6 d). In case of the interference has the same chirp duration but has a different chirp slope $k_{\text{int}} \neq k$, the coherent WB interference scenario occurs, and the received interference causes a diagonal line for the complex mixer as shown Figure 6.6 f. For the real mixer, such interference will create “V-shape" in the spectrogram as discussed earlier. It is important to note that coherent interference scenarios create the same effect for each chirp pulse. In case of the interference has different chirp duration $T_{\text{int}} \neq T$ and chirp slope $k_{\text{int}} \neq k$, the non-coherent WB interference scenario occurs, and the received interference causes different diagonal lines for each chirp pulse. The spectrogram of the dechirped signal with non-coherent WB interference is shown for the first pulse in 6.6 h. For comparison, we also illustrate the following five pulses for the non-coherent WB interference case in Figure 6.7. It can be seen that the location of the diagonal line changes for different chirp pulses in the non-coherent WB interference case. Afterwards,

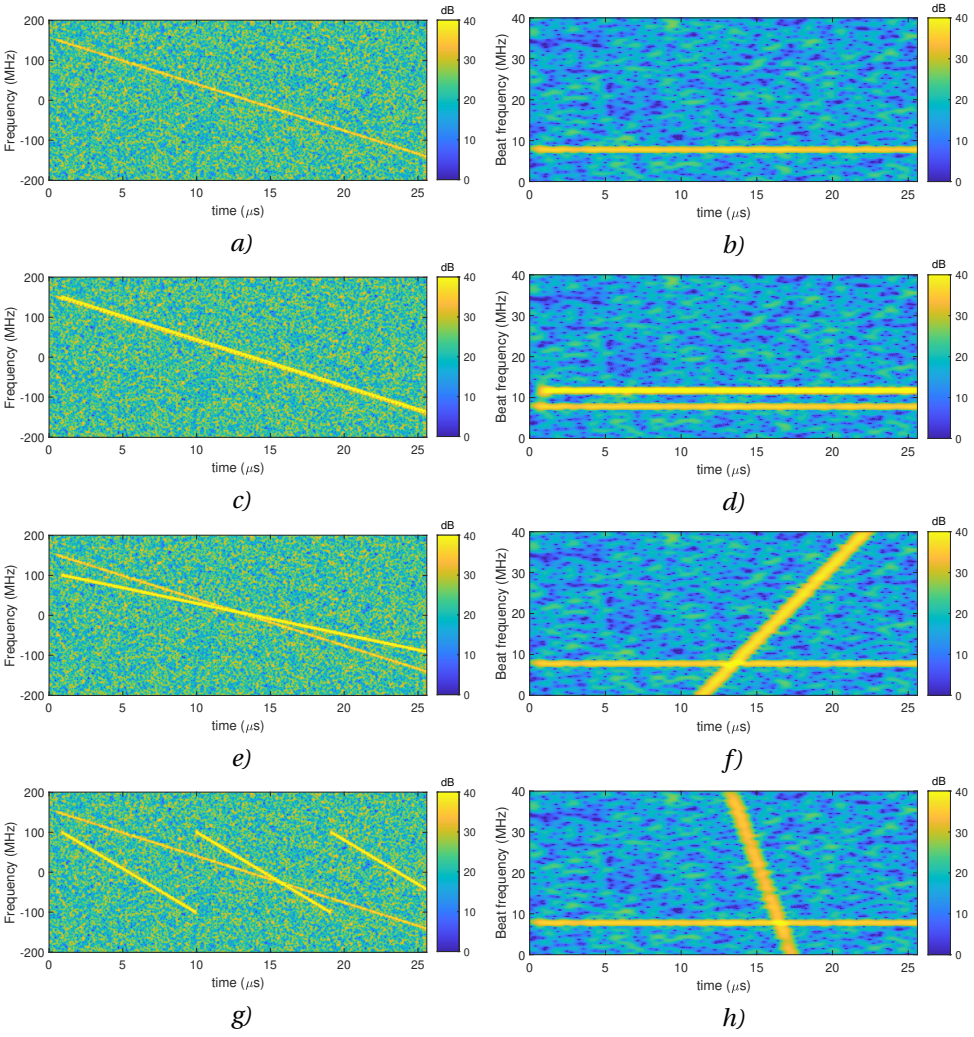

Figure 6.6: Spectrogram of the FMCW victim radar with different interference scenarios. The received signal on the left column and the dechirped signal on the right column: a-b) No interference c-d) Coherent NB interference e-f) Coherent WB interference g-h) Non-coherent WB interference.

we demonstrate the spectrogram of the PC-FMCW victim radar with $N_c = 1024$ against investigated interference scenarios in Figure 6.8. It is observed that the self-transmitted signal (signal reflected from the target) is perfectly decoded, and a single tone beat signal associated with the target is recovered after applying the group delay filter and decoding as explained in Chapter 4. On the other hand, all other interferer signals remain coded, and thus their peak powers are spread over fast-time for each chirp pulse. Note that the suppression performance is proportional to the code bandwidth $B_c = N_c / T$ as the spectrum spread with the time-bandwidth product. Thus, the suppression performance

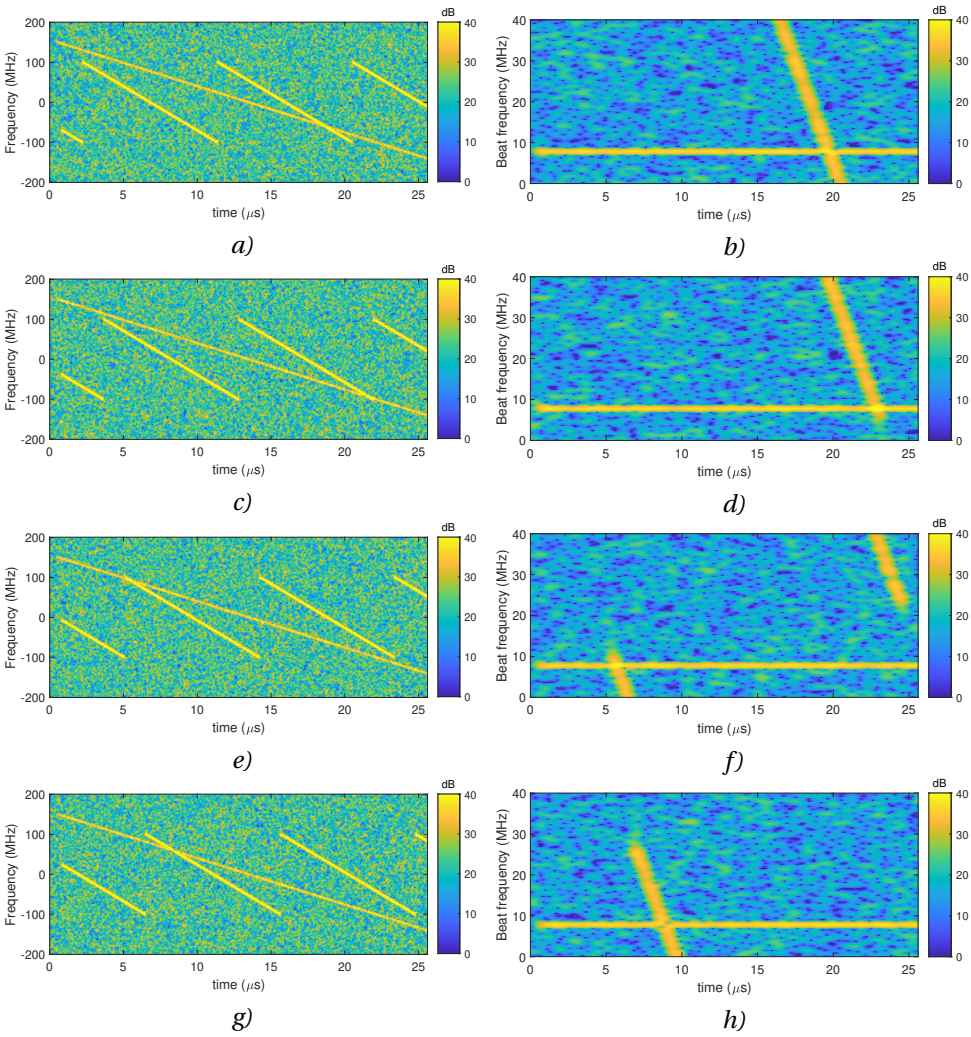

Figure 6.7: Spectrogram of the FMCW victim radar for illustration of different chirp pulses with non-coherent WB interference. The received signal on the left column and the dechirped signal on the right column: a-b) 2nd pulse c-d) 3rd pulse e-f) 4th pulse g-h) 5th pulse.

improves as we increase the number of chips per chirp and can be written as $10\log_{10}(N_c)$ for a single chirp.

Next, we examine the range-Doppler profiles of the FMCW and PC-FMCW victim radars in Figure 6.9, and we compare their range profiles in Figure 6.10. In the interference-free case, both radars have the target response with ~ 51 dB dynamic range at 100 m with a -10 m/s radial velocity. In the coherent NB interference case, the interference peak power concentrates at one particular range bin and leads to a ghost target at 150 m with a -10 m/s radial velocity for the FMCW victim radar (Figure 6.9 c). The resulting ghost target

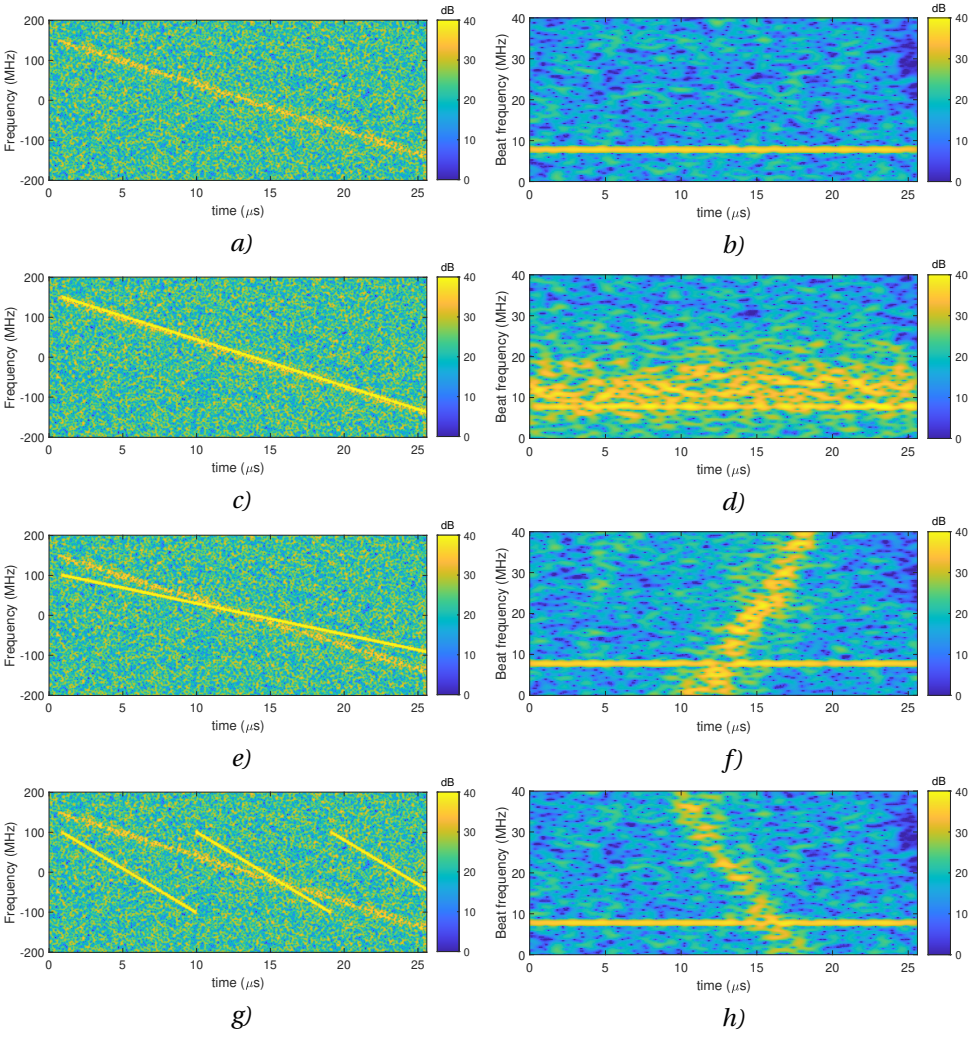

Figure 6.8: Spectrogram of the PC-FMCW victim radar ($N_c = 1024$) with different interference scenarios. The received signal on the left column and the decoded dechirped signal on the right column: a-b) No interference c-d) Coherent NB interference e-f) Coherent WB interference g-h) Non-coherent WB interference.

has ~ 57 dB power as seen in Figure 6.10 a. This ghost target can not be distinguished from the real target and hence needs to be mitigated. Note that the ghost target scenario is very difficult to be generated by other radars as the interference radar should be fully synchronized with the victim radar. On the other hand, such a coherent interference case can mimic a self-interference scenario, which is the interference case seen in the simultaneous MIMO transmission. As shown in Figure 6.9 d, the PC-FMCW victim radar spread the peak power of such an interference over the range-Doppler plane using both fast-time and slow-time coding. Thus, the peak power of the ghost target is expected to

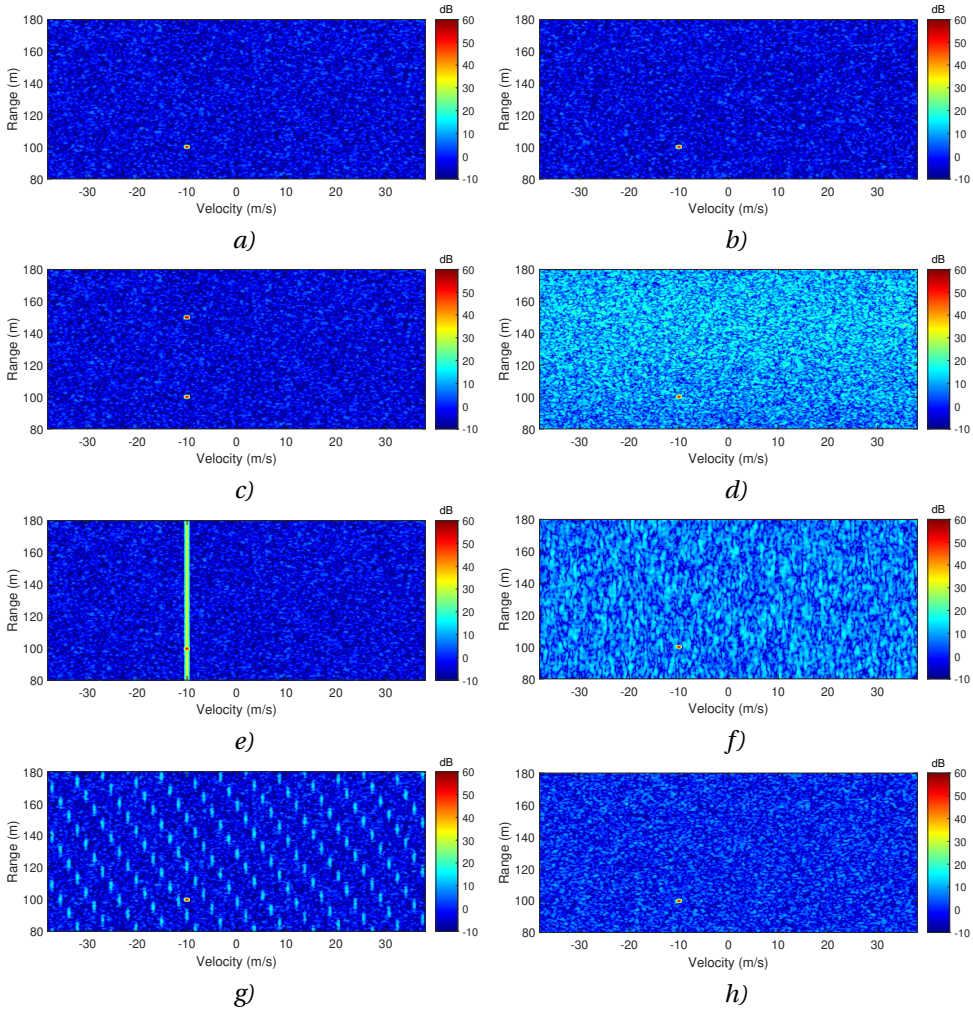

Figure 6.9: Comparison of range-Doppler profiles. The FMCW victim radar on the left column and the PC-FMCW victim radar ($N_c = 1024$, $N_p = 256$) on the right column: a-b) No interference c-d) Coherent NB interference e-f) Coherent WB interference g-h) Non-coherent WB interference.

be suppressed $10\log_{10}(N_c) + 10\log_{10}(N_p) = 54$ dB on average for the perfectly orthogonal codes. In Figure 6.10 b, we observe that the ghost target peak power is decreased and has a noise-like pattern with a maximum of around 18 dB. In the coherent WB interference case, the interference peak power starts to spread over multiple range bins and increases the noise floor in the range profile of the FMCW victim radar (Figure 6.9 e). However, since the interference is coherent over Doppler processing, this interference type affects only the range profile. In this particular example, we observe that the noise floor of the FMCW victim radar raised from 0 dB to ~ 30 dB as shown in Figure 6.10 c. On the other hand, the PC-FMCW victim radar further suppresses the coherent WB interference

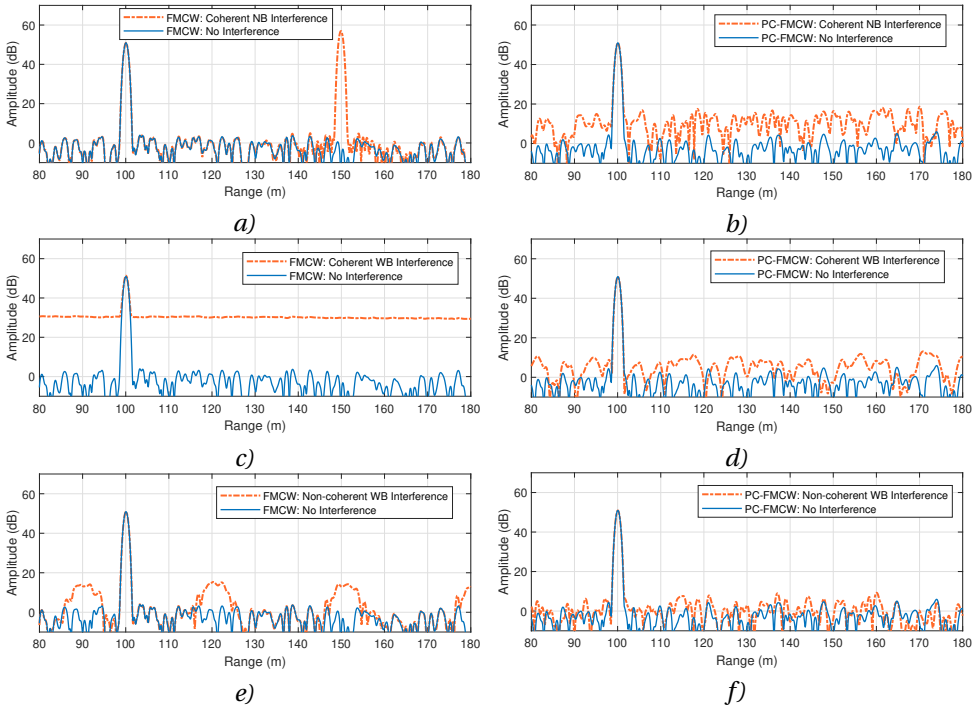

Figure 6.10: Comparison of range profiles. The FMCW victim radar on the left column and the PC-FMCW victim radar ($N_c = 1024$, $N_p = 256$) on the right column: a-b) Coherent NB interference c-d) Coherent WB interference e-f) Non-coherent WB interference.

and noise floor due to interference is decreased to around 10 dB (Figure 6.10 d). In the non-coherent WB interference case, the interference peak power starts to spread over multiple range-Doppler cells of the FMCW victim radar (Figure 6.9 g). It is important to note that the non-coherent WB interference already has a noise-like pattern as it spans multiple range-Doppler cells, and hence the interference peak power is already spread. For this setting, we observe that such an interference causes responses periodically every 30 m with ~ 15 dB power (Figure 6.10 e). By combining both slow-time and fast-time coding, the PC-FMCW victim radar further spreads such an interference over the whole range-Doppler profile, and the peak power of this interference is reduced to ~ 8 dB as shown in Figure 6.10 f. Thus, the PC-FMCW waveforms can be used to mitigate both narrow-band and wide-band interference types.

To assess the interference resilience of the PC-FMCW radar against different interference types, we illustrate signal-to-interference ratio (SIR) in range as a function number of chips for fast-time coding of the PC-FMCW victim radar in Figure 6.11. It should be noted that the PC-FMCW victim radar also utilizes $N_p = 256$ chirp pulses for slow-time coding. As the number of chips for fast-time coding is increased from $N_c = 0$ to $N_c = 1024$, we observe that the SIR in range is improved from -6 dB to 33 dB for the coherent NB interference, 21 dB to 39 dB for the coherent WB interference, and 36 dB to 45 dB for the

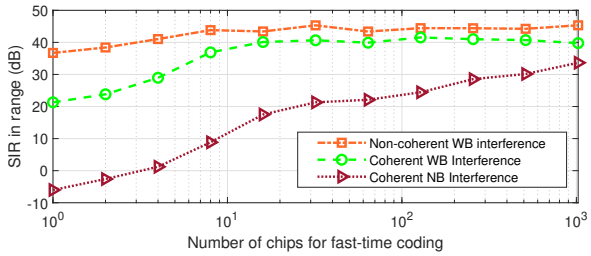

Figure 6.11: Signal-to-interference ratio in range versus the number of chips for fast-time coding of the PC-FMCW victim radar ($N_p = 256$).

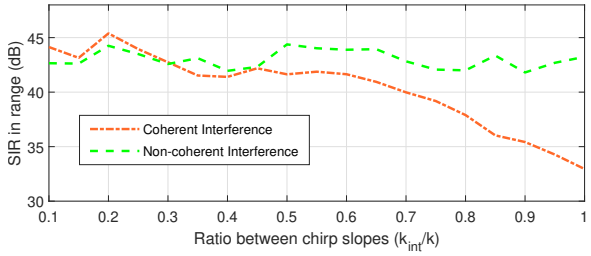

Figure 6.12: Signal-to-interference ratio in range versus the ratio between chirp slopes (k_{int}/k) of the PC-FMCW victim radar ($N_c = 1024$, $N_p = 256$).

non-coherent WB interference. In addition, we demonstrate the SIR in range versus the ratio between chirp slopes in Figure 6.12. Herein, we use $N_c = 1024$ and $N_p = 256$ for the PC-FMCW victim radar. Moreover, we set $T_{\text{int}} = 25.6$ μs for coherent and $T_{\text{int}} = 9$ μs for non-coherent interference types and then change the interference chirp bandwidth B_{int} to investigate different chirp slope ratio. It can be seen that the SIR in range is around ~ 43 dB for different chirp slope values in the non-coherent interference case as shown in Figure 6.12. However, SIR in range changes from 45 dB to 33 dB as the ratio k_{int}/k raises from 0.1 to 1. This is because the wide-band interference becomes narrow-band that causes the ghost target case as the ratio k_{int}/k approaches 1.

6.5. COMMUNICATION CAPABILITIES OF PC-FMCW

In this section, we illustrate the communication capability of the PC-FMCW waveform and assess the communication performance of two signal processing approaches, the filter bank and the PLC group delay filter. For communication purposes, the PC-FMCW waveforms must be synchronized to compensate the delay between the transmitted and received signals. Such synchronization can be achieved using global positioning system (GPS), and synchronized chirp can be generated to minimize the delay between transmitting and receiving channels [95]. Alternatively, the time, frequency and phase offset can be estimated in a data-driven fashion by transmitting initial (pivot) radar-only sweep during predetermined time intervals, and the beat frequency signal can be compensated from the communication signal [33]. Identifying the most effective ways for PC-FMCW waveforms synchronization is an ongoing research topic. In this thesis,

we assume the communication receiver knows the delay of the transmitted waveform and uses the synchronized chirp signal as the reference signal for compensating the beat frequency signal. Then, the received PC-FMCW signal (2.12) captured along with the noise is mixed with the complex conjugate of the reference signal and low-pass filtered to get rid of the chirp signal. Then, the received communication signal with delay can be obtained as:

$$\begin{aligned} x_{\mathrm{s}}(t) &= \{x_{\mathrm{r}}(t) + n(t)\}\, e^{j(2\pi f_c(t-\tau(t))+\pi k(t-\tau(t))^2)} \\ &= \alpha_0 s(t-\tau_0) + \bar{n}(t), \end{aligned} \tag{6.30}$$

where $n(t)$ is a white complex Gaussian noise signal with power spectral density N_0, and $\bar{n}(t)$ is the resulting white complex Gaussian noise signal after dechipring and filtering. Herein, the signal-to-noise ratio (SNR) can be defined as SNR $= {\alpha_0}^2/N_0$. After the mixer, the beat frequency signal will have either zero carrier frequency or a very small frequency offset for the mutually moving transmitter and receiver. Given the knowledge of the delay and waveform parameters, the communication receiver can compensate the delay offset in the code $s(t)$. After delay compensation, the received communication signal can be written as:

$$x_{\mathrm{c}}(t) = \alpha_0 s(t) + \bar{n}(t), \tag{6.31}$$

Subsequently, the transmitted communication data can be reconstructed by using techniques such as the Viterbi algorithm, which is widely used for optimal maximum likelihood sequence detection [122]. Note that the filter bank approach will obtain the noisy communication signal given in (6.31). On the other hand, the phase lag compensated group delay receiver will have the noisy received signal where the communication signal is modified with a PLC filter as $x_{\mathrm{c}}(t) = \alpha_0 \hat{s}(t) + \bar{n}(t)$. In this case, the spectrum of the received communication signal needs to be multiplied with the group delay filter (4.12) to compensate the effect on a code term initiated by a PLC filter. However, this will distort (lose) some parts of the communication signal due to applying a non-linear shift. The impact of such a distortion on communication performance will be investigated in the following simulations.

Assume an automotive radar transmits the PC-FMCW waveform at a carrier frequency $f_c = 77$ GHz with chirp duration $T = 25.6$ μs and chirp bandwidth $B = 300$ MHz. For numerical simulations, we consider GMSK coding for the phase modulation of communication signal $s(t)$ since it can provide low spectral broadening as explained in Chapter 3. We utilize the random code sequences and set the 3-dB bandwidth of the Gaussian filter to two times the chip bandwidth. The code bandwidth is controlled with the number of chips per chirp as $B_c = N_c/T$, e.g., the code with $N_c = 1024$ number of chips within a sweep has $B_c = 40$ MHz code bandwidth. For the PLC group delay receiver, we perform phase lag compensation before transmission for the GMSK phase-coded signal. In addition, we assume a complex Gaussian noise with a power spectral density N_0 is captured with the received signal, and we define SNR $= {\alpha_0}^2/N_0$. The received signal is mixed with the reference signal. Then, the resulting signal (6.30) is low-pass filtered with $f_{\mathrm{cut}} = \pm 40$ MHz and sampled with $f_s = 80$ MHz. After delay compensation, the filter bank method obtains the received communication signal as given in (6.31). For the PLC group delay filter receiver, we apply the group delay filter to the received communication signal. Then, we apply the Viterbi Algorithm to reconstruct the communication data.

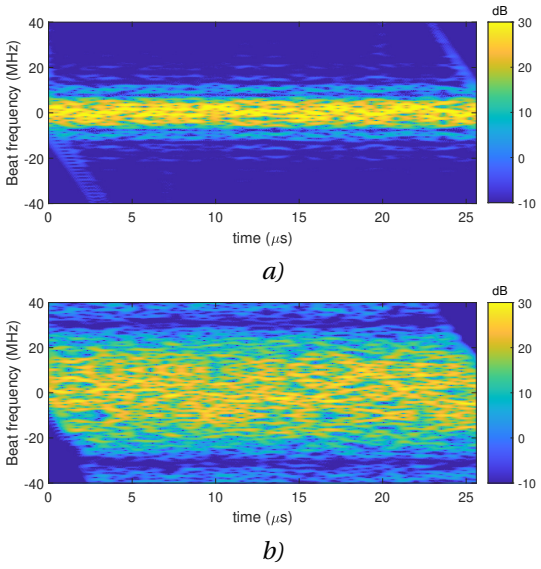

Figure 6.13: Spectrogram of the communication signal after PLC and group delay filter: a) $N_c = 256$ b) $N_c = 1024$.

First, we investigate the distortion effect on the received code due to the group delay filter. To focus on the impact, we consider a noise-free case and demonstrate the spectrogram of the communication signal after the group delay filter in Figure 6.13. It can be seen that the group delay filter applies a non-linear frequency shift and distorts (loses some

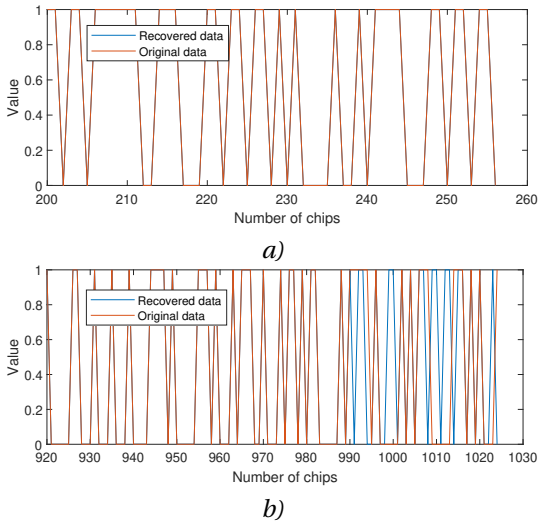

Figure 6.14: Recovered data with a different code bandwidth after using PLC group delay receiver: a) $N_c = 256$ b) $N_c = 1024$.

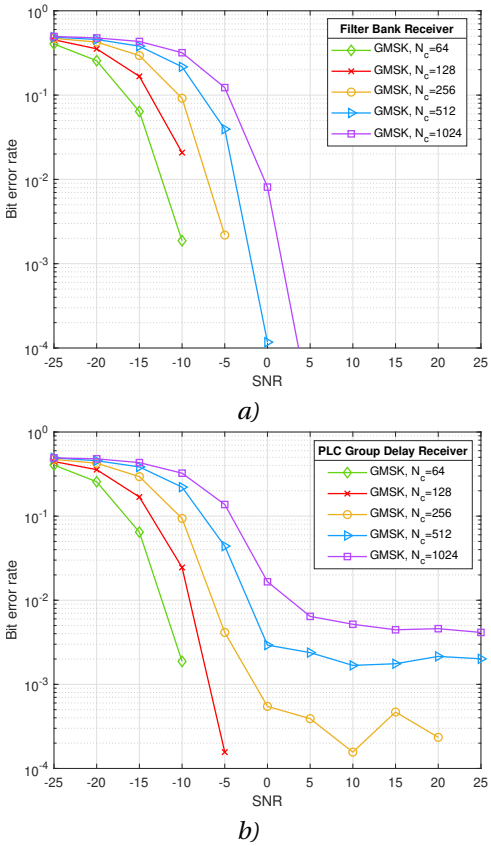

Figure 6.15: Communication performance comparison: Bit error rate versus SNR a) Filter bank receiver b) PLC Group delay filter receiver.

parts of) the received communication signal. Such a distortion becomes crucial when the code bandwidth increases as it is affected more by the non-linear shifts (Figure 6.13 b). To examine this issue, we illustrate the recovered data with a different code bandwidth for the noise-free case in Figure 6.14. It can be observed that the communication data is fully recovered with $N_c = 256$ case. However, the code with $N_c = 1024$ chips is not recovered properly due to the severe distortion effect on the code, i.e. the end of the recovered communication data is obtained differently than the original data (Figure 6.14). To avoid such a problem, the guarding cells need to be placed on the transmitted communication signal. The application of proper guarding cells to protect the received communication data from this distortion effect is a subject to be considered in future.

To highlight the degradation in the communication performance, we compare the bit error rate versus SNR for both processing methods in Figure 6.15. We set the noise power N_0 relative to the absolute of α_0 and change SNR in the interval $SNR \in [-25, 25]$ dB. For a given SNR, we perform 100 trials with different code sequences and count the number of errors. Note that both receivers use the same code sequence during each iteration for a

fair comparison. Then for a given SNR, we calculate the bit error rate as the ratio between the total number of errors and the total number of chips. As shown in Figure 6.15, the bit error rate is comparable up to $N_c = 256$ in the low SNR cases for both processing methods. Thereafter, the PLC group delay filter receiver provides a notably higher bit error rate. In particular, the bit error rate raises up to $\sim 10^{-2}$ as the number of chips goes $N_c = 1024$ in 5 dB SNR case. It can be seen that the bit error rate of the PLC group delay filter receiver remains stable for the codes with more than $N_c = 256$ symbols, although SNR increases.

6.6. CONCLUSIONS

In this chapter, the interference resilience and communication capabilities of the developed PC-FMCW radar have been studied. First, the automotive radar interference problem between different types of continuous waveforms has been investigated. The radar-to-radar interference analysis for various types of continuous waveforms is extended, and a novel generalised radar-to-radar interference equation which can cover different specific cases described in the literature is introduced. The derived generalised equation can be directly applied in cases of multiple interferers and multiple targets. By using the proposed equation, it is possible to simulate various interference scenarios in the intermediate (beat) frequency fast and accurately. Furthermore, the introduced equation describes the instantaneous spectrum of the victim radar for different waveforms to examine the features of the interference. This knowledge can be exploited to create data set for the interference classification and identify the received interference type.

Afterwards, the PC-FMCW waveforms are processed with the phase lag compensated group delay filter receiver, and the interference resilience of the PLC GMSK PC-FMCW radar is investigated. Based on the spectral characteristics of the captured FMCW interference, the interference can appear as wide-band or narrow-band interference. To this end, we consider coherent NB, coherent WB and non-coherent WB interference scenarios and compare their influence on the FMCW and PC-FMCW victim radar's sensing performance. For the FMCW victim radar, it is shown that the interference peak power is concentrated at one particular range bin and appears as a ghost target in the coherent NB interference case. In the case of WB interference, the interference peak power is spread over multiple range bins for coherent WB and multiple range-Doppler cells for non-coherent WB. As a result, these WB interference cases raise the noise floor of the FMCW victim radar. On the other hand, since each PC-FMCW waveform is modulated with its own orthogonal code, only the self-transmitted signal is perfectly decoded while the other interferer signals remain coded, i.e. their peak powers are spread and suppressed. To this end, the effectiveness of the PC-FMCW radar in suppressing both narrow-band interference and wide-band interference is demonstrated and verified by simulations. It is shown that the developed PC-FMCW radar spreads the peak power of the interference signal over the range-Doppler profile by combining phase coding in both fast-time and slow-time. Consequently, the PC-FMCW radar improves the SIR in range profile compared to the FMCW radar case.

Finally, the communication capabilities of PC-FMCW radars with dechirping receivers are studied. We compared the communication performance of the PC-FMCW waveform processed with the phase lag compensated group delay filter and filter bank receivers. It is shown that the phase lag compensated group delay filter receiver distorts the received

communication signal. The reason for distortion is that the phase lag compensated group delay filter receiver applies a non-linear shift to the communication signal, which results in losing some part of the communication signal during data recovery. We investigate the bit error rate versus SNR for both processing approaches. It is demonstrated that both methods provide a similar bit error rate for a short to moderate bandwidth of the code signal. However, the bit error rate degradation increases with code bandwidth, and thus the phase lag compensated group delay receiver provides worse communication performance than the filter bank approach in case of large code bandwidth.

7

Conclusions And Future Work

7.1. MAJOR RESULTS AND NOVELTIES

This thesis describes research on the design of new waveforms and processing steps for the FMCW MIMO radar, which will be robust against mutual and self-interference. The major results of this PhD research are discussed in the following subsections.

- *Phase-Coded FMCW: Waveform Properties and Receivers (Chapter 2)*

  The sensing properties of the PC-FMCW is investigated using the ambiguity function. It is demonstrated that the PC-FMCW waveforms have good Doppler tolerance and high range resolution similar to a chirp signal. Furthermore, different code families, namely random, Gold, ZCZ and Kasami codes, are investigated to use with the PC-FMCW waveform. The sensing performance of the investigated code families in application to PC-FMCW is demonstrated and compared for the first time. It is shown that the sidelobe values in the range profile of PC-FMCW might be essentially different from the sidelobe levels of code auto-correlation function, and hence different code families can provide very similar sensing performance for PC-FMCW. Afterwards, the filter bank and group delay filter receiver structures are investigated to reduce the sampling requirements of the PC-FMCW waveforms. The sensing performance of the investigated receivers is compared numerically and demonstrated experimentally for the first time. It is shown that the sensing performance is degraded as the code bandwidth increases for both processing methods, and there is a trade-off between the sensing and the code bandwidth of the waveform. In the case of the large code bandwidth, the filter bank approach provides favourable performance as the distortion of the phase-coded signal becomes crucial for the group delay filter. Hence, the performance degradation due to the undesired dispersion effect limits the code bandwidth in the group delay filter. However, the group delay filter has much lower computational complexity ($\mathcal{O}(N\log_2(N))$) compared to the filter bank approach ($\mathcal{O}(N^2)$). Moreover, the group delay filter receiver aims to decode the phase-coded signal completely and obtain a beat signal similar to conventional FMCW radar. This will potentially help to re-utilize all software algorithms previously developed for the FMCW radar. Therefore, the group delay filter receiver is more suitable for automotive radars if the current limitations are addressed and decoding is done properly.

- *Smoothed PC-FMCW Waveform and its Properties (Chapter 3)*

  The beat signal spreading is studied analytically, and the spectrum of the BPSK phase-coded beat signal spectrum signal is derived. It is demonstrated that the BPSK coding leads to a short burst in the instantaneous frequency (mathematically represented as Dirac delta) due to abrupt phase changes. Such sharp phase changes broaden the coded beat signal spectrum, and hence the coded beat signals suffer from filtering of the spectrum in the limited receiver analogue bandwidth. Moreover, the group delay filter dispersion effect becomes more severe for such sharp phase changes. Phase smoothing operation is proposed to reduce the spectrum widening of the coded beat signals, and the SPC-FMCW waveforms are introduced. In particular, the Gaussian filter is utilized for smoothing operation, and Gaussian PC-FMCW and GMSK PC-FMCW waveforms are derived. The introduced wave-

forms are analyzed in different domains for the first time. It is shown that the proposed smoothing operation reduces the spectrum widening of the coded beat signal. Afterwards, the investigated waveforms are processed with the group delay filter receiver, and their sensing performance is assessed. It is illustrated that the GMSK PC-FMCW waveform provides lower sidelobe levels and superior sensing performance compared to BPSK PC-FMCW and Gaussian PC-FMCW waveforms.

- *Receiver Design for PC-FMCW Radar (Chapter 4)*

  The group delay filter receiver's current limitations are addressed, and the proper receiving strategy with a low cost and computational complexity is developed to process the PC-FMCW waveforms. The effects of the group delay filter on the coded beat signal are analyzed in detail, and the phase lag compensation on the transmitted phase coded signal is proposed to recover the beat signals after the decoding. The properties of the phase lag compensated PC-FMCW waveforms are investigated analytically and verified experimentally. It is seen that the PSL of the waveforms improved substantially (especially for large code bandwidth) by performing the proposed phase lag compensation. Moreover, the introduced waveforms and processing steps keep the good Doppler tolerance of the FMCW waveforms. It is demonstrated that the smoothing operation helps to decrease the PSL and PAPR while using large code bandwidth to provide high cross-isolation performance. Both numerical simulations and experimental measurements show that the phase lag compensated GMSK PC-FMCW can provide sensing performance similar to the conventional FMCW radar while achieving high cross-isolation performance to improve the coexistence of multiple radars within the same spectrum.

- *PC-FMCW MIMO Radar (Chapter 5)*

  The PC-FMCW waveforms are used to achieve simultaneous MIMO transmission, and the coherent PC-FMCW MIMO radar is investigated. The MIMO ambiguity function is examined for the separation capability of the PC-FMCW waveforms with different codes. Moreover, it is seen that the MIMO ambiguity function of the PMCW suffers from the Doppler frequency shift while the sidelobe levels in the PC-FMCW waveforms remain stable with the increased Doppler frequency. Afterwards, the developed PLC GMSK PC-FMCW waveform is applied to a coherent MIMO radar, and a novel PC-FMCW MIMO structure is proposed. Phase codings in both fast-time and slow-time are jointly utilized to lower the sidelobe levels in the range-Doppler-azimuth domains for the simultaneous MIMO transmission. The performance of the introduced MIMO radar is evaluated and compared with the state-of-the-art techniques. Such a system's sensing performance and practical limitations are analyzed numerically and verified experimentally for the first time. It is demonstrated that the proposed MIMO structure provides low sidelobe levels with simultaneous transmission while keeping high range resolution, unambiguous velocity, good Doppler tolerance, low ADC sampling requirement and computational efficiency. Therefore, the proposed MIMO technique can be effectively utilized by automotive radar sensors to enhance the sensing performance of coherent MIMO transmission.

- *PC-FMCW: Interference Resilience and Communication Capabilities (Chapter 6)*

  The automotive radar interference between different types of continuous waveforms is investigated, and a novel generalised radar-to-radar interference equation is proposed. It is shown that the various interference scenarios described in the literature can be obtained from the introduced equation fast and adequately. Moreover, the experimental verification of the introduced equation to describe the instantaneous spectrum of the victim radar for different waveforms is demonstrated. Afterwards, the robustness of the developed PLC GMSK PC-FMCW radar against different types of FMCW interference scenarios is investigated for the first time. The numerical simulations illustrate and verify the effectiveness of the PC-FMCW waveforms in suppressing both narrow-band and wide-band interference cases. It is demonstrated that the developed PC-FMCW radar spreads the peak power of the interference signal over the range-Doppler map, and thus it improves the SIR in range profile compared to the FMCW radar case. Furthermore, the communication performance of the GMSK PC-FMCW with phase lag compensated group delay filter and filter bank receivers are examined. It is shown that the former receiver distorts the received communication signal due to applying a non-linear shift, and hence it suffers from the bit error rate degradation as the code bandwidth increases.

The major conclusion from these studies is that a new waveform for the FMCW MIMO radar has been proposed, which is compatible with existing FMCW technology, and the signal processing methods are established to be implemented keeping the current low signal sampling requirements in the FMCW radars. The new waveform is more robust to both external interference of radars with different transmitted waveforms (PMCW, FMCW, PC-FMCW) but also self-interference in the MIMO radars, allowing simultaneous MIMO transmission using both fast-time and slow-time coding of transmitted waveforms. The waveform and accompanying radar structure have been patented by NXP Semiconductors [142].

7.2. RECOMMENDATIONS FOR FUTURE WORK

The following recommendations are intended as possible starting points for further research:

- *Finding optimal parameters for smoother and investigation of different smoothing filters.* This thesis utilizes the Gaussian filter to obtain a smooth phase transition. Based on the required spectral characteristics, different smoothing filters can be selected. Moreover, the smoother bandwidth (3-dB bandwidth of the Gaussian filter) is set two times the chip bandwidth in this thesis. The smoother parameters can be optimized to improve the PSL, PAPR and cross-isolation performance of the waveform. Therefore, it is recommended to explore possible improvements using different smoother filters and their parameter optimization.

- *Code optimization.* In this thesis, we generally use the random code sequence as other codes with different auto-correlation functions provide very similar sensing performance for PC-FMCW. It is demonstrated that codes optimized for the PMCW

application, such as the ZCZ code, might not be suitable for using with PC-FMCW. Since the correlation property of the code changes after frequency modulation, it would be interesting to explore code optimization depending on what goal the PC-FMCW waveform is supposed to achieve. Moreover, the existing codes are optimized for periodic correlation properties. For the PC-FMCW waveforms, however, aperiodic auto-correlation properties are important. Thus, it is recommended to have a closer look at a new code design to enhance the sensing, communication and cross-isolation performance of the PC-FMCW waveform.

- *Investigation of the communication performance.* Within this thesis, we focus on the sensing performance of the waveform and illustrate the communication capability briefly. The detailed analysis of the communication performance is outside of the scope of this thesis. For future research, the impacts of group delay filter receiver and smoothing operation on the communication bit error rate are suggested to be examined in detail. Moreover, synchronization of the PC-FMCW waveforms and appropriate placement of the guarding cells to protect the received communication data are recommended to be investigated.

A

DERIVATIVES OF DIFFERENT TYPES OF PHASE CODE

In this proof, we demonstrate the taking derivative of the different types of phase code with respect to time. Recall that the rectangle function can be written as:

$$\text{rect}\left(\frac{t-x}{y}\right) = u\left(t-x+\frac{y}{2}\right) - u\left(t-x-\frac{y}{2}\right), \tag{A.1}$$

where u is a unit step function. Similarly, the code term can be written as:

$$\phi_n \text{rect}\left(\frac{t-(n-\frac{1}{2})T_c}{T_c}\right) = \phi_n u\left(t-(n-\frac{1}{2})T_c+\frac{T_c}{2}\right) - \phi_n u\left(t-(n-\frac{1}{2})T_c-\frac{T_c}{2}\right), \tag{A.2}$$

and

$$\phi_{n+1} \text{rect}\left(\frac{t-(n+\frac{1}{2})T_c}{T_c}\right) = \phi_{n+1} u\left(t-(n+\frac{1}{2})T_c+\frac{T_c}{2}\right) - \phi_{n+1} u\left(t-(n+\frac{1}{2})T_c-\frac{T_c}{2}\right), \tag{A.3}$$

for the n^{th} and $(n+1)^{\text{th}}$ elements, respectively. Note that the $\phi_n \in \{0,\pi\}$ denotes the phase corresponding to the n^{th} bit of the N_c bits sequence. To take the summation of unit step functions, we have to consider a junction point in which the adjacent elements are linked. Thus, the relevant junction point includes the right part of the n^{th} and left part of the $(n+1)^{\text{th}}$ elements and the phase of the BPSK code can be represented as:

$$\phi_{\text{bpsk}}(t) = \sum_{n=1}^{N_c} (\phi_{n+1} - \phi_n)\, u(t-nT_c). \tag{A.4}$$

where the amplitude of the unit step function varies between π and $-\pi$ depending on the value $(\phi_{n+1}-\phi_n)$, and the summation of the unit step functions gives the phase of the BPSK code sequence $\phi_{\text{bpsk}}(t) \in \{0,\pi\}$. In the following subsections, we derive the instantaneous frequency of the different types of phase code.

A

A.1. BPSK

Taking the derivative of the $\phi_{\text{bpsk}}(t)$ gives:

$$\frac{1}{2\pi}\frac{d}{dt}\phi_{\text{bpsk}}(t) = \frac{1}{2\pi}\sum_{n=1}^{N_c}(\phi_{n+1}-\phi_n)\,\delta(t-nT_c). \tag{A.5}$$

where δ is the Dirac delta function. Same result can be seen in [8].

A.2. GAUSSIAN

The convolution of the unit step function with filter $h_0(t) = e^{-t^2}$ where $t \geq 0$ can be represented as:

$$\begin{aligned} u(t)\otimes h_0(t) &= \int_{-\infty}^{\infty} h_0(\tau)\,u(t-\tau)\,d\tau = \int_0^t h_0(\tau)\,d\tau \\ &= \int_0^t e^{-\tau^2}\,d\tau = \frac{\sqrt{\pi}}{2}\text{erf}(t), \end{aligned} \tag{A.6}$$

where erf(t) represents the error function as:

$$\text{erf(t)} = \frac{2}{\sqrt{\pi}}\int_0^{\text{t}} \text{e}^{-\text{t}^2}\,\text{dt}. \tag{A.7}$$

Subsequently, the convolution of the unit step function and the Gaussian filter $h(t) = \frac{\eta}{\sqrt{\pi}}e^{-\eta^2 t^2}$ can be written as:

$$u(t)\otimes h(t) = \int_0^t h(\tau)\,d\tau = \int_0^t \frac{\eta}{\sqrt{\pi}}e^{-\eta^2\tau^2}\,d\tau. \tag{A.8}$$

Replacing $\gamma = \eta\tau$ and $d\gamma = \eta d\tau$, the equation becomes:

$$\begin{aligned} u(t)\otimes h(t) &= \frac{1}{\sqrt{\pi}}\int_0^{\eta t} e^{-\gamma^2}\,d\gamma \\ &= \frac{1}{2}\text{erf}(\eta t). \end{aligned} \tag{A.9}$$

Consequently, the phase of the Gaussian binary code can be written as:

$$\begin{aligned} \phi_{\text{gauss}}(t) &= \phi_{\text{bpsk}}(t)\otimes h(t) \\ &= \frac{1}{2}\sum_{n=1}^{N_c}(\phi_{n+1}-\phi_n)\,\text{erf}\big(\eta(t-nT_c)\big). \end{aligned} \tag{A.10}$$

The derivative of the error function can be obtained as:

$$\frac{d}{dt}\left(\text{erf(t)}\right) = \frac{2}{\sqrt{\pi}}e^{-t^2}. \tag{A.11}$$

Subsequently, taking the derivative of (A.10) with respect to time gives:

$$\frac{1}{2\pi}\frac{d}{dt}\phi_{\text{gauss}}(t) = \frac{\eta}{2\pi\sqrt{\pi}}\sum_{n=1}^{N_c}(\phi_{n+1}-\phi_n)e^{-\eta^2(t-nT_c)^2}. \tag{A.12}$$

A.3. GMSK

The phase of the GMSK can be represented as:

$$\phi_{\text{gmsk}}(t) = \int_{-\infty}^{\infty} \phi_{\text{gauss}}(t)\,dt = \int_{-\infty}^{\infty} (\phi_{\text{bpsk}}(t) \otimes h(t))\,dt. \tag{A.13}$$

Taking the derivative of the $\phi_{\text{gmsk}}(t)$ gives:

$$\begin{aligned} \frac{1}{2\pi}\frac{d}{dt}\phi_{\text{gmsk}}(t) &= \frac{1}{2\pi}\phi_{\text{gauss}}(t) \\ &= \frac{1}{4\pi}\sum_{n=1}^{N_c}(\phi_{n+1}-\phi_n)\,\text{erf}\big(\eta(t-nT_c)\big). \end{aligned} \tag{A.14}$$

B

CHARACTERISTICS OF DIFFERENT AUTOMOTIVE RADAR INTERFERENCE TYPES

In this part, we use the proposed generalised radar-to-radar equation to model the characteristics of other common interference cases seen in automotive radars.

FMCW RADAR VS CW INTERFERER

We can realise this scenario by choosing $N_a = 0$, $k \neq 0$, $N_b = 0$ and $k_{\text{int}} = 0$ in (6.17) and (6.18). The mixer output on the victim radar becomes:

$$\begin{aligned} x_m(t) = \alpha_0 \exp\left(j2\pi\left(f_c\tau + k\tau t - \frac{1}{2}k\tau^2\right)\right) \\ + \alpha_{\text{int}} \exp\left(j2\pi\left(t(f_c - f_{c\text{int}}) + f_{c\text{int}}\tau_{\text{int}} + \frac{1}{2}kt^2\right)\right), \end{aligned} \tag{B.1}$$

and its time-frequency distribution consists of:

$$f_{i_m}(t) \supseteq \{f_{i_{\text{target}}}(t), f_{i_{\text{int}}}(t)\}, \tag{B.2a}$$

$$f_{i_{\text{target}}}(t) = k\tau, \tag{B.2b}$$

$$f_{i_{\text{int}}}(t) = t(k) + (f_c - f_{c\text{int}}). \tag{B.2c}$$

PMCW RADAR VS PMCW INTERFERER

The phase-modulated continuous waveform is usually used for communication purposes [11]. In addition, it may provide possible improvement against interference [83]. Therefore, it has been used in automotive radars in particular cases. It is possible to investigate such a scenario by allowing $N_a \neq 0$, $k = 0$, $N_b \neq 0$ and $k_{\text{int}} = 0$ in (6.17) and (6.18). The mixer output on the victim radar becomes:

$$\begin{aligned} x_m(t) = \alpha_0 \exp\left(j2\pi f_c\tau + \phi_{\text{tar}_{\text{code}}}(t)\right) \\ + \alpha_{\text{int}} \exp\left(j2\pi\left(t(f_c - f_{c\text{int}}) + f_{c\text{int}}\tau_{int}\right) + \phi_{\text{int}_{\text{code}}}(t)\right), \end{aligned} \tag{B.3}$$

and its time-frequency distribution consists of:

$$f_{i_m}(t) \supseteq \{f_{i_{\text{target}}}(t), f_{i_{\text{int}}}(t)\}, \tag{B.4a}$$

$$f_{i_{\text{target}}}(t) = \frac{1}{2\pi}\sum_{n=1}^{N_a}(\phi_{n+1}-\phi_n)\delta(t-\tau-nT_a), \tag{B.4b}$$

$$f_{i_{\text{int}}}(t) = (f_c - f_{c_{\text{int}}}) + \frac{1}{2\pi}\sum_{n=1}^{N_b}(\phi_{n+1}-\phi_n)\delta(t-\tau_{\text{int}}-nT_b). \tag{B.4c}$$

FMCW RADAR VS PMCW INTERFERER

The impacts of PMCW interference on FMCW radar are studied in [77]. In addition to that paper, we can analyse the interference features for this specific scenario by setting $N_a = 0$, $k \neq 0$, $N_b \neq 0$ and $k_{\text{int}} = 0$ in (6.17) and (6.18). The mixer output on the victim radar becomes:

$$\begin{aligned} x_m(t) = {} & \alpha_0 \exp\left(j2\pi\left(f_c\tau + k\tau t - \frac{1}{2}k\tau^2\right)\right) \\ & + \alpha_{\text{int}} \exp\left(j2\pi\left(t(f_c - f_{c_{\text{int}}}) + f_{c_{\text{int}}}\tau_{\text{int}} + \frac{1}{2}kt^2\right) + \phi_{\text{int}_{\text{code}}}(t)\right), \end{aligned} \tag{B.5}$$

and its time-frequency distribution consists of:

$$f_{i_m}(t) \supseteq \{f_{i_{\text{target}}}(t), f_{i_{\text{int}}}(t)\}, \tag{B.6a}$$

$$f_{i_{\text{target}}}(t) = k\tau, \tag{B.6b}$$

$$f_{i_{\text{int}}}(t) = t(k) + (f_c - f_{c_{\text{int}}}) + \frac{1}{2\pi}\sum_{n=1}^{N_b}(\phi_{n+1}-\phi_n)\delta(t-\tau_{\text{int}}-nT_b). \tag{B.6c}$$

PC-FMCW RADAR VS PC-FMCW INTERFERER

The scenario in which PC-FMCW radar is interfered with by another PC-FMCW can be explored by choosing $N_a \neq 0$, $k \neq 0$, $N_b \neq 0$ and $k_{\text{int}} \neq 0$ in (6.17) and (6.18). The mixer output on the victim radar becomes:

$$\begin{aligned} x_m(t) = {} & \alpha_0 \exp\left(j2\pi\left(f_c\tau + k\tau t - \frac{1}{2}k\tau^2\right) + \phi_{\text{tar}_{\text{code}}}(t)\right) \\ & + \alpha_{\text{int}} \exp\left(j2\pi\left(t\left(f_c - f_{c_{\text{int}}} + k_{\text{int}}\tau_{\text{int}}\right) + f_{c_{\text{int}}}\tau_{\text{int}} + t^2\left(\frac{1}{2}k - \frac{1}{2}k_{\text{int}}\right) - \frac{1}{2}k_{\text{int}}\tau_{\text{int}}^2\right)\right) \\ & \times \exp\left(\phi_{\text{int}_{\text{code}}}(t)\right), \end{aligned} \tag{B.7}$$

and its time-frequency distribution consists of:

$$f_{i_m}(t) \supseteq \{f_{i_{\text{target}}}(t), f_{i_{\text{int}}}(t)\}, \tag{B.8a}$$

$$f_{i_{\text{target}}}(t) = k\tau + \frac{1}{2\pi}\sum_{n=1}^{N_a}(\phi_{n+1}-\phi_n)\delta(t-\tau-nT_a), \tag{B.8b}$$

$$f_{i_{\text{int}}}(t) = t(k-k_{\text{int}}) + (f_c - f_{c_{\text{int}}}) + k_{\text{int}}\tau_{\text{int}} + \frac{1}{2\pi}\sum_{n=1}^{N_b}(\phi_{n+1}-\phi_n)\delta(t-\tau_{\text{int}}-nT_b). \tag{B.8c}$$

C

IMPACTS OF FMCW INTERFERENCE ON RANGE-DOPPLER

In this part, we focus on the FMCW radar vs FMCW interferer case, and quantitatively analyze the influence of FMCW interference on the FMCW victim radar's range-Doppler profile.

C.1. EFFECTS ON THE RANGE PROFILE

The time-domain representation of mixer output for the FMCW vs FMCW interference case is given (6.19). After dechirping, the target echo signal starts at τ and ends at T. For an arbitrary starting and ending point of the interference, we denote t_1 and t_2 as the starting and ending time instances of the dechirping process between captured interference signal and the reference transmit signal. Then, we take the Fourier transform of the mixer output to investigate the effect of interference on the range profile. The resulting signal in the frequency domain can be written as:

$$X_m(f_1) = X_{m_{\text{target}}}(f_1) + X_{m_{\text{int}}}(f_1) \tag{C.1}$$

where the spectrum of the target and interference signals can be represented as:

$$\begin{aligned} X_{m_{\text{target}}}(f_1) &= \alpha_0 \int_{\tau}^{T} e^{\left(j2\pi\left(f_c\tau + k\tau t - \frac{1}{2}k\tau^2\right)\right)} e^{(-j2\pi f_1 t)}\, dt \\ &= \alpha_0 e^{\left(j2\pi\left(f_c\tau - \frac{1}{2}k\tau^2\right)\right)} \int_{\tau}^{T} e^{(j2\pi(k\tau - f_1)t)}\, dt \\ &= \alpha_0 e^{\left(j2\pi\left(f_c\tau - \frac{1}{2}k\tau^2\right)\right)} \frac{1}{j2\pi(k\tau - f_1)} \left(e^{(j2\pi(k\tau - f_1)T)} - e^{(j2\pi(k\tau - f_1)\tau)}\right), \end{aligned} \tag{C.2}$$

and

$$
\begin{aligned}
X_{m_{\text{int}}}(f_1) &= \alpha_{\text{int}} \int_{t_1}^{t_2} e^{\left(j2\pi\left(t(f_c - f_{c_{\text{int}}} + k_{\text{int}}\tau_{\text{int}}) + f_{c_{\text{int}}}\tau_{\text{int}} + t^2\left(\frac{1}{2}k - \frac{1}{2}k_{\text{int}}\right) - \frac{1}{2}k_{\text{int}}\tau_{\text{int}}^2\right)\right)} e^{(-j2\pi f_1 t)}\, dt \\
&= \alpha_{\text{int}} e^{\left(j2\pi\left(f_{c_{\text{int}}}\tau_{\text{int}} - \frac{1}{2}k_{\text{int}}\tau_{\text{int}}^2\right)\right)} \int_{t_1}^{t_2} e^{\left(j\pi(k-k_{\text{int}})t^2 + j2\pi(f_c - f_{c_{\text{int}}} - f_1 + k_{\text{int}}\tau_{\text{int}})t\right)}\, dt \\
&= \alpha_{\text{int}} e^{\left(j2\pi\left(f_{c_{\text{int}}}\tau_{\text{int}} - \frac{1}{2}k_{\text{int}}\tau_{\text{int}}^2\right)\right)} \int_{t_1}^{t_2} e^{-(j\pi\alpha_1 t^2 - j2\pi\beta_1 t)}\, dt \\
&= \alpha_{\text{int}} e^{\left(j2\pi\left(f_{c_{\text{int}}}\tau_{\text{int}} - \frac{1}{2}k_{\text{int}}\tau_{\text{int}}^2\right)\right)} \int_{t_1}^{t_2} e^{-\left(j\pi\alpha_1 t^2 - j2\pi\beta_1 t + \left(\frac{j\pi\beta_1}{\sqrt{j\pi\alpha_1}}\right)^2 - \left(\frac{j\pi\beta_1}{\sqrt{j\pi\alpha_1}}\right)^2\right)}\, dt \\
&= \alpha_{\text{int}} e^{\left(j2\pi\left(f_{c_{\text{int}}}\tau_{\text{int}} - \frac{1}{2}k_{\text{int}}\tau_{\text{int}}^2\right)\right)} e^{\left(\frac{j\pi\beta_1}{\sqrt{j\pi\alpha_1}}\right)^2} \int_{t_1}^{t_2} e^{-\left(\sqrt{j\pi\alpha_1}t - \frac{j\pi\beta_1}{\sqrt{j\pi\alpha_1}}\right)^2}\, dt \\
&= \alpha_{\text{int}} e^{\left(j2\pi\left(f_{c_{\text{int}}}\tau_{\text{int}} - \frac{1}{2}k_{\text{int}}\tau_{\text{int}}^2\right)\right)} e^{\left(\frac{j\pi\beta_1}{\sqrt{j\pi\alpha_1}}\right)^2} \frac{1}{\sqrt{j\pi\alpha_1}} \int_{\gamma_1}^{\gamma_2} e^{-(\gamma)^2}\, d\gamma \\
&= \alpha_{\text{int}} e^{\left(j2\pi\left(f_{c_{\text{int}}}\tau_{\text{int}} - \frac{1}{2}k_{\text{int}}\tau_{\text{int}}^2\right)\right)} e^{\left(\frac{j\pi\beta_1}{\sqrt{j\pi\alpha_1}}\right)^2} \frac{1}{\sqrt{j\pi\alpha_1}} \frac{\sqrt{\pi}}{2}\left(\text{erf}(\gamma_2) - \text{erf}(\gamma_1)\right) \\
&= \alpha_{\text{int}} e^{\left(j2\pi\left(f_{c_{\text{int}}}\tau_{\text{int}} - \frac{1}{2}k_{\text{int}}\tau_{\text{int}}^2\right)\right)} e^{\left(\frac{j\pi\beta_1}{\sqrt{j\pi\alpha_1}}\right)^2} \\
&\times \frac{1}{2\sqrt{j\alpha_1}}\left(\text{erf}\left(\sqrt{j\pi\alpha_1}\, t_2 - \frac{j\pi\beta_1}{\sqrt{j\pi\alpha_1}}\right) - \text{erf}\left(\sqrt{j\pi\alpha_1}\, t_1 - \frac{j\pi\beta_1}{\sqrt{j\pi\alpha_1}}\right)\right) \\
&= \alpha_{\text{int}} e^{\left(j2\pi\left(f_{c_{\text{int}}}\tau_{\text{int}} - \frac{1}{2}k_{\text{int}}\tau_{\text{int}}^2\right)\right)} e^{\left(\frac{j\pi(f_c - f_{c_{\text{int}}} - f_1 + k_{\text{int}}\tau_{\text{int}})}{\sqrt{j\pi(k_{\text{int}} - k)}}\right)^2} \\
&\times \frac{1}{2\sqrt{j(k_{\text{int}} - k)}}\left(\text{erf}\left(\sqrt{j\pi(k_{\text{int}} - k)}\, t_2 - \frac{j\pi(f_c - f_{c_{\text{int}}} - f_1 + k_{\text{int}}\tau_{\text{int}})}{\sqrt{j\pi(k_{\text{int}} - k)}}\right)\right. \\
&\qquad \left. - \text{erf}\left(\sqrt{j\pi(k_{\text{int}} - k)}\, t_1 - \frac{j\pi(f_c - f_{c_{\text{int}}} - f_1 + k_{\text{int}}\tau_{\text{int}})}{\sqrt{j\pi(k_{\text{int}} - k)}}\right)\right),
\end{aligned}
\tag{C.3}
$$

where erf is the error function. Herein, we used the substitutes as $\gamma = \sqrt{j\pi\alpha_1}\, t - \frac{j\pi\beta_1}{\sqrt{j\pi\alpha_1}}$, $d\gamma = \sqrt{j\pi\alpha_1}\, dt$, $\alpha_1 = (k_{\text{int}} - k)$, $\beta_1 = (f_c - f_{c_{\text{int}}} - f_1 + k_{\text{int}}\tau_{\text{int}})$. The beat frequency component in the resulting signal can be converted to range using $f_b = k\tau$ as:

$$
R = \frac{cT}{2B} f_1, \tag{C.4}
$$

where the positive frequency bins span $0 \leq f_1 \leq f_s/2$ and the associated range bins span $0 \leq R \leq R_{\max}$ for a given ADC sampling frequency f_s. As explained in Chapter 1, the captured interference might create narrowband or wideband interference scenarios based on the spectral characteristics of the interference. The relationship between the interference spectral characteristic and the resulting interference effect can be seen in (C.3). In the case of $k_{\text{int}} \neq k$, the error functions cause a chirp-like signal with the

combination of two ripples while the error functions start to create a sinc-like response, as k_{int} approaches to k.

C.2. EFFECTS ON THE RANGE-DOPPLER PROFILE

In the FMCW automotive radars, multiple chirp pulses are used for velocity estimation. In the case of having different chirp duration, the starting time instance of captured interference will be different for each chirp pulse, resulting in non-coherent interference. Since the non-coherent interference causes different Doppler frequency shifts for each chirp, it is difficult to model such a scenario. However, the coherent interference case, where the victim and interfering sensors have the same chirp duration, can be modelled to derive an analytical expression for the range-Doppler profile. Assume both victim and interfering radars transmit N_p number of pulses with a chirp duration T. The velocity difference among the chirp pulses introduces a term $\exp(j2\pi f_d mT)$, where f_d is the Doppler frequency shift and m is the index of chirp pulses (slow-time) as $0 \leq m \leq N_p - 1$. Then, the fast-time and slow-time representation of mixer output for the FMCW vs FMCW interference case given in (6.19) can be recast as:

$$\begin{aligned} x_m(t,m) = {} & \alpha_0 \exp\left(j2\pi\left(f_c\tau + k\tau t - \frac{1}{2}k\tau^2\right)\right)\exp\left(j2\pi f_{d_{\text{tar}}} mT\right) \\ & + \alpha_{\text{int}} \exp\left(j2\pi\left(t\left(f_c - f_{c_{\text{int}}} + k_{\text{int}}\tau_{\text{int}}\right) + f_{c_{\text{int}}}\tau_{\text{int}} + t^2\left(\frac{1}{2}k - \frac{1}{2}k_{\text{int}}\right) - \frac{1}{2}k_{\text{int}}\tau_{\text{int}}^2\right)\right) \\ & \times \exp\left(j2\pi f_{d_{\text{int}}} mT\right), \end{aligned} \tag{C.5}$$

To obtain the range-Doppler profile, we take the Fourier transform in both domains. Taking the two-dimensional Fourier transform, the resulting mixer output on the victim radar can be written as:

$$X_m(f_1, f_2) = X_{m_{\text{target}}}(f_1, f_2) + X_{m_{\text{int}}}(f_1, f_2). \tag{C.6}$$

Note that while taking the Fourier transform along the particular domain, the terms related to other domain is constant and can be taken outside of the integral. Then, taking the Fourier transform along the fast-time and slow-time gives the signal associated with the target as:

$$\begin{aligned} X_{m_{\text{target}}}(f_1, f_2) &= \alpha_0 e^{\left(j2\pi\left(f_c\tau - \frac{1}{2}k\tau^2\right)\right)} \frac{1}{j2\pi(k\tau - f_1)}\left(e^{(j2\pi(k\tau - f_1)T)} - e^{(j2\pi(k\tau - f_1)\tau)}\right) \\ &\quad \times \int_0^{N_p-1} e^{\left(j2\pi f_{d_{\text{tar}}} mT\right)} e^{(-j2\pi f_2 m)}\, dm \\ &= \alpha_0 e^{\left(j2\pi\left(f_c\tau - \frac{1}{2}k\tau^2\right)\right)} \frac{1}{j2\pi(k\tau - f_1)}\left(e^{(j2\pi(k\tau - f_1)T)} - e^{(j2\pi(k\tau - f_1)\tau)}\right) \\ &\quad \times \frac{1}{j2\pi\left(2\frac{v_{\text{tar}}}{\lambda}T - f_2\right)}\left(e^{\left(j2\pi\left(2\frac{v_{\text{tar}}}{\lambda}T - f_2\right)(N_p-1)\right)} - 1\right), \end{aligned} \tag{C.7}$$

where $f_{d_{\text{tar}}} = \frac{2v_{\text{tar}}}{\lambda}$ and v_{tar} is the target velocity. Similarly, taking the two-dimensional Fourier transform along the fast-time and slow-time gives the signal associated with

interference as:

$$
\begin{aligned}
X_{m_{\text{int}}}(f_1, f_2) &= \alpha_{\text{int}} e^{\left(j2\pi\left(f_{c\text{int}}\tau_{\text{int}} - \frac{1}{2}k_{\text{int}}\tau_{\text{int}}^2\right)\right)} e^{\left(\frac{j\pi(f_c - f_{c\text{int}} - f_1 + k_{\text{int}}\tau_{\text{int}})}{\sqrt{j\pi(k_{\text{int}}-k)}}\right)^2} \\
&\times \frac{1}{2\sqrt{j(k_{\text{int}}-k)}} \left(\text{erf}\left(\sqrt{j\pi(k_{\text{int}}-k)}\, t_2 - \frac{j\pi(f_c - f_{c\text{int}} - f_1 + k_{\text{int}}\tau_{\text{int}})}{\sqrt{j\pi(k_{\text{int}}-k)}} \right) \right. \\
&\qquad \left. -\text{erf}\left(\sqrt{j\pi(k_{\text{int}}-k)}\, t_1 - \frac{j\pi(f_c - f_{c\text{int}} - f_1 + k_{\text{int}}\tau_{\text{int}})}{\sqrt{j\pi(k_{\text{int}}-k)}} \right) \right) \\
&\times \int_0^{N_p-1} e^{\left(j2\pi f_{d_{\text{int}}} mT\right)} e^{(-j2\pi f_2 m)}\, dm \\
&= \alpha_{\text{int}} e^{\left(j2\pi\left(f_{c\text{int}}\tau_{\text{int}} - \frac{1}{2}k_{\text{int}}\tau_{\text{int}}^2\right)\right)} e^{\left(\frac{j\pi(f_c - f_{c\text{int}} - f_1 + k_{\text{int}}\tau_{\text{int}})}{\sqrt{j\pi(k_{\text{int}}-k)}}\right)^2} \\
&\times \frac{1}{2\sqrt{j(k_{\text{int}}-k)}} \left(\text{erf}\left(\sqrt{j\pi(k_{\text{int}}-k)}\, t_2 - \frac{j\pi(f_c - f_{c\text{int}} - f_1 + k_{\text{int}}\tau_{\text{int}})}{\sqrt{j\pi(k_{\text{int}}-k)}} \right) \right. \\
&\qquad \left. -\text{erf}\left(\sqrt{j\pi(k_{\text{int}}-k)}\, t_1 - \frac{j\pi(f_c - f_{c\text{int}} - f_1 + k_{\text{int}}\tau_{\text{int}})}{\sqrt{j\pi(k_{\text{int}}-k)}} \right) \right) \\
&\times \frac{1}{j2\pi\left(\frac{v_{\text{int}}}{\lambda_{\text{int}}}T - f_2\right)} \left(e^{\left(j2\pi\left(\frac{v_{\text{int}}}{\lambda_{\text{int}}}T - f_2\right)(N_p-1)\right)} - 1 \right).
\end{aligned}
\tag{C.8}
$$

where $f_{d_{\text{int}}} = \frac{v_{\text{int}}}{\lambda_{\text{int}}}$ and v_{int} is the relative velocity between victim and interfering sensors. Note that the interference signal has one-way propagation, and hence its Doppler frequency shift is determined with v_{int} instead of $2v_{\text{int}}$.

BIBLIOGRAPHY

[1] Society of Automotive Engineers, *Taxonomy and Definitions for Terms Related to Driving Automation Systems for On-Road Motor Vehicles.* SAE International, 2018.

[2] M. Li, R. J. Evans, E. Skafidas, B. Moran, H. T. Doang, R. Koottala, G. Felic, and H. V. Le, "A high performance low cost cmos radar for advanced driving assistance applications," in *2012 International Conference on Connected Vehicles and Expo (ICCVE)*, pp. 197–200, 2012.

[3] R. J. Evans, P. M. Farrell, G. Felic, H. T. Duong, H. V. Le, J. Li, M. Li, W. Moran, and E. Skafidas, "Consumer radar: Opportunities and challenges," in *2014 11th European Radar Conference*, pp. 5–8, 2014.

[4] J. Hasch, E. Topak, R. Schnabel, T. Zwick, R. Weigel, and C. Waldschmidt, "Millimeter-wave technology for automotive radar sensors in the 77 ghz frequency band," *IEEE Transactions on Microwave Theory and Techniques*, vol. 60, no. 3, pp. 845–860, 2012.

[5] I. Bilik, O. Longman, S. Villeval, and J. Tabrikian, "The rise of radar for autonomous vehicles: Signal processing solutions and future research directions," *IEEE Signal Processing Magazine*, vol. 36, no. 5, pp. 20–31, 2019.

[6] G. M. Brooker, "Mutual interference of millimeter-wave radar systems," *IEEE Transactions on Electromagnetic Compatibility*, vol. 49, no. 1, pp. 170–181, 2007.

[7] M. Goppelt, H. L. Blöcher, and W. Menzel, "Automotive radar investigation of mutual interference mechanisms," *Advances in Radio Science*, vol. 8, pp. 55–60, Sept. 2010.

[8] U. Kumbul, F. Uysal, C. S. Vaucher, and A. Yarovoy, "Automotive radar interference study for different radar waveform types," *IET Radar, Sonar & Navigation*, vol. 16, no. 3, pp. 564–577, 2022.

[9] M. Kunert, H. Meinel, C. Fischer, and M. Ahrholdt, "Report on interference density increase by market penetration forecast," in *MOSARIM Consortium, CNTR, Tech. Rep. D1.6, Sep.*, 2010.

[10] T. Schipper, T. Mahler, M. Harter, L. Reichardt, and T. Zwick, "An estimation of the operating range for frequency modulated radars in the presence of interference," in *2013 European Radar Conference*, pp. 227–230, 2013.

[11] S. Alland, W. Stark, M. Ali, and M. Hegde, "Interference in automotive radar systems: Characteristics, mitigation techniques, and current and future research," *IEEE Signal Processing Magazine*, vol. 36, no. 5, pp. 45–59, 2019.

[12] C. Aydogdu, M. F. Keskin, G. K. Carvajal, O. Eriksson, H. Hellsten, H. Herbertsson, E. Nilsson, M. Rydstrom, K. Vanas, and H. Wymeersch, "Radar interference mitigation for automated driving: Exploring proactive strategies," *IEEE Signal Processing Magazine*, vol. 37, no. 4, pp. 72–84, 2020.

[13] T. Schipper, S. Prophet, M. Harter, L. Zwirello, and T. Zwick, "Simulative prediction of the interference potential between radars in common road scenarios," *IEEE Transactions on Electromagnetic Compatibility*, vol. 57, no. 3, pp. 322–328, 2015.

[14] M. Hischke, "Collision warning radar interference," in *Proceedings of the Intelligent Vehicles '95. Symposium*, pp. 13–18, 1995.

[15] A. Al-Hourani, R. J. Evans, S. Kandeepan, B. Moran, and H. Eltom, "Stochastic geometry methods for modeling automotive radar interference," *IEEE Transactions on Intelligent Transportation Systems*, vol. 19, no. 2, pp. 333–344, 2018.

[16] M. Goppelt, H. . Blöcher, and W. Menzel, "Analytical investigation of mutual interference between automotive fmcw radar sensors," in *2011 German Microwave Conference*, pp. 1–4, 2011.

[17] F. Roos, J. Bechter, C. Knill, B. Schweizer, and C. Waldschmidt, "Radar sensors for autonomous driving: Modulation schemes and interference mitigation," *IEEE Microwave Magazine*, vol. 20, no. 9, pp. 58–72, 2019.

[18] D. Schindler, B. Schweizer, C. Knill, J. Hasch, and C. Waldschmidt, "Mimo-ofdm radar using a linear frequency modulated carrier to reduce sampling requirements," *IEEE Transactions on Microwave Theory and Techniques*, vol. 66, no. 7, pp. 3511–3520, 2018.

[19] J. Overdevest, F. Laghezza, F. Jansen, and A. Filippi, "Radar waveform coexistence: Interference comparison on multiple-frame basis," in *2020 17th European Radar Conference (EuRAD)*, pp. 168–171, 2021.

[20] L. L. Tovar Torres, M. Steiner, and C. Waldschmidt, "Channel influence for the analysis of interferences between automotive radars," in *2020 17th European Radar Conference (EuRAD)*, pp. 266–269, 2021.

[21] J. Wang, M. Ding, and A. Yarovoy, "Matrix-pencil approach-based interference mitigation for fmcw radar systems," *IEEE Transactions on Microwave Theory and Techniques*, vol. 69, no. 11, pp. 5099–5115, 2021.

[22] S. M. Patole, M. Torlak, D. Wang, and M. Ali, "Automotive radars: A review of signal processing techniques," *IEEE Signal Processing Magazine*, vol. 34, no. 2, pp. 22–35, 2017.

[23] S. Sun, A. P. Petropulu, and H. V. Poor, "Mimo radar for advanced driver-assistance systems and autonomous driving: Advantages and challenges," *IEEE Signal Processing Magazine*, vol. 37, no. 4, pp. 98–117, 2020.

[24] K. V. Mishra, M. R. Bhavani Shankar, V. Koivunen, B. Ottersten, and S. A. Vorobyov, "Toward millimeter-wave joint radar communications: A signal processing perspective," *IEEE Signal Processing Magazine*, vol. 36, no. 5, pp. 100–114, 2019.

[25] F. Liu, C. Masouros, A. Petropulu, H. Griffiths, and L. Hanzo, "Joint radar and communication design: Applications, state-of-the-art, and the road ahead," *IEEE Transactions on Communications*, vol. 68, pp. 3834–3862, 2020.

[26] R. M. Gutierrez, H. Yu, A. R. Chiriyath, G. Gubash, A. Herschfelt, and D. W. Bliss, "Joint sensing and communications multiple-access system design and experimental characterization," in *2019 IEEE Aerospace Conference*, pp. 1–8, 2019.

[27] S. D. Blunt and E. L. Mokole, "Overview of radar waveform diversity," *IEEE Aerospace and Electronic Systems Magazine*, vol. 31, no. 11, pp. 2–42, 2016.

[28] A. Aubry, V. Carotenuto, A. De Maio, A. Farina, and L. Pallotta, "Optimization theory-based radar waveform design for spectrally dense environments," *IEEE Aerospace and Electronic Systems Magazine*, vol. 31, no. 12, pp. 14–25, 2016.

[29] L. G. de Oliveira, B. Nuss, M. B. Alabd, A. Diewald, M. Pauli, and T. Zwick, "Joint radar-communication systems: Modulation schemes and system design," *IEEE Transactions on Microwave Theory and Techniques*, vol. 70, no. 3, pp. 1521–1551, 2022.

[30] C. Sturm and W. Wiesbeck, "Waveform design and signal processing aspects for fusion of wireless communications and radar sensing," *Proceedings of the IEEE*, vol. 99, no. 7, pp. 1236–1259, 2011.

[31] S. A. Hassani, A. Guevara, K. Parashar, A. Bourdoux, B. van Liempd, and S. Pollin, "An in-band full-duplex transceiver for simultaneous communication and environmental sensing," in *2018 52nd Asilomar Conference on Signals, Systems, and Computers*, pp. 1389–1394, 2018.

[32] C. Sahin, J. Jakabosky, P. M. McCormick, J. G. Metcalf, and S. D. Blunt, "A novel approach for embedding communication symbols into physical radar waveforms," in *2017 IEEE Radar Conference (RadarConf)*, pp. 1498–1503, 2017.

[33] P. M. McCormick, C. Sahin, S. D. Blunt, and J. G. Metcalf, "FMCW implementation of phase-attached radar-communications (PARC)," in *2019 IEEE Radar Conference (RadarConf)*, pp. 1–6, 2019.

[34] D. Ma, N. Shlezinger, T. Huang, Y. Liu, and Y. C. Eldar, "Joint radar-communication strategies for autonomous vehicles: Combining two key automotive technologies," *IEEE Signal Processing Magazine*, vol. 37, no. 4, pp. 85–97, 2020.

[35] C. Aydogdu, M. F. Keskin, N. Garcia, H. Wymeersch, and D. W. Bliss, "RadChat: Spectrum sharing for automotive radar interference mitigation," *IEEE Transactions on Intelligent Transportation Systems*, vol. 22, no. 1, pp. 416–429, 2021.

[36] S. A. Hassani, B. van Liempd, A. Bourdoux, F. Horlin, and S. Pollin, "Joint in-band full-duplex communication and radar processing," *IEEE Systems Journal*, vol. 16, no. 2, pp. 3391–3399, 2022.

[37] J. Bechter, C. Sippel, and C. Waldschmidt, "Bats-inspired frequency hopping for mitigation of interference between automotive radars," in *2016 IEEE MTT-S International Conference on Microwaves for Intelligent Mobility (ICMIM)*, pp. 1–4, 2016.

[38] T.-N. Luo, C.-H. E. Wu, and Y.-J. E. Chen, "A 77-ghz cmos automotive radar transceiver with anti-interference function," *IEEE Transactions on Circuits and Systems I: Regular Papers*, vol. 60, no. 12, pp. 3247–3255, 2013.

[39] S. Skaria, A. Al-Hourani, R. Evans, K. Sithamparanathan, and U. Parampalli, "Interference mitigation in automotive radars using pseudo-random cyclic orthogonal sequences," *Sensors*, vol. 19, p. 4459, 10 2019.

[40] W. Machowski, G. S. Koutsogiannis, and P. A. Ratliff, "Novel pulse-sequences design enables multi-user collision-avoidance vehicular radar," in *2007 International Waveform Diversity and Design Conference*, pp. 155–159, 2007.

[41] G. Cuypers, K. Vanbleu, G. Ysebaert, M. Moonen, and P. Vandaele, "Combining raised cosine windowing and per tone equalization for rfi mitigation in dmt receivers," in *IEEE International Conference on Communications, 2003. ICC '03.*, vol. 4, pp. 2852–2856 vol.4, 2003.

[42] J. Khoury, R. Ramanathan, D. McCloskey, R. Smith, and T. Campbell, "Radarmac: Mitigating radar interference in self-driving cars," in *2016 13th Annual IEEE International Conference on Sensing, Communication, and Networking (SECON)*, pp. 1–9, 2016.

[43] M. F. Keskin, C. Aydogdu, and H. Wymeersch, "Stepped-carrier OFDM V2V resource allocation for sensing and communication convergence," in *2020 14th European Conference on Antennas and Propagation (EuCAP)*, pp. 1–5, 2020.

[44] C. Aydogdu, N. Garcia, L. Hammarstrand, and H. Wymeersch, "Radar communications for combating mutual interference of fmcw radars," in *2019 IEEE Radar Conference (RadarConf)*, pp. 1–6, 2019.

[45] M. F. Keskin, R. F. Tigrek, C. Aydogdu, F. Lampel, H. Wymeersch, A. Alvarado, and F. M. J. Willems, "Peak sidelobe level based waveform optimization for ofdm joint radar-communications," in *2020 17th European Radar Conference (EuRAD)*, pp. 1–4, 2021.

[46] J. Bechter, K. Eid, F. Roos, and C. Waldschmidt, "Digital beamforming to mitigate automotive radar interference," in *2016 IEEE MTT-S International Conference on Microwaves for Intelligent Mobility (ICMIM)*, pp. 1–4, 2016.

[47] J. Bechter, M. Rameez, and C. Waldschmidt, "Analytical and experimental investigations on mitigation of interference in a dbf mimo radar," *IEEE Transactions on Microwave Theory and Techniques*, vol. 65, no. 5, pp. 1727–1734, 2017.

[48] C. Fischer, H. L. Blöcher, J. Dickmann, and W. Menzel, "Robust detection and mitigation of mutual interference in automotive radar," in *2015 16th International Radar Symposium (IRS)*, pp. 143–148, 2015.

[49] M. Rameez, M. Dahl, and M. I. Pettersson, "Adaptive digital beamforming for interference suppression in automotive fmcw radars," in *2018 IEEE Radar Conference (RadarConf18)*, pp. 0252–0256, 2018.

[50] T. Nozawa, Y. Makino, N. Takaya, M. Umehira, S. Takeda, X. Wang, and H. Kuroda, "An anti-collision automotive fmcw radar using time-domain interference detection and suppression," in *International Conference on Radar Systems (Radar 2017)*, pp. 1–5, 2017.

[51] J. Bechter and C. Waldschmidt, "Automotive radar interference mitigation by reconstruction and cancellation of interference component," in *2015 IEEE MTT-S International Conference on Microwaves for Intelligent Mobility (ICMIM)*, pp. 1–4, 2015.

[52] M. Wagner, F. Sulejmani, A. Melzer, P. Meissner, and M. Huemer, "Threshold-free interference cancellation method for automotive fmcw radar systems," in *2018 IEEE International Symposium on Circuits and Systems (ISCAS)*, pp. 1–4, 2018.

[53] K.-W. Gurgel, Y. Barbin, and T. Schlick, "Radio frequency interference suppression techniques in fmcw modulated hf radars," in *OCEANS 2007 - Europe*, pp. 1–4, 2007.

[54] S. Murali, K. Subburaj, B. Ginsburg, and K. Ramasubramanian, "Interference detection in fmcw radar using a complex baseband oversampled receiver," in *2018 IEEE Radar Conference (RadarConf18)*, pp. 1567–1572, 2018.

[55] S. Neemat, O. Krasnov, and A. Yarovoy, "An interference mitigation technique for fmcw radar using beat-frequencies interpolation in the stft domain," *IEEE Transactions on Microwave Theory and Techniques*, vol. 67, no. 3, pp. 1207–1220, 2019.

[56] M. Barjenbruch, D. Kellner, K. Dietmayer, J. Klappstein, and J. Dickmann, "A method for interference cancellation in automotive radar," in *2015 IEEE MTT-S International Conference on Microwaves for Intelligent Mobility (ICMIM)*, pp. 1–4, 2015.

[57] W.-Q. Wang and H. Shao, "Radar-to-radar interference suppression for distributed radar sensor networks," *Remote Sensing*, vol. 6, no. 1, pp. 740–755, 2014.

[58] J.-H. Choi, H.-B. Lee, J. Choi, and S.-C. Kim, "Mutual interference suppression using clipping and weighted-envelope normalization for automotive fmcw radar systems," *IEICE Trans. Commun.*, vol. 99-B, pp. 280–287, 2016.

[59] F. Jin and S. Cao, "Automotive radar interference mitigation using adaptive noise canceller," *IEEE Transactions on Vehicular Technology*, vol. 68, no. 4, pp. 3747–3754, 2019.

[60] E. Elsehely and M. Sobhy, "Reduction of interference in automotive radars using multiscale wavelet transform," in *2001 IEEE International Conference on Acoustics, Speech, and Signal Processing. Proceedings (Cat. No.01CH37221)*, vol. 5, pp. 2881–2884 vol.5, 2001.

[61] J. Bechter, F. Roos, M. Rahman, and C. Waldschmidt, "Automotive radar interference mitigation using a sparse sampling approach," in *2017 European Radar Conference (EURAD)*, pp. 90–93, 2017.

[62] F. Uysal and S. Sanka, "Mitigation of automotive radar interference," in *2018 IEEE Radar Conference (RadarConf18)*, pp. 0405–0410, 2018.

[63] F. Uysal, "Synchronous and asynchronous radar interference mitigation," *IEEE Access*, vol. 7, pp. 5846–5852, 2019.

[64] A. Correas-Serrano and M. A. Gonzalez-Huici, "Sparse reconstruction of chirplets for automotive fmcw radar interference mitigation," in *2019 IEEE MTT-S International Conference on Microwaves for Intelligent Mobility (ICMIM)*, pp. 1–4, 2019.

[65] Y.-S. Son, H.-K. Sung, and S. W. Heo, "Automotive frequency modulated continuous wave radar interference reduction using per-vehicle chirp sequences," *Sensors (Basel, Switzerland)*, vol. 18, 2018.

[66] H. Zhou, P. Cao, and S. Chen, "A novel waveform design for multi-target detection in automotive fmcw radar," in *2016 IEEE Radar Conference (RadarConf)*, pp. 1–5, 2016.

[67] Y. Kim, "Identification of fmcw radar in mutual interference environments using frequency ramp modulation," in *2016 10th European Conference on Antennas and Propagation (EuCAP)*, pp. 1–3, 2016.

[68] M. Umehira, T. Nozawa, Y. Makino, X. Wang, S. Takeda, and H. Kuroda, "A novel iterative inter-radar interference reduction scheme for densely deployed automotive fmcw radars," in *2018 19th International Radar Symposium (IRS)*, pp. 1–10, 2018.

[69] M. Umehira, Y. Makino, T. Okuda, X. Wang, S. Takeda, and H. Kuroda, "Inter-radar interference analysis and concept of scalable fast chirp fmcw radar for automotive applications," in *2019 20th International Radar Symposium (IRS)*, pp. 1–8, 2019.

[70] J.-G. Kim, S.-H. Sim, S. Cheon, and S. Hong, "24 ghz circularly polarized doppler radar with a single antenna," in *2005 European Microwave Conference*, vol. 2, pp. 4 pp.–1386, 2005.

[71] H. Kato and T. Kobayashi, "Detection probability of automotive radars using maximum length sequences to suppress interference from nearby radars," in *NAECON 2014 - IEEE National Aerospace and Electronics Conference*, pp. 396–400, 2014.

[72] H. Kato, T. Kobayashi, and I. Pasya, "Interference suppression performance of automotive uwb radars using pseudo random sequences," *Radioengineering*, vol. 24, pp. 932–939, 2015.

[73] T. Liu, M. Hsu, and Z. Tsai, "Mutual interference of pseudorandom noise radar in automotive collision avoidance application at 24 ghz," in *2016 IEEE 5th Global Conference on Consumer Electronics*, pp. 1–2, 2016.

[74] G. Babur, Z. Wang, O. Krasnov, and L. Ligthart, "Design and implementation of cross-channel interference suppression for polarimetric lfm-cw radar," *Proceedings of SPIE - The International Society for Optical Engineering*, 06 2010.

[75] Z. Xu and Q. Shi, "Interference mitigation for automotive radar using orthogonal noise waveforms," *IEEE Geoscience and Remote Sensing Letters*, vol. 15, no. 1, pp. 137–141, 2018.

[76] L. Sakkila, Y. Elhillali, A. Rivenq, C. Tatkeu, and J. Rouvaen, "Short range automotive radar based on uwb pseudo-random coding," in *2007 7th International Conference on ITS Telecommunications*, pp. 1–6, 2007.

[77] J. Overdevest, F. Jansen, F. Laghezza, F. Uysal, and A. Yarovoy, "Uncorrelated interference in 79 ghz fmcw and pmcw automotive radar," in *2019 20th International Radar Symposium (IRS)*, pp. 1–8, 2019.

[78] G. Babur, O. A. Krasnov, A. Yarovoy, and P. Aubry, "Nearly orthogonal waveforms for mimo fmcw radar," *IEEE Transactions on Aerospace and Electronic Systems*, vol. 49, no. 3, pp. 1426–1437, 2013.

[79] G. Babur, P. Aubry, and F. L. Chevalier, "Simple transmit diversity technique for phased array radar," *IET Radar, Sonar & Navigation*, vol. 10, no. 6, pp. 1046–1056, 2016.

[80] A. Bourdoux, K. Parashar, and M. Bauduin, "Phenomenology of mutual interference of fmcw and pmcw automotive radars," in *2017 IEEE Radar Conference (RadarConf)*, pp. 1709–1714, 2017.

[81] V. Giannini, D. Guermandi, Q. Shi, A. Medra, W. Van Thillo, A. Bourdoux, and P. Wambacq, "A 79 ghz phase-modulated 4 ghz-bw cw radar transmitter in 28 nm cmos," *IEEE Journal of Solid-State Circuits*, vol. 49, no. 12, pp. 2925–2937, 2014.

[82] A. Bourdoux, U. Ahmad, D. Guermandi, S. Brebels, A. Dewilde, and W. Van Thillo, "Pmcw waveform and mimo technique for a 79 ghz cmos automotive radar," in *2016 IEEE Radar Conference (RadarConf)*, pp. 1–5, 2016.

[83] A. Bourdoux and M. Bauduin, "Pmcw waveform cross-correlation characterization and interference mitigation," in *2020 17th European Radar Conference (EuRAD)*, pp. 164–167, 2021.

[84] J. Overdevest, F. Jansen, F. Uysal, and A. Yarovoy, "Doppler influence on waveform orthogonality in 79 ghz mimo phase-coded automotive radar," *IEEE Transactions on Vehicular Technology*, vol. 69, no. 1, pp. 16–25, 2020.

[85] F. Uysal, "Phase-coded fmcw automotive radar: System design and interference mitigation," *IEEE Transactions on Vehicular Technology*, vol. 69, no. 1, pp. 270–281, 2020.

[86] J. Reneau and R. R. Adhami, "Phase-coded lfmcw waveform analysis for short range measurement applications," in *2014 IEEE Aerospace Conference*, pp. 1–6, 2014.

[87] S. D. Blunt, M. Cook, J. Jakabosky, J. De Graaf, and E. Perrins, "Polyphase-coded fm (pcfm) radar waveforms, part i: implementation," *IEEE Transactions on Aerospace and Electronic Systems*, vol. 50, no. 3, pp. 2218–2229, 2014.

[88] F. Lampel, R. F. Tigrek, A. Alvarado, and F. M. J. Willems, "A performance enhancement technique for a joint fmcw radcom system," in *2019 16th European Radar Conference (EuRAD)*, pp. 169–172, 2019.

[89] R. Feger, H. Haderer, and A. Stelzer, "Optimization of codes and weighting functions for binary phase-coded fmcw mimo radars," in *2016 IEEE MTT-S International Conference on Microwaves for Intelligent Mobility (ICMIM)*, pp. 1–4, 2016.

[90] U. Kumbul, F. Uysal, A. Yarovoy, and C. S. Vaucher, "Coded-radar for interference suppression in super-dense environments." Union Radio-Scientifique Internationale (URSI) BENELUX Forum 2019, Brussel, 2019.

[91] F. Uysal, "Phase coded frequency modulated continuous wave radar system." Patent Number NL2020050066W, and WO2020162751A1, Aug 2020.

[92] F. G. Jansen, F. Laghezza, and F. Lampel, "Radar-based communication." U.S Patent Application Number US11204410B2, Dec 2021.

[93] F. Laghezza and F. Lampel, "Predistortion technique for joint radar/communication systems." U.S Patent Application Number US20210341567A1, Nov 2021.

[94] U. Kumbul, N. Petrov, C. S. Vaucher, and A. Yarovoy, "Smoothed phase-coded fmcw: Waveform properties and transceiver architecture," *IEEE Transactions on Aerospace and Electronic Systems*, pp. 1–18, 2022. doi: 10.1109/TAES.2022.3206173.

[95] F. Lampel, F. Uysal, F. Tigrek, S. Orru, A. Alvarado, F. Willems, and A. Yarovoy, "System level synchronization of phase-coded fmcw automotive radars for radcom," in *2020 14th European Conference on Antennas and Propagation (EuCAP)*, pp. 1–5, 2020.

[96] S. D. Blunt, J. K. Jakabosky, C. A. Mohr, P. M. McCormick, J. W. Owen, B. Ravenscroft, C. Sahin, G. D. Zook, C. C. Jones, J. G. Metcalf, and T. Higgins, "Principles and applications of random fm radar waveform design," *IEEE Aerospace and Electronic Systems Magazine*, vol. 35, no. 10, pp. 20–28, 2020.

[97] U. Kumbul, N. Petrov, F. van der Zwan, C. S. Vaucher, and A. Yarovoy, "Experimental investigation of phase coded fmcw for sensing and communications," in *2021 15th European Conference on Antennas and Propagation (EuCAP)*, pp. 1–5, 2021.

[98] U. Tan, C. Adnet, O. Rabaste, F. Arlery, J. . Ovarlez, and J. . Guyvarch, "Phase code optimization for coherent mimo radar via a gradient descent," in *2016 IEEE Radar Conference (RadarConf)*, pp. 1–6, 2016.

[99] M. Bekar, C. J. Baker, E. G. Hoare, and M. Gashinova, "Joint mimo radar and communication system using a psk-lfm waveform with tdm and cdm approaches," *IEEE Sensors Journal*, vol. 21, no. 5, pp. 6115–6124, 2021.

[100] C. A. Mohr, P. M. McCormick, C. A. Topliff, S. D. Blunt, and J. M. Baden, "Gradient-based optimization of pcfm radar waveforms," *IEEE Transactions on Aerospace and Electronic Systems*, pp. 1–1, 2020.

[101] U. Kumbul, N. Petrov, C. S. Vaucher, and A. Yarovoy, "Receiver structures for phase modulated fmcw radars," in *2022 16th European Conference on Antennas and Propagation (EuCAP)*, pp. 1–5, 2022.

[102] M. A. Richards, *Fundamentals of Radar Signal Processing*. US: McGraw-Hill, 2005.

[103] M. I. Skolnik, *Introduction to Radar Systems*. New York: McGraw-Hill, 2 ed., 1980.

[104] M. I. Skolnik, *Radar handbook*. McGraw-Hill Education, 2008.

[105] A. G. Stove, "Linear fmcw radar techniques," *IEE Proceedings F - Radar and Signal Processing*, vol. 139, no. 5, pp. 343–350, 1992.

[106] M. Jankiraman, *FMCW Radar Design*. Massachusetts: Artech House, 2018.

[107] P. Z. Fan, N. Suehiro, N. Kuroyanagi, and X. M. Deng, "Class of binary sequences with zero correlation zone," *Electronics Letters*, vol. 35, no. 10, pp. 777–779, 1999.

[108] A. M. D. Turkmani and U. S. Goni, "Performance evaluation of maximal-length, gold and kasami codes as spreading sequences in cdma systems," in *Proceedings of 2nd IEEE International Conference on Universal Personal Communications*, vol. 2, pp. 970–974 vol.2, 1993.

[109] M. Golay, "Complementary series," *IRE Transactions on Information Theory*, vol. 7, no. 2, pp. 82–87, 1961.

[110] R. Frank, "Polyphase complementary codes," *IEEE Transactions on Information Theory*, vol. 26, no. 6, pp. 641–647, 1980.

[111] E. García, J. A. Paredes, F. J. Álvarez, M. C. Pérez, and J. J. García, "Spreading sequences in active sensing: A review," *Signal Processing*, vol. 106, pp. 88 – 105, 2015.

[112] F. Uysal and S. Orru, "Phase-coded fmcw automotive radar: Application and challenges," in *2020 IEEE International Radar Conference (RADAR)*, pp. 478–482, 2020.

[113] N. Levanon and E. Mozeson, *Radar signals*. NJ, USA: John Wiley & Sons, Ltd, 2004.

[114] U. Kumbul, N. Petrov, C. S. Vaucher, and A. Yarovoy, "Sensing performance of different codes for phase-coded fmcw radars," in *2022 19th European Radar Conference (EuRAD)*, pp. 1–4, 2022.

[115] M.-E. Chatzitheodoridi, A. Taylor, and O. Rabaste, "A mismatched filter for integrated sidelobe level minimization over a continuous doppler shift interval," in *2020 IEEE Radar Conference (RadarConf20)*, pp. 1–6, 2020.

[116] N. Petrov, *Migrating Target Detection in Wideband Radars*. Phd thesis, TU Delft, Delft, The Netherlands, 2019.

[117] N. Petrov and A. G. Yarovoy, "Fractional fourier transform receiver for modulated chirp waveforms," *IEEE Transactions on Microwave Theory and Techniques*, pp. 1–9, 2022. doi: 10.1109/TMTT.2022.3222225.

[118] O. A. Krasnov, L. P. Ligthart, Zhijian Li, P. Lys, and F. van der Zwan, "The PARSAX - full polarimetric FMCW radar with dual-orthogonal signals," in *2008 European Radar Conference*, pp. 84–87, 2008.

[119] K. Miller and M. Rochwarger, "On estimating spectral moments in the presence of colored noise," *IEEE Transactions on Information Theory*, vol. 16, no. 3, pp. 303–309, 1970.

[120] R. J. Doviak and D. S. Zrnić, *Doppler Radar and Weather Observations*. US: Academic Press, 1993.

[121] T. J. Rouphael, *RF and digital signal processing for software-defined radio: A multi-standard multi-mode approach*. Amsterdam: Newnes, 2009.

[122] M. K. Simon, *Bandwidth-Efficient Digital Modulation with Application to Deep Space Communications*. New Jersey: John Wiley & Sons, Inc., 2003.

[123] T. Svedek, M. Herceg, and T. Matić, "A simple signal shaper for gmsk/gfsk and msk modulator based on sigma-delta look-up table," *Radioengineering*, vol. 18, pp. 230–237, 2009.

[124] A. Papoulis, *Systems and Transforms with Applications in Optics*. New-York: McGraw-Hill, 1968.

[125] F. Lampel, A. Alvarado, and F. M. Willems, "Dispersion compensation for phase-coded fmcw radars," in *2022 23rd International Radar Symposium (IRS)*, pp. 36–41, 2022.

[126] H. Sun, F. Brigui, and M. Lesturgie, "Analysis and comparison of mimo radar waveforms," in *2014 International Radar Conference*, pp. 1–6, 2014.

[127] U. Kumbul, N. Petrov, S. Yuan, C. S. Vaucher, and A. Yarovoy, "Mimo ambiguity functions of different codes with application to phase-coded fmcw radars," in *IET International Radar Conference (IET IRC 2022)*, pp. 1–6, 2022.

[128] U. Kumbul, N. Petrov, C. S. Vaucher, and A. Yarovoy, "Phase-coded fmcw for coherent mimo radar," *IEEE Transactions on Microwave Theory and Techniques*, pp. 1–13, 2022. doi: 10.1109/TMTT.2022.3228950.

[129] J. Guetlein, S. Bertl, A. Kirschner, and J. Detlefsen, "Switching scheme for a fmcw-mimo radar on a moving platform," in *2012 9th European Radar Conference*, pp. 91–94, 2012.

[130] D. Zoeke and A. Ziroff, "Phase migration effects in moving target localization using switched mimo arrays," in *2015 European Radar Conference (EuRAD)*, pp. 85–88, 2015.

[131] J. Bechter, F. Roos, and C. Waldschmidt, "Compensation of motion-induced phase errors in tdm mimo radars," *IEEE Microwave and Wireless Components Letters*, vol. 27, no. 12, pp. 1164–1166, 2017.

[132] F. Jansen, "Automotive radar doppler division mimo with velocity ambiguity resolving capabilities," in *2019 16th European Radar Conference (EuRAD)*, pp. 245–248, 2019.

[133] P. Wang, P. Boufounos, H. Mansour, and P. V. Orlik, "Slow-time mimo-fmcw automotive radar detection with imperfect waveform separation," in *ICASSP 2020 - 2020 IEEE International Conference on Acoustics, Speech and Signal Processing (ICASSP)*, pp. 8634–8638, 2020.

[134] S. Li, L. Zhang, N. Liu, J. Zhang, and S. Tang, "Transmit diversity technique based on joint slow-time coding with circulating code," *IET Radar, Sonar & Navigation*, vol. 11, no. 8, pp. 1243–1250, 2017.

[135] D. Schindler, B. Schweizer, C. Knill, J. Hasch, and C. Waldschmidt, "Mimo-ofdm radar using a linear frequency modulated carrier to reduce sampling requirements," *IEEE Transactions on Microwave Theory and Techniques*, vol. 66, no. 7, pp. 3511–3520, 2018.

[136] J. Li and P. Stoica, *MIMO Radar Signal Processing*. NJ, USA: John Wiley & Sons, Ltd, 2008.

[137] D. R. Fuhrmann and G. San Antonio, "Transmit beamforming for mimo radar systems using signal cross-correlation," *IEEE Transactions on Aerospace and Electronic Systems*, vol. 44, no. 1, pp. 171–186, 2008.

[138] S. Ahmed, P. Aubry, and A. Yarovoy, "Experimental study on multi-channel waveform agile beamforming and testbed calibration," in *2021 IEEE Conference on Antenna Measurements & Applications (CAMA)*, pp. 248–253, 2021.

[139] M. Toth, P. Meissner, A. Melzer, and K. Witrisal, "Analytical investigation of non-coherent mutual fmcw radar interference," in *2018 15th European Radar Conference (EuRAD)*, pp. 71–74, 2018.

[140] F. Norouzian, A. Pirkani, E. Hoare, M. Cherniakov, and M. Gashinova, "Phenomenology of automotive radar interference," *IET Radar, Sonar & Navigation*, vol. 15, no. 9, pp. 1045–1060, 2021.

[141] Y. He, X. Li, R. Li, J. Wang, and X. Jing, "A deep-learning method for radar micro-doppler spectrogram restoration," *Sensors*, vol. 20, no. 17, p. 5007, 2020.

[142] C. S. Vaucher, U. Kumbul, N. Petrov, and A. Yarovoy, "Phase-coded fmcw radar waveform and accompanying radar architecture." US Patent Application, patent is filed, 2022.

ACKNOWLEDGEMENTS

My PhD journey has been one of the most important stages of my life for my personal and scientific development. This PhD study would not be possible without a great deal of support and feedback from the people surrounding me. I would like to thank all of them for helping me during my PhD journey.

First of all, I would like to express my sincere gratitude to my promotor Prof. dr. Alexander Yarovoy, for his continuous support during my PhD study. His guidance, encouragement and advice during the difficult stages of my research helped me a lot in the past four years. It is thanks to him that I have learned how to sharpen my research questions, obtain novel results and effectively present them. I am grateful for his support, patience and guidance during my development as an individual researcher.

Second, I would like to sincerely thank my promotor Prof. dr. Cicero Silveria Vaucher, for giving me the opportunity to conduct this PhD research. I am thankful to him for introducing me to this challenging topic, sharing his expertise and always providing me feedback. His immense knowledge and practical point of view on automotive radars have led to many insightful discussions and suggestions. I feel lucky to have the privilege of working with an inspirational person like him.

Third, I would like to thank my co-promotor and daily supervisor Dr. Nikita Petrov. His meticulous personality and crucial comments improved the quality of my research and this dissertation substantially. I am grateful to him for letting me grow as an independent researcher by making my own mistakes and discoveries. Aside from the healthy professional relationship, I have enjoyed the time sharing the office with Nikita. His friendship and constructive feedback have helped me to broaden the scope of my research.

Furthermore, I sincerely thank Dr. Faruk Uysal for his daily supervision during the first year of my PhD. He has always been willing to help, and I could rely on his prompt feedback and support whenever there was a problem. His wide knowledge and experience in radar signal processing and simulations taught me a lot. I truly appreciate our fruitful discussions and his support for my research. His positive outlook has made the hard work look easier.

I would like to thank my senior colleagues Dr. Yanki Aslan, Dr. Francesco Fioranelli, Dr. Oleg Krasnov and Dr. Hans Driessen for the insightful scientific discussions and the time we spent together in the MS3 group and conferences. I also wish to acknowledge the assistance of Fred van der Zwan, Pascal Aubry and Peter Swart for the measurements and to collect the experimental radar data. I also express my gratitude to Esther de Klerk and Minke van der Put for their great help with administrative issues.

Moreover, I would like to thank my committee members Prof. Dr. Leo de Vreede, Prof. Dr. Frans Willems, Prof. Dr. Kostas Doris, Prof. Dr. Martin Vossiek and Prof. Dr. Geert Leus, for their comments and for evaluating my thesis. I would also like to thank NXP Semiconductors N.V. for the financial support during my research. Special thanks to

company engineers Feike Jansen, Nur Engin and Alessio Filippi for the discussions we had during the meetings and conferences.

I would like to express my sincere thanks to my current and former office mates Max Schöpe, Tworit Dash, Feza Celik, Sen Yuan and Saravanan Nagesh for the insightful discussions and the fun time we spent together. I would like to convey my thanks to all the former and present colleagues in the MS3 group for the time spent there. Of the many, I want to thank: Nicolas Kruse, Berk Onat, Jianping Wang, Ozan Dogan, Ignacio Roldan, Ronny Guendel, Wietse Bouwmeester, Merel Verhoef, Romain Vergez, Rutkay Guneri, Prithvi Thyagarajan, Shengzhi Xu, Sharef Neemat and Simin Zhu.

Additionally, I would like to thank my friends Fehmi Kunter, Deniz Kunter, Berk Ekici and Aybuke Erol for spending a good time together in the Netherlands. I appreciate your accompany in every way that considerably helped me while dealing with the pandemic. I also wish to thank my friends from Turkey: Burak Dogan, Aral Zorkun, Serhat Karatas, Umut Toker and Ekim Kurtulmaz for having a great time together.

I am infinitely grateful to my parents Bekir Kumbul and Zübeyde Kumbul for their unconditional love, support and sacrifice over all these years. I will be forever in debt to you. I would also like to express my gratitude to my brother Uygar Kumbul for his support, encouragement and inspiration since my childhood. I love you with all my heart.

Finally, I would like to express my deepest gratitude to my beloved wife Manolya Nur Kumbul for her unwavering support, continuous encouragement and sacrifice. You have always been there to support me, share my stress and change my depressed mood into an optimistic one. Thank you for your patience over all these years when seeing me working in the evenings or at the weekends, and for accompanying me even when I was intolerable. I would not have finished my thesis without you. Thank you for creating the most memorable moments of my life.

CURRICULUM VITÆ

Utku KUMBUL

BIOGRAPHY

Utku Kumbul was born in Antalya, Turkey, in 1990. He received his BSc degree with honors in Electrical and Electronics Engineering in 2014 and his second BSc degree with honors in Computer Engineering (Double Major Program) in 2015, both from the Atilim University, Ankara, Turkey. In 2017, he received the MSc degree in Electrical and Electronics Engineering from the TOBB University of Economics and Technology, Ankara, Turkey. Between 2017 and 2018, he worked as a hardware engineer at Havelsan Ehsim, Air Electronic Warfare Systems Eng. Inc., in Ankara, where he was part of the passive radar and decoy projects. In March 2019, he joined the Microwave Sensing, Signals and Systems (MS3) group in the Faculty of Electrical Engineering, Mathematics, and Computer Science (EEMCS) at Delft University of Technology as a PhD candidate. He is a member of IEEE society and he serves as a reviewer for IEEE Transactions on Aerospace and Electronic Systems, and IET Radar, Sonar and Navigation. His main research interests include waveform design, radar signal processing, interference mitigation, MIMO systems and automotive radars.

EDUCATION

2019-2023 PhD. Electrical Engineering
Delft University of Technology, The Netherlands
Thesis: Phase-Coded FMCW for Automotive Radars
Promotor: Prof. dr. A. Yarovoy
Promotor: Prof. dr. C. S. Vaucher
Copromotor: Dr. N. Petrov

2015-2017 MSc. Electrical and Electronics Engineering
TOBB University of Economics and Technology, Turkey
C.GPA: 4.00/4.00
Research area: Radar Signal Processing
Thesis: Knowledge-Aided Adaptive Detection with Multipath Exploitation Radar
Supervisor: Dr. H.Y. Hayvaci

2011-2015 BSc. Computer Engineering
Atilim University, Turkey
Double Major Program
C.GPA: 3.85/4.00

2009-2014 BSc. Electrical and Electronics Engineering
Atilim University, Turkey
C.GPA: 4.00/4.00

AWARDS

2015 1st rank graduate from the Department of Computer Engineering, Atilim University, Turkey

2014 1st rank graduate from the Atilim University, Turkey
Top scoring student in the University, Faculty of Engineering and Department of Electrical & Electronics Engineering, Atilim University, Turkey

2013 Runner-up award with the project entitled “Wireless Telemetry System for Solar Car” in undergraduate research project festival, Atilim University, Turkey

LIST OF PUBLICATIONS

10. **U. Kumbul**, N. Petrov, C. S. Vaucher, and A. Yarovoy, "Performance Analysis of Phase-Coded FMCW for Joint Sensing and Communication," in *2023 24th International Radar Symposium (IRS)*, submitted.

9. **U. Kumbul**, Y. Chen, N. Petrov, C. S. Vaucher, and A. Yarovoy, "Impacts of Mutual Interference Analysis in FMCW Automotive Radar," in *2023 17th European Conference on Antennas and Propagation (EuCAP)*, accepted.

8. **U. Kumbul**, N. Petrov, C. S. Vaucher, and A. Yarovoy, "Phase-Coded FMCW for coherent MIMO radar", in *IEEE Transactions on Microwave Theory and Techniques*, pp. 1–13, 2022.

7. **U. Kumbul**, N. Petrov, C. S. Vaucher, and A. Yarovoy, "Smoothed phase-coded FMCW: Waveform properties and transceiver architecture", in *IEEE Transactions on Aerospace and Electronic Systems*, pp. 1–18, 2022.

6. **U. Kumbul**, N. Petrov, S. Yuan, C. S. Vaucher, and A. Yarovoy, "MIMO ambiguity functions of different codes with application to phase-coded FMCW radars", in *IET International Radar Conference (IET IRC 2022)*, pp. 1–6, 2022.

5. **U. Kumbul**, N. Petrov, C. S. Vaucher, and A. Yarovoy, "Sensing performance of different codes for phase-coded FMCW radars", in *2022 19th European Radar Conference (EuRAD)*, pp. 1–4, 2022.

4. **U. Kumbul**, N. Petrov, C. S. Vaucher, and A. Yarovoy, "Receiver structures for phase modulated FMCW radars", in *2022 16th European Conference on Antennas and Propagation (EuCAP)*, pp. 1-5, 2022.

3. **U. Kumbul**, F. Uysal, C. S. Vaucher, and A. Yarovoy, "Automotive radar interference study for different radar waveform types", in *IET Radar, Sonar & Navigation*, vol. 16, no. 3, pp. 564-577, 2022.

2. **U. Kumbul**, N. Petrov, F. van der Zwan, C. S. Vaucher, and A. Yarovoy, "Experimental investigation of phase coded FMCW for sensing and communications", in *2021 15th European Conference on Antennas and Propagation (EuCAP)*, pp. 1-5, 2021.

1. **U. Kumbul**, F. Uysal, A. Yarovoy and C. S. Vaucher,"Coded-radar for interference suppression in super-dense environments,", Union Radio-Scientifique Internationale (URSI) BENELUX Forum 2019, Brussel, 2019.

Patent

1. C. S. Vaucher, **U. Kumbul**, N. Petrov, and A. Yarovoy, "Phase-Coded FMCW radar waveform and accompanying radar architecture", in *US Patent Application*, patent is filed, 2022.